Modeling and simulation of the boiling crisis within PWR at CFD scale

Luc Favre

▶ **To cite this version:**

Luc Favre. Modeling and simulation of the boiling crisis within PWR at CFD scale. Fluid mechanics [physics.class-ph]. Institut National Polytechnique de Toulouse - INPT, 2023. English. ⟨NNT : 2023INPT0018⟩. ⟨tel-04244931⟩

HAL Id: tel-04244931

https://theses.hal.science/tel-04244931v1

Submitted on 16 Oct 2023

HAL is a multi-disciplinary open access archive for the deposit and dissemination of scientific research documents, whether they are published or not. The documents may come from teaching and research institutions in France or abroad, or from public or private research centers.

L'archive ouverte pluridisciplinaire **HAL**, est destinée au dépôt et à la diffusion de documents scientifiques de niveau recherche, publiés ou non, émanant des établissements d'enseignement et de recherche français ou étrangers, des laboratoires publics ou privés.

HAL Authorization

THÈSE

En vue de l'obtention du

DOCTORAT DE L'UNIVERSITÉ DE TOULOUSE

Délivré par :

Institut National Polytechnique de Toulouse (Toulouse INP)

Discipline ou spécialité :

Energétique et Transferts

Présentée et soutenue par :

M. LUC FAVRE

le vendredi 10 février 2023

Titre :

Modélisation et simulation de la crise d'ébullition dans les REP à l'échelle CFD

Ecole doctorale :

Mécanique, Energétique, Génie civil, Procédés (MEGeP)

Unité de recherche :

Institut de Mécanique des Fluides de Toulouse (IMFT)

Directeurs de Thèse :

MME CATHERINE COLIN

M. STÉPHANE MIMOUNI

Rapporteurs :

M. EMILIO BAGLIETTO, MASSACHUSSETS INSTITUTE OF TECHNOLOGY

M. LUCAS DIRK, HZDR

Membres du jury :

M. MICHEL GRADECK, UNIVERSITÉ LORRAINE, Président

M. GUILLAUME BOIS, CEA SACLAY, Invité(e)

MME CATHERINE COLIN, TOULOUSE INP, Membre

M. STÉPHANE MIMOUNI, EDF CHATOU, Membre

M. STÉPHANE PUJET, EDF CHATOU, Membre

MODELING AND SIMULATION OF THE BOILING CRISIS WITHIN PWR AT CFD SCALE

LUC FAVRE

Towards Improvement of the Modeling of Wall Boiling for Multiphase CFD Simulations

Paris, December 2022

Luc Favre: *Modeling and Simulation of the Boiling Crisis within PWR at CFD scale,* Towards Improvement of the Modeling of Wall Boiling for Multiphase CFD Simulations , December 2022

Great success !

— **Borat Sagdiyev**

Science sans conscience n'est que ruine de l'âme.

— **François Rabelais**

ACKNOWLEDGEMENTS / REMERCIEMENTS

Après trois années de doctorat, je me demande si la section des remerciements n'est pas parmi celles auxquelles j'ai le plus réfléchi. Chaque moment passé avec des proches ou petite pensée nostalgique n'incite qu'à ajouter une ligne pour quelqu'un. Cette thèse ne fera donc pas exception : préparez-vous pour des remerciements à rallonge !

First of all, I want to deeply thank Emilio Baglietto and Dirk Lucas for having accepted to read and evaluate my thesis work as referees. I truly enjoyed the time we spent together before and after the defense and it was a true honor to have both of you as members of the jury.
Merci à Michel Gradeck d'avoir accepté le rôle de président du jury ainsi qu'à Guillaume Bois pour ses questions pertinentes le jour de la soutenance. De manière générale : Merci à tous les membres du jury pour votre bienveillance et l'intérêt que vous avez porté à mes travaux !

Ensuite, mes premières penseés vont évidemment à mes trois encadrants avec qui j'ai eu la chance de travailler pendant ces trois années : Catherine, Stéphane P. et Stéphane M. Leurs qualités tant scientifiques qu'humaines ont clairement été les piliers de ces travaux de doctorat.

Catherine, il va sans dire que cette thèse n'aurait pas connu cet aboutissement sans ton expérience et ton regard affuté sur la physique des écoulements multiphasiques et des changements de phase. En plus d'être la "spécialiste de bulles" (comme j'aimais le dire à mes proches), ta gentillesse, ton humanité et ta présence ont été d'une aide inestimable et je t'en suis profondément reconnaissant. T'avoir comme directrice de thèse fut une réelle chance et est sans aucun doute une des principales raisons m'ayant donné l'envie de m'essayer à une carrière académique ! J'espère sincèrement pouvoir à nouveau échanger et travailler avec toi à l'avenir.

Stéphane P., avec qui je ne compte plus les discussions captivantes tant autour du nucléaire que de la science en général ou encore de politique depuis que je suis arrivé en stage dans le groupe I8C. Ton soutien permanent durant ces trois années, la liberté d'action que tu m'as laissée ainsi que tes remarques et ton expertise d'une pertinence rare ont su me laisser appréhender le travail de recherche dans les meilleures conditions possibles. En ajoutant à cela tous les très bon moments passés ensemble que ça soit de la salle café jusque dans les rues de Los Angeles, tu es à la fois un collègue, un tuteur et un ami. Merci infiniment, pour tout.

Stéphane M., dont l'expérience en tant qu'encadrant de thèse n'est plus à prouver, merci pour ta sympathie naturelle, ton positivisme à toute épreuve et ta curiosité permanente. Avoir une personne intéressée et bienveillante comme toi fut une réelle source de motivation pendant ces trois années. Merci !

Un grand merci tout particulier pour leur soutien à :

- Erwan pour son aide et son intérêt constant pour mes travaux, en particulier sur le cas AGATE sur lequel nous avons beaucoup échangé ainsi que sur les subtilités de *code_saturne* !
- Damien pour sa disponibilité, sa sympathie, son écoute et son aide. Je pense qu'un doctorant ne peut guère rêver meilleur chef de groupe !
- Vladimir sans qui les dernières figures de ce manuscrit n'auraient jamais vu le jour, merci infiniment d'avoir rendu possible le pont entre l'aspect académique et industriel appliqué de ces travaux de thèse !
- Christophe, sans qui je n'aurais jamais vu une crise d'ébullition de mes propres yeux. Merci pour ton intérêt et ton efficacité sans faille sur la FIL ! Promis on finira ça avec un film à la caméra rapide ;)

Il va sans dire que la vie à Chatou ne serait pas la même sans toutes les personnes qui en font un lieu de travail aussi agréable ! En commençant pas le groupe I8C dont l'ambiance me manquera à coup sûr. Des

mercis à foison à : Morgane (promis je te débloquerai sur Zelda un jour), Ueva (sans qui la formation à Zürich n'aurait pas eu la même saveur), Olivier, PV, Igor, Franck M., Eric, Mugurel, Antoine, Muriel, Pierre, André, Pauline, Franck D., Thomas, Qinqing et Sébastien.

Une pensée aussi aux ex-I8C partis vers de nouveaux horizons depuis : Simon, Enrico et Joël !

Un grand merci à tous les autres MFEE avec qui j'ai pu échanger et passer des bons moments, je pense en particulier à Nasser (avec qui passer l'été de 3^{e} année aux pauses cafés du soir a tout autant retardé mon manuscrit que sauvé ma santé mentale), Chaï (pour son aide sur NEPTUNE_CD), William (pour ses retours sur mes travaux et présentations), Aurélien, Joël et Michaël.

Pour les nombreuses bières, partages de galères et soutiens indéfectibles, un immense merci à mes co-doctorants I8C:

- Jacques, co-bureau éternel et spécialiste hardware informatique de référence. Vivre les mêmes enfers avec NEPTUNE_CFD nous a lié à tout jamais je pense... J'espère qu'on pourra se refaire une soirée comme chez toi à coups de discussions jusqu'au bout de la nuit !
- Martin, le seul capable de cumuler une pratique surhumaine du sport en parallèle d'un doctorat en bataillant avec les modes de Graetz, tout en étant sûrement la personne la plus gentille de toute l'île des impressionnistes !
- Gauthier, la relève qui va rendre THYC plus rapide que jamais (entre deux parties de jeux de société).
- Pierre, avec qui j'ai déjà hâte de boire un coup à nouveau à Toulouse pour débattre science, potins et politique !

Parmi tous les doctorants, il y en a qui resteront définitivement des amis bien plus que des collègues:

- Bilal, le frère, le sat depuis le stage de fin d'études. Merci d'avoir été là toutes ces années et d'être encore là aujourd'hui. J'ai déjà hâte de notre prochaine cohabitation en appart à parler politique ma3a jwane et à déconner ensemble.
- Hector, le meilleur partenaire de soirées, jeux, sport, bar, déconnades, et bien sûr CFD de toute l'île des Impressionnistes. En plus d'être un DJ d'exception et un scientifique de haut vol, tu es juste un pilier dans cette histoire donc merci bae. Je sens que cette prochaine année et demie de post-doc à Chatou promet encore de régaler ! (envi de coder)
- Elisa, la fraté toulousaine toujours al à la salle et camarade indéfectible de jeux de rôles. Je suis sûr que tu vas nous sortir des PIV de l'espace pour ta thèse que tu finiras en grandes pompes !

Merci à tous les autres doctorants du site, qu'ils soient MFEE (Guilhem, Guillaume, Antoine, Roger, Gaëtan, Théo et Clément) ou LNHE (Guillaume, Bastien et JP) pour tous les bons moments passés ensemble !

Cette thèse n'aurait jamais vu le jour sans ceux qui m'ont donné l'opportunité de faire mon stage de fin d'étude à MFEE en 2019 : Jérémie et Romain. Merci à tous les deux pour m'avoir initié au milieu de la recherche appliquée au nucléaire, pour votre soutien et pour vos enseignements qui m'ont grandement servi ces trois années !

Un grand merci aux personnes de l'IMFT avec qui j'ai pu discuter science et recherche lors de mes quelques passages, en particulier Frédéric et Julien !

Merci aux personnes du CEA avec qui j'ai pu avoir des discussions durant cette thèse et avec qui j'espère continuer à échanger à l'avenir : Tanguy, Sébastien, Corentin, Antoine et Alan.

Merci à Frédéric Le Quéré et Frédéric Praslon de l'Université Gustave Eiffel pour m'avoir permis d'enseigner un semestre en mathématiques pour la L1 PC/SPI. Cette expérience fut une des plus enrichissantes que j'aie pu vivre et m'a définitivement convaincu de me tourner vers le domaine académique et l'enseignement.

Ce doctorat est l'aboutissement d'une vie d'étudiant, et ne saurait exister sans l'ensemble des professeur.e.s dont j'ai eu la chance de recevoir les enseignements et qui ont construit ma passion pour la science. Un très grand merci (chronologiquement) à : Abdelaziz Benzidia, Jean-François Matte, Charles Vix, Gaëlle Mulard, Antoine Senger, Pascal Guelfi et Emmanuel Plaut.

Un merci tout particulier à (camarade) Rainier et Jean-François, qui m'ont mis le pied à l'étrier pour la recherche et la CFD pendant le projet de recherche en deuxième année d'école d'ingénieur. J'ai déjà hâte de notre prochaine bière ensemble à Nancy !

Merci à ma team Peinkess, Mehdi et Messmer, qui en plus d'être des frères avec qui il est tout aussi passionnant de parler science et politique que de clubber chez Kalle Malle, ont fait le déplacement depuis Liverpool et Oldenburg pour assister à ma soutenance. J'ai maintenant deux voyages de prévus pour aller assister aux vôtres en Y. On l'écrira un jour cet article en commun !

Une grosse pensée va aux amis de l'école, dont le soutien et l'intérêt pour mes bulles les ont poussés jusqu'à écouter toute ma soutenance ! Merci à Chloé (la fraté), Cécilia (la soeur de chicha), Micess (le ienchoss), Kot (mon gros dégueulasse), le B (frère de manif), Solti (que je démonte sur smash à une main), Bucquet (envi de jammer), Iris (mon aubergiste toulousaine), Martin M. (le parrain sûr) et Martin P. (le sosie de Robespierre).

Un grand merci à tous les potes qui ont été présents de près ou de loin toutes ces années :

- La bande d'école d'ingé : Keller, Diane, Nico (L. et P.), Juliette, Théophile et tous les autres de cette grande bande de fous !
- Les sats et colocs à vie Younes, Rody, Marouane, Alae et Hirvin
- La team Bilnancy : Catherine, Bousti, Farès, Mathieu, Thomas, Nadir et Lothaire
- L'ékip ta7 Boudonville et l'école primaire : Justine et Clara
- La mi,f les meufs sûres, les amours : Maru et Marion

Évidemment une vague d'amour et d'olives ininterrompues pour mon FC Chômage à tout jamais : Burno et Suzie (avec qui la coloc pendant cette thèse fut tout autant une source de folie, de motivation et d'amour), Zooky (fan number one de farine de blé), Jean-Loutre (mon antéchrist malchanceux), Lulu (survivant aux déboires de Ferrari et des Canadiens), Sydney (soleil de beau gosse qui a embelli mon séjour aux US), Bouboule (pano poivrot) et Anto (la pornstar).

Merci à Clo (Swagbaiouch à jamais) pour la force et le soutien depuis Marseille bb.

Merci à Myriam, camarade de lutte, pour le plus beau cadeau de thèse : le décapsuleur CGT.

Merci à Dany et Raz pour leurs lives Twitch réguliers qui m'ont permis de tenir bon pendant la rédaction. Le cocktail d'émotions mêlant concentration, fatigue, politisation, explosions de rire et avis tout autant basés que désastreux fut plus efficace que tout pour me donner la force. (désolé d'aspirer à devenir prof.....)

Comment ne pas finir par la famille ! Un immense merci à Suzanne, Pierrot et Fanfan pour être venus depuis la Bourgogne et la Franche-Comté pour venir m'écouter parler de mes bulles en anglais !

Et évidemment, un merci infini et éternel à mes parents. Pour ce que vous êtes, pour ce que vous avez fait de moi, pour votre présence, vos encouragements, votre confiance et votre présence qui continuent aujourd'hui d'être ma chance et mon plus grand soutien.
Merci papa pour m'avoir mis les pieds sur le chemin de la science, m'avoir tant appris, pour m'y avoir laissé faire mon parcours sans jamais me l'imposer, pour m'avoir soutenu, encouragé et conseillé dès que

j'en avais besoin. Pour toutes ces heures passées à discuter en mêlant conneries, recherche, science, et la vie dans son entièreté : sans elles, je ne serais pas devenu la personne que je suis aujourd'hui.
Merci maman pour ton écoute, ton intérêt et ton attention constante tout en me laissant une liberté totale dans mes choix. Toujours prête à venir aider au moindre pépin, au moindre changement de situation : sans toi, ma vie ne serait clairement pas aussi sereine et agréable qu'elle ne l'est depuis toutes ces années. Tu as fait tout ça en supportant mes blagues répétées et insupportables, une maman comme on en fait pas deux !

Merci à Elina, ma sœur, pour les innombrables fous rires (et disputes!) qu'on a pu avoir ensemble, pour nos discussions passionnées de politique, pour sa présence, son humour et son soutien. Tu es une petite sœur par l'âge mais presque une grande sœur par ton esprit et ton intelligence. Hâte de te voir devenir une juriste de génie zebi !

Cette famille est indescriptible de par sa perfection, donc merci à mes trois gros pour tous ces moments chalereux, amusants, sérieux, touchants et passionnants que l'on a vécus tous les quatre (et pour tous ceux à venir).

Enfin, merci à celle qui m'a soutenu tout du long de cette thèse, à celle qui m'a vu dans mes meilleurs comme mes pires moments et qui a toujours su trouver les mots pour me préserver et me motiver. Merci Louise pour tout l'amour que tu me donnes et pour me faire vivre des moments aussi incroyables avec toi. Maintenant c'est à toi d'aller au bout de ta thèse qu'on célébrera comme il se doit dans un an et demi !

À Emmanuel Plaut,
pour ses enseignements et sa rigueur scientifique.

TO THE READER

Dear reader,

This small section aims to detail and acknowledge some of the tools I used during my PhD to produce this work :

- This thesis has been written using LaTeXwith TeXmaker (https://www.xm1math.net/texmaker/) along with the MikTeX distribution (https://miktex.org/), based on the `classicthesis` package (https://ctan.org/pkg/classicthesis).

- The bibliography has been handled using Zotero (https://www.zotero.org/).

- All the models used outside of CFD computations have been developed using Python 3 (https://www.python.org/).

- Most of the figures in this manuscript have been drawn using the Python 3 package `matplotlib` (https://matplotlib.org/) or the LaTeXpackage TikZ (https://tikz.net/).

- Fluid properties in Python 3 models have been computed using the `CoolProp` package (http://www.coolprop.org/):

  Bell Ian H., Wronski Jorrit, Quoilin Sylvain and Lemort Vincent, Pure and Pseudo-pure Fluid Thermophysical Property Evaluation and the Open-Source Thermophysical Property Library CoolProp, Industrial & Engineering Chemistry Research, 53-6 (pp. 2498–2508), 2014, doi:10.1021/ie4033999, http://pubs.acs.org/doi/abs/10.1021/ie4033999

You will find some extra documentation as well as some appendices to this work on my personal website https://www.lfavre.org/ (still to be updated, it should be ready in a couple of months).

If you notice any mistake in the core of the document, if you have any question regarding this work, or if you would like to obtain data, Python programs or results, **feel absolutely free to contact me at my permanent mail address**:

favre.luc05@gmail.com

I hope you will enjoy reading this thesis ! ☺

ABSTRACT

In Pressurized Water Reactors (PWR), the heat released by the nuclear fuel is transferred to the water flowing in the primary circuit, which is pressurized at 150 bar to avoid boiling. However, water can sometimes reach the Onset of Nucleate Boiling (ONB) under accident conditions that can further lead to the Boiling Crisis. At this point, an instantaneous transition between nucleate and film boiling occurs, inducing the formation of a vapor blanket around the fuel rods which acts as a thermal insulation and causes a rapid rise of their temperature, posing a risk of fuel cladding damage. Prediction of the Critical Heat Flux (corresponding to Boiling Crisis occurrence) is thus a primal safety stake, currently achieved using dedicated experimental correlations that do not include detailed description of the boiling physics.

This thesis aims to study the modeling of the boiling physics at a local scale, so-called "CFD" (Computational Fluid Dynamics), which allows simulating boiling flows using a millimeter spatial discretization. The in-house code NEPTUNE_CFD is the reference tool used by EDF R&D to investigate local-scale multiphase physics.

First, simulations of boiling flows in a vertical tube are achieved using NEPTUNE_CFD. Results are compared to the DEBORA experiment (flow boiling of refrigerant R12 that mimics PWR dimensionless numbers) in conditions representative of the industrial situation. The results show a global agreement with the measurements, but display significant discrepancies regarding bubble diameter and wall temperature. The latter is computed through the wall boiling model of NEPTUNE_CFD called "Heat Flux Partitioning", which splits the wall heat flux between different heat transfer mechanisms (convection, phase change, transient conduction, etc.).

The main objective of the thesis then consisted in the development of a new Heat Flux Partitioning model in order to account for a more extensive description of the boiling phenomena, including notably the effect of bubble sliding. A fine modeling of bubble dynamics at the wall has been proposed through a mechanistic approach based on a force balance over the bubble. Forces at stake have been reassessed (drag, added mass, etc.) and allowed satisfactory prediction of bubble detachment diameter as well as sliding velocity at low and high pressure. The Heat Flux Partitioning model has been completed by conducting a precise evaluation of the numerous required closure laws (waiting time, nucleation site density, etc.) through comparisons with experimental measurements from the literature. The newly assembled model has finally been validated against wall temperature measurements and implemented in NEPTUNE_CFD.

The Critical Heat Flux prediction is anchored as a perspective of this framework. Recent experiments showed that the Boiling Crisis can be described using physical parameters involved in the Heat Flux Partitioning formulation. A criterion based on the proportion of wall area covered by bubbles has further been tested using the old NEPTUNE_CFD formulation and showed a coherent qualitative behavior.

Finally, the focus was put on a configuration consisting of a tube with mixing vanes similar to those present in PWR cores. Results of NEPTUNE_CFD simulations showed significant discrepancy regarding core void fraction prediction. Single-phase flow simulations of the same case displayed an overestimation of the liquid's rotation, which could explain the too large vapor gathering at the center for the boiling cases.

keywords : phase change, heat transfer, fluid mechanics, multiphase flows, numerical simulations

RÉSUMÉ

Dans un Réacteur à Eau Pressurisée (REP), la chaleur dégagée par le combustible nucléaire est transférée à l'eau du circuit primaire, pressurisée à 150 bars pour éviter son ébullition. Cependant, en situation accidentelle, elle peut entrer en régime d'ébullition nucléée pouvant s'intensifier jusqu'à atteindre la crise d'ébullition. Ce point de transition quasi instantané entre l'ébullition nucléée et l'ébullition en film entraîne la formation d'une couche de vapeur stable sur les crayons combustible, associée à une forte augmentation de leur température pariétale créant un risque de rupture de leur gaine. La prédiction du flux critique (flux de chaleur auquel se produit la crise d'ébullition) représente donc un enjeu de sûreté majeur et est actuellement réalisée à l'aide de corrélations expérimentales spécifiques à une configuration, n'incluant pas de représentation fine de la physique de l'ébullition.

Cette thèse s'intéresse à la modélisation de la physique de l'ébullition à l'échelle locale dite « CFD » (Computational Fluid Dynamics), à laquelle il est possible de réaliser des simulations d'écoulements bouillants avec une discrétisation spatiale de l'ordre du millimètre. Le code maison NEPTUNE_CFD, proposant une description eulérienne des écoulements multiphasiques à changement de phase, est l'outil de référence de EDF R&D pour enquêter sur ces problématiques aux échelles locales.

Dans un premier temps, des simulations d'écoulements bouillants convectifs en tube vertical sont réalisées avec NEPTUNE_CFD. Des comparaisons avec l'expérience DEBORA (écoulement bouillant de réfrigérant R12 en similitude REP sur plusieurs adimensionnels) ont permis une évaluation du code dans des conditions similaires au cas industriel. Les résultats obtenus sont globalement en accord avec l'expérience, mais présentent des écarts notables sur le diamètre des bulles et la température paroi. Cette dernière est calculée au travers du modèle d'ébullition en paroi de NEPTUNE_CFD dit à « Partition du Flux Pariétal » (Heat Flux Partitioning), où le flux appliqué est découpé entre plusieurs mécanismes de transfert de chaleur (convection, évaporation, conduction instationnaire, etc.).

Le coeur des travaux de thèse a alors consisté en la construction d'un nouveau modèle de Partition du Flux, avec objectif une prise en compte plus fine de la phénoménologie de l'ébullition en considérant notamment le glissement des bulles. Une modélisation de la dynamique des bulles en paroi a été développée par une approche mécaniste décrivant les forces appliquées sur la bulle. Les formulations de certaines forces (masse ajoutée, traînée, etc.) ont été réévaluées et permettent une prédiction satisfaisante des diamètres de détachement et des vitesses de glissement à basse et haute pression. Le modèle de Partition du Flux a été complété par une évaluation des nombreuses lois de fermetures requises (temps d'attente, densité de sites de nucléation, etc.) par comparaison avec des mesures expérimentales tirées de la littérature. Le nouveau modèle ainsi développé a ensuite été validé par comparaison avec des mesures de température de paroi et implémenté dans NEPTUNE_CFD.

La prédiction du flux critique s'ancre en perspective de ces développements. Des observations expérimentales récentes décrivent la crise d'ébullition à l'aide de paramètres physiques inclus dans le modèle de Partition du Flux. Un critère basé sur la proportion de surface occupée par les bulles a été testé avec l'ancien modèle de NEPTUNE_CFD et semble proposer un comportement qualitativement cohérent.

Enfin, on s'intéresse à une configuration de type tube avec des ailettes de mélange similaires à celles présentes en coeur de REP. Les simulations NEPTUNE_CFD montrent des écarts significatifs à l'expérience sur la prédiction du taux de vide à coeur. Des simulations monophasiques montrent une surestimation de la rotation du liquide, pouvant expliquer la trop grande accumulation de vapeur dans le cas bouillant.

mots-clés : changement de phase, transfert de chaleur, mécanique des fluides, écoulements multiphasiques, simulations numériques

PUBLICATIONS

Conference Proceedings

Luc Favre, Stéphane Pujet, Stéphane Mimouni and Catherine Colin, *NEPTUNE_CFD Simulations of DEBORA-Promoteur experiments : Boiling Freon in a Vertical Pipe with Mixing Vanes*, Proceedings of the 19th International Topical Meeting on Nuclear Reactor Thermal Hydraulics (NURETH 19), Brussels, Belgium, 2022

Luc Favre, Catherine Colin, Stéphane Pujet and Stéphane Mimouni , *An Analytical Approach of Bubble Departure by Sliding in Vertical Flow Boiling*, Advances in Thermal Hydraulics 2022 (ATH 2022), Anaheim, CA, USA, 2022

Journal Papers

Luc Favre, Catherine Colin, Stéphane Pujet and Stéphane Mimouni, *An updated force balance approach to investigate bubble sliding in vertical flow boiling at low and high pressures*, International Journal of Heat and Mass Transfer, 211, 124227, 2023, 10.1016/j.ijheatmasstransfer.2023.124227

And probably an other paper on Heat Flux Partitioning currently in preparation... ☺

CONTENTS

1 INTRODUCTION 1
1.1 Nuclear Energy in France . . . 1
1.2 Physical and Technological Background . . . 1
1.2.1 Pressurized Water Reactor Operation . . . 1
1.2.2 Structure and Geometry of PWR Core . . . 3
1.3 Safety and Thermal Design of PWR . . . 5
1.4 Thermal-Hydraulics of Boiling Two-Phase Flows . . . 6
1.4.1 Vertical Subcooled Boiling Flow Regimes . . . 6
1.4.2 Boiling Crisis and Critical Heat Flux in PWR . . . 7
1.4.3 Boiling Curves . . . 8
1.5 Current Industrial Treatment of the Boiling Crisis . . . 9
1.6 Towards Local Predictions of the CHF Using Computational Multi-Fluid Dynamics . . . 9
1.7 Contents of This Thesis . . . 10

I MODELING AND SIMULATION OF BOILING FLOWS USING NEPTUNE_CFD 12

2 PRESENTATION OF THE NEPTUNE_CFD CODE 13
2.1 Introduction . . . 13
2.2 Governing Equations for Turbulent Boiling Bubbly Flows . . . 13
2.2.1 Mass Conservation . . . 14
2.2.2 Momentum Balance . . . 14
2.2.3 Energy Conservation . . . 14
2.3 Interfacial Transfers Closure Laws . . . 14
2.3.1 Heat and Mass Transfers . . . 14
2.3.2 Interfacial Forces . . . 16
2.4 Turbulence Modeling . . . 17
2.5 Wall Boiling Model . . . 18
2.6 Wall Function for Dispersed Boiling Flows . . . 19
2.7 Conclusions . . . 20

3 FLOW BOILING EXPERIMENTS REPRESENTATIVE OF PWR: THE DEBORA DATABASE 21
3.1 Introduction . . . 21
3.2 Simulating PWR water using R12 . . . 21
3.2.1 Conservation of the Phase Density Ratio . . . 22
3.2.2 Conservation of the Weber Number . . . 23
3.2.3 Conservation of the Boiling Number . . . 23
3.2.4 Conservation of the Inlet Thermodynamic Quality . . . 23
3.2.5 Same Geometry . . . 24
3.2.6 Transposition ranges . . . 24
3.3 Description of the Test Section . . . 25
3.3.1 Geometrical Description . . . 25
3.3.2 Measurement Instrumentation . . . 25
3.4 Measurements Campaigns and Results . . . 28
3.4.1 Cases Nomenclature and Test Series . . . 28
3.4.2 Verification of Control Parameters Coherency . . . 29
3.4.3 Qualitative Analysis of the Experimental Results . . . 30
3.5 Further Verification . . . 35
3.5.1 Reconstruction of the Applied Heat Flux . . . 35
3.5.2 Verification of Wall Temperature Measurements . . . 38
3.6 Conclusions . . . 40

4 NEPTUNE_CFD SIMULATIONS OF DEBORA CASES 41
4.1 Introduction . . . 41
4.2 Simulation Setup . . . 41
4.3 Mesh Sensitivity Study . . . 42
4.4 C800 Cases Simulations : Thermal Measurements . . . 43

4.4.1 High Subcooling Cases . . . 43
4.4.2 Low Subcooling Cases . . . 44
4.4.3 Saturated Cases . . . 45
4.5 C3000 Cases Simulations : Topology Measurements . . . 46
4.5.1 Subcooled Boiling Cases . . . 46
4.5.2 Saturated Boiling Cases . . . 47
4.6 Simulations Sensitivity Tests . . . 48
4.6.1 Sensitivity to Wall Heat Flux Correction . . . 48
4.6.2 Influence of a Wall Boiling Parameter : the Nucleation Site Density . . . 50
4.7 Conclusion . . . 51

II DEVELOPMENT OF A NEW WALL HEAT FLUX PARTITIONING MODEL 54

5 INTRODUCTION TO HEAT FLUX PARTITIONING 55
5.1 Introduction . . . 55
5.1.1 Empirical Approaches . . . 55
5.1.2 First Heat Flux Partitioning Approaches . . . 56
5.2 Kurul & Podowski (1990) . . . 57
5.3 Basu, Warrier & Dhir (2005) . . . 58
5.3.1 Case 1 : Bubble Sliding, $D_d < s$ . . . 60
5.3.2 Case 2 : Bubble Coalescence without Sliding, $D_d \geq s$ . . . 61
5.4 Gilman (2017) . . . 61
5.5 Kommajosyula (2020) . . . 63
5.6 Conclusion . . . 65

6 BOILING BUBBLE DYNAMICS 66
6.1 Introduction . . . 67
6.1.1 Experimental Insights . . . 67
6.1.2 Existing Approaches . . . 69
6.2 Bubble Force Balance in Vertical Flow Boiling . . . 73
6.2.1 Introduction . . . 73
6.2.2 General Considerations . . . 74
6.2.3 Buoyancy and Contact Pressure Forces . . . 75
6.2.4 Capillary Force . . . 75
6.2.5 Drag and Lift Forces . . . 76
6.2.6 Inertia Force . . . 81
6.2.7 Force Balance Summary . . . 83
6.2.8 Liquid Velocity . . . 84
6.3 Bubble Growth . . . 86
6.3.1 Introduction . . . 86
6.3.2 Heat Diffusion in Uniformly Superheated Liquid . . . 86
6.3.3 Microlayer Evaporation . . . 87
6.3.4 Bubble Growth in Subcooled Flow Boiling . . . 88
6.3.5 Analytic Approach of Bubble Growth in a Linear Thermal Boundary Layer . . . 90
6.3.6 Comparison with DNS Results . . . 92
6.3.7 Comparison with Experimental Measurements . . . 92
6.3.8 Conclusions on Bubble Growth Modeling . . . 96
6.4 Departure by Sliding . . . 96
6.4.1 Non-Dimensional Analysis . . . 96
6.4.2 Application to Experimental Data . . . 99
6.4.3 Departure Diameter Prediction . . . 101
6.4.4 Discussion and accounting for parameters uncertainties . . . 103
6.5 Sliding phase . . . 105
6.5.1 Modeling . . . 105
6.5.2 Low Pressure Sliding . . . 105
6.5.3 High Pressure Sliding . . . 105
6.5.4 Comparison of Forces in Sliding Stage . . . 107
6.6 Bubble Lift-Off . . . 109
6.6.1 Introduction . . . 109
6.6.2 Experimental Measurements of Lift-Off Diameter . . . 111

6.6.3 Influence of the Flow Boiling Conditions . . . 111
6.6.4 Predicting the Lift-Off with a Force Balance . . . 113
6.6.5 A Simple Non-Dimensional Correlation . . . 114
6.6.6 Conclusion on the Lift-Off . . . 115
6.7 Conclusion . . . 117
7 CLOSURE LAWS AND CONSTRUCTION OF A NEW HEAT FLUX PARTITIONING MODEL 118
7.1 Introduction . . . 118
7.2 Single-Phase Heat Transfer Coefficient . . . 119
7.3 Nucleation Site Density . . . 121
7.3.1 Existing Correlations . . . 122
7.3.2 Comparison with Experimental Measurements . . . 124
7.4 Growth time . . . 126
7.5 Waiting Time . . . 126
7.5.1 Existing Models . . . 126
7.5.2 Experimental Measurements . . . 128
7.5.3 Evaluation of the Models . . . 130
7.6 Considerations on Bubble Interactions and Nucleation Sites Deactivation . . . 131
7.6.1 Nucleation Site Distribution . . . 131
7.6.2 Static Deactivation . . . 133
7.6.3 Static Coalescence . . . 134
7.6.4 Sliding Coalescence . . . 135
7.7 Bubble Sliding Length . . . 136
7.8 Single Bubble Quenching Area . . . 139
7.9 Assembling a New Heat Flux Partitioning . . . 140
7.9.1 Liquid Convective Heat Flux . . . 140
7.9.2 Static Coalescence Evaporation Heat Flux . . . 141
7.9.3 Sliding Coalescence Evaporation Heat Flux . . . 141
7.9.4 Quenching Heat Flux . . . 141
7.9.5 Vapor Convective Heat Flux . . . 142
7.9.6 Liquid Convection Area . . . 142
7.9.7 Model Summary . . . 142
7.10 Conclusion . . . 145
8 VALIDATION OF THE HEAT FLUX PARTITIONING MODEL 147
8.1 Detailed Comparison and Assessment of the Heat Flux Partitioning . . . 147
8.1.1 Active Nucleation Site Density . . . 148
8.1.2 Wait Time, Growth Time, Quenching Time and Nucleation Frequency . . . 148
8.1.3 Single Bubble Area and Total Bubble Area . . . 149
8.1.4 Flux Proportions and Wall Superheat . . . 151
8.2 Wall Temperature Predictions . . . 152
8.2.1 Kossolapov Data . . . 152
8.2.2 Jens-Lottes Data . . . 155
8.2.3 Kennel Data . . . 158
8.3 Validation for DEBORA Experiment . . . 159
8.4 Conclusions . . . 159
9 PERSPECTIVES TOWARDS CRITICAL HEAT FLUX PREDICTION 161
9.1 Previous Modeling of the Boiling Crisis . . . 161
9.1.1 Empirical Approaches . . . 161
9.1.2 Physical Phenomenology Approaches . . . 161
9.2 Recent Approaches and Advances for CHF Prediction . . . 164
9.2.1 Dry Patch Formation . . . 164
9.2.2 Model of Baglietto, Demarly & Kommajosyula [5] : Stability of the Heat Flux Partitioning . . . 165
9.2.3 Model of Zhang, Seong & Bucci [178]: Bubble Interaction and Scale-Free Footprint distribution . . . 165
9.3 Simple test of the Zhang Criterion . . . 166
9.4 Conclusions . . . 167

III TOWARDS THE INDUSTRIAL GEOMETRY 169
10 TUBE WITH MIXING VANES : DEBORA-PROMOTEUR AND AGATE-PROMOTEUR EXPERIMENTS 170
10.1 Introduction . . . 170
10.2 DEBORA-Promoteur . . . 170
10.2.1 Test Section and Experimental Campaigns . . . 170
10.3 AGATE-Promoteur . . . 172
10.4 Analysis of the DEBORA-Promoteur Experimental Measurements . . . 173
10.4.1 Estimation of the Bubble Diameter . . . 175
10.5 Conclusions . . . 177
11 NEPTUNE_CFD SIMULATIONS OF DEBORA-PROMOTEUR AND AGATE-PROMOTEUR CASES 179
11.1 NEPTUNE_CFD simulations of DEBORA-Promoteur cases . . . 179
11.1.1 Simulation Setup . . . 179
11.1.2 Results . . . 180
11.2 NEPTUNE_CFD simulations of AGATE-Promoteur cases . . . 182
11.2.1 Simulation Setup . . . 182
11.2.2 Results . . . 184
11.3 Regarding CHF Detection in Mixing Vanes Geometry . . . 188
11.4 Conclusions . . . 190
12 GENERAL CONCLUSION AND PERSPECTIVES 191
12.1 Conclusions . . . 191
12.2 Perspectives . . . 193

BIBLIOGRAPHY 196

LIST OF FIGURES

Figure 1.1 Sketch of a Pressurized Water Reactor [44] . . . 2
Figure 1.2 Picture of the Reactor Pressure Vessel of the Finnish European Pressurized Reactor [125], ©Areva . . . 3
Figure 1.3 Sketch of a full nuclear fuel assembly and rod. [32] . . . 4
Figure 1.4 Picture of a fuel rod during a control test. [81] . . . 4
Figure 1.5 Picture of a fuel assembly grid. [173] . . . 5
Figure 1.6 Model of a 5×5 grid (scale 5:1) from EDF Lab Chatou. Mixing vanes circled in red, dimples in green and springs in orange. . . . 5
Figure 1.7 Sketch of the different vertical flow boiling regimes in a vertical tube at low heat flux from Collier & Thome (1994, [29]). Here, x denotes the local thermodynamic quality noted x_{eq} in the text. . . . 6
Figure 1.8 Experimental shadowgrams from Bloch *et al.* [11] of the flow boiling at CHF for a 27 K subcooled liquid flowing upwards at 0.6 m/s and atmospheric pressure. . . . 7
Figure 1.9 Visualization of a DNB-type boiling crisis on a rod with a mixing grid by Liu *et al.* [104]. The fluid is R134a at $P = 2184$ kPa, $G = 2076$ kg/m^2/s , $T_{sat} - T_{L,in} =$ 22.8°C. The insulating vapor blanket is clearly visible upstream the mixing grid. . 8
Figure 1.10 Example of Nukiyama / boiling curve for water from [45]. Here q'' denotes the wall heat flux. . . . 8
Figure 1.11 Damaged electrically heated components (used for CHF experimental tests in PWR conditions) after the boiling crisis (from CEA Omega experiment [44]). . . 9
Figure 1.12 Sketch of a sub-channel in a rod bundle (dashed lines). The equivalent hydraulic diameter here is $D_h = 11.78$ mm. . . . 10
Figure 3.1 Density ratio of pressurized R12 and water . . . 22
Figure 3.2 Weber number for R12 and water at $G = 2000$ kg/m^2/s and $R = 0.1$ mm . . . 23
Figure 3.3 Boiling number for R12 and water at $G = 2000$ kg/m^2/s . . . 24
Figure 3.4 Sketch of the DEBORA test section. Adapted from [53]. . . . 26
Figure 3.5 Example of Phase Indicator Function signal . . . 26
Figure 3.6 Picture of the bi-optical probe with a zoom over the two optical fibers. Reproduced from [64]. . . . 27
Figure 3.7 30G2P26W16 and 29G2P26W16 results. Vapor velocity for C2900 cases is estimated using Eq. 3.8. . . . 31
Figure 3.8 8G2P26W16 results . . . 32
Figure 3.9 30G2P14W16 and 29G2P14W16 results . . . 33
Figure 3.10 8G2P14W16 results . . . 34
Figure 3.11 Interpolation profiles for cases Te66 (Table 3.7). . . . 37
Figure 3.12 Correlations comparison with P14 cases. . . . 38
Figure 3.13 Correlations comparison with P26 cases. . . . 39
Figure 4.1 View of the computational domain. . . . 42
Figure 4.2 View of the radial meshes. . . . 42
Figure 4.3 Mesh sensitivity study for 30G2P26Te66.6 case . . . 43
Figure 4.4 Simulation results for cases 8G2P26W16Te31. 5& Te44.9 . . . 44
Figure 4.5 Simulation results for cases 8G2P26W16Te55.7 & Te61.5 . . . 45
Figure 4.6 Simulation results for cases 8G2P26W16Te66.6 & Te70.3 . . . 46
Figure 4.7 Simulation results for cases 30G2P26W16Te62 & Te64 . . . 47
Figure 4.8 Simulation results for cases 30G2P26W16Te66 & Te70 . . . 48
Figure 4.9 Simulation results for cases 8G2P26W16Te66.6 & Te70.3 with corrected wall heat flux . . . 49
Figure 4.10 Simulation results for cases 30G2P26W16Te66 & Te70 with corrected wall heat flux 50
Figure 4.11 Simulation results for case 8G2P26W16Te55.7 using different nucleation site density correlations . . . 52
Figure 5.1 Sketch of the HFP considered by Kurul & Podowski (by Manon [109]). . . . 57

Figure 5.2 Sketch of the heat transfers zones and bubble behavior considered by Basu *et al.*. (Adapted from [7]). Q represents the heat transfer. . . . 59
Figure 5.3 Heat Flux Partitioning mind-map description by Gilman [58] (Adapted from [59]). 62
Figure 5.4 Heat Flux Partitioning considered by Kommajosyula [89]. . . . 63
Figure 6.1 Visualization of bubble sliding at various pressures. . . . 67
Figure 6.2 Visualization of bubble sliding thermal impact. . . . 68
Figure 6.3 Sketch of a typical bubble lifetime in vertical flow boiling. Left depicts a typical side view of the heater with identification of departure, sliding and lift-off. Right depicts a top view of the heater, exhibiting the area that will undergo transient heat transfer. . . . 68
Figure 6.4 Values predicted by the diameter correlations for water. $\Delta T_L = 10°C$, $G_L = 1000$ kg/m^2/s, $\theta = 40°$ and $D_h = 10$ mm. . . . 71
Figure 6.5 Sketch of the forces applied to the bubble facing an upward flow $\overline{U_L}$ and sliding at velocity $\overline{U_b}$ . . . 74
Figure 6.6 Physical situation considered by Shi *et al.* [147]. . . . 77
Figure 6.7 Drag correction from Shi *et al.* [147]. . . . 78
Figure 6.8 C_L computed using Shi *et al.* correlation. . . . 80
Figure 6.9 Values of the computed added mass coefficients in Eq. 6.64 and 6.66. . . . 83
Figure 6.10 Microlayer appearing beneath the bubble in DNS conducted by and adapted from Urbano *et al.* [163]. . . . 88
Figure 6.11 Studied geometry . . . 90
Figure 6.12 Comparison with DNS results of Urbano *et al.* [162] ($\delta = 3$mm and $\theta = 50°$). Lines : Model predictions - Markers : DNS . . . 93
Figure 6.13 Comparison with experimental measurements of Maity [108]. . . . 93
Figure 6.14 $G_L = 239.6$ kg/m^2/s, $\Delta T_w = 5.9K$, $\Delta T_L = 0.3K$ . . . 94
Figure 6.15 Comparison with experimental measurements of Kossolapov [90]. ΔT_w values are recalculated from analytic growth profiles fitted by the author. . . . 95
Figure 6.16 Regime map regarding departure by sliding. Boundaries plotted for water at 1 bar and $D_d = 0.5$mm. ($K = 2$) . . . 97
Figure 6.17 Regime map plotted for water at different pressures and bubble departure diameters. ($K = 2$) . . . 98
Figure 6.18 Regime map for R12 as simulating fluid for PWR. $D_d = 0.05$mm is chosen according to R12 measurements from Garnier *et al.* [53] who observed bubbles of ~ 0.1mm diameter after lift-off. The same value is taken for water. ($K = 2$) . . . 98
Figure 6.19 Regime maps for each water data sets from Table 6.3. . . . 100
Figure 6.20 Predicted bubble departure diameters. $\pm 50\%$ error bars are indicated. . . . 102
Figure 6.21 Initially assumed, real and reassessed bubble shape for Sugrue cases (picture adapted from [152]). . . . 103
Figure 6.22 Proposed model performance while accounting for contact angle uncertainties . . 104
Figure 6.23 Bubble sliding velocity predictions on Maity cases . . . 106
Figure 6.24 Bubble sliding length predictions on Kossolapov cases - $P = 20$ bar . . . 107
Figure 6.25 Bubble sliding length predictions on Kossolapov cases - $P = 40$ bar . . . 108
Figure 6.26 Amplitude of each force during sliding . . . 108
Figure 6.27 Visualization of bubble lift-off in horizontal boiling conducted by and adapted from Maity [108]. The detachment the the bubble base from the surface is clear in the last frame. . . . 109
Figure 6.28 Visualization of bubble lift-off in vertical boiling. The moment when bubble leaves the surface appears less clearly than for horizontal boiling. . . . 110
Figure 6.29 Visualization of boiling surfaces in vertical boiling, where single bubble lift-off is not systematically observed. . . . 110
Figure 6.30 Evolution of D_{lo}/L_c depending on the flow conditions. . . . 113
Figure 6.31 Prediction of Eq. 6.115 versus data from Table 6.5. Value of $K = 0.24$ (same as in Figure 6.22) was used and only converged points are presented. . . . 115
Figure 6.32 Comparison of simple direct correlations with data from Table 6.5 . . . 116
Figure 7.1 Predictive capability of wall temperature by single-phase heat transfer correlations. $\pm 3K$ error bars indicated. . . . 120
Figure 7.2 Predictive capability of wall temperature by NCFD law and Gnielinski correlation including corrections. $\pm 3K$ error bars indicated (dashed lines). . . . 121

Figure 7.3 HSV Visualization of bubble density at various pressures adapted from Kossolapov [90] (left to right: 1.01 bar, 3 bar, 19.8 bar, 75.8 bar). . . . 122
Figure 7.4 Sketch of the link between bubble contact angle and wettability / cavity flooding 123
Figure 7.5 Predictions of the chosen models against the experimental data of Table 7.3 with ±50% error bars. The contact angles . . . 125
Figure 7.6 Evolution of the wait time values with the wall Jakob number. . . . 129
Figure 7.7 Evolution of the product $t_w \times f$ with the reduced Jakob number. . . . 130
Figure 7.8 Predictions using the correlations. ±50% dashed lines are represented. . . . 130
Figure 7.9 Yeoh *et al.* formulation of t_w with Han & Griffith cavity radius. ±50% dashed lines are represented. . . . 131
Figure 7.10 Nucleation site distribution by and adapted from Kossolapov [90]. Red circles represent the active sites positions with diameter increasing with the site's nucleation frequency. . . . 132
Figure 7.11 Examples of experimental nucleation sites distribution in flow boiling. . . . 133
Figure 7.12 Sketch of the geometrical overlapping leading to static deactivation. Bubbles in red can not be accommodated on the surface due to their site laying below an existing bubble. . . . 134
Figure 7.13 Static deactivation correction tested with Hibiki & Ishii and Li *et al.* correlations for water at 40 bar, $f = 200$ Hz, $t_{g,d} = 0.1$ ms, $\theta = 80°$ and $R_d = 0.01$ mm. . . . 135
Figure 7.14 Sketch of the static coalescence phenomenon. . . . 135
Figure 7.15 Static coalescence probability with corrected Li *et al.* for water at 40 bar, $f =$ 200 Hz, $t_{g,d} = 0.1$ ms and $\theta = 80°$. . . . 136
Figure 7.16 Comparison of sliding distance estimations with Kossolapov measurements [90]. NSD was estimated using Li *et al.* correlation (Eq. 7.11). . . . 137
Figure 7.17 Quenching area shape depending on the relation between R_d, R_{lo} and l_{sl}, if the bubble do not experience multiple coalescence while sliding. . . . 139
Figure 7.18 Sketch of all the considered heat transfers for the new HFP model. . . . 140
Figure 8.1 Comparison of active nucleation site density with and without a correction for Li *et al.* formulation. . . . 148
Figure 8.2 Comparison of bubble nucleation frequency, wait time, average growth time and quenching time. . . . 149
Figure 8.3 Comparison of average area visited by a bubble and total wall fraction area impacted by bubbles (footprint or transient conduction). . . . 150
Figure 8.4 Bubble radiuses, sliding length and distances between sites. . . . 150
Figure 8.5 Comparison of the resulting heat flux partitioning along with the boiling curve. . 151
Figure 8.6 Comparison with measured boiling curves from Kossolapov [90]. $\Delta T_L = 10$°C and $G_L = 1000$ kg/m^2/s. ϕ_w axis is sometimes set to logarithmic scale if a HFP model largely overcomes the experiment. . . . 153
Figure 8.7 Wall temperature predictions achieved by the different HFP models on Kossolapov data. ±50% error bars in dashed lines. . . . 154
Figure 8.8 Comparison with measured boiling curve by Jens & Lottes [78]. $P = 138$ bar, $G = 2600$ kg/m^2/s, $\Delta T_L = 64$°C. . . . 155
Figure 8.9 Wall temperature predictions achieved by the different HFP models on Jens data. ±50% error bars in dashed lines. . . . 157
Figure 8.10 Wall temperature predictions achieved by the different HFP models on Kennel data. ±50% error bars in dashed lines. . . . 158
Figure 8.11 Comparison of different HFP and NCFD simulation on the 8G2P26W16Te49 DEBORA case. . . . 159
Figure 9.1 Sketch of the boiling crisis description by Zuber [183]. l_z and λ_H are respectively the Rayleigh-Taylor and Kelvin-Helmholtz instability wavelengths. . . . 162
Figure 9.2 Sketch of the boiling crisis description by Lee & Mudawar. Here, the boiling crisis is supposed to be triggered when the evaporation rate of the sublayer exceeds the entering liquid flux (*i. e.* when velocity $U_b - U_m$ approaches 0). . . . 163
Figure 9.3 Sketch of the boiling crisis description by Weisman & Pei . . . 163
Figure 9.4 Sketch of the dry patch formation mechanism by and adapted from Ha & No [69]. 164
Figure 9.5 Illustration of CHF prediction by Baglietto *et al.* [5]. . . . 165

Figure 9.6 Example of Monte-Carlo simulation of the bubble clustering process, by and adapted from [178]. G and SG respectively denote the largest and second largest bubble clusters. . . . 166
Figure 9.7 Value of the CHF triplet for the DEBORA case 30G2P26W16Te70 (Chapter 4). The heat flux applied corresponds approximately to 90% of the CHF in those conditions [47] and the wall void fraction approaches 40% (Figure 3.7a). . . . 167
Figure 10.1 Picture of the mixing device. (Adapted from [46]) . . . 171
Figure 10.2 Description of the DEBORA-Promoteur experiment. . . . 171
Figure 10.3 Covered measurements positions in AGATE-Promoteur experiment. . . . 173
Figure 10.4 Experimental results from the 48G3P26WA series. . . . 174
Figure 10.5 Experimental results from the 52G3P26WA series. . . . 174
Figure 10.6 Experimental results from the 52G3P26WB series. . . . 175
Figure 10.7 Relative difference of interference frequency for the two probes. . . . 176
Figure 10.8 Average relative importance of radial velocity to axial velocity in AGATE-Promoteur experiment. Black dotted lines denotes the position of the MV. . . . 176
Figure 10.9 Estimation of bubble diameter on C5200 measurements series. . . . 177
Figure 11.1 Meshing of the mixing vanes region. . . . 180
Figure 11.2 NCFD results on the DEBORA-Promoteur cases. MV at 23.5 D_h and 10 $D_h$respectively correspond to C4800 and C5200 cases. . . . 181
Figure 11.3 Sensitivity test on case 48G3P26WATe75 leaving only the drag force in the inter-facial momentum closure. . . . 182
Figure 11.4 Fine meshing of the mixing vanes region for the LES calculation. . . . 183
Figure 11.5 Results for $z = 0.8\ D_h$ . . . 184
Figure 11.6 Visualization of the radial velocity field and ratio between radial and axial velocity obtained with the LES, $z = 1\ D_h$ downstream the MV. . . . 185
Figure 11.7 Results for $z = 10.4\ D_h$ . . . 185
Figure 11.8 Visualization of the radial velocity field and ratio between radial and axial velocity obtained with the LES, $z = 10\ D_h$ downstream the MV. . . . 186
Figure 11.9 Results for $z = 22.9\ D_h$ . . . 187
Figure 11.10 Visualization of the radial velocity field and ratio between radial and axial velocity obtained with the LES, $z = 23\ D_h$ downstream the MV. . . . 187
Figure 11.11 Visualization of the CHF triplet value around the first grid. (Computation results courtesy of Vladimir Duffal) . . . 189
Figure 11.12 Visualization of the CHF triplet value around the second grid. (Computation results courtesy of Vladimir Duffal) . . . 189

LIST OF TABLES

Table 2.1 Constant values for the SSG model in NEPTUNE_CFD . . . 18
Table 3.1 Water and R12 saturation properties. . . . 24
Table 3.2 Water R12 scaling, $R = 0.01$mm for We . . . 25
Table 3.3 Uncertainties for DEBORA results [33, 64] . . . 28
Table 3.4 Test matrix of the DEBORA cases. ◯: C800 - ▽: C2900 - △: C3000. Campaigns in the same matrix cell usually cover the same range of outlet quality $x_{eq,out}$ *i. e.* inlet temperature $T_{L,in}$. . . . 28
Table 3.5 Recalculated control parameters for the 30G2P14W16 cases. ($T_{sat} = 58.07$°C) . . . 30
Table 3.6 Recalculated control parameters for the 30G2P26W16 cases. ($T_{sat} = 86.81$°C) . . . 30
Table 3.7 Similar conditions cases between the C3000 and C800 campaigns. Outlet quality calculated with Eq. 3.9. . . . 36
Table 3.8 Heat flux recalculation results . . . 37
Table 4.1 Mesh parameters . . . 42
Table 4.2 Corrected heat fluxes applied in the simulations . . . 49
Table 6.1 Summary of the presented correlations . . . 72
Table 6.2 Summary of different force-balance mechanistic approaches. . . . 84
Table 6.3 Bubble departure diameters data sets in vertical flow boiling . . . 99
Table 6.4 Average relative error reached by the models. . . . 104
Table 6.5 Bubble lift-off diameters data sets in vertical flow boiling . . . 112
Table 7.1 Experimental data range of wall temperature measurements from the single-phase part of boiling curves. N_{mes} is the number of measurements of each data set. . . . 119
Table 7.2 Average errors achieved by the considered models on each data sets. . . . 121
Table 7.3 Nucleation Site Density data in flow boiling . . . 124
Table 7.4 Bubble wait time data in vertical flow boiling. Wall superheat values for Richenderfer data are estimated using Frost & Dzakowic correlation (Eq. 6.109). . . . 128
Table 7.5 Summary of the HFP model closure laws . . . 144
Table 7.6 Summary of the HFP model formulation . . . 145
Table 8.1 Experimental data range of wall temperature measurements in the boiling region. 152

NOMENCLATURE

Acronyms

ASN	Autorité de Sûreté Nucléaire
BC	Boiling Crisis
BDD	Bubble Departure Diameter
BDF	Bubble Departure Frequency
CEA	Commissariat à l'Énergie Atomique et aux Énergies Alternatives
CFD	Computational Fluid Dynamics
CHF	Critical Heat Flux
CMFD	Computational Multi-Fluid Dynamics
DNB	Departure from Nucleate Boiling
DNBR	Departure from Nucleate Boiling Ratio
DNS	Direct Numerical Simulation
EDF	Électricité De France
HFP	Heat Flux Partitioning
IRSN	Institut de Radioprotection et de Sûreté Nucléaire
LES	Large Eddy Simulation
LOCA	Loss of Coolant Accident
LSD	Liquid Sublayer Dryout
MV	Mixing Vanes
NSD	Nucleation Site Density
ONB	Onset of Nucleate Boiling
OSV	Onset of Significant Void
PWR	Pressurized Water Reactor
RANS	Reynolds Averaged Navier-Stokes
RMS	Root Mean Square
RPE	Rayleigh-Plesset Equation
RPV	Reactor Pressure Vessel

Greek Symbols

α	Volumetric fraction (or void fraction for vapor) [-]
δ	Thickness [m]
η	Thermal diffusivity [m^2/s]
Γ	Interfacial Mass Transfer [$kg/m^3/s$]
γ	Shear rate [s^{-1}]

λ	Thermal conductivity [W/m/K]
μ	Dynamic viscosity [Pa.s]
ν	Kinematic viscosity [m^2/s]
$\mathbf{\Phi}$	Heat power [W]
ϕ	Heat flux [$J/m^2/s$]
ρ	Density [kg/m^3]
σ	Surface tension [J/m^2]
$\tau_{i,j}$	Stress tensor components [N/m^2]
θ, $\mathrm{d}\theta$	Contact angle and half-hysteresis [° or rad]
θ_i	Bubble inclination angle [° or rad]

Latin Symbols

$\Delta T_k = \lvert T_k - T_{sat} \rvert$	Temperature difference to saturation (superheat or subcooling) [K]
$\mathcal{P}$	Probability
$\mathcal{W}$	Lambert's W-function
$\overline{\overline{I}}$	Identity tensor [-]
$\overline{n}$	Normal unit vector [-]
A	Area [m^2] or area fraction [-]
a_i	Interfacial area concentration [m^{-1}]
C_{AM}	Added Mass coefficient [-]
C_D	Drag coefficient [-]
C_L	Lift coefficient [-]
c_p	Isobaric heat capacity [J/kg/K]
D	Diameter [m]
E	Kinetic energy [J]
F	Force [N]
f	Frequency [s^{-1}]
G	Mass flux [$kg/m^2/s$]
g	Gravity acceleration [m^2/s]
h	Enthalpy per unit of mass [J/kg] or heat transfer coefficient [$W/m^2/K$]
h_{LV}	Latent heat of vaporization [J/kg]
K	Bubble growth constant [-]
L	Length [m]
$L_c = \sqrt{\frac{\sigma}{(\rho_L - \rho_V)\, g}}$	Capillary length [m]
L_g	Distance between two PWR grids [m]
l_{sl}	Bubble sliding length [m]
N_b	Bubble density [m^{-1}]

$N_{sit,a}$	Active nucleation site density [m^{-1}]
N_{sit}	Nucleation site density [m^{-1}]
P	Pressure [bar]
Q	Interfacial heat transfer [J] or [J/m^3]
q''	Interfacial heat flux density [J/m^2]
R	Bubble radius or tube radius [m]
r	Radial coordinate [m]
R_c	Bubble curvature radius [m]
R_{ij}	Reynolds stress tensor components [m^2/s^2]
r_w	Bubble foot radius [m]
r_w	Bubble wall contact radius [m]
S	Surface [m^2]
T	Temperature [K]
t	Time [s]
U	Velocity [m/s]
U_τ	Wall friction velocity [m/s]
$U_{rel} = U_L - U_b$	Relative velocity [m/s]
V	Volume [m^3]
x_{eq}	Thermodynamic quality [-]
z	Axial coordinate [m]

Mathematical Conventions

$\dfrac{D}{Dt}$	Lagrangian derivative
$\dot{R}$, $\ddot{R}$	Time derivatives
$\langle . \rangle$	Time-averaging
$\langle . \rangle_2$	Surface-averaging
$\langle . \rangle_k$	Phase-averaging
$\otimes$	Tensor product
$\overline{\overline{R}}$	Tensor
$\overline{\nabla} \cdot$	Divergence operator
$\overline{\nabla} (.)$	Gradient operator
$\overline{U}$	Vector

Dimensionless Numbers

$\mathrm{Bo} = \dfrac{\phi_w}{G h_{LV}}$	Boiling number [-]
$\mathrm{Ca} = \dfrac{\mu_L U_L}{\sigma}$	Capillary number [-]
$\mathrm{Eo} = \dfrac{(\rho_L - \rho_V)\, g R^2}{\sigma}$	Eotvos number [-]

$\mathrm{Fr} = \frac{\rho_L U_L^2}{(\rho_L - \rho_V)\, gR}$	Froude number [-]
$\mathrm{Ja} = \frac{\rho_L c_{P,L} \Delta T}{\rho_V h_{LV}}$	Jakob number [-]
$\mathrm{Ja}^* = \frac{c_{P,L} \Delta T}{h_{LV}}$	Reduced Jakob number [-]
$\mathrm{Nu} = \frac{hL}{\lambda}$	Nusselt number [-]
$\mathrm{Pe} = \mathrm{Re} \times \mathrm{Pr}$	Péclet number [-]
$\mathrm{Pr} = \frac{\nu}{\eta}$	Prandtl number [-]
$\mathrm{Re}_b = \frac{U_{rel} D_b}{\nu_L}$	Bubble Reynolds number [-]
$\mathrm{Re}_{D_h} = \frac{G D_h}{\mu_L}$	Liquid bulk Reynolds number [-]
$\mathrm{Sr} = \frac{2\gamma R}{\lvert U_{rel} \rvert}$	Non-dimensional shear rate [-]
$\mathrm{We} = \frac{G^2 L}{\rho \sigma}$	Weber number [-]
$y^+ = \frac{y U_\tau}{\nu_L}$	Non-dimensional wall distance [-]

Subscripts

$1b$	Single bubble
τ	Wall shear
A	Axial
AM	Added-Mass
b	Bubble
c	Forced Convection
$calc$	Calculated
$coal$	Coalescence
D	Drag
d	Departure or Downstream
e	Evaporation
exp	Experimental
fc	Forced convection
g	Growth
h	Hydraulic
i	Interfacial
in	Inlet or Initial
L	Liquid or Lift
lo	Lift-off

M	Mixture
mes	Measurements
ML	Micro-layer
mod	Model
q	Quenching
R	Radial
sat	Saturation
sit	Nucleation site
sl	Sliding
SP	Single phase
st	Static
T	Turbulent
TD	Turbulent Dispersion
tot	Total
u	Upstream
V	Vapor
w	Wall or wait

1

INTRODUCTION

Contents

1.1 Nuclear Energy in France 1
1.2 Physical and Technological Background 1
1.2.1 Pressurized Water Reactor Operation 1
1.2.2 Structure and Geometry of PWR Core 3
1.3 Safety and Thermal Design of PWR 5
1.4 Thermal-Hydraulics of Boiling Two-Phase Flows 6
1.4.1 Vertical Subcooled Boiling Flow Regimes 6
1.4.2 Boiling Crisis and Critical Heat Flux in PWR 7
1.4.3 Boiling Curves 8
1.5 Current Industrial Treatment of the Boiling Crisis 9
1.6 Towards Local Predictions of the CHF Using Computational Multi-Fluid Dynamics . 9
1.7 Contents of This Thesis 10

1.1 NUCLEAR ENERGY IN FRANCE

In 2020, France had a total of 136.2 GW of installed electrical power plants with a total production over the year of 500.1 TWh, 67.1% of which coming from nuclear reactor. Actually, nuclear energy plays a pivotal role in France's electrical mix since the 1950's and is promoted as a mean to reduce the global carbon dioxide emissions of the country's energy production. The french government currently plans to build a total of six new nuclear reactors before 2050.

1.2 PHYSICAL AND TECHNOLOGICAL BACKGROUND

1.2.1 *Pressurized Water Reactor Operation*

Pressurized Water Reactors are the only type of nuclear power plants operated in France for electricity production. A simplified sketch of a PWR is presented on Figure 1.1.

1.2.1.1 *Primary Loop*

The primary loop aims to collect the thermal energy expelled by the fission reactions within the nuclear fuel rods. The water flowing through the core gathers this energy and transfers it towards the vapor generator, while ensuring a moderating effect to maintain the nuclear chain reaction in the fuel. The primary loop is fully closed and operates at a pressure around 155 bar, a temperature of 300°C and mass flow rates between 3000 and 5000 kg/m^2/s (approximately 20 tons per second) at the core inlet.

The reactor vessel is fed with water by numerous pumps, each of them being connected to its own cooling circuit and steam generator. One of those coolant circuit is connected to the pressurizer to set the pressure of the whole primary loop. In France, 900 MW reactors comprise three primary pumps while 1300 MW and 1450 MW reactors have four of them.

The main components of the primary loop are:

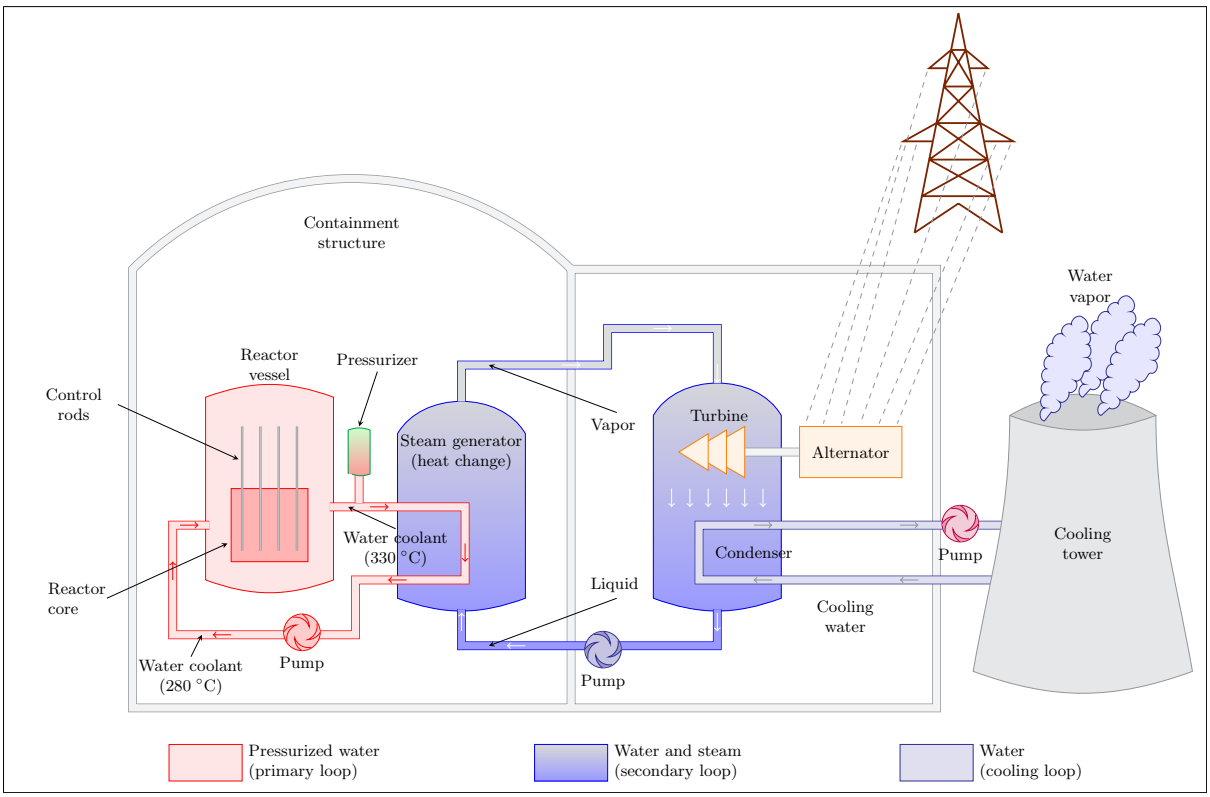

Figure 1.1: Sketch of a Pressurized Water Reactor [44]

- **The reactor vessel** containing the core where fission reactions take place within the nuclear fuel rods, gathered in so-called "fuel assemblies". The pressurized water flow between the rods to remove the heat released at their surface and moderates the neutrons to maintain the chain reaction.
- **The primary pumps** which role is to ensure the water flow throughout the loop. Each pump requires an electrical power supply of approximately 7 MW.
- **The pressurizer**, imposing the pressure and keeps the water in a liquid state. It is actually a vessel with a liquid-vapor mixture in which pressure can be increased through vaporization of the liquid water (using heating resistors) or diminished by vapor condensation (using water aspersion system).
- **Steam generator tubes** being the interface between the primary and secondary loop through which the thermal energy gathered in the core is transferred from the primary water to vaporize the secondary water.

1.2.1.2 *Secondary Loop*

The secondary loop is designed to receive the thermal energy from the primary loop to vaporize its own water. The generated vapor is used to produce electricity by conversion of its mechanical energy through the rotation of power-generating turbines connected to alternators. At the outlet of the turbines, the vapor has logically been expanded and is then condensed before being sent back into the secondary loop and the steam generators. Therefore, the secondary loop is a closed water-steam circuit. The operating conditions in the steam generator are usually a pressure of 60 bar, with water heated from 220°C to 275°C and evaporated.

1.2.1.3 *Cooling Loop*

The cooling loop's goal is to cool down and condense the steam coming out of the turbines. Depending on the geographical situation of the nuclear power plant, the associated heat sink may either be natural (lake, sea, etc.) or built (cooling tower). It is a completely open circuit.

1.2.2 *Structure and Geometry of PWR Core*

1.2.2.1 *Reactor Pressure Vessel*

The whole reactor core is contained in a stainless steel vessel (Figure 1.2) called "Reactor Pressure Vessel" (RPV). Together with the primary loop, they represent the second "containment barrier" (name given to the parts of the reactor avoiding the escape of radioactive species) of the core. Therefore, the RPV is a pivotal safety element of the reactor which mechanical strength and performances must be ensured in any conditions that may occur during operations.

> **Note :** A RPV can not be replaced, thus scaling the whole reactor's lifetime. The longer the vessel is durable, the longer the nuclear unit will operate.

Figure 1.2: Picture of the Reactor Pressure Vessel of the Finnish European Pressurized Reactor [125], ©Areva

1.2.2.2 *Fuel Assembly and Core Structure*

A fuel assembly is composed of 17×17 rods and guide thimbles among which 264 are nuclear fuel rods. 24 of them are guide thimbles in which absorbing rods (used to shut down the chain reaction by neutron absorption in incidental or accidental situations) can be inserted, one of them being dedicated to instrumentation. The top nozzle of the assembly ensures its stability using a hold-down spring. The whole structure is 4 m high and is also maintained by 8 grids placed every 50 cm (Figure 1.3) for french PWR reactors.

In a reactor core, the number of fuel assemblies can vary depending on its final electrical power production: 157 assemblies for 900 MW units, 193 for 1300 MW units and 205 for 1450 MW units.

1.2.2.3 *Fuel Rod*

Fuel rods are the elementary component of the reactor's core since they contain the nuclear fuel pellets made of enriched uranium. A pellet measures 13.5 mm height for an 8 mm diameter, weighing approximately 8.3 g. They are placed in a neutron-transparent tubular cladding made of Zircaloy (an alloy made of 98% of zirconium and tin), allowing neutrons to move through the core to trigger fission reactions in nearby rods. This cladding is the first containment barrier and contains a total of 272 pellets (Figure 1.3).

The bundle organization of the rods allows water to flow between them and to moderate neutrons coming out of recent fission. Moreover, this geometry ensures a large heat exchange surface to enhance the fuel cooling. A single fuel rod usually measures 4 m height for a 9.5 mm diameter and weighs 2 kg (Figure 1.4).

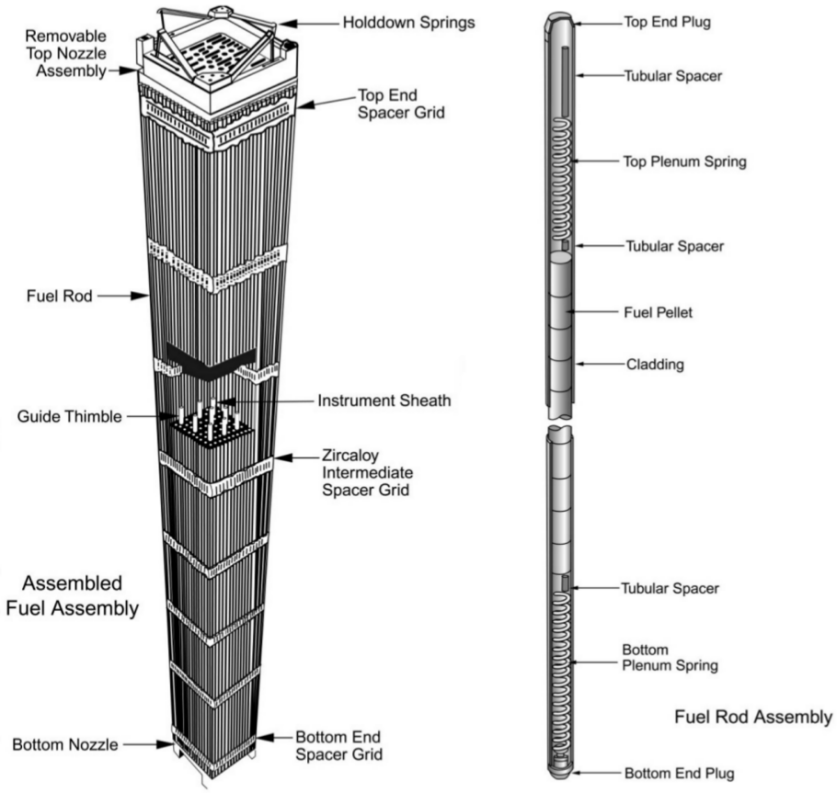

Figure 1.3: Sketch of a full nuclear fuel assembly and rod. [32]

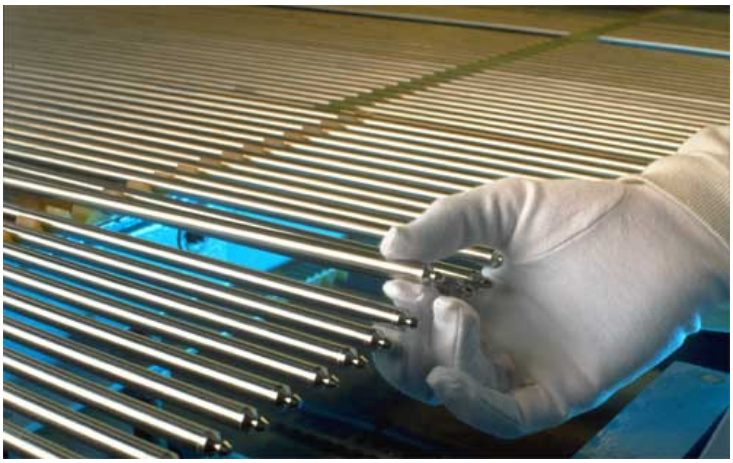

Figure 1.4: Picture of a fuel rod during a control test. [81]

Note : In normal PWR conditions, the heat flux at the rods lies roughly between 500 kW/m^2 and 1.5 MW/m^2 [132]. In accidental conditions, it can rise up to several MW/m^2 [109].

1.2.2.4 *Grids*

Within the fuel assembly, the rods are held by 8 grids (Figure 1.5) placed with an even spacing of 50 cm.

They help the whole structure to withstand the huge hydrodynamic effort exerted by the water flowing over the rods at high flow rates. Two types of grids are used in fuel assemblies:

- Spacer grids which role is solely to ensure the mechanical stability of the assembly and avoid rods deformation when they heat up.

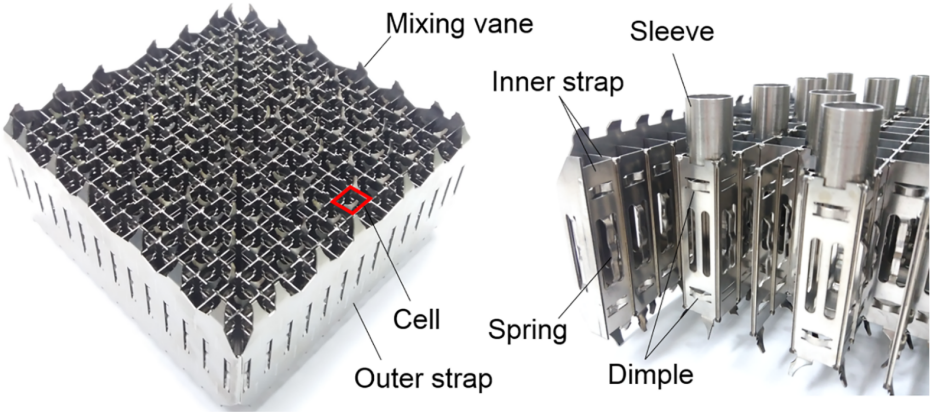

Figure 1.5: Picture of a fuel assembly grid. [173]

- Mixing grids equipped with mixing vanes (Figure 1.5) that adds a rotational motion to the axially flowing fluid enhancing the turbulence and mixing to homogenize its temperature.

Figure 1.6 shows an enlarge model of a grid for a 5×5 rod bundle. The 25 cells holding the rods are clearly visible along with the different components being the mixing vanes, the dimples and the springs. The latter two holding the rods straight when they are inserted through the grid.

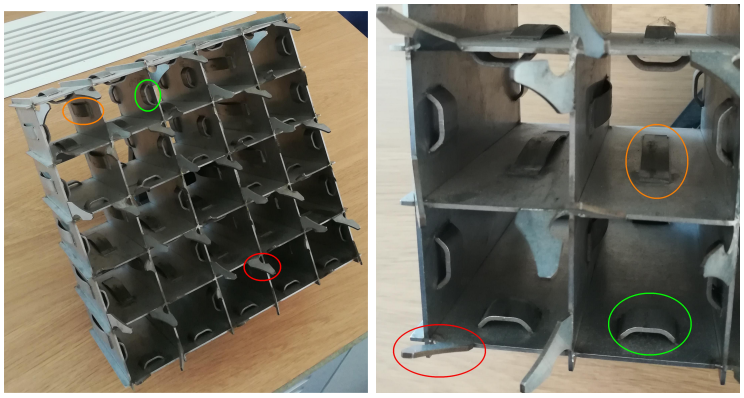

Figure 1.6: Model of a 5×5 grid (scale 5:1) from EDF Lab Chatou. Mixing vanes circled in red, dimples in green and springs in orange.

1.3 SAFETY AND THERMAL DESIGN OF PWR

Regarding radioactivity, the safety of a PWR is ensured by three containment barriers:

- The fuel rod cladding (Figure 1.3) ;
- The Reactor Pressure Vessel and primary loop (Figure 1.2) ;
- The containment building (Figure 1.1).

Therefore, thermal-hydraulic design of a PWR has to account for any situation that can potentially pose a threat to those containment barriers. In particular, the water used as coolant in the core has to be able to remove the heat from the fuel rods in conditions being nominal, transient and also incidental. The different elements of the primary loop involved in the cooling process both have to be able to withstand the possible violent dynamic changes during the operation of the reactor and avoid to damage other parts of the circuit, especially those related to a containment barrier (fuel rods, RPV, etc.).
In incidental conditions, the water around the fuel rods can be exposed to a huge increase of the thermal power it receives per unit of volume and being heated up above its saturation temperature, starting its

vaporization. This can then lead to multiphase boiling flow regimes in the core, with a risk of reaching the critical situation called the **boiling crisis** (BC).

The Boiling Crisis (described in the next Section) is among the most important thermal-hydraulic phenomenon that has to be accounted for in the design of nuclear reactors since it can severely damage the nuclear fuel rods cladding and thus requires dedicated studies and modeling.

1.4 THERMAL-HYDRAULICS OF BOILING TWO-PHASE FLOWS

In nuclear reactors, the water enters in the fuel assemblies from bottom and flows upwards while being heated along the 4 m height of the rods. It is initially highly subcooled *i. e.* at a temperature $T_{L,in}$ much below the saturation temperature (usually a difference of $\Delta T_L = T_{sat} - T_{L,in} \approx 50°C$, $T_{sat} \approx 345°C$ at 155 bar) and exits the fuel assembly at $\Delta T_L = 15°C$. Therefore, the physics at stake relates to **vertical subcooled boiling flows**.

1.4.1 *Vertical Subcooled Boiling Flow Regimes*

When the liquid heats up while flowing upwards, different heat exchange regimes can occur along with various multiphase flow regimes during phase-change. They are usually defined depending on the liquid thermodynamic quality $x_{eq} = \dfrac{h_{V,sat} - h_M}{h_{V,sat} - h_{L,sat}}$ ($x_{eq} < 0$ if the the flow is subcooled, $0 \leq x_{eq} \leq 1$ if the mixture is at saturation) and the time-space distribution of the liquid and vapor phases. In the case of a simple tube, Figure 1.7 presents a sketch of the different flow and heat transfer regimes occurring for vertical flow boiling in a tube with a negative inlet liquid quality. A low but constant heat flux is applied over the tube, long enough to end-up with pure vapor flow ($x_{eq} \geq 1$).

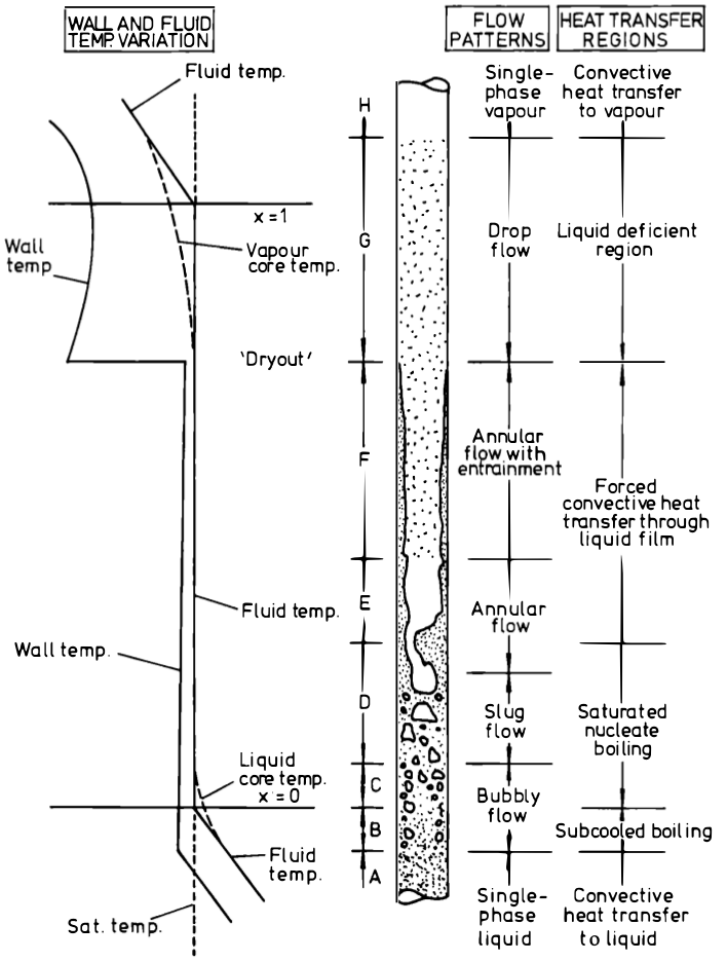

Figure 1.7: Sketch of the different vertical flow boiling regimes in a vertical tube at low heat flux from Collier & Thome (1994, [29]). Here, x denotes the local thermodynamic quality noted x_{eq} in the text.

First, the liquid enters in a subcooled state *i. e.* below saturation temperature, leading to a pure *liquid convective heat transfer* (zone A).

Then, the wall heats up above the saturation temperature to reach the **Onset of Nucleate Boiling** (ONB), allowing vapor bubbles to nucleate at the wall on so-called "nucleation sites" (which density increases with the heat flux or wall temperature). This happens first in regions where the average temperature of the fluid is still below the saturation temperature, thus called *subcooled boiling* (zone B). As we move upwards the tube, the boiling intensifies and bubbles start to leave the wall, corresponding to the **Onset of Significant Void** (OSV). They migrate into the bulk flow where they condense due to the locally subcooled liquid. In this region, the multiphase vapor-liquid flow is qualified as *bubbly flow* and the vapor phase can be considered as dispersed into the main continuous liquid phase.

When the average liquid temperature reaches saturation, $x_{eq} = 0$ and we enter the *saturated boiling* regime. The vapor phase is first still composed of small dispersed bubbles in the bulk flow (zone C). Since liquid is at saturation temperature, vapor bubbles do not condense anymore and start to coalesce with each other, forming larger inclusions leading to a *slug flow* (zone D).

Further downstream, the volume occupied by vapor at a given height starts to overcome that of the liquid phase *i. e.* we reach high local "void fractions" (ratio of the vapor volume over the total volume). This leads to a significant change in the flow regime where the core flow is composed of vapor while liquid is pushed towards the wall, called *annular flow*. The liquid film trapped between the vapor and the wall increases the effective thermal conductivity and limits the possibilities of wall nucleation (zones E & F).

Finally, when the liquid film has totally evaporated, the wall is in direct contact with the vapor phase (zones G & H). This phenomenon is called **dryout** and is associated to a steep increase of the wall temperature due to the decrease of the heat transfer coefficient induced by the low vapor thermal conductivity.

1.4.2 *Boiling Crisis and Critical Heat Flux in PWR*

The rapid rise of the wall temperature when dryout occurs actually corresponds to the so-called **boiling crisis**. The example of Figure 1.7 shows the occurrence of a boiling crisis triggered by the evaporation of a thin liquid film separating the bulk vapor and the wall, called **Liquid Sublayer Dryout** (LSD), happening at low heat fluxes and high outlet quality ($x_{eq} > 0.2$ usually).

However in PWR, the very low inlet flow quality ($T_{L,in} \approx T_{sat} - 50°C$) combined with the high heat flux at the rods can trigger a boiling crisis of different nature. If the wall boiling becomes too intense, it may result in the formation of a vapor blanket at the wall insulating it from the liquid water cooling (Figures 1.8 and 1.9), thus abruptly increasing its temperature and posing a high risk of material damage. This type of boiling crisis is called the **Departure from Nucleate Boiling** (DNB). The heat flux at which the boiling crisis occurs is named **Critical Heat Flux** (CHF).

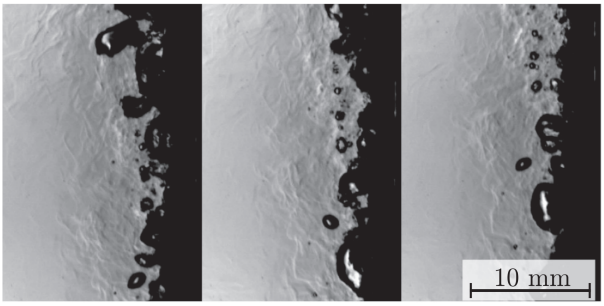

Figure 1.8: Experimental shadowgrams from Bloch *et al.* [11] of the flow boiling at CHF for a 27 K subcooled liquid flowing upwards at 0.6 m/s and atmospheric pressure.

According to Bricard (1995, [16]), the LSD boiling crisis is well identified both by experimental and modeling approaches [72] where the scientific community seems to have reached a consensus. On the contrary, DNB-type boiling crisis is much more debated since it results from local boiling phenomena

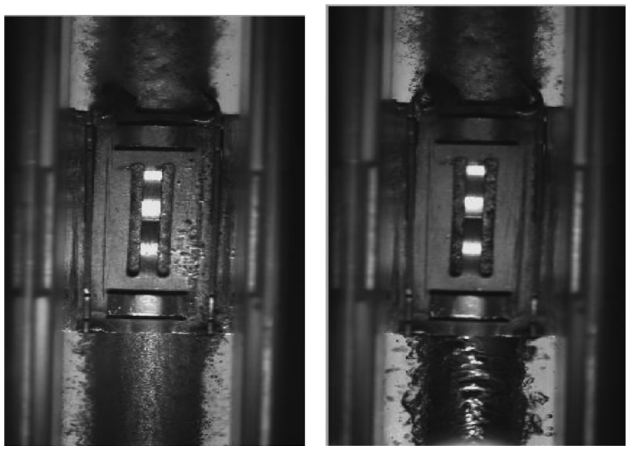

(a) $\phi_w \approx 0.96\phi_{w,CHF}$ (b) $\phi_w \approx \phi_{w,CHF}$

Figure 1.9: Visualization of a DNB-type boiling crisis on a rod with a mixing grid by Liu *et al.* [104]. The fluid is R134a at $P = 2184$ kPa, $G = 2076$ kg/m^2/s , $T_{sat} - T_{L,in} = 22.8$°C. The insulating vapor blanket is clearly visible upstream the mixing grid.

including bubble dynamics at the wall and is still under thorough scientific investigation today [11, 12, 37, 90, 139].

1.4.3 *Boiling Curves*

The boiling crisis phenomenon has been reported among the first times in the pioneering work of Nukiyama [126] who observed the variety of heat transfer regimes occurring during boiling and identified the maximum accessible heat flux as the Critical Heat Flux. He summarized his findings on a so-called "boiling curve" representing the evolution of the wall temperature (or superheat) against the applied heat flux ϕ_w (Figure 1.10).

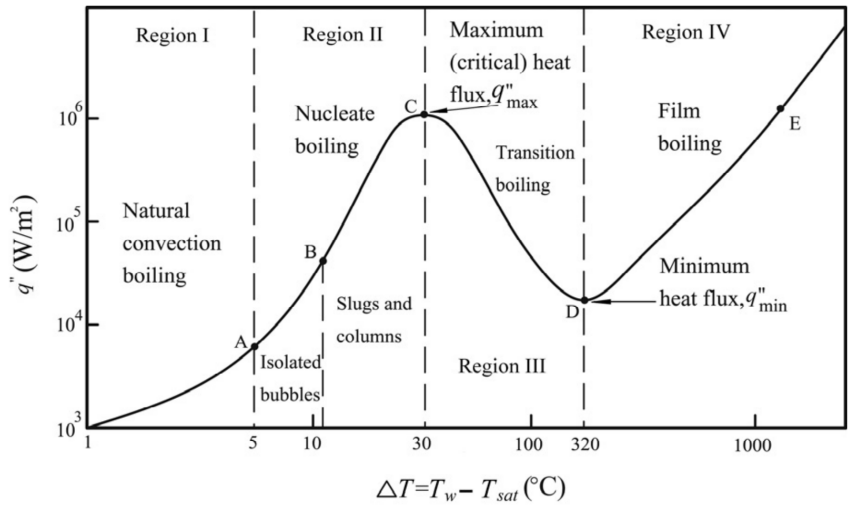

Figure 1.10: Example of Nukiyama / boiling curve for water from [45]. Here q'' denotes the wall heat flux.

For a flux-controlled experiment, reaching the CHF triggers a nearly instantaneous transition from point C to point E (Figure 1.10) which graphically shows the violent increase in wall temperature that can damage the heater.

1.5 CURRENT INDUSTRIAL TREATMENT OF THE BOILING CRISIS

Even if boiling can be a very efficient way of increasing the global heat transfer between a solid wall and surrounding liquid, the existence of the CHF as an upper limit over which the heater material integrity is threatened represents a huge physical limitation that has to be anticipated. Figure 1.11 shows an example of fuel damage after undergoing a boiling crisis.

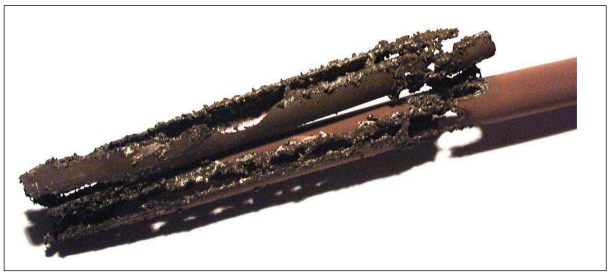

(a) Post-BC damage on a rod

(b) Post-BC damage on an assembly (deformation not due to the BC)

Figure 1.11: Damaged electrically heated components (used for CHF experimental tests in PWR conditions) after the boiling crisis (from CEA Omega experiment [44]).

Any nuclear power unit operator, such as EDF, consequently has to prevent the occurrence of DNB in the core to ensure the full integrity of the nuclear fuel rods. Safety margins imposed by the french Nuclear Safety Authority (ASN) have to be respected at all time. Otherwise, the nuclear unit will have to be stopped in order to prevent any incident or accident. Such constraints represent a very challenging aspect for nuclear core thermal-hydraulics which primary goal is to be able to anticipate and predict the value of the CHF for a large range of operating conditions.

Earlier, we mentioned the fact that the DNB was still a very debated phenomenon over which a general scientific agreement has still to be reached. Therefore, CHF predictions for safety studies are currently achieved using dedicated experimental correlations. Using experiments on a nearly full-scale assembly (5×5 electrically heated rods, grids, 4 m height, water at 155 bar, etc.), values of the CHF are measured in a large variety of operating conditions that covers the expected ranges for industrial operations. An empirical correlation based on those results is then constructed for the specific test geometry, usually of the form:

$$\phi_{w,CHF} = f\left(P, G, L_g, D_h, x_{eq}\right) \tag{1.1}$$

where P is the pressure, G the total mass flux, L_g the distance between two grids (Figure 1.3), D_h the hydraulic diameter and x_{eq} the thermodynamic quality.

This correlation is then used in multidimensional codes based on porous medium approaches (to avoid fine representation of the geometry), where the scale of a computation cell is usually that of a "sub-channel" (Figure 1.12) *i. e.* the space between four rods.

Using the average thermal-hydraulics values of the flow at the scale of the subchannel, the dedicated correlation then estimates CHF in the cell which can be compared to the applied heat flux ϕ_w to estimate the **Departure to Nucleate Boiling Ratio** (DNBR) $\phi_w/\phi_{w,CHF}$ that gives the safety margin to the boiling crisis. For EDF, those numerical studies are conducted using the THYC code [3].

1.6 TOWARDS LOCAL PREDICTIONS OF THE CHF USING COMPUTATIONAL MULTI-FLUID DYNAMICS

Investigating the boiling crisis physics has showed that the associated time-space scale was sometimes lower than 1 ms and 1 mm [12], *i. e.* smaller than the sub-channel scale. Achieving wall-boiling modeling at those scales is impossible with traditional safety studies codes and thus put the light onto Computational Multi-Fluid Dynamics (CMFD), which recent improvements over the past decades (model formulations,

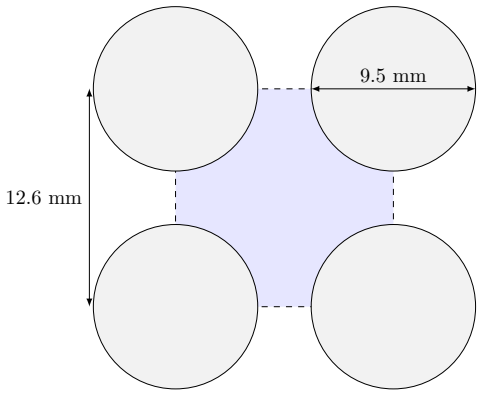

Figure 1.12: Sketch of a sub-channel in a rod bundle (dashed lines). The equivalent hydraulic diameter here is $D_h = 11.78$ mm.

computational capacity, meshing techniques, etc.) has demonstrated its capability of simulating nearly industrial-scaled situations.

With CMFD codes, simulations of multiphase flows can be conducted at small local scales that are interesting to achieve:

- Finer descriptions of the multiphase flow structure and phase-change ;
- More detailed relationship between the wall local thermal-hydraulics properties and the boiling crisis using dedicated models including new physical phenomena related to wall boiling.

At EDF R&D, the in-house CFD code *code_saturne* has its own module dedicated to multiphase flows: NEPTUNE_CFD [65]. NEPTUNE_CFD is the chosen numerical tool to investigate the modeling and simulation of the boiling crisis at CFD scale.

1.7 CONTENTS OF THIS THESIS

In this thesis, we want to address the problem of boiling crisis prediction using CFD in PWR conditions. This can be summed up in the following question:

Is it nowadays possible to reach a proper modeling of the wall boiling phenomenon to predict boiling crisis occurrence in PWR using CFD simulations ?

This manuscript is organized as follows. **Part I** is dedicated to boiling flow simulations using NEPTUNE_CFD:

- **Chapter 2** details the constitutive equations and the different closure laws used in the 7.0 version of NEPTUNE_CFD.
- **Chapter 3** presents the DEBORA experimental database that will be used for CFD validation. Some analyses regarding the database consistency and physical implications are proposed.
- **Chapter 4** compares the simulation results obtained using NEPTUNE_CFD with the DEBORA experiment. This allows to identify the strengths and weaknesses of the current modeling for boiling dispersed bubbly flows.

Following those investigations, **Part II** focuses on the development of a new Heat Flux Partitioning (HFP) model:

- **Chapter 5** briefly presents some bibliographic aspects regarding the modeling of wall boiling heat transfer.
- **Chapter 6** then investigates in details the dynamics of bubble boiling at the wall. A particular care is given to the modeling of the bubble force balance to reach a representative description of the nucleated bubble movement.

- **Chapter 7** discusses the different closure laws required to complete the Heat Flux Partitioning model and gathers experimental measurements for their assessment. The formulation of the new model is finally presented.
- **Chapter 8** presents validation aspects of the model with comparisons to fine experimental measurements and wall temperature predictions from different literature databases.
- **Chapter 9** discusses perspectives regarding the prediction of the Critical Heat Flux using Heat Flux Partitioning models.

Finally, **Part III** investigates the impact of mixing vanes over the boiling flow:

- **Chapter 10** studies the DEBORA-Promoteur and AGATE-Promoteur experiments of a boiling and single-phase flow in a tube including mixing vanes. Analyses of the measurements are conducted to further understand the structure of boiling flows in PWR.
- **Chapter 11** presents NEPTUNE_CFD simulations of the tube and mixing vanes case. Comparisons to the experiments evaluates the capacity of CFD to properly capture the effect of such geometries.

Chapter 12 closes this manuscript by summarizing the different conclusions of the presented work and details the different perspectives emerging from the presented results.

Part I

MODELING AND SIMULATION OF BOILING FLOWS USING NEPTUNE_CFD

2

PRESENTATION OF THE NEPTUNE_CFD CODE

Contents

2.1 Introduction 13
2.2 Governing Equations for Turbulent Boiling Bubbly Flows 13
2.2.1 Mass Conservation 14
2.2.2 Momentum Balance 14
2.2.3 Energy Conservation 14
2.3 Interfacial Transfers Closure Laws 14
2.3.1 Heat and Mass Transfers 14
2.3.2 Interfacial Forces 16
2.4 Turbulence Modeling 17
2.5 Wall Boiling Model 18
2.6 Wall Function for Dispersed Boiling Flows 19
2.7 Conclusions 20

2.1 INTRODUCTION

The NEPTUNE_CFD project (started in 2001) is a research program coordinated by four entities : EDF, CEA, IRSN and Framatome. The initial goals of the project were related to nuclear safety by developing a thermal-hydraulics simulation tool to :

- Predict the Boiling Crisis in PWR cores ;
- Study the Loss Of Coolant Accident (LOCA) to predict fuel rod cladding temperature.

As a multiphase eulerian code, NEPTUNE_CFD consists of a local three-dimensional modeling based on a two fluids-one pressure approach combined with mass, momentum and energy conservation equations for each phase [65].

The constitutive equations are solved using a pressure correction and is based on a finite-volume discretization along with a collocated arrangement of the variables. Moreover, NEPTUNE_CFD allows the use of all type of meshes (hexahedral, tetrahedral, pyramids, etc.), even non-conforming ones, thanks to its face-based data structure. Finally, the code is well-suited for parallel computing, widening its computing capacity to very large meshes.

The simulations presented in this thesis have all been conducted using the NEPTUNE_CFD 7.0 modeling framework for dispersed bubbly flows. In the next sections, we will detail the constitutive equations and physical modeling of the code for the simulation of boiling bubbly flows.

2.2 GOVERNING EQUATIONS FOR TURBULENT BOILING BUBBLY FLOWS

To simulate two-phase dispersed boiling flows, NEPTUNE_CFD solves the ensemble-averaged equations of mass conservation, momentum balance and energy conservation for each phase (see Ishii [76] for details on the derivation).

2.2.1 *Mass Conservation*

$$\frac{\partial \alpha_k \rho_k}{\partial t} + \overline{\nabla} \cdot \left(\alpha_k \rho_k \overline{U_k}\right) = \Gamma_k \tag{2.1}$$

Where α_k, ρ_k, $\overline{U_k}$ are the volumetric fraction, average density and velocity of phase k ; $\Gamma_k = \Gamma_{k,i} + \Gamma_{k,w}$ the interfacial mass transfer term per unit of volume and time split between bulk and wall contribution. Subscripts $k = L$ or V denotes the liquid or vapor phase, i the interfacial quantities and w the wall contribution.

2.2.2 *Momentum Balance*

$$\frac{\partial \alpha_k \rho_k \overline{U_k}}{\partial t} + \overline{\overline{\nabla}} \cdot \left(\alpha_k \rho_k \overline{U_k} \otimes \overline{U_k}\right) = -\alpha_k \overline{\nabla}\left(P\right) + \overline{F_{k,i}} + \Gamma_k \overline{U_{k,i}} + \alpha_k \rho_k \overline{g} + \overline{\overline{\nabla}} \cdot \left(\alpha_k \left(\overline{\overline{\tau_{k,m}}} + \overline{\overline{\tau_{k,T}}}\right)\right) \tag{2.2}$$

Where P is the pressure, $\overline{g}$ the gravity, $\overline{F_{k,i}}$ the interfacial forces accounting for momentum transfer between phases per unit of volume and time, $\overline{U_{k,i}}$ the interfacial velocity, $\overline{\overline{\tau_{k,m}}}$ and $\overline{\overline{\tau_{k,T}}}$ respectively the viscous and turbulent (or Reynolds) stress tensor. Subscript m and T respectively denote the molecular (or laminar) and turbulent terms.

2.2.3 *Energy Conservation*

$$\begin{aligned}\frac{\partial \alpha_k \rho_k H_k}{\partial t} + \overline{\nabla} \cdot \left(\alpha_k \rho_k H_k \overline{U_k}\right) =& \frac{\partial \alpha_k P}{\partial t} + \Gamma_k H_{k,i} + \overline{F_{k,i}} \cdot \overline{U_k} + Q_{k,I} + \overline{\nabla} \cdot \left(\alpha_k \left(\overline{\overline{\tau_k}} + \overline{\overline{\tau_{k,T}}}\right) \cdot \overline{U_k}\right) \\ &+ \overline{\nabla} \cdot \left(\alpha_k \left(-\left(\lambda_{k,m} + \lambda_{k,T}\right) \overline{\nabla}\left(T_k\right)\right)\right) + \alpha_k \rho_k \overline{g} \cdot \overline{U_k} + Q_{k,w}\end{aligned} \tag{2.3}$$

Where $H_k = e_k + \dfrac{U_k^2}{2} + \dfrac{P}{\rho_k} = h_k + \dfrac{U_k^2}{2}$ is the total enthalpy of phase k, $H_{k,i}$ the interfacial-averaged enthalpy, $Q_{k,i}$ the interfacial heat flux per unit of volume and time, $\lambda_{k,m}$ and $\lambda_{k,T}$ respectively being the laminar and turbulent thermal conductivity, T_k the temperature, $Q_{k,w}$ the heat flux from the wall to phase k per unit of volume and time.

The viscous and Reynolds stress tensors read:

$$\overline{\overline{\tau_{k,m}}} = \mu_k \left(\overline{\overline{\nabla}}\left(\overline{U_k}\right) + \overline{\overline{\nabla}}\left(U_k\right)^T - \frac{2}{3}\overline{\nabla} \cdot \left(\overline{U_k}\right) \overline{\overline{I}}\right) \tag{2.4}$$

$$\left(\overline{\overline{\tau_{k,T}}}\right)_{i,j} = -\rho_k \left\langle U'_{k,i} U'_{k,j} \right\rangle_k \tag{2.5}$$

with $\overline{U'_k}$ is the fluctuating part of velocity for phase k.

This ensemble-average approach requires a given number of closure laws since this mathematical averaging operation removes most of the information about smaller scales physics (compared to the mesh size) such as interfacial exchanges between phases or wall-fluid interaction. Terms for which this modeling effort is needed are colored in orange in equations 2.1, 2.2 and 2.3. Following sections detail the physical modeling for each of those terms.

2.3 INTERFACIAL TRANSFERS CLOSURE LAWS

The interfacial transfers of mass, momentum and energy are respectively noted in equations 2.1, 2.2 and 2.3 : Γ_k, $\overline{F_{k,i}}$ and $Q_{k,i}$.

2.3.1 *Heat and Mass Transfers*

The mass transfer term, can be written as:

$$\Gamma_{L,i} + \Gamma_{V,i} = 0 \tag{2.6}$$

$$\Gamma_{L,w} + \Gamma_{V,w} = 0 \tag{2.7}$$

with $\Gamma_{V,w} \geq 0$ in the case of boiling flows. This finally gives:

$$\Gamma_L = -\Gamma_V \tag{2.8}$$

The interfacial heat flux $Q_{k,i}$ can be rewritten in terms of interfacial area concentration a_i :

$$Q_{k,i} = q''_{k,i} a_i \tag{2.9}$$

Neglecting the mechanical contribution compared to the thermal terms, the energy jump condition can then be expressed as :

$$\sum_{k=L,V} \left(\Gamma_{k,i} h_{k,i} + q''_{k,i} a_i \right) = 0 \tag{2.10}$$

The estimation of $h_{k,i}$ is not straightforward since it can either be supposed as:

H1) The saturation enthalpy of phase k at the system pressure ;

H2) The phase-averaged enthalpy.

In NEPTUNE_CFD, the assumption H2 is chosen, thus giving the bulk condensation rate :

$$\Gamma_{L,i} = \frac{a_i \left(q''_{L,i} + q''_{V,i} \right)}{h_V - h_L} \tag{2.11}$$

The interfacial heat flux densities $q''_{k,i}$ and interfacial area concentration a_i are expressed as:

$$q''_{k,i} = C_{k,i} \left(T_{sat}(P) - T_k \right) \tag{2.12}$$

$$a_i = 6\alpha_V / D_V \tag{2.13}$$

with D_V being the vapor phase Sauter mean bubble diameter and $C_{k,i}$ the interfacial heat transfer coefficient.

> **Note :** The interfacial area is computed using the transport equation of Ruyer & Seiler [142] that accounts for bubble breakup and coalescence to estimate bubble diameter.

2.3.1.1 *Subcooled Liquid*

For subcooled liquid, the following heat transfer coefficient is used [109, 133]:

$$C_{L,i} = \frac{\mathrm{Nu}_L \lambda_L}{D_V} \tag{2.14}$$

$$Nu_L = 2 + 0.6 \mathrm{Re}_b^{1/2} \mathrm{Pr}_L^{1/3} \tag{2.15}$$

Where Re_b is the bubble Reynolds number $Re_b = \dfrac{\left|\left|\overline{U_V} - \overline{U_L}\right|\right| D_V}{\nu_L}$ and $\mathrm{Pr}_L = \dfrac{\nu_L}{\eta_L}$ the liquid Prandtl number with ν_L and η_L respectively being the liquid kinematic viscosity and thermal diffusivity.

> **Remark :** This formulation initially proposed by Ranz & Marshall [133] is based on experiments for evaporating droplets. In that regard, its application to bubble condensation could be further discussed.

2.3.1.2 *Superheated Liquid*

On the other hand, if the liquid is overheated, the maximum of three heat transfer coefficients accounting for different heat transfer mechanisms is taken [9]:

$$C_{L,i} = \max\left(C_{L,i,1}\ ;\ C_{L,i,2}\ ;\ C_{L,i,3}\right) \tag{2.16}$$

With $C_{L,i,n} = \dfrac{\lambda_L \mathrm{Nu}_{L,n}}{D_V}$ and :

$$Nu_{L,1} = 2\ ;\ Nu_{L,2} = \frac{12}{\pi}\mathrm{Ja}_L\ ;\ Nu_{L,3} = \sqrt{\frac{4}{\pi}Pe} \tag{2.17}$$

where $\mathrm{Pe} = \mathrm{Re}_b\mathrm{Pr}_L$ is the Peclet number, $\mathrm{Ja}_L = \dfrac{\rho_L c_{p,L}\left|T_{sat} - T_L\right|}{\rho_V h_{LV}}$ the liquid Jakob number and h_{LV} the latent heat of vaporization.

Those three Nusselt numbers respectively correspond to stationary conduction around a sphere, transient conduction for a spherical bubble growth in uniformly superheated liquid [129] and transient convection around a sphere in a superheated flow [141].

2.3.1.3 *Vapor Heat Transfer*

For the vapor phase, a simple law that ensures the vapor temperature to stay close to the saturation temperature is used (which is expected for small bubbles, *e. g.* in a PWR) :

$$C_{V,i}a_i = \frac{\alpha_V \rho_V c_{p,V}}{t_c} \tag{2.18}$$

where $c_{p,V}$ is the vapor heat capacity at constant pressure and t_c a characteristic (relaxation) time given by the user (default value being $t_c = 0.01$ s) .

2.3.2 *Interfacial Forces*

The interfacial momentum transfer (excluding transfer associated to transfer of mass Γ_k) is assumed to be composed of 4 different forces being the, drag D, the added mass AM, the lift L and the turbulent dispersion TD:

$$\overline{F_{k,i}} = \overline{F_{k,D}} + \overline{F_{k,AM}} + \overline{F_{k,L}} + \overline{F_{k,TD}} \tag{2.19}$$

The turbulent dispersion force $\overline{F_{k,TD}}$ originates from the averaging operation conducted on the three other forces expressions, detailed in equations 2.20, 2.24, 2.25 and 2.28.

2.3.2.1 *Drag Force*

The drag force is modeled according to Ishii & Zuber [77]:

$$\overline{F_{V,D}} = -\overline{F_{L,D}} = -\frac{1}{8}a_i\rho_L C_D\left|\left|\overline{U_V} - \overline{U_L}\right|\right|\left(\overline{U_V} - \overline{U_L}\right) \tag{2.20}$$

$$C_D = \frac{2}{3}D_V\sqrt{\frac{g\left(\rho_L - \rho_V\right)}{\sigma}}\left(\frac{1 + 17.67\ f\left(\alpha\right)^{1.67}}{18.67 f\left(\alpha\right)}\right),\ f\left(\alpha\right) = \left(1-\alpha\right)^{1.5}\ \text{for distorted bubbles.} \tag{2.21}$$

$$C_D = \frac{8}{3}\left(1-\alpha\right)^2\ \text{for churn-turbulent regime.} \tag{2.22}$$

2.3.2.2 *Added Mass Force*

The added mass force is modeled following Zuber [182]:

$$\overline{F_{V,AM}} = -\overline{F_{L,AM}} = -C_{AM}\frac{1+2\alpha_V}{1-\alpha_V}\alpha_V\rho_L \tag{2.23}$$

$$\times\left[\left(\frac{\partial\overline{U_V}}{\partial t}+\overline{\overline{\nabla}}\left(\overline{U_V}\right)\cdot\overline{U_V}\right)-\left(\frac{\partial\overline{U_L}}{\partial t}+\overline{\overline{\nabla}}\left(\overline{U_L}\right)\cdot\overline{U_L}\right)\right] \tag{2.24}$$

with $C_{AM}=\dfrac{1}{2}$ and the term $\dfrac{1+2\alpha_V}{1-\alpha_V}$ accounts for the impact of bubble concentration.

2.3.2.3 *Lift Force*

The lift force is modeled based on the experiments of Tomiyama *et al.* [159]:

$$\overline{F_{V,L}} = -\overline{F_{L,L}} = -C_L\alpha_V\rho_L\left(\overline{U_V}-\overline{U_L}\right)\wedge\left(\overline{\nabla}\wedge\overline{U_L}\right) \tag{2.25}$$

$$C_L=\begin{cases}\min\left(0.288\tanh\left(0.121\mathrm{Re}_b\right)\ ;\ 0.00105\mathrm{Eo}_H^3-0.0159\mathrm{Eo}_H^2-0.0204\mathrm{Eo}_H+0.474\right), & \text{if } \mathrm{Eo}_H<4\\ 0.00105\mathrm{Eo}_H^3-0.0159\mathrm{Eo}_H^2-0.0204\mathrm{Eo}_H+0.474, & \text{if } 4\leq\mathrm{Eo}_H\leq 10\\ -0.27, & \text{if } \mathrm{Eo}_H>10\end{cases} \tag{2.26}$$

where $\mathrm{Eo}_H=\dfrac{g\left(\rho_V-\rho_L\right)D_H^2}{\sigma}$ is a modified Eötvös number with:

$$D_H = D_V\sqrt[3]{1+0.163\mathrm{Eo}^{0.757}} \tag{2.27}$$

2.3.2.4 *Turbulent Dispersion Force*

The turbulent dispersion force is computed following the General Turbulent Dispersion approach from Haynes [71] and presented by Lavieville *et al.* [95]:

$$\overline{F_{V,TD}} = -\overline{F_{L,TD}} = -\frac{2}{3}\alpha_L\alpha_V C_{TD}\overline{\nabla}\left(\alpha_V\right) \tag{2.28}$$

The value of C_{TD} notably depends on the fluid turbulence, drag force, added mass force. Further details on its derivation are presented in Lavieville *et al.* [95].

2.4 TURBULENCE MODELING

For bubbly flow simulations, only liquid phase turbulence is taken into account while it is neglected for the vapor phase. The prescribed model is the Reynolds Stress Model $R_{ij}-\varepsilon$ *SSG* from Speziale, Sarkar and Gatski [150] adapted to two-phase boiling flows by Mimouni *et al.* [118]. Noting $R_{ij}=\left\langle U'_{L,i}U'_{L,j}\right\rangle_L$ and $\alpha=\alpha_V$, it reads:

$$(1-\alpha)+\frac{\mathrm{D}\rho_L R_{ij}}{\mathrm{D}t} = \frac{\partial}{\partial x_k}\left[\left(\rho_L\nu_L+\rho_L C_s\frac{k}{\varepsilon}R_{ij}\right)\frac{\partial}{\partial x_k}\left(\left(1-\alpha\right)R_{ij}\right)\right] \tag{2.29}$$

$$+\left(1-\alpha\right)\left(P_{ij}+G_{ij}+\Phi_{ij}+\varepsilon_{ij}\right) \tag{2.30}$$

where $\mathrm{D}/\mathrm{D}t$ is the Lagrangian derivative, k the turbulent kinetic energy, ε the turbulent pseudo-dissipation rate, $\overline{\overline{P}}$ the turbulent production term, $\overline{\overline{G}}$ the work of gravity force, $\overline{\overline{\Phi}}$ the pressure-strain term and $\overline{\overline{\varepsilon}}$ the viscous dissipation.

All those terms need a proper modeling, for which we refer the reader to Mimouni *et al.* [118].

The transport equation on ε also includes the impact of α:

$$(1-\alpha)+\frac{\mathrm{D}\varepsilon}{\mathrm{D}t}=\frac{\partial}{\partial x_k}\left[C_\varepsilon\frac{k}{\varepsilon}\left\langle U'_{L,k}U'_{L,l}\right\rangle_L\frac{\partial\left(1-\alpha\right)\epsilon}{\partial x_l}\right] \tag{2.31}$$

$$+\left(C_{\varepsilon_1}+C_{\varepsilon_3}G+C_{\varepsilon_4}k\frac{\partial U_{L,k}}{\partial x_k}-C_{\varepsilon_2}\epsilon\right)\frac{\left(1-\alpha\right)\epsilon}{k} \tag{2.32}$$

We conclude by specifying the values used for the constants in NEPTUNE_CFD (Table 2.1).

C_s	C_1	C_2	C_1^ω	C_2^ω	C_ε	C_{ε_1}	C_{ε_2}	C_{ε_3}	C_{ε_4}
0.2	1.8	0.6	0.5	0.3	0.18	1.44	1.92	1.44	0.33

Table 2.1: Constant values for the SSG model in NEPTUNE_CFD

2.5 WALL BOILING MODEL

The modeling of the heterogeneous boiling phenomenon at the wall is based on a Heat Flux Partitioning (HFP) model, from Kurul & Podowski original work[92] who divided the wall heat flux density ϕ_w in three terms :

- A single phase convective heat flux $\phi_{c,L}$ heating the liquid through the fraction of the wall area unaffected by the vapor bubbles ;
- A vaporization heat flux ϕ_e which accounts for the generation of vapor through heterogeneous nucleation ;
- A quenching heat flux ϕ_q to represent the thermal impact of bubbles departing from the wall and being replaced by cool liquid

A fourth flux is added to this HFP in NEPTUNE_CFD, following Mimouni *et al.* [117] who consider a convective heat flux towards the vapor $\phi_{c,V}$ when the wall area is covered by a dense accumulation of bubbles.

The model is then ponderated by a phenomenological function f_{α_L} enhancing $\phi_{c,V}$ when the void fraction at the wall becomes large. It thus gives Equation 2.33 :

$$\phi_w=f_{\alpha_L}\left(\phi_{c,L}+\phi_e+\phi_q\right)+\left(1+f_{\alpha_L}\right)\phi_{c,V} \tag{2.33}$$

where f_{α_L} verifies smooth conditions $\lim\limits_{\alpha_L\to1}f_{\alpha_L}=1$, $\lim\limits_{\alpha_L\to0}f_{\alpha_L}=0$, $\lim\limits_{\alpha_L\to0}\dfrac{f_{\alpha_L}}{\alpha_L}=0$ and $\lim\limits_{\alpha_L\to1}\dfrac{1-f_{\alpha_L}}{1-\alpha_L}=0$.

The convective heat fluxes are expressed as:

$$\phi_{c,k}=A_k h_{k,log}\left(T_w-T_k\right) \tag{2.34}$$

$$h_{k,log}=\frac{\rho_k c_{p,k}U_\tau}{T_L^+} \tag{2.35}$$

where A_k the fraction of the wall area facing phase k, T_w the wall temperature and $h_{k,log}$ the wall logarithmic convective heat transfer coefficient to phase k based on the wall functions for friction velocity U_τ and non-dimensional liquid temperature T_L^+ described in 2.6.

The vaporization heat flux is computed following:

$$\phi_e=N_{sit}f\rho_V h_{LV}\frac{\pi D_d^2}{6} \tag{2.36}$$

Closure of physical parameters needed are :

- N_{sit} the nucleation site density modeled as [100]:

$$N_{sit} = \left[210\left(T_w - T_{sat}\right)\right]^{1.8} \tag{2.37}$$

- f the bubble detachment frequency expressed as [28]:

$$f = \sqrt{\frac{4}{3}\frac{g\left|\rho_V - \rho_L\right|}{\rho_L D_d}} \tag{2.38}$$

- D_d the bubble detachment diameter given by Ünal correlation [186] corrected by Borée *et al.* [14] (Equation 2.39).

$$D_d = 2.42\times10^{-5}P^{0.709}\frac{a}{\sqrt{b\varphi}} \text{ with} \tag{2.39}$$

$$a = \frac{\left(T_w - T_{sat}\right)\lambda_w}{2\rho_V h_{LV}\sqrt{\pi\eta_w}} \tag{2.40}$$

$$b = \begin{cases} \dfrac{T_{sat}-T_L}{2\left(1-\dfrac{\rho_V}{\rho_L}\right)}, & \text{if } St \leq 0.0065 \\ \dfrac{1}{2\left(1-\rho_V/\rho_L\right)}\dfrac{\phi_{c,L}+\phi_e+\phi_q}{0.0065\rho_L c_{p,L}\left|\left|\overline{U_L}\right|\right|}, & \text{if } St > 0.0065 \end{cases} \tag{2.41}$$

where λ_w and η_w are the wall thermal conductivity and diffusivity, $St = \dfrac{\phi_{c,L}+\phi_e+\phi_q}{\rho_L c_{p,L}\left|\left|\overline{U_L}\right|\right|\left(T_{sat}-T_L\right)}$ is the Stanton number and $\varphi = \max\left(1; \left(\dfrac{\left|\left|\overline{U_L}\right|\right|}{U_0}\right)^{0.47}\right)$ with $U_0 = 0.61\text{m/s}$

Finally, the quenching heat flux follows the approach of Del Valle & Kenning [35] supposing that it follows a semi-infinite transient conduction regime:

$$\phi_q = A_q t_q f \frac{2\lambda_L\left(T_w - T_L\right)}{\sqrt{\pi\eta_L t_q}} \tag{2.42}$$

where t_q is the quenching time, supposed to be equal to $1/f$, and $A_q = N_{sit}\pi R^2$ the area experiencing quenching.

2.6 WALL FUNCTION FOR DISPERSED BOILING FLOWS

In boiling flows, the formation of bubbles at the wall may disturb the liquid velocity profile in the boundary layer. To take this phenomena into account, Mimouni *et al.* [117] proposed a wall function for boiling flows which tends to the single-phase formulation when $\alpha_V \to 0$ and depends on the bubble diameter and density at the wall:

$$U^+ = \frac{1}{\kappa}\ln\left(y^+\right) + B - \Delta U^+ \text{ with} \tag{2.43}$$

where κ=0.41 is the Von Karman constant, $B = 5.3$ the standard single-phase logarithmic law constant and ΔU^+ represents the offset of U^+ due to the wall roughness induced by the presence of bubble.

The correction Δu^+ is computed as:

$$\Delta U^+ = \begin{cases} 0 & \text{if } k_r^+ \leq 11.3 \\ \dfrac{1}{\kappa}\ln\left(1+C_{kr}k_r^+\right) & \text{if } k_r^+ > 11.3 \end{cases} \tag{2.44}$$

$$k_r^+ = \frac{k_r\sqrt{U_\tau U_T}}{\nu_L} \tag{2.45}$$

$$k_r = \alpha_V d_V \tag{2.46}$$

$$U_T = C_\mu^{1/4}\sqrt{k_L} \tag{2.47}$$

with $C_{kr} = 0.5$, k_r a "bubble roughness Reynolds number", $C_\mu = 0.09$ defined from the $k-\varepsilon$ and k_L the liquid turbulent kinetic energy.

The non-dimensional wall phase temperature T_k^+ is modeled according following a Van Driest formulation:

$$T_k^+ = \int_0^{y^+} \frac{2\mathrm{d}y}{1 + \frac{1}{2}\frac{\mathrm{Pr}_k}{\mathrm{Pr}_{k,T}}\sqrt{1 + 4\kappa^2 {y^+}^2 \left(1 - \exp\left(-y^+/A\right)\right)^2}} \tag{2.48}$$

with $A = 25.6$, $\mathrm{Pr}_{k,T} = 0.9$ and $y^+ \approx 100$ usually for liquid water.

2.7 CONCLUSIONS

In this chapter, we presented the constitutive equations of NEPTUNE_CFD. As a summary, the main features of the modeling for dispersed bubbly flows are:

- Conservation equation for mass, momentum and energy are solved for liquid and vapor ;
- Interfacial momentum transfer is modeled by including different forces, with in particular recent formulations for turbulent dispersion and lift ;
- Turbulence is modeled by accounting for vapor presence in the $R_{ij} - \varepsilon$ SSG model along with a wall law based on local bubble size ;
- Wall boiling is based on a Heat Flux Partitioning approach extending the original formulation of Kurul & Podowski [92] by accounting for vapor convection at high wall void fraction.

In order to assess this modeling framework, we will further perform simulations using NEPTUNE_CFD. In next Chapter, we present the DEBORA database that will serve as validation reference in Chapter 4.

3

FLOW BOILING EXPERIMENTS REPRESENTATIVE OF PWR: THE DEBORA DATABASE

Contents

3.1 Introduction **21**
3.2 Simulating PWR water using R12 . . . . . **21**
3.2.1 Conservation of the Phase Density Ratio 22
3.2.2 Conservation of the Weber Number 23
3.2.3 Conservation of the Boiling Number 23
3.2.4 Conservation of the Inlet Thermodynamic Quality 23
3.2.5 Same Geometry 24
3.2.6 Transposition ranges 24
3.3 Description of the Test Section **25**
3.3.1 Geometrical Description 25
3.3.2 Measurement Instrumentation 25
3.4 Measurements Campaigns and Results **28**
3.4.1 Cases Nomenclature and Test Series 28
3.4.2 Verification of Control Parameters Coherency 29
3.4.3 Qualitative Analysis of the Experimental Results 30
3.5 Further Verification **35**
3.5.1 Reconstruction of the Applied Heat Flux 35
3.5.2 Verification of Wall Temperature Measurements 38
3.6 Conclusions **40**

3.1 INTRODUCTION

The validation of any existing modeling of multiphase flows must rely on extensive databases from experimental investigations in operating conditions that are representative of industrial configurations in PWR. This naturally lead to an important demand for measurements of local phase-related properties of vertical pressurized subcooled boiling flows.

To meet this need, CEA and EDF built a test facility called DEBORA in the 1990's. Its goal was to establish a consistent database of local measurements of the flow structure for vertical subcooled boiling Freon Refrigerant 12 (R12) from the Onset of Nucleate Boiling to the Boiling Crisis.

Many authors contributed to the establishment and analysis of the DEBORA database, among which Cubizolles [33], Garnier *et al.* [53], Manon [109], Guéguen [64] or Klédy [85].

In this chapter, we will describe the test section and analyze the available results from past measurements campaigns.

3.2 SIMULATING PWR WATER USING R12

The choice of using R12 as the working fluid in the DEBORA loop emerged from the interesting properties that boiling Freon presents when compared to the highly pressurized water in PWR cores. Indeed, the conditions for which the Boiling Crisis must be studied for water in PWR are:

- Pressure P between 100 and 180 bar ;
- Inlet liquid mass flux G between 1000 and 5000 kg/m^2/s (*i. e.* $10^5 \leq \mathrm{Re}_{D_h} \leq 7 \times 10^5$) ;
- Wall heat flux ϕ_w between 0.5 and 6 MW/m^2 ;
- Inlet thermodynamic flow quality $x_{eq,in}$ between -0.4 and 0.4.

In those ranges, sensors dedicated to local measurements are not suited to sustain such conditions.

The experimental strategy is then to "simulate" the aimed industrial conditions using a different fluid. It has to present thermophysical properties that allow to reproduce non-dimensional numbers of the industrial flow using less constraining operating conditions.

This explains the choice of R12 as it permits to transpose relevant parameters for PWR as detailed below.

Remark : Although interesting for PWR similitude, R12 is not expected to reproduce some fine physical properties such as surface wetting and bubble contact angle, which can be of significant importance regarding the boiling process (nucleation site density, wait time, etc.).

3.2.1 *Conservation of the Phase Density Ratio*

Freon 12 can reach the same density ratio as water in PWR using limited pressurized conditions no larger than 30 bar. It is an important parameter to mimic the behavior of the boiling two-phase flow since it has a strong influence over the bubble size for example [87].

$$\left(\frac{\rho_{V,sat}}{\rho_{L,sat}}\right)^{water}_{P_1} = \left(\frac{\rho_{V,sat}}{\rho_{L,sat}}\right)^{R12}_{P_2} \tag{3.1}$$

with $P_2 < P_1$.

The evolution of the density ratio of water and R12 with pressure are shown on Figure 3.1.

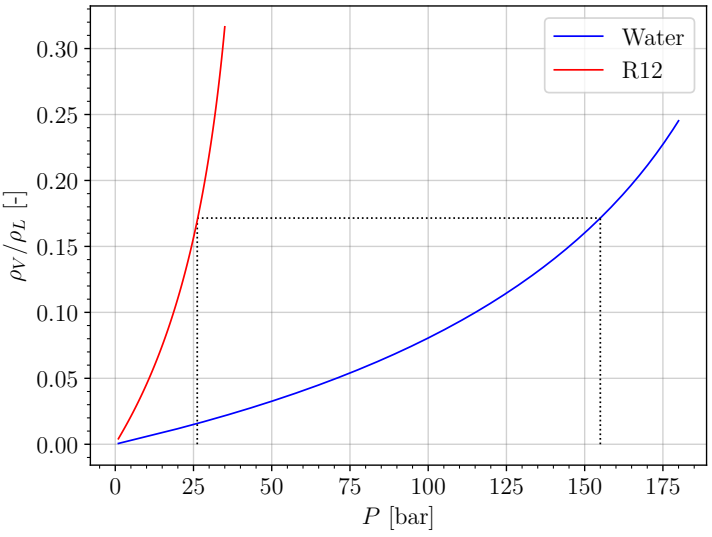

Figure 3.1: Density ratio of pressurized R12 and water

For instance, we can see that R12 at approximately 26 bar ($T_{sat} \approx 86.8$°C) has the same density ratio as water at 155 bar ($T_{sat} \approx 344.8$°C).

Note : This transposition criteria thus scales the operating pressure P of the experiment.

3.2.2 *Conservation of the Weber Number*

The Weber number is also similar to those encountered in PWR.

$$\mathrm{We} = \frac{G^2 R}{\rho_L \sigma} \tag{3.2}$$

This number characterizes physical phenomena such as bubble break-up or deformation under the influence of the liquid inertia, or bubble coalescence.

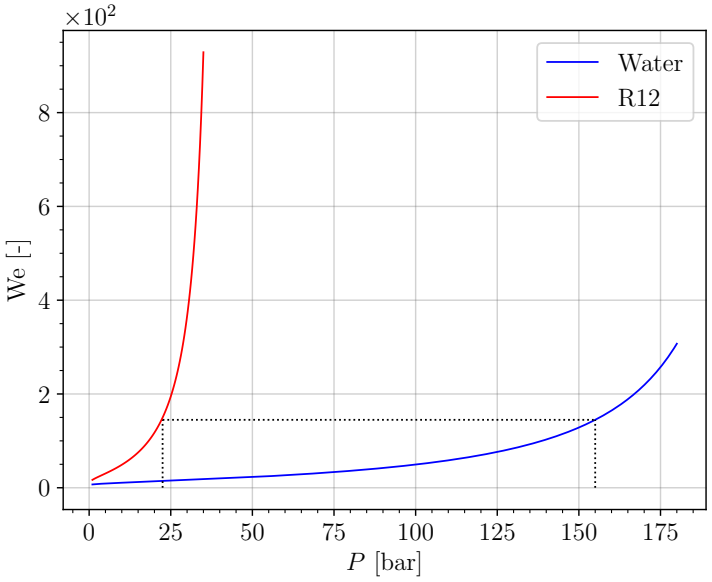

Figure 3.2: Weber number for R12 and water at $G = 2000$ kg/m^2/s and $R = 0.1$ mm

Similar to the phase density ratio, Figure 3.2 shows that Weber number equivalent to water at 155 bar can be reached with R12 around 23 bar.

> **Note :** For a same value of R, this transposition scales the inlet liquid mass flux G.

3.2.3 *Conservation of the Boiling Number*

The boiling number is defined as:

$$\mathrm{Bo} = \frac{\phi_w}{G h_{LV}} \tag{3.3}$$

It represents the comparison between the vapor mass flux ϕ_w / h_{LV} if all the heat flux contributes to phase change versus the inlet liquid mass flux. Thus, its value can be associated to the boiling and two-phase flow regime.
Figure 3.3 shows that Boiling number values similar to PWR can be reproduced using R12 with wall heat fluxes one order of magnitude lower and pressure around 23 bar.

> **Note :** This transposition criteria scales the applied heat flux ϕ_w.

3.2.4 *Conservation of the Inlet Thermodynamic Quality*

Water in PWR being highly subcooled to avoid boiling, reproducing the inlet subcooling in the DEBORA experiment allows to mimic the early stages of boiling between the ONB and OSV. It allows to reproduce Boiling Crisis by Departure from Nucleate Boiling for low quality flows. This is achieved through the inlet thermodynamic quality:

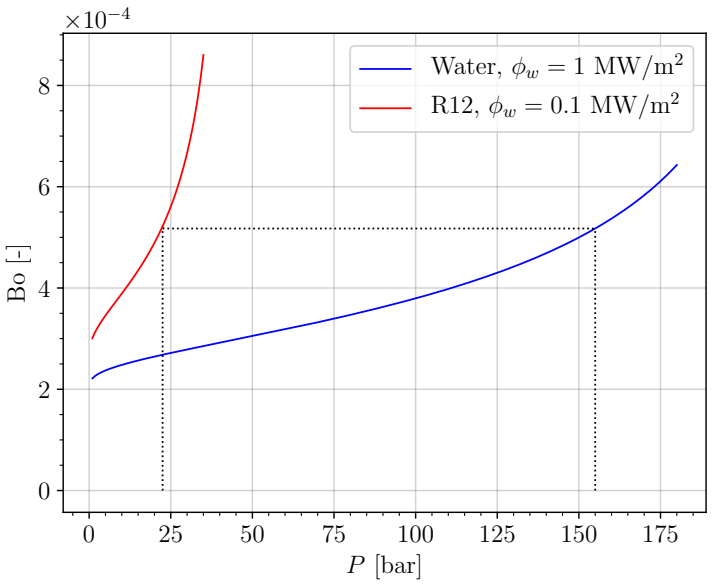

Figure 3.3: Boiling number for R12 and water at $G = 2000$ kg/m^2/s

$$x_{eq,in} = \frac{h_{L,in} - h_{L,sat}}{h_{LV}} \tag{3.4}$$

Note : This transposition is achieved by scaling the R12 inlet temperature.

3.2.5 *Same Geometry*

The last similarity achieved in the DEBORA experiment is related to the geometry. The heated length L_{heat} of the test section is similar to the height of a nuclear fuel assembly and the hydraulic diameter D_h is equal to that of a subchannel.

3.2.6 *Transposition ranges*

On Table 3.1, we sum up some thermodynamic properties of saturated R12 and water at similarity pressures respectively of 26 bar and 155 bar.

Fluid	Water	Freon R12
P [bar]	155	26
T_{sat} [°C]	344.9	86.5
ρ_L [kg/m^3]	594.4	1019.3
$c_{p,L}$ [kJ/kg]	8.950	1.413
λ_L [W/m/K]	0.472	0.0458
μ_L [W/m/K]	6.82×10^{-5}	9.23×10^{-5}
ρ_V [kg/m^3]	101.9	170.7
$c_{p,V}$ [kJ/kg]	14.0	1.281
λ_V [W/m/K]	0.126	0.0175
μ_V [W/m/K]	2.30×10^{-5}	1.57×10^{-5}
σ [J/m^2]	4.65×10^{-3}	1.80×10^{-3}
h_{LV} [kJ/kg]	966.2	86.48

Table 3.1: Water and R12 saturation properties.

As a result of the conservation criteria, Table 3.2 sums up the transposition ranges for each parameters.

Fluid	Water	Freon R12
P [bar]	100 - 180	14 - 30
G [kg/m^2/s]	1000 - 5000	1000 - 5000
ϕ_w [MW/m^2]	0.5 - 6	0.05 - 0.65
$x_{eq,in}$ [-]	(-0.4) - (+0.4)	(-0.4) - (+0.4)
$\rho_{V,sat}/\rho_{L,sat}$ [-]	0.08 - 0.25	0.07 - 0.22
We [-]	49.5 - 307.1	69.1 - 365.8
Bo $\times 10^{-3}$ [-]	0.19 - 3.86	0.21 - 4.33

Table 3.2: Water R12 scaling, $R = 0.01$mm for We

3.3 DESCRIPTION OF THE TEST SECTION

3.3.1 *Geometrical Description*

To apply the aforementioned transport criteria, four thermal-hydraulic control parameters are imposed in the test section:

- The outlet pressure P ;
- The inlet mass flow rate $G \times S_{in}$ with $S_{in} = \pi R^2 \approx 2.9 \times 10^{-4}$ m^2 the inlet area ;
- The inlet liquid temperature $T_{L,in}$;
- The electrical power transferred to the liquid $\phi_w \times S_{heat}$ with S_{heat} the heated area.

The test section is presented on Figure 3.4. It consists of an inconel tube with inner diameter $D_h = 19.2$ mm, a 1 mm thickness and a heated length L_{heat}=3.5 m. A detailed description of the whole experimental loop is given in Garnier *et al.* [53].

3.3.2 *Measurement Instrumentation*

The control parameters are adjusted and measured using pressure, temperature, flow rate and power measurements. They are further detailed in Cubizolles [33].

The local measurements are conducted at the end of the heating length using a controllable probe that can move all along the diameter of the test section with an accuracy of 10μm . Only one diameter is covered since the chosen geometry induces an axisymmetry.
Three types of measurements have been conducted over different experimental campaigns.

3.3.2.1 *Mono-Optical Probe Measurements*

Optical probe measurement rely on the difference of optical refractive index between the liquid and vapor phase. Using an optical fiber in which light is emitted towards the probe tip allows to detect the actual phase flowing on the probe.

The resulting signal is called a Phase Indicator Function (PIF) which looks like to a square signal (Figure 3.5) that can be post-processed to identify the average time spent by the probe in each phase and then estimate their volume fraction *e. g.* the void fraction (for the vapor phase).
If the PIF is measured over a period T, the void fraction α at the measurement point x can be estimated by:

$$\alpha(x) = \nu(x) \langle t_V \rangle = \frac{1}{T} \sum t_V \tag{3.5}$$

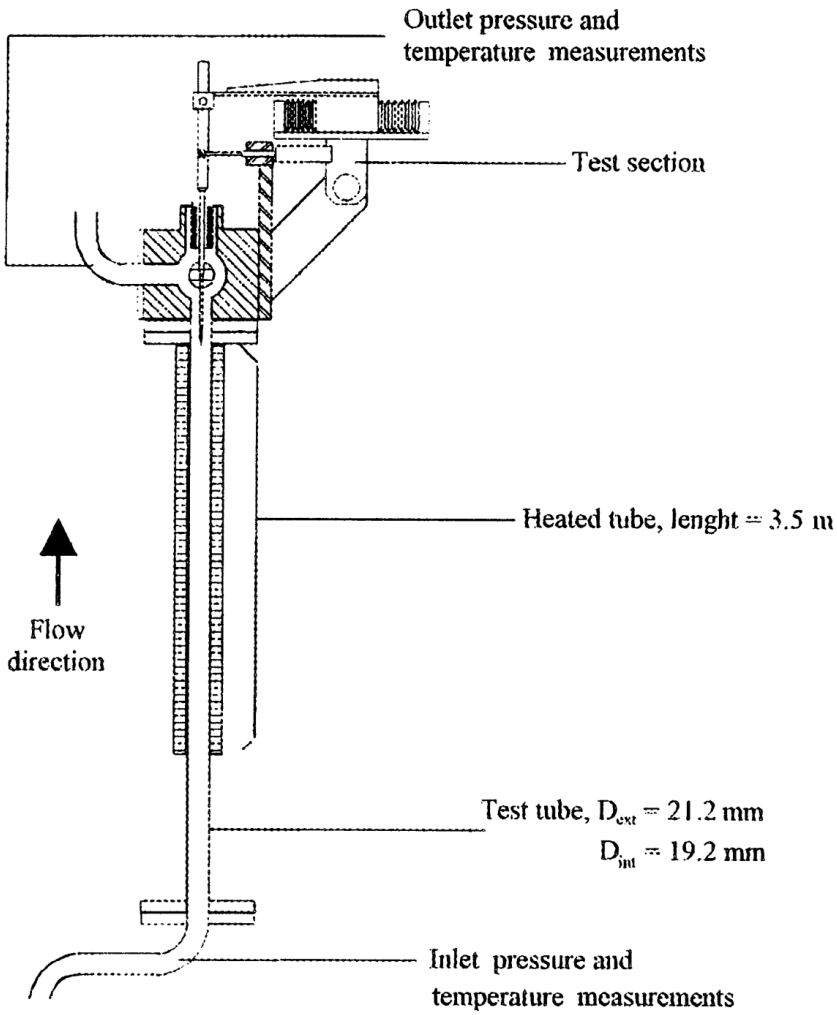

Figure 3.4: Sketch of the DEBORA test section. Adapted from [53].

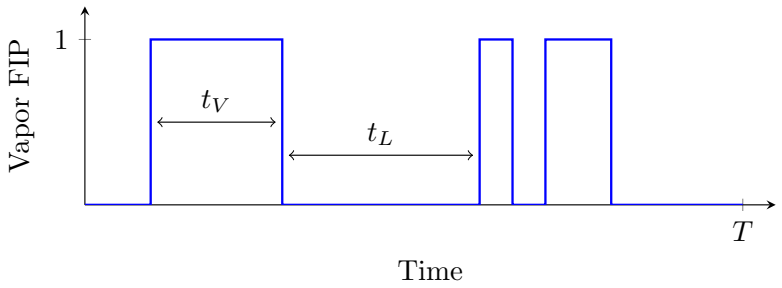

Figure 3.5: Example of Phase Indicator Function signal

where ν is called the interference frequency that represents the number of phase interface detection per second by the probe.

Note : This measurement technique was performed in the **measurement campaign C2900** where void fraction profiles at the outlet were obtained for various flow conditions.

3.3.2.2 *Bi-Optical Probe Measurements*

Using the technology of the optical phase detection, adding a second optical probe permits to measure more parameters of the two-phase flow. Indeed, the use of two probes placed close to each other with a small shift in the flow direction (Figure 3.6) allows to estimate the velocity of the interface between the two probes by measuring the time difference between the two PIF.

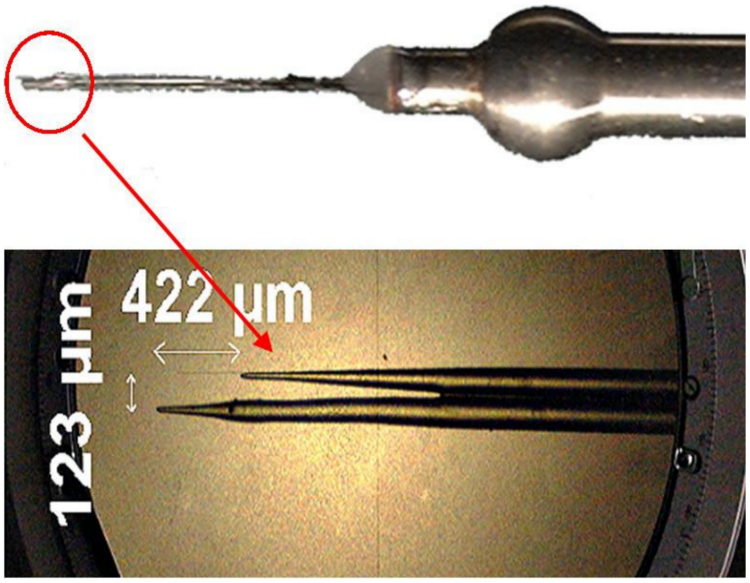

Figure 3.6: Picture of the bi-optical probe with a zoom over the two optical fibers. Reproduced from [64].

Considering the following assumptions:

- The flow is mainly one-directional and aligned with the probes ;
- The vapor phase is composed of spherical inclusions ;
- The velocity gradient and center density (number of bubble centers flowing through a unit of area) gradient are small along a bubble diameter length.

Then we can estimate:

- The vapor axial velocity $U_{V,z}$ that can be supposed equal to the measured interface velocity between the probes ;
- The interfacial area density a_i (as detailed in Cubizolles [33]):

$$a_i = \frac{4\nu}{U_{V,z}} \tag{3.6}$$

- The bubble Sauter diameter:

$$D_V = \frac{6\alpha}{a_i} \tag{3.7}$$

Note : This measurement technique was performed in the **measurement campaign C3000**.

3.3.2.3 *Thermocouples Measurements*

Thermal measurements are conducted using chromel-alumel thermocouples. The liquid temperature is measured along the outlet diameter at the end of the heating length. Wall temperature measurements are conducted with 4 thermocouples placed at different heights (1.465 m, 2.465 m, 2.965 m, 3.485 m) on the outside of the tube.

Note : This measurement technique was performed in the **measurement campaign C800**.

3.3.2.4 *Measurements Uncertainties*

On Table 3.3 we mention the uncertainties associated to each control parameter and measurement.

Quantity	Notation	Uncertainty
Mass flux	G	±1% (relative)
Outlet pressure	P	5000 Pa (absolute)
Inlet temperature	$T_{L,in}$	±0.2°C (absolute)
Heat flux	ϕ_w	±4% (relative)
Void fraction	α	±2% (absolute)
Bubble diameter	D_V	±12% (relative)
Vapor velocity	$U_{V,z}$	±10% (relative)
Wall & liquid temperature	T_w & T_L	±0.2°C (absolute)

Table 3.3: Uncertainties for DEBORA results [33, 64]

3.4 MEASUREMENTS CAMPAIGNS AND RESULTS

3.4.1 *Cases Nomenclature and Test Series*

As mentioned before, three different campaigns have been performed:

- Campaign C2900 with solely void fraction measurements using mono-optical probe ;
- Campaign C3000 with void fraction, vapor velocity, bubble Sauter diameter and interfacial area density measurements using bi-optical probe ;
- Campaign C800 with liquid and wall temperature measurements using thermocouples.

Each measurement series is conducted under fixed outlet pressure, liquid mass flux and electrical power. Inlet temperature is then changed to cover different inlet quality. Experimental cases are named in the form C**cc**G**g**P**pp**W**ww**Te**tt** with **cc** the campaign number (29, 30 or 8), **g** the inlet mass velocity (G in t/m^2/s), **pp** the outlet pressure (P in bar), **ww** the total heat power applied (Φ_w in kW) and **tt** the inlet temperature ($T_{L,in}$ in K). For instance, the case named C30G2P26W16Te66 has been conducted with $P = 26.2$ bar, $G = 2049$ kg/m^2/s, $\Phi_w = 15.6$ kW $\equiv \phi_w = 73.89$ kW/m^2 and $T_{L,in} = 66.59$°C.

P	G	W16	W17	W23	W24	W25	W27	W29	W30	W31	W33	W34	W36	W38	W39	W40	W42	W44
14	2	◯ ▽ △	△															
	4				◯													
	5							▽	▽		▽	▽	▽	▽		▽	▽	
26	2	◯ ▽ △																
	3			▽ △		▽	▽ △	▽		▽ △	▽		▽ △	▽	▽	▽ △	▽	▽ △
	5	◯			◯													

P	G	W12	W14
30	1	▽	▽

Table 3.4: Test matrix of the DEBORA cases. ◯: C800 - ▽: C2900 - △: C3000. Campaigns in the same matrix cell usually cover the same range of outlet quality $x_{eq,out}$ *i. e.* inlet temperature $T_{L,in}$.

If we want to obtain a full description of the two-phase flow from the DEBORA tests, we need to have measurements from campaigns C3000 and C800 (flow topology and thermal) with the same control parameters. Table 3.4 unfortunately shows that only very few test series between C3000 and C800 have common operating conditions, namely:

- Series 8G2P14W16 and 30G2P14W16 ;
- Series 8G2P26W16 and 30G2P26W16.

Other flow conditions have either been covered with thermal measurements or topology measurements but not both.

Remark : Cases from the campaign C2900 would only be relevant for void fraction profiles comparison. Estimations of the bubble diameter can not be achieved except if one assumes a velocity profile as suggested by Cubizolles [33] and re-used by Guéguen [64] who supposes:

$$U_{V,z}(r) \approx U_{M,z}(r) = 1.22 \frac{G}{\langle \rho_M \rangle_2} \left(\frac{R-r}{R} \right)^{1/7} \tag{3.8}$$

where $U_{M,z}$ is the mixture axial velocity, assuming a mechanical equilibrium (*i. e.* zero slip velocity) between the phases.

For further studies, we will mainly focus on the G2P26W16 and G2P14W16 test series. Although we will mainly rely on the results from the C3000 campaign (where vapor velocity was actually measured) for flow topology qualification, we will evaluate the assumption of Eq. 3.8 with the C2900 measurements.

3.4.2 *Verification of Control Parameters Coherency*

For each case, the total heat input Φ_w is given along with the inlet mass flux G, inlet liquid temperature $T_{L,in}$ and outlet quality $x_{eq,out}$. To verify the consistency of those values, we can recalculate the outlet quality:

$$x_{eq,out,calc} = \frac{h_{M,out,calc} - h_{L,sat}}{h_{LV}} \tag{3.9}$$

with $h_{M,out,calc}$ the recalculated outlet mixture enthalpy:

$$h_{M,out,calc} = h_{in} + \frac{\Phi_w}{G S_{in}} = h_{in} + \frac{4 \phi_w L_{heat}}{G D_h} \tag{3.10}$$

with h_{in} the inlet enthalpy calculated from the fluid properties using the inlet liquid temperature.

The difference between the given and recalculated outlet quality can also be converted to input power error by recalculating the heat needed to reach the given $x_{eq,out}$:

$$\Phi_{w,calc} = \frac{G \pi R^2}{\underbrace{\left[x_{eq,out} h_{LV} + h_{L,sat} \right]}_{h_{M,out}} - h_{L,in}} \tag{3.11}$$

Moreover, for a given set of experiments at the same P, G and Φ_w changing the inlet quality can be equivalent to move the measurement test section along the axial direction following the relationship:

$$x_{eq}(z) = x_{eq,in} + \frac{4 \phi_w z}{G D_h h_{LV}} \tag{3.12}$$

Thus, taking the maximum inlet quality case $x_{eq,in,max}$ as a reference ($z = 3.5$ m), we can estimate the corresponding measurement height z_{eq} of each other cases if the inlet quality was $x_{eq,in,max}$.

We calculated the equivalent heights and outlet quality / power input errors for two series of the C3000 campaigns. Results are displayed on Tables 3.5 and 3.6.
As we can see, the given values of outlet quality for the 30G2P14W16 tests are coherent with the one-dimensional enthalpy balance with errors mostly less than 0.1% on the recalculated quality and less than 100 W on the recalculated power input. This naturally leads to an equivalent height very close to 3.5 m for the hottest case.
However, a more significant error is observed on the 30G2P26W16 cases where errors up to 0.75% on the outlet quality and close to 0.4 kW on the power input are found. Those values are significant especially

$T_{L,in}$ [K]	$x_{eq,in,calc}$ [-]	$x_{eq,out,calc}$ [-]	$x_{eq,out}$ [-]	z_{eq} [m]	$x_{eq,out}$ error [-]	Φ_w error [kW]
22.39	-0.317	-0.0821	-0.0832	1.075	0.114 %	-0.078
26.8	-0.28	-0.0422	-0.0431	1.653	0.089 %	-0.061
28.76	-0.263	-0.0267	-0.0273	1.896	0.056 %	-0.038
30.08	-0.252	-0.0152	-0.0157	2.065	0.05 %	-0.034
31.39	-0.241	-0.004	-0.0043	2.234	0.035 %	-0.023
38.95	-0.175	0.0674	0.0681	3.229	-0.072 %	0.049
39.96	-0.166	0.077	0.0776	3.357	-0.063 %	0.042
41.16	-0.155	0.0875	0.0882	3.509	-0.064 %	0.043

Table 3.5: Recalculated control parameters for the 30G2P14W16 cases. (T_{sat} = 58.07°C)

$T_{L,in}$ [K]	$x_{eq,in,calc}$ [-]	$x_{eq,out,calc}$ [-]	$x_{eq,out}$ [-]	z_{eq} [m]	$x_{eq,out}$ error [-]	Φ_w error [kW]
58.57	-0.395	-0.0893	-0.0819	1.792	-0.747 %	0.381
60.54	-0.370	-0.0650	-0.0578	2.072	-0.722 %	0.369
62.54	-0.344	-0.0392	-0.0318	2.369	-0.741 %	0.378
64.6	-0.318	-0.0123	-0.0050	2.674	-0.736 %	0.376
66.59	-0.292	0.0140	0.0213	2.973	-0.728 %	0.371
68.57	-0.266	0.0402	0.0473	3.271	-0.716 %	0.365
70.59	-0.239	0.0670	0.0743	3.583	-0.723 %	0.369

Table 3.6: Recalculated control parameters for the 30G2P26W16 cases. (T_{sat} = 86.81°C)

for cases close to saturation where uncondensed vapor will start to appear in the bulk. Moreover, this results in an equivalent height 8.3 cm longer than the actually 3.5m heated length.

Since the inlet temperature, mass flux and power input are controlled parameters for each test, it is likely that the error may come from the given value of outlet quality $x_{eq,out}$ which is calculated and not imposed.

Note : Similar quality / input power errors were obtained on corresponding C29 and C8 campaigns:

- Negligible errors on for 29G2P14W16 and 8G2P14W16 cases ;
- Roughly 0.7 % outlet quality error and 0.3 to 0.4 kW power error for 29G2P26W16 and 8G2P26W16 cases.

3.4.3 *Qualitative Analysis of the Experimental Results*

On Figures 3.7, 3.8, 3.9 and 3.10 we respectively plot the experimental measurements of cases 29/30G2P26W16, 8G2P26W16, 29/30G2P14W16 and 8G2P14W16. The color-bar representing the outlet quality of each test is based on the computed value of $x_{eq,out}$ (Eq. 3.9).

3.4.3.1 *G2P26W16 cases*

Void fraction profiles obtained for C2900 (single optical probe) and C3000 (bi-optical probe) cases are compared to verify the consistency of the measurements (Figure 3.7a). The two campaigns are in good agreement with each other, displaying a void fraction profile monotonously increasing with the outlet quality. The estimation of the vapor velocity by Eq. 3.8 for the C29 results is acceptable but presents a growing underestimation as the outlet title increases (Figure 3.7b) which is a consequence of the power 1/7 law for the liquid velocity profile, no longer valid when the void fraction increases. This results in bubble diameter underestimation close to the wall and consequently interfacial area overestimation using Eq. 3.7 and 3.6.

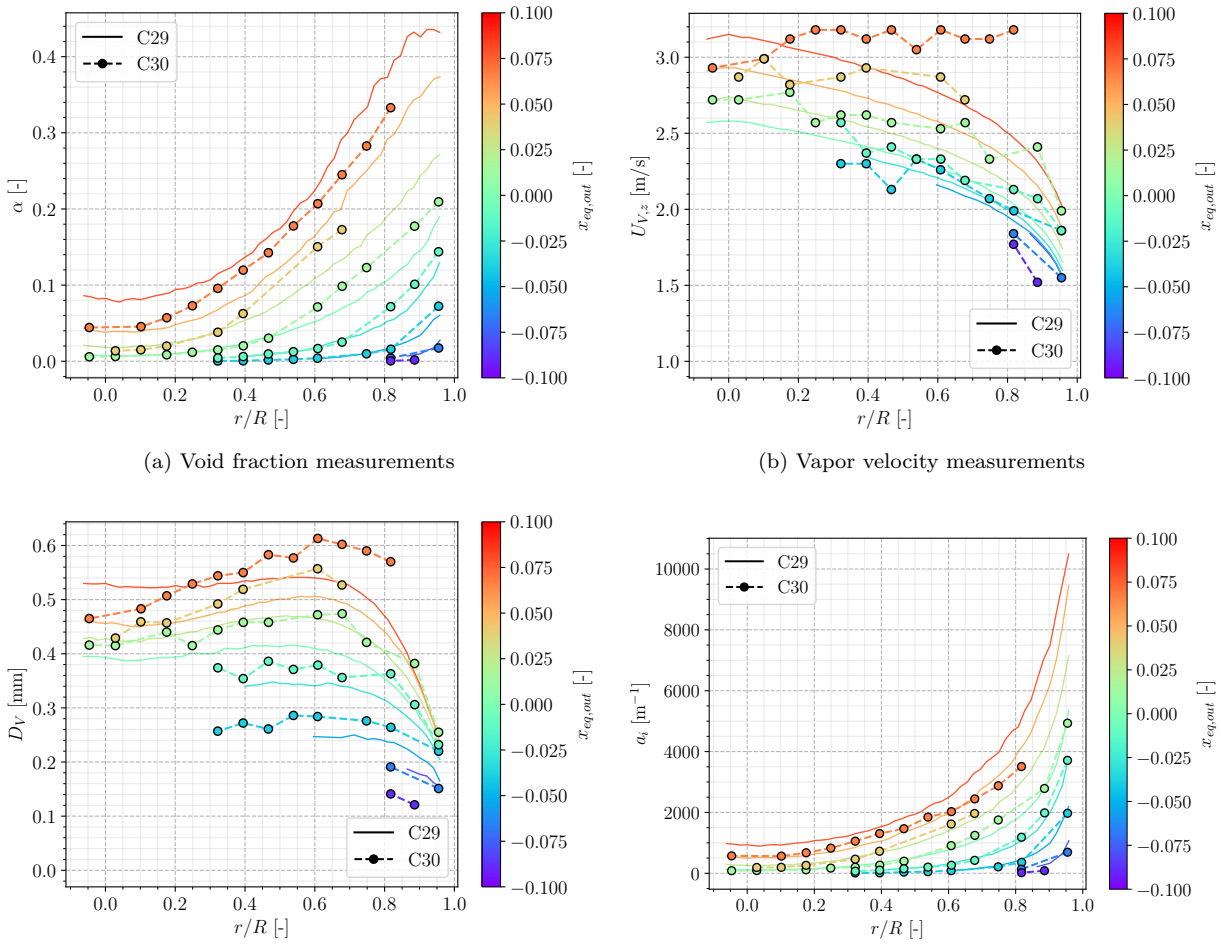

(a) Void fraction measurements

(b) Vapor velocity measurements

(c) Bubble diameter measurements

(d) Interfacial area concentration measurements

Figure 3.7: 30G2P26W16 and 29G2P26W16 results. Vapor velocity for C2900 cases is estimated using Eq. 3.8.

We observe that the void fraction naturally increases with the outlet quality and that we reach net vapor generation with $\alpha\,(R=0) > 0$ when $x_{eq,out} > 0$. Otherwise, vapor is not detected over the whole measurement section. Each case has its maximum void fraction near the wall with values up to approximately 40% when the outlet quality approaches 0.1.

The bubble diameter displays different behaviors (Figure 3.7c):

- It grows from the wall and reaches a maximum around $r/R \approx 0.6$, indicating bubble coalescence ;
- It stays nearly constant for negative outlet quality cases ;
- It decreases from $r/R = 0.6$ to $r/R = 0$ for saturated cases , indicating either bubble break-up or bulk condensation.

Remark : It seems that bubble diameter very close to the wall do not vary much between different cases, indicating that bubbles leave the wall at a nearly constant diameter over the different explored liquid temperatures ($D_V \approx 0.2$ mm).

Vapor velocity also increases with the outlet quality, with a nearly flat profile reached for saturated cases. The increase in vapor velocity may result of the larger bubble diameters which enhance the effect of buoyancy, acting as an accelerating term increasing the drift velocity. In addition, the liquid velocity profile is flattened due to bubbles locally driving and accelerating the surrounding liquid close to the wall.

Remark : Eq. 3.8 fails to predict this flattening of the vapor velocity on C2900 cases, which may indicate a change in the flow structure that can not be detected when assuming liquid-vapor mechanical equilibrium ($U_{L,z} - U_{V,z} = 0$).

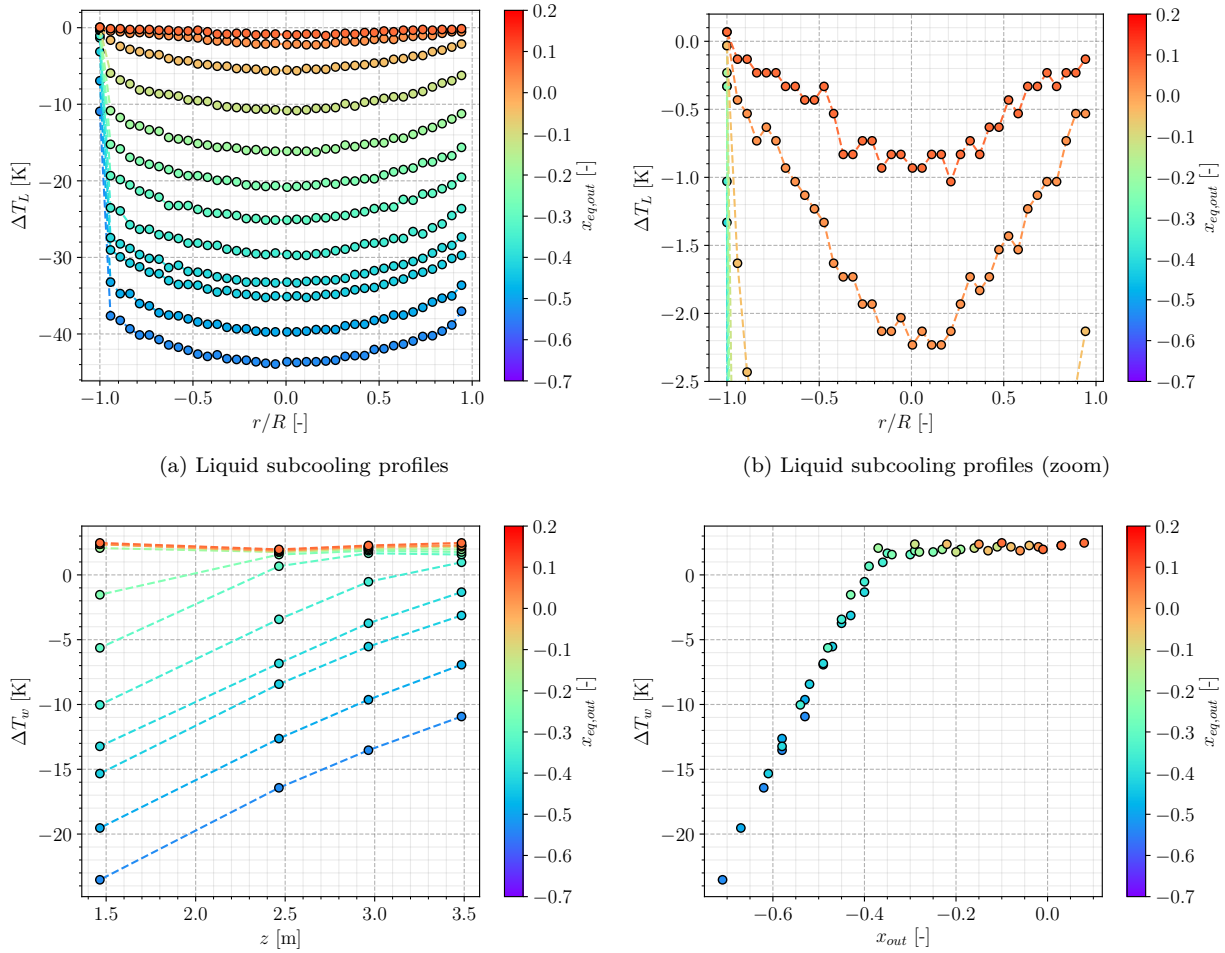

(a) Liquid subcooling profiles

(b) Liquid subcooling profiles (zoom)

(c) Wall superheat vs. axial position

(d) Wall superheat vs. local flow quality

Figure 3.8: 8G2P26W16 results

Regarding the liquid temperature measurements (Figures 3.8a and 3.8b), we see that temperature profiles linearly rise with the inlet quality while presenting an unmodified parabolic shape. The only change appears when reaching significant superheated conditions ($x_{eq,out} \sim 0.1$) where the liquid temperature profile flattens over the test section.
Moreover, we observe that measurements very close to the wall present a very large temperature gradient even for low quality cases (temperature jump of nearly 30 degrees for coldest cases). This jump reduces as flow quality increases and reduces even more for boiling cases, indicating the well-known rise of the global heat transfer coefficient in boiling regime vs. single-phase convection regime.
We can also note that for the hottest case, the liquid becomes superheated near the wall ($\Delta T_L\,(\pm 1) \approx 0.1$°C). The bulk is still slightly subcooled with $\Delta T_L\,(0) = -1$°C

Remark : The liquid being subcooled in the bulk for superheated cases hints that the decrease in bubble diameter observed in Figure 3.7c for $r/R < 0.6$ may be associated to condensation.

Wall temperature measurements (Figures 3.8c) display linear growth for subcooled cases which is in agreement with traditional liquid convection problems. When reaching boiling, the wall superheat stabilizes at $\Delta T_w \approx 2$°C. Rearranging the different wall temperature measurements versus the local flow quality

(Figure 3.8d) presents a coherent overlapping between cases with different inlet subcooling. This further validates the transposition of inlet quality into variation into an evolution of the measurement probe's axial position.

3.4.3.2 *G2P14W16 cases*

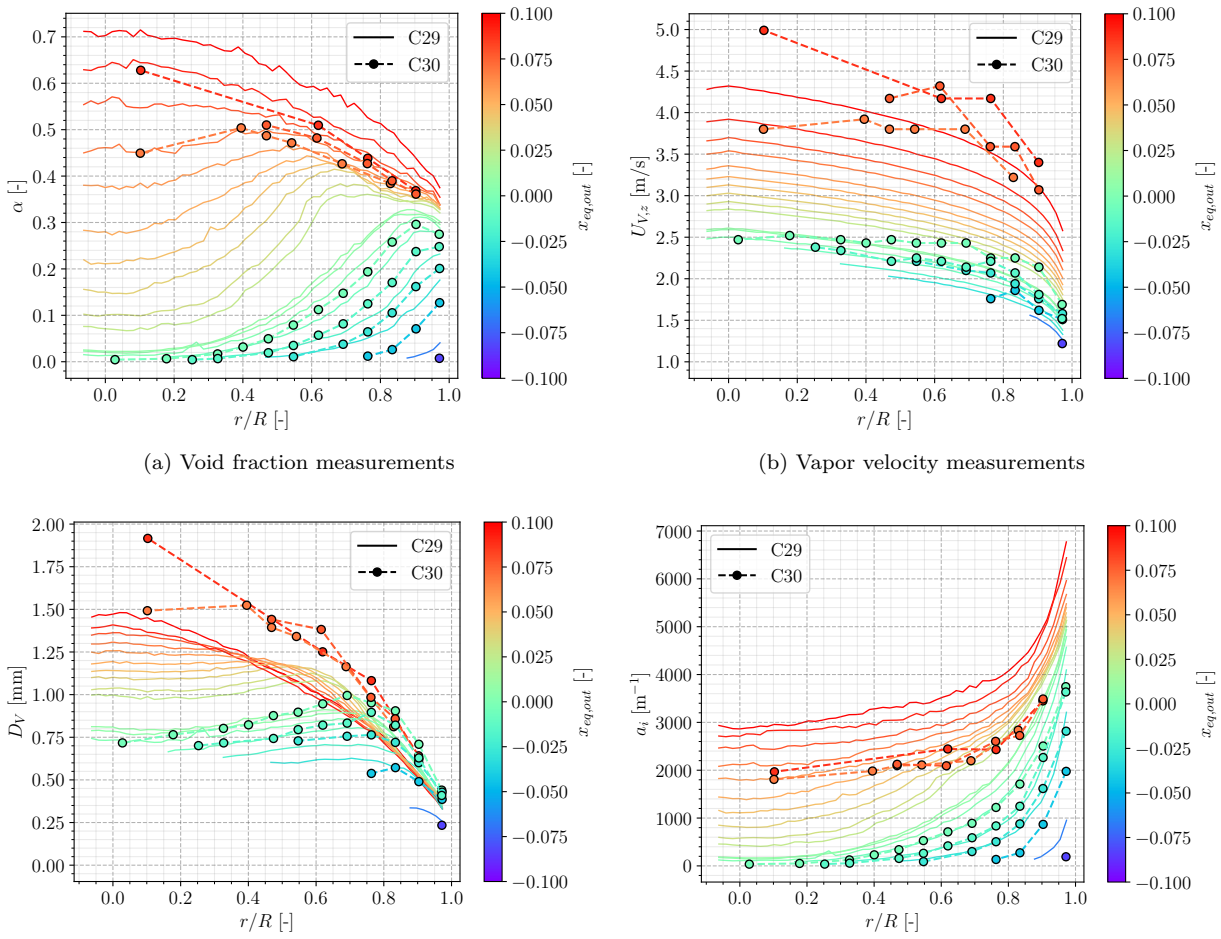

(a) Void fraction measurements

(b) Vapor velocity measurements

(c) Bubble diameter measurements

(d) Interfacial area concentration measurements

Figure 3.9: 30G2P14W16 and 29G2P14W16 results

Similar to the G2P26W16 cases, we observe the consistency of the void fraction measurements between the C2900 and C3000 campaigns (Figure 3.9a). Although the vapor velocity estimation using Eq. 3.8 for C2900 cases also produces acceptable results for subcooled cases, the discrepancy when saturation is reached is even more observed here (Figure 3.9b). The overestimation when $x_{eq,out} > 0$ is larger than for the G2P26W16 cases, with nearly 1 m/s error on hottest cases.
This logically yields larger underestimations of the bubble diameter and associated overestimation of the interfacial area concentration.

The void fraction profiles (Figure 3.9a) present a particular evolution with a moving α peak that shifts from the wall to the bulk as the outlet quality increases. This may indicate a particular bubble dynamics regime inducing transverse bubble migration and accumulation far from the wall. Bulk void fraction can reach values as high as 70% with a flattening profile when $x_{eq,out} \to 0.1$.

Remark : It seems that saturated cases tend to reach a fixed value of near-wall void fraction between 35% and 40%.

Similar to previous observations, the bubble diameter grows when moving to the bulk, also presenting a peak value around $0.8 > r/R > 0.6$ for subcooled cases (Figure 3.9c). The saturated cases however

present much larger increase in bubble diameter when reaching the bulk flow, with D_V close to 2 mm for the hottest case. This definitely indicates predominant coalescence effects.

> **Remark :** $D_V \approx 2$ mm is observed at a point where $\alpha > 60\%$ which shows that even at such high void fraction values, the flow is still in a regime with small vapor inclusions ($D_V \approx 0.1 D_h$). However such a high void fraction will lead to flow configurations that are likely to behave like a foam (so-called *froth flow*) composed of millimeters vapor structures.

The vapor velocity also increases with the outlet quality (Figure 3.9b), but reaches much larger value compared to the G2P26W16 cases. This may be due to the larger bubble size and local void fractions associated to the imposed mass flow rate.

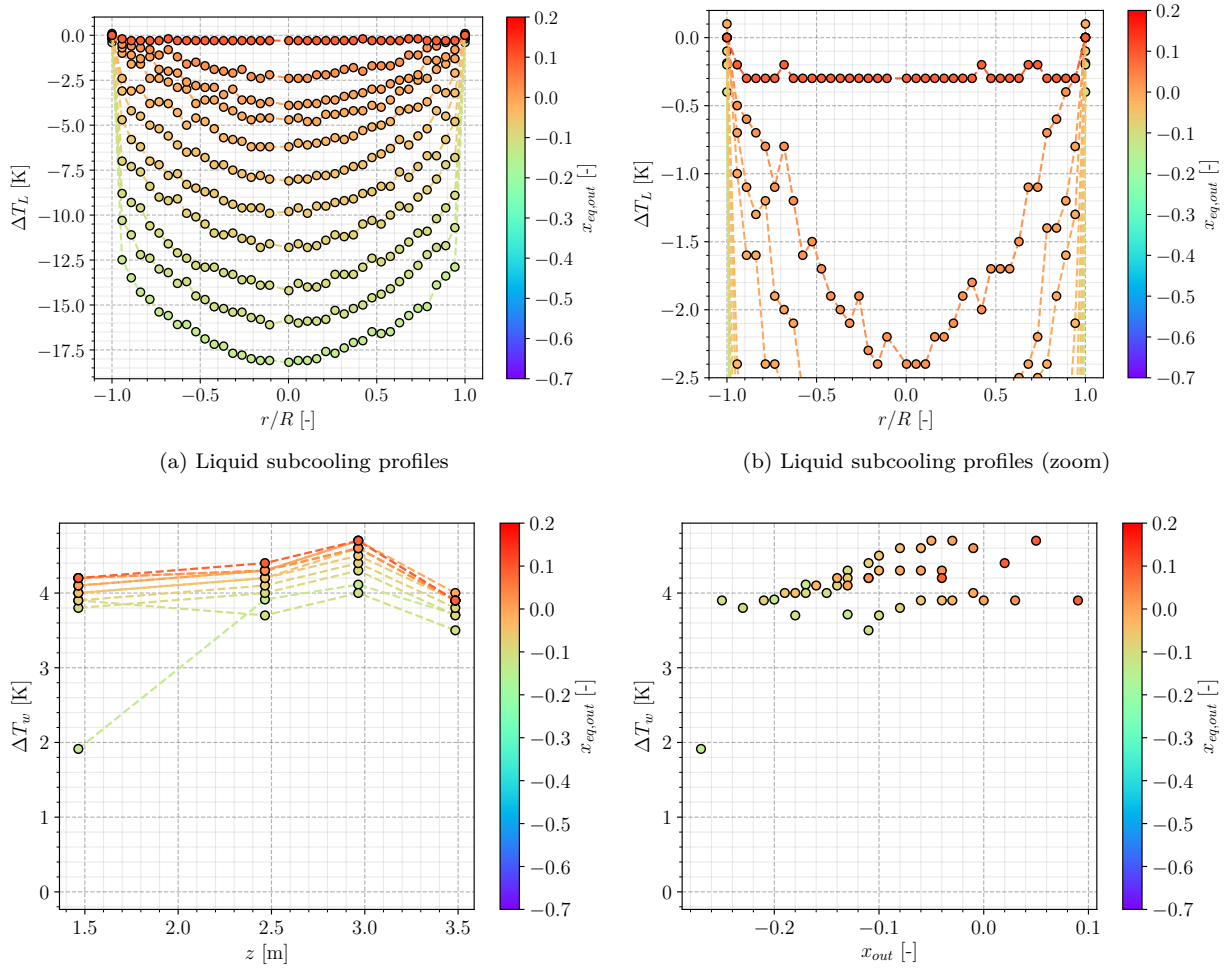

(a) Liquid subcooling profiles

(b) Liquid subcooling profiles (zoom)

(c) Wall superheat vs. axial position

(d) Wall superheat vs. local flow quality

Figure 3.10: 8G2P14W16 results

The liquid temperature profiles (Figure 3.10a) are behaving in a very similar way to the G2P26W16 cases (Figure 3.8a): stable parabolic profile, linear shift with inlet quality and flattening when reaching superheated conditions ($x_{eq,out} \sim 0.1$).
We also have the huge temperature jump when approaching the wall which reduces when reaching boiling regimes. The measurements also detect superheated liquid near the wall for the hottest cases ($\Delta T_L \approx 0.1°$). The case with the greatest outlet quality presents a surprisingly flat liquid temperature profile with measurements being nearly constant ($\Delta T_L = -0.3°$C) over the whole measurement section.

Remark : Such a constant temperature profile could be interpreted as a limit of the liquid temperature in this regime. Since it corresponds to flow conditions where void fraction is large ($\alpha > 60\%$) and bubbles do not condense (Figure 3.9c), any extra heat input may only contribute to phase change and leave the liquid phase thermally unchanged. This thermodynamically implies that the liquid is nearly exactly at T_{sat}, which means the value of $\Delta T_L = -0.3°C$ is probably associated to the measurement uncertainty (Table 3.3).

Unfortunately, the 8G2P15W16 campaign did not cover as large quality range as the 8G2P26W16 campaign. We thus do not have access to many single-phase flow wall temperature measurements (Figure 3.10c). Only one point for $x_{eq,out} \approx -0.1$ seems to be in the single-phase convection region. All the other measurements are close to each other and correspond to boiling regimes where we observe a wall superheat stabilization around $\Delta T_w = 4°C$.

Note : The wall superheat is approximately 2°C higher than 26 bar cases, which is coherent with the effect of pressure on boiling temperature [73, 90].

The comparison of wall temperature with local flow quality (Figure 3.10d) is not as interesting as the G2P26W16 cases but still display a welcomed overlapping of the measurements over the different inlet temperatures.

3.5 FURTHER VERIFICATION

3.5.1 *Reconstruction of the Applied Heat Flux*

To further quantify the coherency of the DEBORA database, we want to reconstruct the wall heat flux injected in the flow from the experimental measurements of void fraction, vapor velocity and liquid temperature measurements.

3.5.1.1 *Methodology*

To do so, we will estimate the total enthalpy change between the inlet and outlet. The inlet liquid enthalpy $h_{L,in}$ is estimated using the inlet temperature and the outlet mixture enthalpy $h_{M,out}$ is computed as:

$$h_{M,out} = x_{M,out} H_{V,sat} + (1 - x_{M,out}) H_{L,out} \tag{3.13}$$

supposing that the vapor is at saturation temperature, where $x_{M,out}$ is the outlet mass quality and $H_{k,out}$ is the flowing enthalpy of phase k averaged over the outlet surface, defined as:

$$H_k(z) = \frac{\langle \rho_k \alpha_k U_{k,z} h_k \rangle_2}{\langle \rho_k \alpha_k U_{k,z} \rangle_2} \tag{3.14}$$

where $\langle . \rangle_2$ is the surface-averaging operator.

Using the experimental values of α and $U_{V,z}$ (C3000 campaign), we can compute the outlet mass quality $x_{M,out}$ as:

$$x_{M,out} = \frac{\rho_V \langle \alpha U_{V,z} \rangle_2}{G} \tag{3.15}$$

where:

$$\langle \alpha U_{V,z} \rangle_2 = \frac{1}{\pi R^2} \int_{\vartheta=0}^{2\pi} \int_{r=0}^{R} \alpha(r) U_{V,z}(r) \, r \mathrm{d}r \mathrm{d}\vartheta = \frac{2}{R^2} \int_{r=0}^{R} \alpha(r) U_{V,z}(r) \, r \mathrm{d}r \tag{3.16}$$

for an axisymmetric profile such as the DEBORA measurements.

Estimating h_L using the local temperature measurements (C800 campaign) and $U_{L,z}$ with the the drift velocity of Ishii [75]:

$$U_{L,z} = U_{V,z} - U_{rel} = U_{V,z} - \sqrt{2}\left(\frac{g\sigma\left(\rho_L - \rho_V\right)}{\rho_L^2}\right)^{1/4}\left(1 - \langle\alpha\rangle_2\right)^{1.75} \tag{3.17}$$

Finally assuming that vapor is at saturation ($H_{V,out} \approx h_{V,sat}$), we can finally compute the outlet mixture enthalpy:

$$h_{M,out} = x_{M,out}h_{V,sat} + \left(1 - x_{M,out}\right)\frac{\left\langle\rho_L\left(1-\alpha\right)U_{L,z}h_L\right\rangle_2}{\left\langle\rho_L\left(1-\alpha\right)U_{L,z}\right\rangle_2} \tag{3.18}$$

Then, writing the one-dimensional energy balance of the flow permits to express the actually applied heat flux:

$$G\pi R^2\left(h_{M,out} - h_{L,in}\right) = \Phi_w = \phi_w 2\pi R L_{heat} \;\Rightarrow \phi_w = \frac{\left(h_{M,out} - h_{L,in}\right)GR}{2L_{heat}} \tag{3.19}$$

which can be compared to the given control parameter for the experiment.

3.5.1.2 *Application*

To apply the presented reconstruction of the heat flux, we either need:

- A pure single-phase case with an outlet liquid temperature profile (C800 case alone);
- A boiling two-phase case with void fraction and vapor velocity measurements (C3000 case) along with liquid temperature (C800 case).

This means that for boiling cases, we need to "merge" cases from the C3000 and C800 campaign conducted in very close operating conditions (P, G, $T_{L,in}$) and assume that the liquid temperature measurements of the C800 case are actually representative of the liquid temperature in the C3000 case and reciprocally for the void fraction and vapor velocity.

Such a constraint leaves us with very few boiling cases that can accommodate those conditions. They are summed up on Table 3.7.

Case Name	P [bar]	G [kg/m^2/s]	ϕ_w [kW/m^2]	$T_{L,in}$ [°C]	$x_{eq,in}$ [-]	$x_{eq,out}$ [-]
30G2P26W16Te66	26.2	2049.0	73.893	66.59	-0.2919	0.014
8G2P26W16Te66.6	26.2	1982.0	73.9	66.57	-0.2927	0.0237
30G2P26W16Te70	26.19	2051.2	73.893	70.59	-0.2386	0.067
8G2P26W16Te70.3	26.2	1983.0	73.9	70.31	-0.2428	0.0734

Table 3.7: Similar conditions cases between the C3000 and C800 campaigns. Outlet quality calculated with Eq. 3.9.

To actually compute the surface-averaged quantities, we need to interpolate the experimental profiles which is done using the `python` package `scipy`. Figure 3.11 presents typical interpolation profiles used in this sections.

Remark : It was verified beforehand that the hypothesis for the drift velocity (3.17) allowed to recompute the inlet mass flux from the outlet vapor velocity. Test for the case 30G2P26W16Te70 yielded $G_{recalc} = 2106$ kg/m^2/s. Excluding the drift term and assuming $U_{V,z} = U_{L,z}$ gives $G_{recalc} = 2145$ kg/m^2/s.

The results obtained for the heat flux recalculations are presented on Table 3.8.

We see that reconstructing the heat flux yields values significantly lower than the experimental values given in the database. The initial uncertainty of the wall heat flux being of 4% (Table 3.3), which is smaller than the computed values but close for the Te66 case.

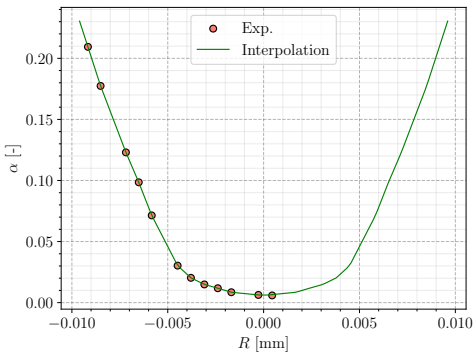

(a) Void fraction interpolation

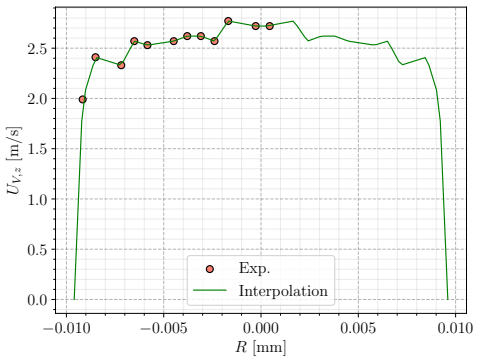

(b) Vapor velocity interpolation

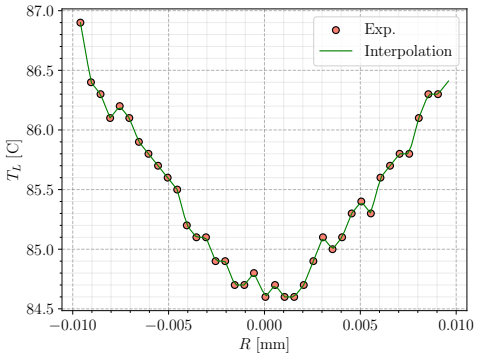

(c) Liquid temperature interpolation

Figure 3.11: Interpolation profiles for cases Te66 (Table 3.7).

Case name	x_m [-]	$\phi_{w,rec}$ [kW/m^2]	$\phi_{w,exp}$ [kW/m^2]	$\Delta\phi_w$ [%]
30G2P26W23Te66	0.0193	70.432	73.893	-4.68%
30G2P26W23Te70	0.0500	68.041	73.893	-7.9%

Table 3.8: Heat flux recalculation results

Note : This underestimation was also noted for single-phase C800 cases in a similar approach conducted by Guéguen [64] who found discrepancy up to 6%.

In our case, these discrepancies can be partially explained by:

- The difference of inlet mass fluxes that are roughly 70 kg/m^2/s lower for the C800 cases ;
- The difference of inlet liquid temperature for the Te70 cases with a C800 case 0.3°C lower than the C300 case.

Those small discrepancies lead to outlet qualities (computed with Eq. 3.9 using the given ϕ_w) that differ of approximately 1%. Even though boiling flows near saturation, such as those studied here, are very sensitive to the local quality and flow parameters, this would hardly suffice to explain differences in heat flux as much as 5%.

Remark : Unfortunately, our methodology do not rely on collocated measurements of all the variables of interest since the campaigns were conducted separately. The "correction" values presented in Table 3.8 can not be considered as accurate estimations but still point out that an uncertainty over the heat flux can be considered in further work.

3.5.2 *Verification of Wall Temperature Measurements*

In order to test the coherency of wall temperature measurements both in single phase and boiling regions, we compare them to one-dimensional correlations along the $(\Delta T_w,\, x_{eq})$ curve.

Single-phase measurements are confronted to the estimations of Dittus-Boelter (Eq. 3.20, DB) correlation and Gnielinski correlation (Eq. 3.21, G), both computing the Nusselt number for forced convection:

$$\mathrm{Nu}_{DB} = 0.023 \left(\mathrm{Re}^{4/5}\right) \mathrm{Pr}^{0.4} \tag{3.20}$$

$$\mathrm{Nu}_{G} = \frac{\frac{C_f}{2}\left(\mathrm{Re} - 1000\right)\mathrm{Pr}}{1 + 12.7\sqrt{\frac{C_f}{2}}\left(\mathrm{Pr}^{2/3} - 1\right)} \tag{3.21}$$

where the friction coefficient C_f is estimated following Churchill [27] as recommended by Delhaye [36] and Guéguen [64]:

$$C_f = 2\left[\left(\frac{8}{\mathrm{Re}}\right)^{12} + \frac{1}{(A+B)^{1.5}}\right]^{1/12} \tag{3.22}$$

$$A = \left[2.457 \ln\left(\frac{1}{\left(\frac{7}{\mathrm{Re}}\right)^{0.9} + 0.27\frac{\varepsilon}{D_h}}\right)\right]^{16} \quad (\varepsilon{=}0 \text{ supposed here})$$

$$B = \left(\frac{37530}{\mathrm{Re}}\right)^{16}$$

Wall superheat in boiling region is compared with the simple correlation of Frost & Dzakowic [51]:

$$\Delta T_{w,FD} = \mathrm{Pr}_{L,sat}\sqrt{\frac{8\sigma\phi_w T_{sat}}{\lambda_{L,sat} h_{LV} \rho_V}} \tag{3.23}$$

where T_{sat} is expressed in Kelvin.

The results are presented on Figure 3.13 for cases at 26 bar and Figure 3.12 for cases at 14 bar. Since we do not need combination with void fraction measurements, every cases of the C800 campaign were used for comparison.

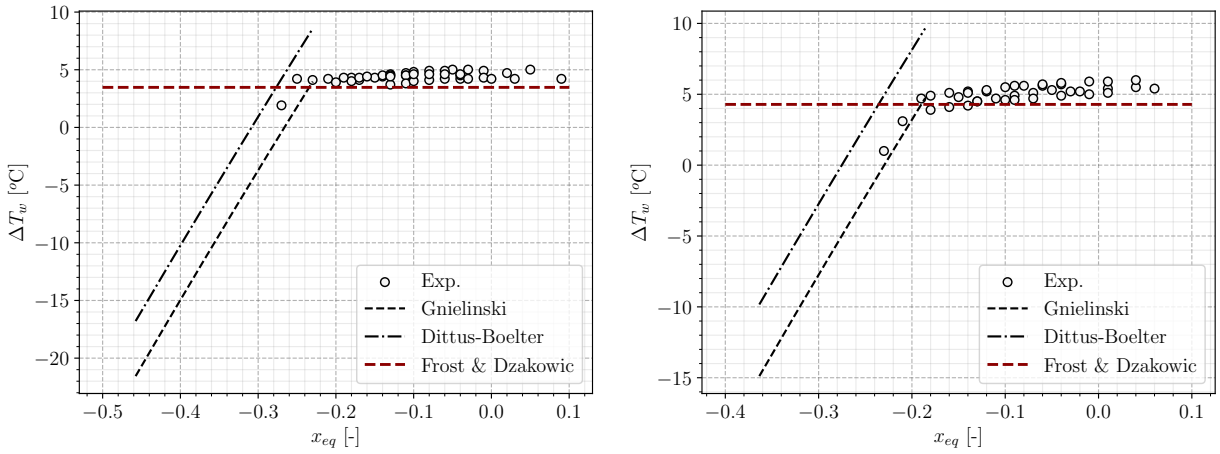

(a) 8G2P14W16 series, $\Delta T_{w,FD} = 3.47$°C

(b) 8G4P14W24 series, $\Delta T_{w,FD} = 4.29$°C

Figure 3.12: Correlations comparison with P14 cases.

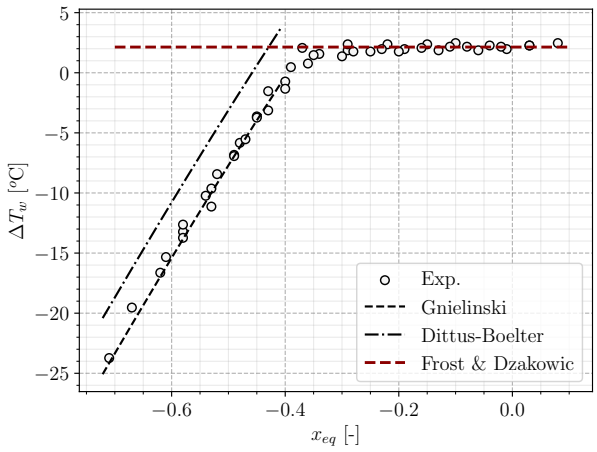

(a) 8G2P26W16 series, $\Delta T_{w,FD} = 2.14$°C

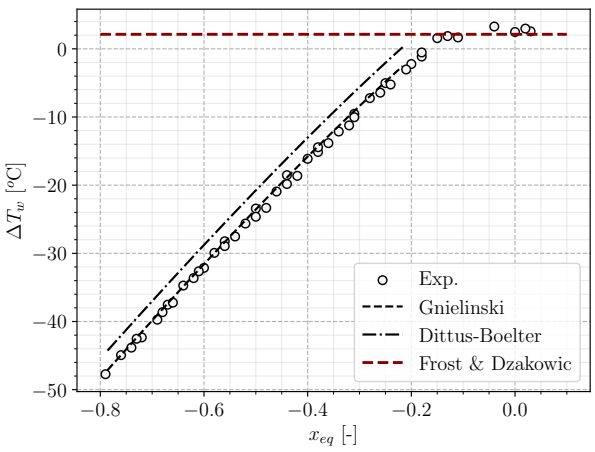

(b) 8G5P26W16 series, $\Delta T_{w,FD} = 2.13$°C

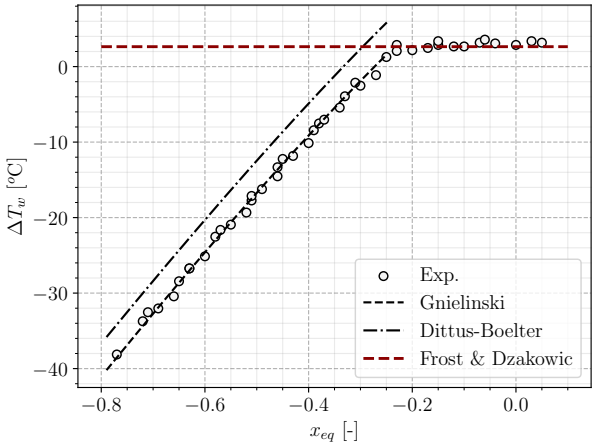

(c) 8G2P26W24 series, $\Delta T_{w,FD} = 2.64$°C

Figure 3.13: Correlations comparison with P26 cases.

Wall temperature measurements for the liquid convective regime are in fairly good agreement with the predictions of the Gnielinski correlation. The slope of the model is very close to the experimental data in the single-phase region. It is particularly true for the P26 cases (Figure 3.13) where a large range of subcooled conditions in the single-phase region was covered.

Regarding the P14 cases (Figure 3.12), very few measurements are available outside of the boiling region. However we can see that the Gnielinski correlation seem to consistently meet the boiling measurements and follow a trend that agrees with the experimental data.

On the other hand, the Dittus-Boelter correlation fails to predict the wall temperature with a constant overestimation of approximately 5°C regardless of the case.

Note : The average liquid temperature at different heights was estimated using a one-dimensional energy balance before computing the local heat transfer coefficient predicted by correlations and finally obtaining the wall temperature. The virtual length used for single-phase correlations was adjusted to cover the whole range of x_{eq}.

The nucleate boiling temperature predicted by Frost & Dzakowic correlation are in good agreement with the experimental observations where we saw the wall temperature stabilization. The prediction is better for the P26 cases than for the P14 cases where an underestimation of 1°C is observed. We can also note that the measurements are more dispersed for the P14 cases and span over a range of more than 1°C around the average temperature.

Those comparisons are comforting the consistency of the wall temperature database which correspond to traditional behavior of wall to fluid heat transfer in both single-phase and boiling two-phase regimes.

3.6 CONCLUSIONS

The DEBORA database is a very rich source of experimental insights for boiling flows representative of PWR industrial conditions. The large range of control parameters that was covered during the tests also is encouraging regarding the variety of flow regimes that can occur in PWR conditions

After a finer analysis of the data, in the continuation of the work of Cubizolles [33], Manon [109] and Guéguen [64], we concluded that:

- The test matrix unfortunately shows that very few series were covered with both bi-optical probe (C3000) and thermocouples (C800) measurements, limiting the availability of a full boiling database to the series G2P26W16 and G2P14W16.
- Small but significant errors on the reported outlet quality could be observed when compared to a one-dimensional energy balance based on the control parameters (Table 3.6).
- Good agreement was found between the void fraction measurements with the single (C2900) and dual-optical probe (C3000), which comforts the validity of the acquired data in close flow conditions.
- Extension of the C2900 data to estimate bubble diameter and interfacial area concentration using Eq. 3.8 to compute vapor velocity was acceptable in subcooled conditions but showed increasing underestimations in the saturated region (Figures 3.7b and 3.9b).
- Void fraction measurements in the G2P14W16 series showed a particular behavior with a peak value moving from the wall to the bulk as the inlet temperature increases.
- Bubble diameter measurements clearly exhibited coalescence phenomena when leaving the wall with a maximum value reached at $r/R \approx 0.6$ before decreasing under condensation and / or break-up (Figure 3.7c). It was also observed that measurements closest to the wall were nearly constant among a given test series regardless of the inlet temperature.
- Liquid temperature can overcome the saturation temperature for the hottest cases close to the wall ($T_L - T_{sat} \approx 0.1$°C) and flattens at the bulk with a subcooling roughly around 0.5°C.
- Wall temperature measurements followed a coherent linear profile in the single-phase region before stabilizing when boiling starts, which was further reproduced by comparison with one-dimensional correlations. Measurements were also overlapping each other when plotted versus the local quality, confirming the transposition between change of inlet temperature and axial translation of the measurement section.
- Reconstruction of the applied wall heat flux in the experiments by merging the values of C3000 and C800 cases for similar conditions (Table 3.7) suggested that the heat flux values provided in the measurements were too large by 5% to 8%. Such a large difference is surprising and could partially be explained by the small change of operating conditions between C3000 and C800 cases.

At last, the different evaluations conducted over the chosen experiments have reasonably validated the consistency and coherency of the measurements. Further comparisons with NEPTUNE_CFD simulations will be conducted using the experimental results of the G2P26W16 series. **Still, we keep in mind that an uncertainty of a few % is possible on ϕ_w.**

4

NEPTUNE_CFD SIMULATIONS OF DEBORA CASES

Contents

4.1 Introduction **41**
4.2 Simulation Setup **41**
4.3 Mesh Sensitivity Study **42**
4.4 C800 Cases Simulations : Thermal Measurements **43**
4.4.1 High Subcooling Cases 43
4.4.2 Low Subcooling Cases 44
4.4.3 Saturated Cases 45
4.5 C3000 Cases Simulations : Topology Measurements **46**
4.5.1 Subcooled Boiling Cases 46
4.5.2 Saturated Boiling Cases 47
4.6 Simulations Sensitivity Tests **48**
4.6.1 Sensitivity to Wall Heat Flux Correction 48
4.6.2 Influence of a Wall Boiling Parameter : the Nucleation Site Density 50
4.7 Conclusion **51**

4.1 INTRODUCTION

Due to the large amount of measurements along with its scaling conditions with PWR flows, the DEBORA cases have been often used for validation of multiphase simulation tools, from simple 1D / 2D codes [64, 86, 109] to CFD softwares [10, 65, 95, 119, 142], helping to conduct separate validation and comparison of several modeling aspects involved in such codes (interfacial heat and momentum transfer, turbulence, interfacial area transport, etc.).

In this Chapter, we present NEPTUNE_CFD simulations of the DEBORA experiment. The objective is to assess the current modeling of the code for dispersed two-phase boiling flows. To do so, we will simulate cases from the different campaigns of the DEBORA database (C800 and C3000) to conduct comparisons of void faction, bubble diameter, vapor velocity, liquid temperature and wall temperature profiles.

As identified in Chapter 3, our focus will be on cases from the G2P26W16 series, since they provide the most extensive set of measurements in very close operating conditions.

4.2 SIMULATION SETUP

Since the geometry of the DEBORA experiment presents an axisymmetry, we simplify the simulation setup in order to realize a 2D axisymmetric computation. The computational domain consists of a 1° angular section of radius $R = 9.6$ mm and 3.85 m length (Figure 4.1).
The boundary conditions are:

- Uniform heat flux for 0.2 m $\leq z \leq$ 3.5 m ;
- Adiabatic wall for $z <$ 0.2 m and $z >$ 3.7 m ;
- Uniform outlet pressure ;
- Uniform liquid inlet velocity and temperature ;

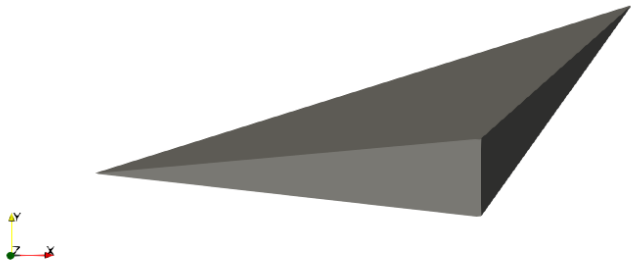

Figure 4.1: View of the computational domain.

- Symmetry condition on remaining faces.

The inlet section before heating is approximately $10D_h$ long and the extracted radial profile for comparisons is located at the end of the heating length. The angular section consists of 1 mesh while radial and axial direction are uniformly discretized. Four meshes are considered, presented on Table 4.1 and Figure 4.2.

Mesh name	M1	M2	M4	M8
Number of cells (radial × axial)	10 × 100	20 × 200	40 × 400	80 × 800

Table 4.1: Mesh parameters

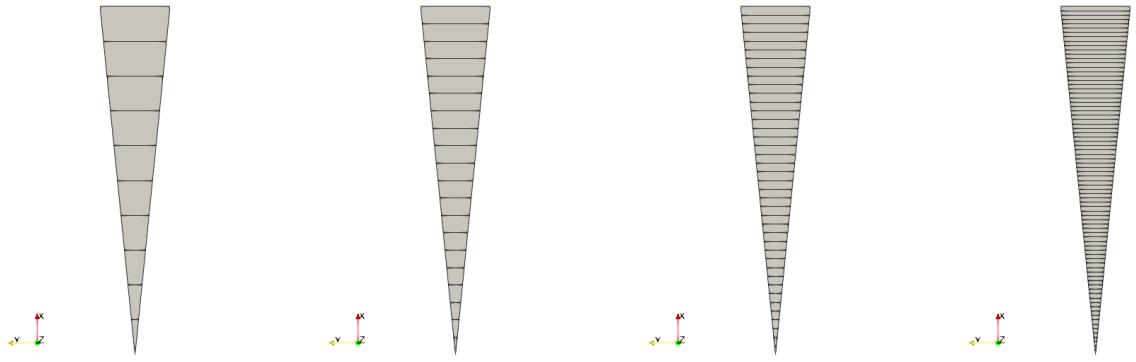

(a) Mesh M1 (b) Mesh M2 (c) Mesh M4 (d) Mesh M8

Figure 4.2: View of the radial meshes.

The computation runs using the transient solver of NCFD for a long enough physical time ensuring temporal stabilization and convergence of the results.

Note : First simulated case was simulated up to a physical time of 40 s, ensuring the time-convergence. Further simulations used this first case as a restart point, allowing to reach time-convergence in less than 10 s when changing boundary conditions.

4.3 MESH SENSITIVITY STUDY

On Figure 4.3, we present simulation results for the 4 meshes (Table 4.1) of the case 30G2P26W16Te66.6.

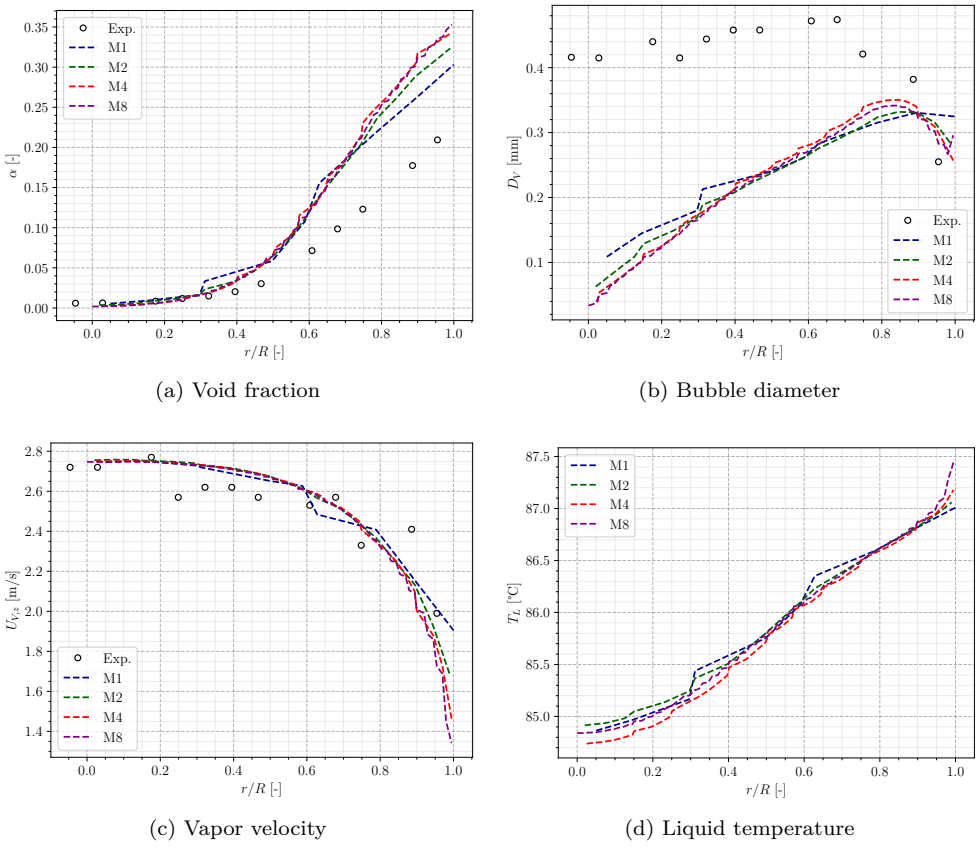

(a) Void fraction

(b) Bubble diameter

(c) Vapor velocity

(d) Liquid temperature

Figure 4.3: Mesh sensitivity study for 30G2P26Te66.6 case

Note : What looks like discontinuities in the results presented in Figure 4.3 is due to the fact that we do not interpolate the CFD results. Therefore, sharp edges correspond to mesh cell centers where values of interest are calculated.

We see that the different meshes provide similar results for the void fraction, bubble diameter, vapor velocity and liquid temperature. This is particularly true for the M4 and M8 meshes, allowing to assume that an acceptable grid convergence is reached with the M4 mesh. **Therefore, further simulations will be conducted using the M4 mesh.**

Remark : One of the most remarkable impact of the mesh concerns the liquid temperature in the wall-adjacent cell. As the mesh refines, the strong temperature gradient at the wall is logically better captured, inducing a net rise in the liquid temperature when $r/R \to 1$.

4.4 C800 CASES SIMULATIONS : THERMAL MEASUREMENTS

In this Section, we focus our attention on cases from the 8G2P26W16 series to assess liquid and wall temperature predictions. We sub-divide the case in three parts depending on the degree of subcooling at the outlet in order to cover both single-phase and fully boiling cases.

4.4.1 *High Subcooling Cases*

We start by simulating cases 8G2P26W16Te31.5 and Te44.9 which both have an outlet quality $x_{eq,out} < -0.25$, meaning that the fluid remains in its liquid phase along nearly the entire heating length. Results obtained for those cases are presented on Figure 4.4.

The liquid temperature profiles are fairly reproduced with the experimental parabolic shape correctly captured along with quite precise prediction of the temperature values in the bulk (Figure 4.4a). Still,

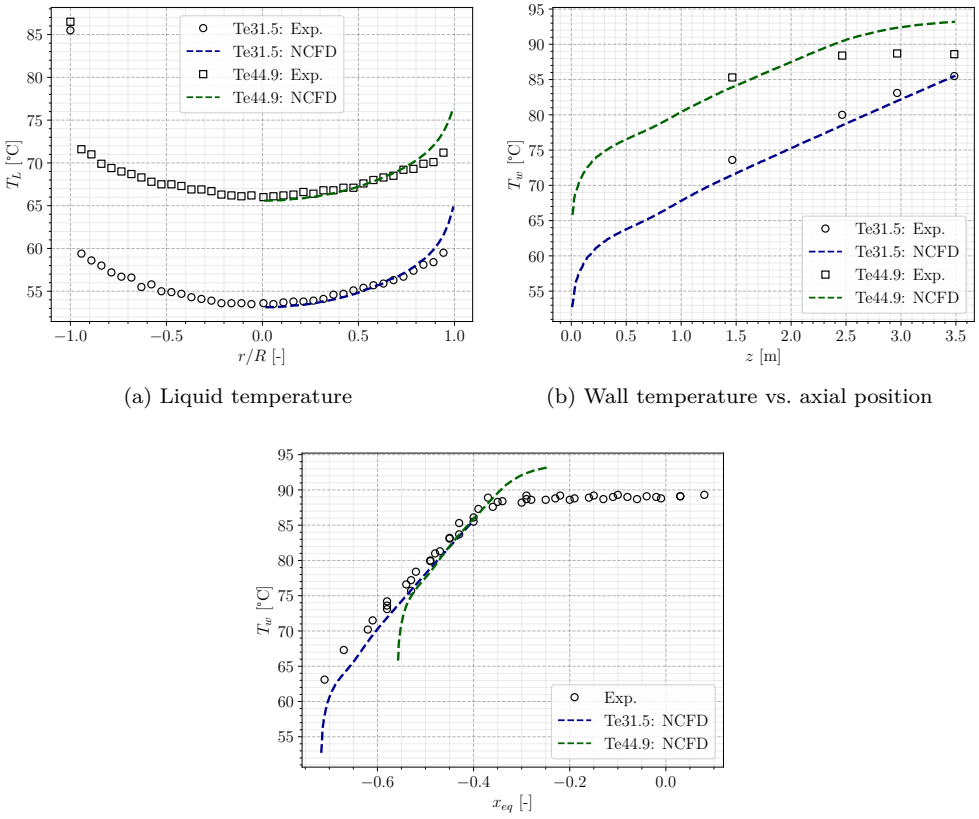

(a) Liquid temperature

(b) Wall temperature vs. axial position

(c) Wall temperature vs. local quality

Figure 4.4: Simulation results for cases 8G2P26W16Te31. 5& Te44.9

we note that an overestimation of the liquid temperature near the wall and a small underestimation (less than 1°C) when approaching the center of the pipe.

Wall temperature predictions in the single-phase region present a good agreement with the experimental measurements along the axial positions (Figure 4.4b). This is further verified by transposition along the local quality x_{eq} (Figure 4.4c) by gathering all the measurements from the 8G2P26W16 campaign, showing an average error of approximately 1°C up to $x_{eq} \approx -0.5$.

Those comparisons highlight the validation of the code for the single-phase flow part, implying that **the local liquid heat transfer coefficient (Eq. 2.35) is correctly computed along with a good heat transport along the radial direction**.

4.4.2 *Low Subcooling Cases*

Next cases to be simulated are 8G2P26W16Te55.7 and Te61.5. Their outlet quality is closer to saturation with $x_{eq,out} \geq -0.1$ and thus present a subcooled boiling region during a significant portion of the heating length. However, the bulk flow is expected to stay fully liquid in those conditions (Figure 3.7a). The results are presented in Figure 4.5.

Liquid temperature profiles (Figure 4.5a) are similar to those of the high subcooling cases (Figure 4.4a). The parabolic shape of the measurements is reasonably reproduced, with liquid temperature values close to the experiment. The same discrepancies are observed, namely a overestimation close to the wall and a small underestimation at the center (also lower than 1°C).

However, the wall temperatures start to show significant discrepancies with the measurements (Figure 4.5b). The deviation from the linear profile observed in the pure-single phase region towards a stabilization corresponding to the boiling regime fails to be reproduced (Figure 4.5c). First, the temperature plateau

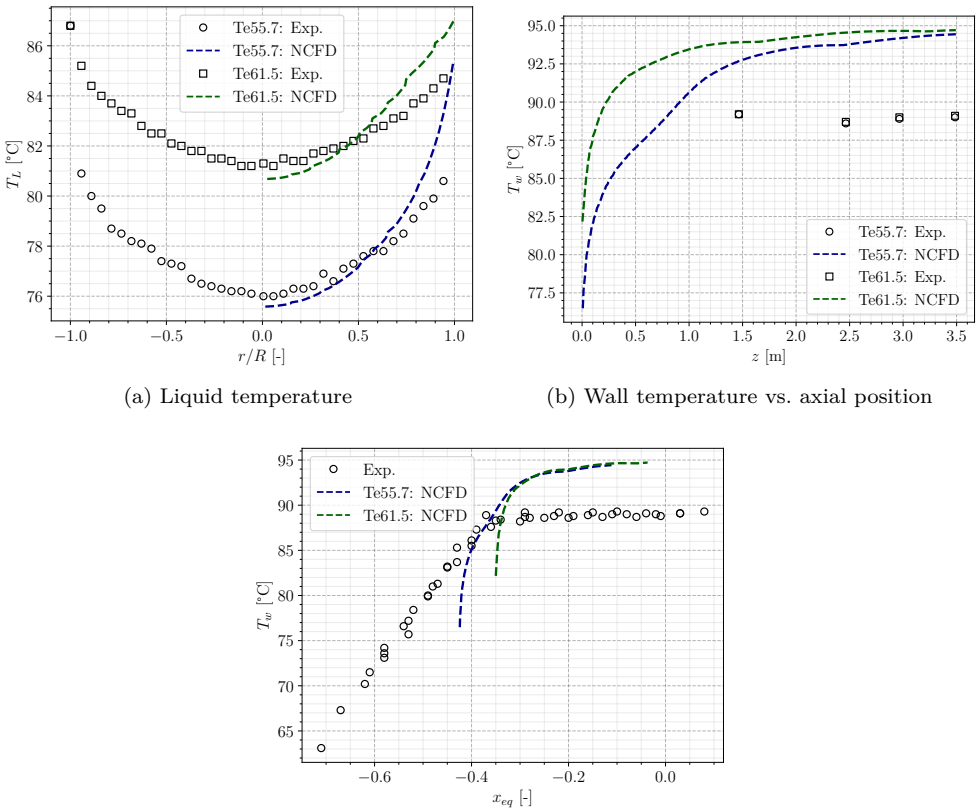

(a) Liquid temperature

(b) Wall temperature vs. axial position

(c) Wall temperature vs. local quality

Figure 4.5: Simulation results for cases 8G2P26W16Te55.7 & Te61.5

appears to start later than the experiment (around $x_{eq} \approx -0.3$ for the simulations contrary to $x_{eq} \approx -0.4$ for the experiments) and further reaches a wall temperature up to 6°C above the measurements.

Albeit the liquid temperature seems correctly distributed along the radial direction in the subcooled boiling region (also meaning that any amount of vapor potentially produced at the wall is correctly re-condensed), the wall temperature behavior significantly deviates from the experiments both by missing the ONB and exhibiting a too large superheat in the boiling region. **This consequently casts interrogations towards the modeling of the wall temperature in the code, which is a result of the wall boiling model (Section 2.5).**

4.4.3 *Saturated Cases*

Finally, we focus on saturated cases 8G2P26W16Te66.6 and Te70.3, both having an outlet quality $x_{eq,out} > 0$. Under those operating conditions, uncondensed vapor is present in the bulk flow (Figure 3.7a). Results of the simulation for those cases are presented on Figure 4.6.
Contrary to previous observations in subcooled cases, the liquid temperature profiles (Figure 4.6a) are overestimated ($\approx +0.6$°C) over the whole radial section for both cases. The shape exhibited are however similar to the experiments, with a flattening of the liquid temperature for the Te70.3 case.

In those conditions, boiling starts immediately at the beginning of the heated length. Therefore, wall temperature is expected to rapidly stabilize to the boiling temperature, which is actually what happens in the simulations (Figure 4.6b)). As previously noted for the low subcooling cases, the wall temperature during boiling is overestimated by approximately 6°C.

Those saturated cases are confirming that **the boiling model fails to predict the wall temperature**.

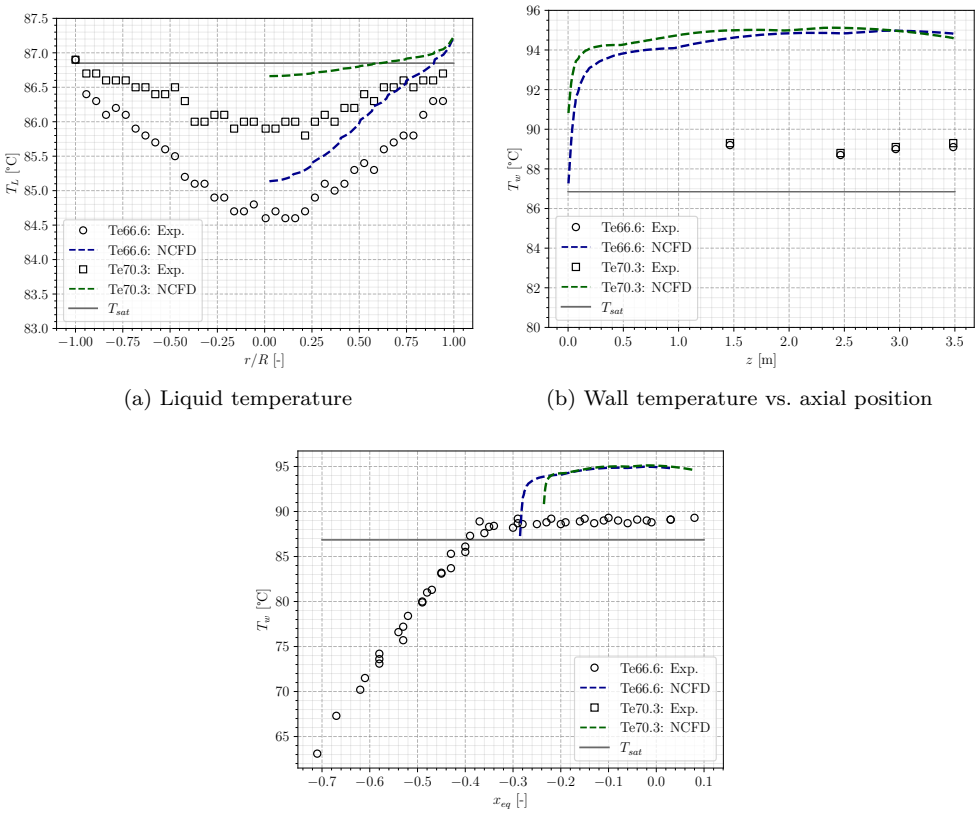

(a) Liquid temperature

(b) Wall temperature vs. axial position

(c) Wall temperature vs. local quality

Figure 4.6: Simulation results for cases 8G2P26W16Te66.6 & Te70.3

Remark : The small yet observed global overestimation of the liquid temperature may be a consequence of either a too large condensation or too large interfacial area concentration (*i. e.* small bubble diameter).

4.5 C3000 CASES SIMULATIONS : TOPOLOGY MEASUREMENTS

Now that comparisons with thermal measurements have been conducted, we move to assessment of core flow topology predictions by the code. Based on results from the 30G2P26W16 campaign, we will compare the predictions of the void fraction, the bubble diameter and the vapor velocity at the end of the heating length. We will separately focus on subcooled boiling and saturated cases.

4.5.1 *Subcooled Boiling Cases*

Subcooled cases 30G2P26W16Te62 and Te64 are simulated. They both have an outlet quality $x_{eq,out} \leq 0$ with pure liquid at the center of the test section, but present significant void fraction when approaching the wall (Figure 3.7a). Results of the NEPTUNE_CFD Simulations are presented on Figure 4.7.

The void fraction (Figure 4.7a) appears globally overestimated over the whole radial section, with a difference $\alpha_{CFD} - \alpha_{exp} \approx 10\%$ at the wall. However the results seem to match the very low void fractions region ($\alpha < 3\%$) and finds a pure liquid flow roughly at the same radial position as the measurements ($r/R \approx 0.5$ and 0.3 for Te62 and Te64 cases respectively).

On the other hand, the bubble diameter (Figure 4.7b) is largely underestimated by vanishing rapidly when $r/R < 0.9$ which is not observed experimentally. Measurements contrarily show a roughly constant bubble diameter after a small increase. The simulations yet present an acceptable agreement with the experiments near the wall and even present a slight growth of the bubble diameter before its immediate decrease. **Such**

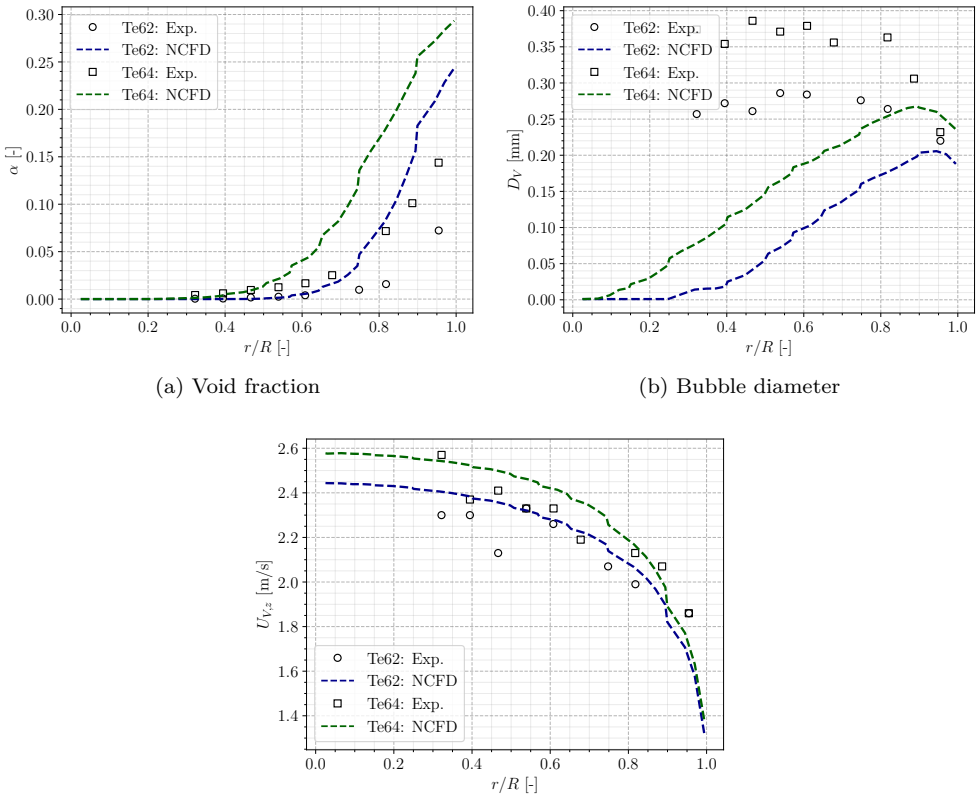

(a) Void fraction

(b) Bubble diameter

(c) Vapor velocity

Figure 4.7: Simulation results for cases 30G2P26W16Te62 & Te64

a discrepancy combined to a too large void fraction points towards an erroneous estimation of bubble break-up and / or condensation.

The vapor velocity profiles (Figure 4.7c) are in accordance with the DEBORA measurements, both in the values and profile shape. **This may be supporting the evaluation of the interfacial momentum transfer determining the drift velocity between liquid and vapor.**

> **Remark :** The interfacial momentum terms (Subsection 2.3.2) also depend on the local void fraction and bubble diameter, meaning that achieving a correct velocity profile while having an erroneous void fraction and bubble diameter does not ensure the validation of the interfacial forces by itself. However, the difference in vapor velocity from one case to another is coherent with the experiments, which at least implies a correct sensitivity to the local thermal-hydraulics conditions.

4.5.2 *Saturated Boiling Cases*

Next we simulate two saturated cases that experimentally present a non-zero void fraction at the tube center : cases 30G2P26W16Te66 and Te70. Results are presented of Figure 4.8.
Similar to the subcooled cases, the void fraction (Figure 4.8a) is overestimated over the whole section. Case Te66 presents a wall overestimation of approximately 10% as for the subcooled simulations (Figure 4.7a)and matches the radial position where $\alpha \approx 0$. On the contrary, case Te70 is largely overestimated over the whole section, which can be explained because the liquid temperature is close to saturation, strongly limiting the impact of condensation.

Bubble diameter (Figure 4.8b) for the Te66 case behaves close to the subcooled cases, with a large underestimation under the sharp decrease when $r/R < 0.8$. However, case Te70 presents a different profile with a larger growth in bubble diameter nearly matching maximum experimental value at $r/R \approx 0.6$, but then decreases too rapidly. Recalling thermal results for the 8G2P26W16Te70.3 case presenting similar operating conditions (Figure 4.6a), $r/R \approx 0.6$ corresponds to the radial position where the

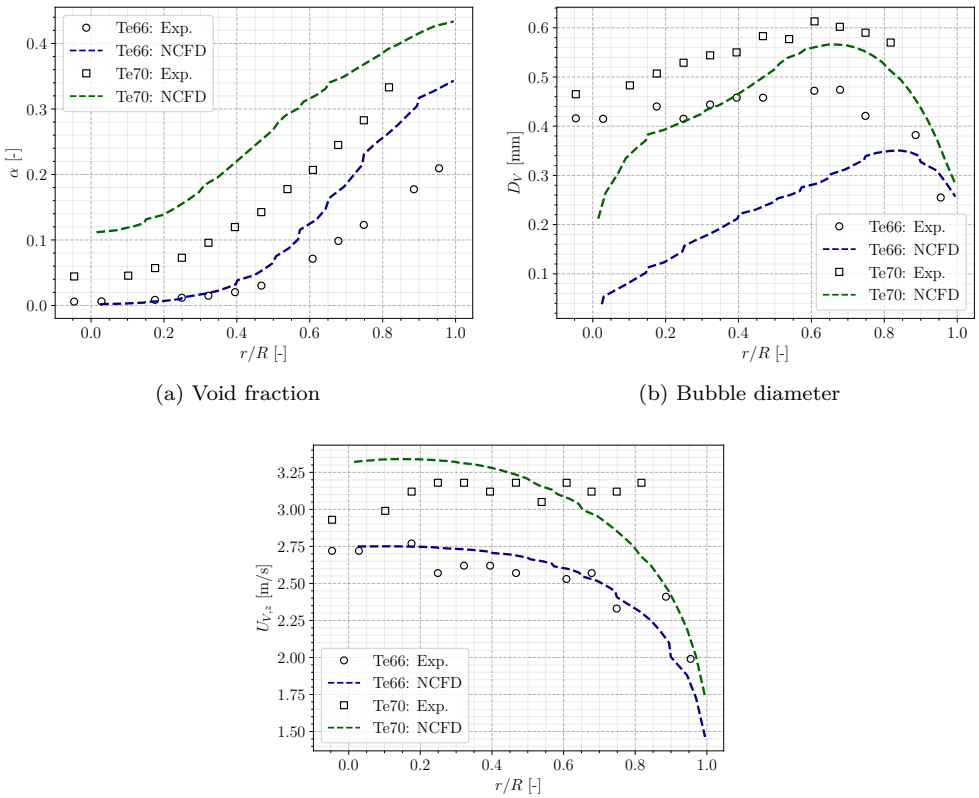

(a) Void fraction

(b) Bubble diameter

(c) Vapor velocity

Figure 4.8: Simulation results for cases 30G2P26W16Te66 & Te70

computed liquid temperature becomes lower than saturation temperature, enabling condensation to occur. This tends to indicate that **condensation may be responsible for most of the bubble diameter underestimation in the sub-cooled region**. On the contrary, **coalescence and break-up terms alone seem to be able to reproduce the bubble diameter increase before condensation starts**.

Finally, vapor velocity (Figure 4.8c) is correctly reproduced for the Te66 case while the Te70 simulation do not reproduce the plateau observed in the measurements by keeping a parabolic profile from which the experiment deviates. The velocity magnitude achieved for the Te70 case are however coherent with the experiments.

4.6 SIMULATIONS SENSITIVITY TESTS

In this section, we perform two sensitivity tests for the CFD results presented in Sections 4.4 and 4.5.

4.6.1 *Sensitivity to Wall Heat Flux Correction*

As observed in previous results, the simulations for saturated cases showed simultaneous overestimation of the void fraction (Figure 4.8a), the liquid temperature (Figure 4.6a) and the wall temperature (Figure 4.6b) for topology (C3000) and thermal (C800) cases in very close experimental conditions. Such a result means that we concurrently overestimate the phase change and the liquid enthalpy, **which physically means that we injected too much energy into the system.**

Considering that the inlet conditions (liquid mass flux / velocity and temperature) are correct, we can question the value of the total heat flux applied in the simulation. This echoes the analysis conducted in Subsection 3.5.1 where assembling tests from C3000 and C800 campaign to recompute the total heat injected in the system yielded calculated heat fluxes up to 8% smaller than the given experimental value (Table 3.8).

Note : We want to insist here that this estimation was based on a "merging" of different experimental tests in similar conditions . Small differences in the control parameters (Table 3.7) between C800 and C3000 cases can partly explain the calculated heat flux "error".

In order to assess this observation, we apply a heat flux correction for the cases 8G2P26W16Te66.6 & Te70.3 respectively associated with 30G2P26W16Te66 & Te70. Recalling Table 3.8 and acknowledging that the error may have been overestimated, we apply the correction showed in Tabled 4.2.

Case name	Initial ϕ_w [kW/m^2]	Correction [%]	Corrected ϕ_w [kW/m^2]
30G2P26W23Te66 and 8G2P26W16Te66.6	73.9	-4%	70.94
30G2P26W23Te70 and 8G2P26W16Te70.3	73.9	-6%	69.47

Table 4.2: Corrected heat fluxes applied in the simulations

The results for each case are compared to the initial heat flux value on Figure 4.9 and Figure 4.10 for C800 and C3000 cases respectively.

4.6.1.1 *Thermal Parameters*

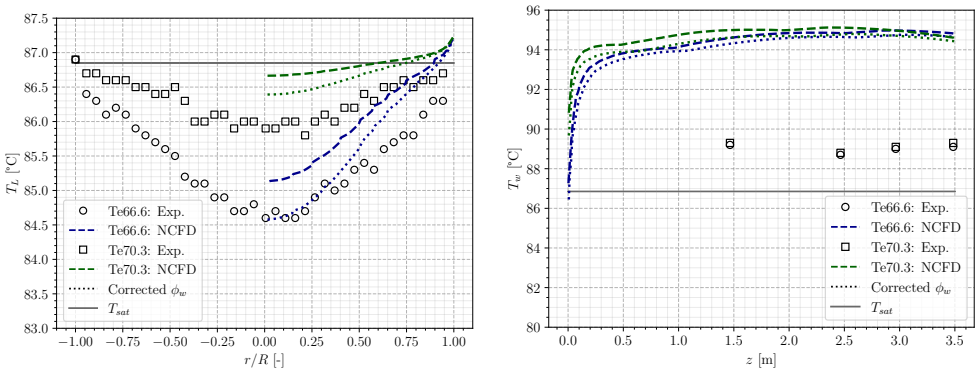

(a) Liquid temperature

(b) Wall temperature vs. axial position

Figure 4.9: Simulation results for cases 8G2P26W16Te66.6 & Te70.3 with corrected wall heat flux

Liquid temperature (Figure 4.9a) is better predicted for both cases but is still globally overestimated. The error is nonetheless no larger than 0.5°C which is close to the measurement uncertainty of 0.2°C (Table 3.3). Case Te66.6 matches very well the bulk experimental liquid temperature with the corrected heat flux.

The wall temperature is slightly reduced at the beginning of the heated length, but stabilizes at the same value as initial simulations in the boiling region. Which leads to the same previously observed wall superheat overestimation.

4.6.1.2 *Topology Parameters*

Void fraction predictions are significantly enhanced for both C3000 cases (Figure 4.10a), especially regarding case Te70 which matches the experiment at the center of the tube and a maximum error $\alpha_{CFD} - \alpha_{exp} \approx 5\%$ over the whole section. Case Te66 still presents a large overestimation at the wall, but better matches bulk measurements for $r/R \leq 0.8$. However, it seems to slightly underestimate the core void fraction for $r/R \leq 0.5$.

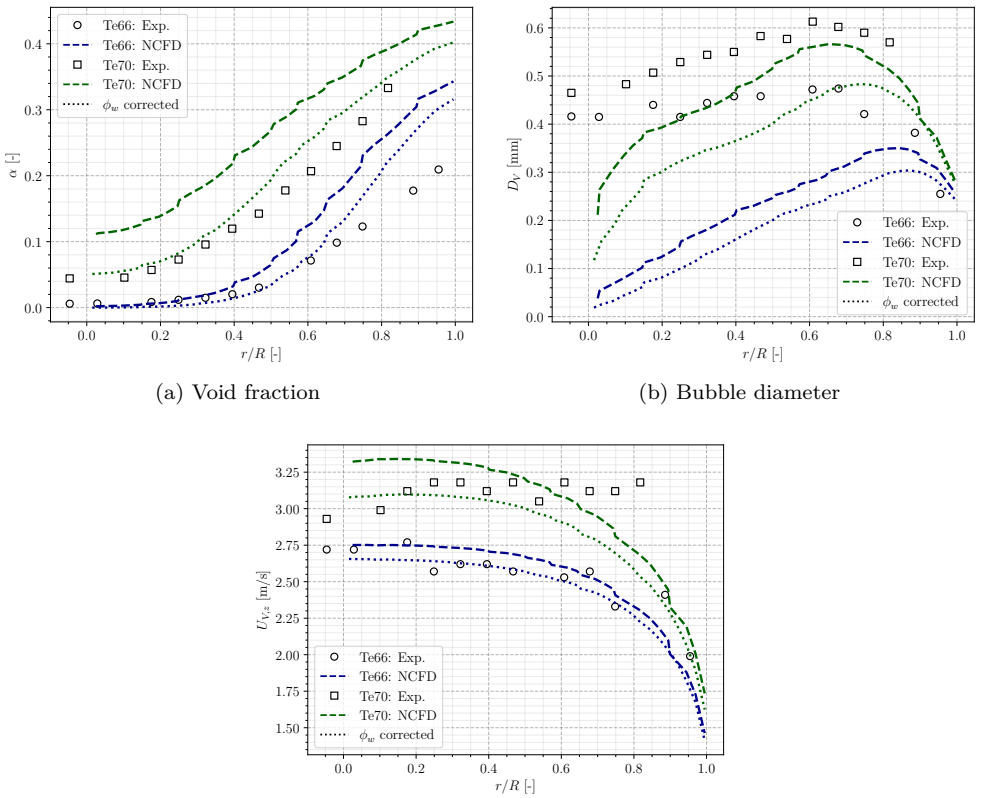

(a) Void fraction

(b) Bubble diameter

(c) Vapor velocity

Figure 4.10: Simulation results for cases 30G2P26W16Te66 & Te70 with corrected wall heat flux

Bubble diameter predictions are degraded when using the heat flux correction. It decreases compared to the first simulations with a decrease starting closer to the wall, further deviating from the experiments. This result could have been expected from previous observations where the strong decrease in D_V corresponds to the point where $T_L = T_{sat}$ (Figures 4.8b and 4.6a). Reducing the applied heat flux thus naturally moves this point towards the wall (Figure 4.9b).

Vapor velocity profiles (Figure 4.10c) are not much impacted by the correction, with values staying relatively close to the experiment in the bulk. However, results for Te70 case even less capture the velocity plateau observed in the measurements.

4.6.2 *Influence of a Wall Boiling Parameter : the Nucleation Site Density*

Previous analyses showed that the wall temperature in the boiling region was badly predicted by NEPTUNE_CFD (Figures 4.5c and 4.6c) with an overestimation up to 6°C. The wall temperature is computed in the code through the model dedicated to wall boiling, namely the "Heat Flux Partitioning" model (Section 2.5).

This model involves the evaluation of many different physical parameters that requires the use of correlations. For instance, the "nucleation site density" (N_{sit}, Eq. 2.36) which controls the number of bubbles that can be generated per unit of area, is evaluated using the law of Lemmert & Chawla [100] (Eq. 2.37) that only depends on the wall superheat $\Delta T_w = T_w - T_{sat}$. More recent correlations dedicated to N_{sit} evaluation have been developed since and notably include of other physical parameters such as pressure or contact angle [7, 73, 103, 181]

To test the CFD results sensitivity to the wall boiling modeling, we conduct simulations of the 8G2P26W16Te55.7 case while changing the N_{sit} correlation. This case covers a local quality range that includes single phase and boiling part (Figure 4.5c). Three nucleation site density correlations are tested:

- Lemmert & Chawla [100] (Eq. 2.37) ;

- Hibiki & Ishii [73] (Eq. 7.5) ;
- Li *et al.* [103] (Eq. 7.11).

The difference between the simulations results are presented on Figure 4.11 along with the different fluxes (liquid convection $\phi_{c,L}$, phase change ϕ_e, quenching ϕ_q and vapor convection $\phi_{c,V}$).

The nucleation site density modification induces very small variations over the bulk quantities (Figures 4.11a to 4.11d). The only observable differences lie very close to the wall with an absolute void fraction change of 1.5% and bubble diameter change less than 0.01 mm. However, the computed heat fluxes (Figure 4.11g) show large difference between the three cases, with an evaporation heat flux enhanced by more than 15% by changing from Lemmert & Chawla to Li *et al.* formulation. The absence of such a difference in the bulk means that models controlling the bulk thermodynamic equilibrium (*e. g.* condensation) rapidly compensate changes in the heat flux partitioning to reach the very similar distribution between α and T_L.

Note : This "compensating" effect of the bulk models in CFD computations when changing the wall Heat Flux Partitioning has also been noted in other works such as in Gilman & Baglietto [59] or Montout [119].

Contrary to bulk values, the wall temperature obtained in the simulations is significantly modified (Figures 4.11e and 4.11f) with an error reduction regarding the experimental measurements. Results using Li *et al.* correlation overestimates the wall temperature by 2.5°C versus up to 6°C for the first simulations. This results is probably due to the increase in evaporation heat flux ϕ_e, thus leaving less heat to be transmitted through convection and reduces the wall temperature.

Remark : The very small amount of quenching heat flux ϕ_q (Figure 4.11g) is surprising. The transient conduction induced by bubbles movements is expected to be larger because PWR-like conditions present a large number of tiny bubbles on the surface that can slide over long distances [90, 110].

4.7 CONCLUSION

This Chapter has investigated the modeling of dispersed boiling flows implemented in NEPTUNE_CFD (Chapter 2) based on simulations of the DEBORA experiment (Chapter 3). At this point, the main conclusions are:

- The single-phase flow region correctly matches the experiments, both regarding liquid and wall temperature (maximum error of approx. 1°C).
- Significant discrepancies are observed for the boiling region. Though a good agreement is found for vapor velocity and liquid temperature for subcooled flows, visible differences are however noted for void fraction (overestimation), bubble diameter (underestimation) and wall temperature (overestimation).
- Condensation is likely to have an important impact in the bubble diameter underestimation, since its too strong decrease coincides with radial position where $T_L = T_{sat}$.
- Interfacial area transport equation seems to be able to reproduce coalescence effects in the absence of subcooled liquid / condensation.
- Testing a heat flux correction showed that a much greater agreement on the void fraction and liquid temperature could be achieved for saturated cases by diminishing ϕ_w by roughly 5%.
- Wall temperature appears to be sensitive to the closure laws involved in the Heat Flux Partitioning that models for the wall boiling phenomenon. This is not the case for the bulk properties that are left nearly unchanged.
- The wall boiling model predicts a very low quenching flux which appears surprising in such flow conditions.

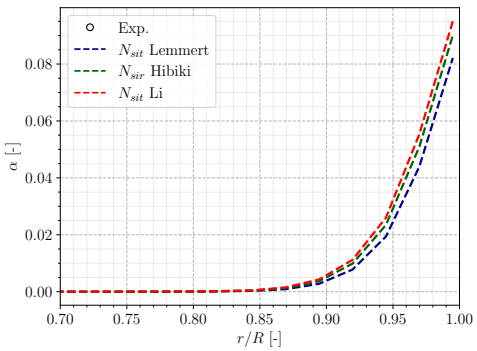

(a) Void fraction (zoomed)

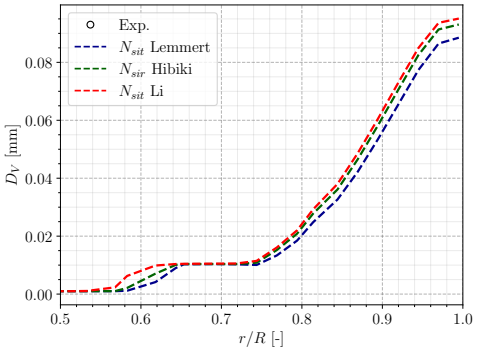

(b) Bubble diameter (zoomed)

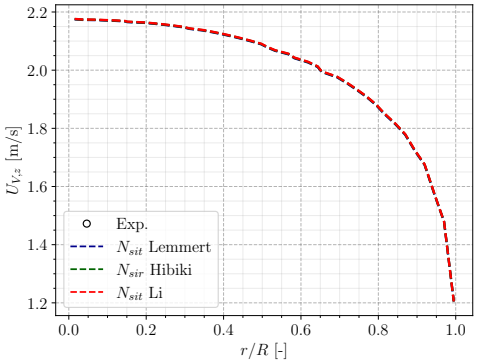

(c) Vapor velocity

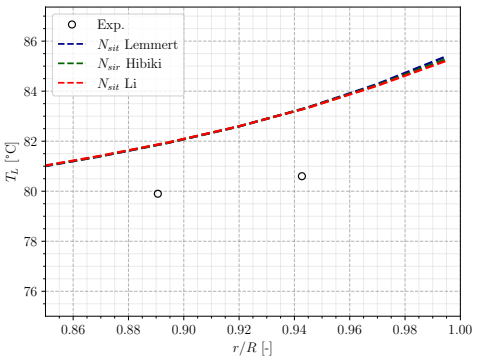

(d) Liquid temperature (zoomed)

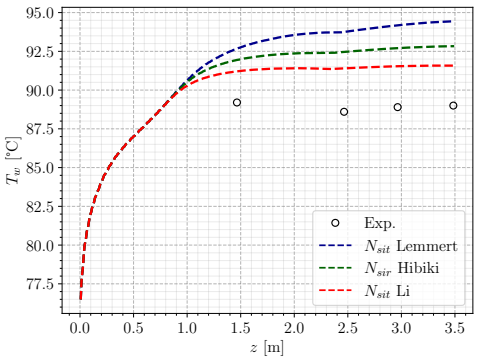

(e) Wall temperature vs. axial position

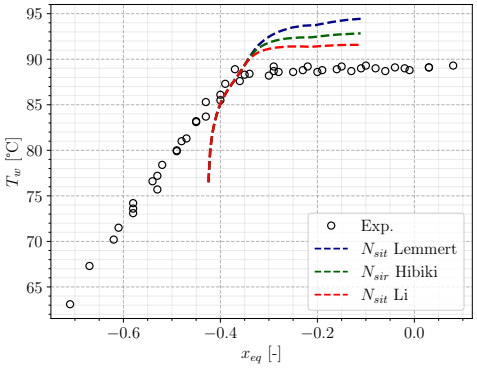

(f) Wall temperature vs. local quality

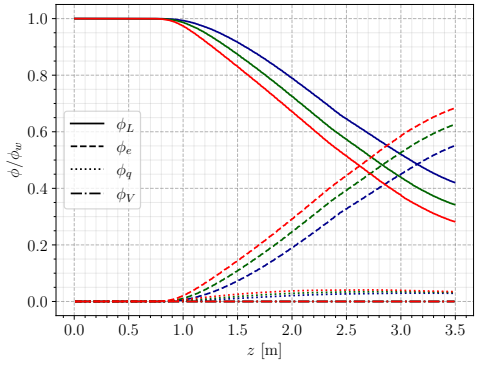

(g) Heat Flux Partitioning vs. axial position

Figure 4.11: Simulation results for case 8G2P26W16Te55.7 using different nucleation site density correlations

All in all, these results are highlighting the difficulty of reaching a precise modeling of the multiple physical phenomena at stake in dispersed boiling flows. Despite the absolute discrepancies, the current modeling

shows an encouraging behavior in the bulk (void fraction and liquid temperature shapes, coalescence / break-up / condensation impact, etc.). This could benefit from further work to precisely model the interfacial heat transfers in the flow along with bubble population quantification. Approaches considering poly-dispersed population of bubbles such as the iMUSIG model [91] could be of interest in that prospect.

On the other hand, the modeling of wall boiling appears to be somewhat old-fashioned due to the use of old closure laws and based on a simple formulation of the Heat Flux Partitioning. In the frame of advancing towards local predictions of the Critical Heat Flux, it seems natural to be looking for a finer and more extensive modeling of the wall boiling.

In that regard, the next part of this manuscript will be dedicated to an investigation and construction of a new Heat Flux Partitioning model. The goal being to account for more physical phenomena at the wall (bubble sliding, interactions, etc.) along with reassessing some of the closure laws required in the formulation, with systematic comparison to experiments when possible.

Part II

DEVELOPMENT OF A NEW WALL HEAT FLUX PARTITIONING MODEL

5

INTRODUCTION TO HEAT FLUX PARTITIONING

Contents

5.1 Introduction 55
5.1.1 Empirical Approaches 55
5.1.2 First Heat Flux Partitioning Approaches 56
5.2 Kurul & Podowski (1990) 57
5.3 Basu, Warrier & Dhir (2005) 58
5.3.1 Case 1 : Bubble Sliding, $D_d < s$ 60
5.3.2 Case 2 : Bubble Coalescence without Sliding, $D_d \geq s$ 61
5.4 Gilman (2017) 61
5.5 Kommajosyula (2020) 63
5.6 Conclusion 65

5.1 INTRODUCTION

5.1.1 *Empirical Approaches*

In the field of heat transfer and boiling, establishing a physical relationship between the applied heat flux at the wall ϕ_w and the wall temperature T_w has always been a primal goal for system design and safety analysis. Traditional approaches for single-phase flows rely on the estimation of the heat transfer coefficient h_{SP} defined as:

$$\phi_w = h_{SP} \left(T_w - T_L \right) \tag{5.1}$$

where T_w and T_L are the wall and bulk liquid temperature.

Estimating h_{SP} is usually done using dedicated correlations depending on flow parameters such as the hydraulic Reynolds number Re_{D_h}, the fluid Prandtl number Pr_L, etc. Correlations of Dittus-Boelter (Eq 3.20) or Gnielinski (Eq. 3.21) that were presented earlier are typical example of widely used expressions to estimate h_{SP}.

For boiling multiphase flows, different types of empirical approaches have been developed through the history. For instance, some authors proposed direct correlations relating wall heat flux and temperature such as:

- Jens & Lottes [78]:

$$\phi_w = \left(\frac{\Delta T_w}{25} e^{P/62} \right)^4 \tag{5.2}$$

- Thom *et al.* [155]:

$$\phi_w = \left(\frac{\Delta T_w}{22.65} e^{P/87} \right)^2 \tag{5.3}$$

with P in bar and ϕ_w in $\mathrm{MW/m^2}$.

On the other hand, some models are based on the estimation of heat transfer coefficients similar to single-phase approaches. They mostly rely on the separation between a single phase h_{SP} and nucleate boiling h_{NB} heat transfer coefficients. Well-known correlations of this type are proposed by Chen [23], Gungor & Winterton [67] or Liu & Winterton [105]. For instance, Chen correlation writes:

$$\phi_w = \phi_{SP} + \phi_{NB} = h_{SP}\left(T_w - T_L\right)F + h_{NB}\left(T_w - T_{sat}\right)S \tag{5.4}$$

with F an amplification factor for the single phase heat transfer due to bubble agitation and S a suppression term hindering the nucleate boiling under the effect of bulk liquid flow.

The single phase part h_{SP} is calculated using Dittus-Boelter [38] formulation (Eq. 3.20) while the nucleate boiling part is:

$$h_{NB} = 0.00122\frac{\lambda_L^{0.79}c_{p,L}^{0.45}\rho_L^{0.49}}{\sigma^{0.5}\mu_L^{0.29}h_{LV}^{0.24}\rho_V^{0.24}}\Delta T_w^{0.25}\left(P_{sat}\left(T_w\right) - P_{sat}\left(T_{sat}\right)\right)^{0.75} \tag{5.5}$$

along with the factors F and S:

$$\frac{1}{X_{tt}} = \left(\frac{x}{1-x}\right)^{0.9}\left(\frac{\rho_L}{\rho_V}\right)^{0.5}\left(\frac{\mu_V}{\mu_L}\right)^{0.1} \tag{5.6}$$

$$F = \begin{cases} 1 & \text{if } X_{tt} \geq 1 \\ 2.35\left(\dfrac{1}{X_{tt}} + 0.213\right)^{0.736} & \text{if } X_{tt} \leq 1 \end{cases} \tag{5.7}$$

$$S = \frac{1}{1 + 2.53\times 10^6 \mathrm{Re}_{D_h}^{1.17}} \tag{5.8}$$

where X_{tt} is the Lockhart-Martinelli parameter [106] and x the vapor quality.

Each of those correlations has been developed for given experimental conditions such as high pressure flows up to 150 bar for Thom and Jens & Lottes correlations while Chen correlation is dedicated for low to moderate pressure ($\sim$ 35 bar).

5.1.2 *First Heat Flux Partitioning Approaches*

The spirit of splitting the different heat transfer mechanisms (single-phase, nucleate boiling) using different heat transfer coefficients is actually a premise to what is nowadays called the "Heat Flux Partitioning" approach. Bowring [15] is among the first author who actually expressed the total heat flux at the wall as separate contributions between different heat transfer mechanisms by writing:

$$\phi_w = \phi_e + \phi_a + \phi_{SP} \tag{5.9}$$

where ϕ_e is the latent-heat transfer associated to evaporation, ϕ_a the convection due to bubble agitation and ϕ_{SP} the single-phase heat transfer to the liquid.

Making steps towards a more mechanistic description of boiling, he wrote:

$$\phi_e = N_{sit} f V_b \rho_V h_{LV} \tag{5.10}$$

where N_{sit} is the nucleation site density on the surface, f the bubble nucleation frequency, V_b the bubble volume. Those parameters need dedicated description and modeling based on experimental measurements. Nonetheless, an empirical parameter is introduced by Bowring to estimate the bubble-agitation term ϕ_a as:

$$\phi_w = \phi_{SP} + (1+\varepsilon)\,\phi_e \tag{5.11}$$

$$\varepsilon = \frac{\phi_a}{\phi_e} \approx \frac{\rho_L c_{p,L}}{\rho_V h_{LV}}\left(T_w - T_L\right) \tag{5.12}$$

where ε has to be experimentally estimated. We can notably observe that its expression is that of a Jakob number based on the temperature difference between the wall and the liquid temperature.

This idea of splitting the wall heat flux and try to precisely model each heat transfer mechanisms using detailed parameters (nucleation site density, frequency, nucleated bubble diameter, etc.) has been since a very active matter of research in the field of boiling heat transfer [35, 79]. With increasing experimental insights allowing to access local parameters relevant for the physics at stake close to the wall [90, 108, 140, 152, 169], the development of such models has become increasingly important both for analytic and simulation grounds. Indeed, the clear separation of the different heat fluxes is a very useful mathematical formulation for multiphase CFD computations where each term can be used as a phase-related source term at the wall [58, 65].

In the following sections, we chronologically present four different Heat Flux Partitioning models developed between 1990 and 2020. For each model, we detail the mathematical formulation of the different fluxes along with associated physical assumptions and highlight the parameters that require a dedicated closure law.

5.2 KURUL & PODOWSKI (1990)

In their original work published in 1990, Kurul & Podowski [92] proposed a complete closure for the wall heat flux partitioning. Their model is among the most referred to by many authors and has been particularly used in CMFD codes due to its simple formulation and closure laws.

> **Note :** The wall boiling model of NCFD mostly rely on the Kurul & Podowski formulation as presented in Chapter 2.

Kurul & Podowski considered the applied heat flux to be divided between three mechanisms (Figure 5.1):

- A liquid single-phase convective heat flux $\phi_{c,L}$;
- A boiling heat flux ϕ_e ;
- A quenching heat flux ϕ_q induced by bubble movement when leaving the surface.

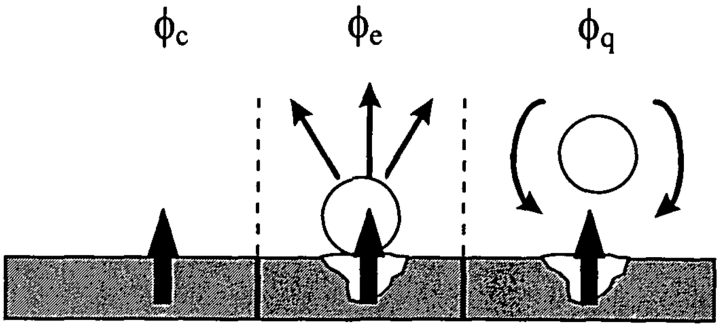

Figure 5.1: Sketch of the HFP considered by Kurul & Podowski (by Manon [109]).

The total wall heat flux being :

$$\phi_w = \phi_{c,L} + \phi_e + \phi_q \tag{5.13}$$

The convective heat flux is expressed as :

$$\phi_{c,L} = A_{c,L}\rho_L c_{p,L} U_{L,\delta} \mathrm{St}_{L,\delta} \left(T_w - T_{L,\delta}\right) \tag{5.14}$$

with $A_{c,L}$ the portion of the wall unaffected by boiling, U_L the liquid velocity, St the Stanton number and δ a location in the buffer layer.

> **Note :** The choice of Kurul & Podowski of taking the liquid properties at the buffer layer is not further detailed in their work. It could however be questioned when comparing the bubble size with δ. Moreover, one should keep in mind that the chosen mechanisms were dedicated to pool boiling description rather than flow boiling.

Assuming bubbles are spherical and leave the surface at diameter D_{lo}, they write:

$$\phi_e = \frac{1}{6}\pi {D_{lo}}^3 \rho_V h_{LV} f N_{sit} \tag{5.15}$$

$$\tag{5.16}$$

with N_{sit} the nucleation site density and f the nucleation frequency.

The quenching heat flux occurring over the wait time t_w between two nucleated bubbles is computed as:

$$\phi_q = t_w f A_q \frac{2\lambda_L \left(T_w - T_{L,\delta}\right)}{\sqrt{\pi \eta_L t_w}} \tag{5.17}$$

This expression corresponds to the time-average (over a time t_w) conductive heat flux from a surface at T_w towards a semi-infinite liquid medium initially at $T_{L,\delta}$ as expressed by Del Valle and Kenning [35].

They also estimate the portion of the surface affected by the bubbles as:

$$A_q = \min\left(1\ ;\ F_A \pi R_{lo}^2 N_{sit}\right) = 1 - A_{c,L} \tag{5.18}$$

where $F_A = 4$ accounts for the bubble area of influence when leaving the surface.

One of the main hypothesis of the model is also to suppose that the bubble departure frequency f is directly related to the wait time t_w by neglecting the bubble growth time as:

$$f = \frac{1}{t_w} \tag{5.19}$$

Required closure relationships : N_{sit}, f (or t_w), D_{lo}

5.3 BASU, WARRIER & DHIR (2005)

In 2005, Basu *et al.* [6, 7] proposed a new HFP model together with a series of experiments to further study the different closure relationships required in their approach. This model was meant to account for finer descriptions of the multiple phenomena at stake in subcooled flow boiling. In particular, they account for bubble sliding and merging and thus distinguish bubble departure diameter D_d (leaving the nucleation site) and lift-off diameter D_{lo} (leaving the wall).

Their approach consists of separating the boiling flow in three regions (Figure 5.2a):

- Before Onset of Nucleate Boiling (ONB) zone, where only liquid forced convection occurs, yielding:

$$\phi_w = h_{c,L}\left(T_w - T_L\right) \tag{5.20}$$

- Zone between the ONB and the OSV, prior to observing a net amount of vapor with bubble lifting off the surface. The heat flux is still totally transferred to the liquid, but the equivalent convective heat transfer coefficient $\overline{h_{c,L}}$ is supposed to be enhanced by 30% due to the presence of bubbles on the wall:

$$\phi_w = \overline{h_{c,L}}\left(T_w - T_L\right) \approx 1.3 h_{c,L}\left(T_w - T_L\right) \tag{5.21}$$

  Basu *et al.* compute the ONB wall temperature as:

$$T_{w,ONB} = T_{sat} + \frac{4\sigma T_{sat}}{D_c \rho_V h_{LV}} \tag{5.22}$$

$$D_c = \sqrt{\frac{8\sigma T_{sat}\lambda_L}{\rho_V h_{LV} \phi_w}}\left(1 - \exp\left(-\theta^3 - 0.5\theta\right)\right) \tag{5.23}$$

  where D_c represents the diameter of active cavities and θ the static contact angle.

- Post-OSV (Onset of Significant Void) zone, where bubbles now leave the surface towards the bulk flow and the other parts of the HFP appear *i. e.* the boiling and quenching fluxes. The beginning of OSV is defined by Basu *et al.* using a critical liquid temperature $T_{L,OSV}$ as:

$$T_{L,OSV} = T_{sat} - 0.7\exp\left(-0.065\frac{D_d h_{c,L}}{\lambda_L}\right)\frac{\phi_w}{h_{c,L}} \tag{5.24}$$

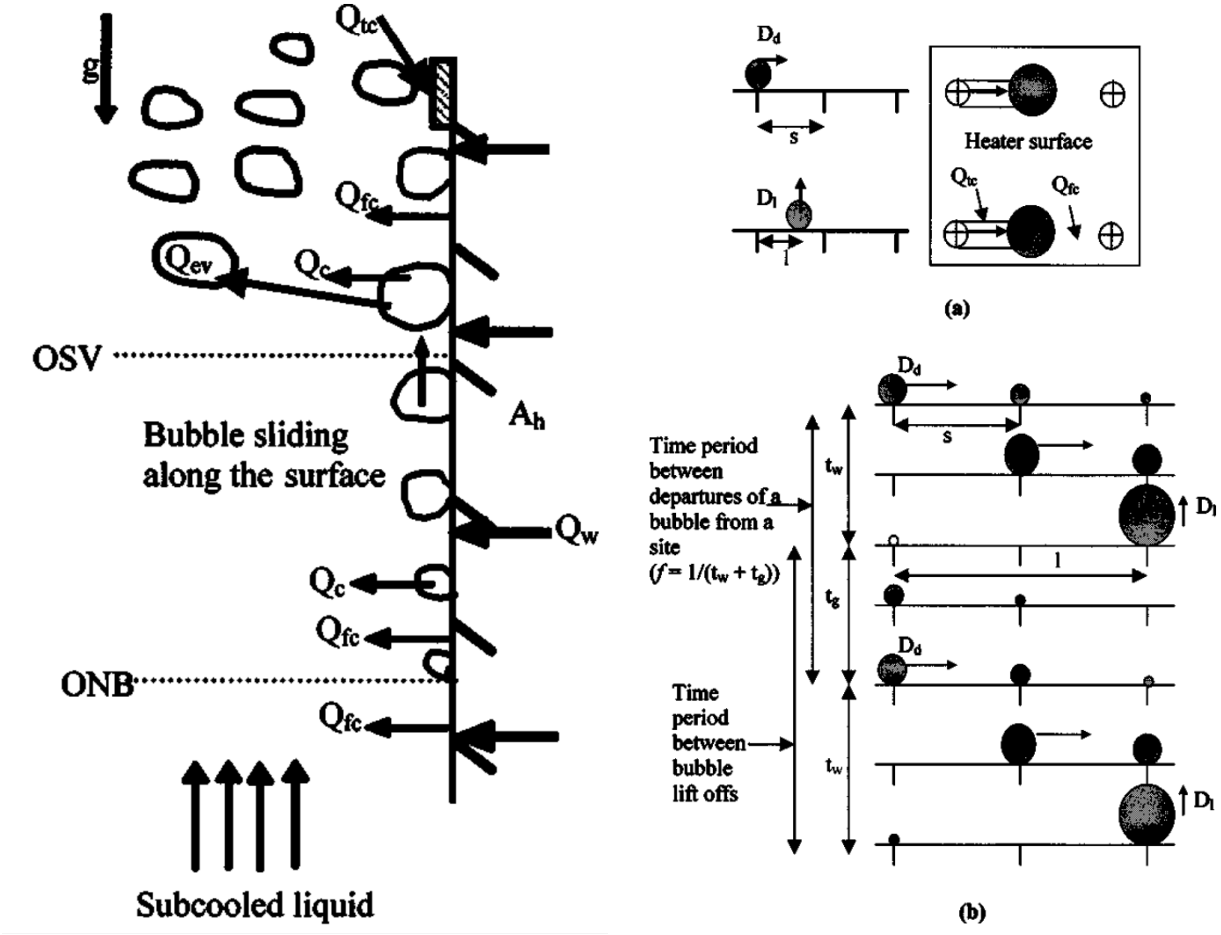

(a) Heat transfer zones subdivision

(b) Considered sliding and merging mechanisms

Figure 5.2: Sketch of the heat transfers zones and bubble behavior considered by Basu *et al.*. (Adapted from [7]). Q represents the heat transfer.

The hypothesis of Basu *et al.* is that the heat flux is first transferred to the superheated liquid close to the wall (by convection and transient quenching), part of which contributing to the evaporation through the liquid-vapor interface. The remaining heat is transferred to the bulk liquid (ϕ_L) either from the superheated liquid layer or bubble condensation. The whole heat transfer mechanism thus writes:

$$\phi_w = \phi_{c,L} + \phi_q = \phi_e + \phi_L \tag{5.25}$$

In order to estimate the quenching heat flux associated to bubble sliding and lift-off, Basu *et al.* consider two cases:

1) Bubble sliding from departure ($D = D_d$) to lift-off ($D = D_{lo}$) ;

2) Bubble coalescence with neighboring sites before departure.

Those two cases are distinguished using the average distance between nucleation sites s, which they suppose equal to $1/\sqrt{N_{sit}}$.

5.3.1 *Case 1 : Bubble Sliding, $D_d < s$*

In this case, the bubble will grow up to its departure diameter D_d and slide over a length $l_{sl,0}$ before lifting-off. If $l_{sl,0} < s$, the bubble will slide up to its lift-off diameter D_{lo} and leave the wall without colliding with other bubbles. On the contrary, if $l_{sl,0} \geq s$ the sliding bubble will merge with bubbles growing on their nucleation site, inducing a sudden growth of the bubble diameter that can exceed D_{lo} and thus trigger lift-off after sliding over a reduced length $l_{sl} < l_{sl,0}$. Those assumptions are summarized on Figure 5.2b.

If bubble coalescence occurs, the number of bubbles lifting-off the surface is lower than the actual number of nucleating sites. Basu *et al.* thus define a reduction factor R_f that damps the total nucleation site density:

$$R_f = \begin{cases} \dfrac{s}{l_{sl}} = \dfrac{1}{l_{sl}\sqrt{N_{sit}}} & \text{if } l_{sl,0} \geq s \\ 1 & \text{if } l_{sl,0} < s \end{cases} \tag{5.26}$$

Regarding bubble sizes, they suppose that bubbles coalesced by a sliding bubble while growing have a diameter D_d *i. e.* they were close to departure. This results in a bubble of diameter $D = \left(D_{sl}^3 + D_d^3\right)^{1/3}$ which will trigger lift-off if $D > D_{lo}$. Consequently, a sliding bubble is allowed to merge with numerous bubbles before lifting off. Noting N_{merg} the number of coalesced bubble and D_N the resulting bubble diameter, the sliding distance is:

$$l_{sl} = N_{merg} s + l_{D_N \to D_{lo}} \tag{5.27}$$

where $l_{D_N \to D_{lo}}$ is the remaining distance to slide if $D_N < D_{lo}$, being 0 if $D_N \geq D_{lo}$.

The surface swiped by the sliding bubble is then expressed as $A_{sl} = C\overline{D} l_{sl}$ with $\overline{D}$ the average bubble diameter during sliding and C the ratio between the bubble diameter and its foot, expressed based on measurements from Maity [108] as :

$$C = 1 - \exp\left(2 - \theta^{0.6}\right) \tag{5.28}$$

After observing in their experiments that $D_d \approx 0.5 D_{lo}$, Basu *et al.* choose:

$$\overline{D} = \frac{D_{lo} + D_d}{2} \approx 0.75 D_{lo} \tag{5.29}$$

Defining:

$$t^* = \left(\frac{\lambda_L}{h_{c,L}}\right)^2 \frac{1}{\pi \eta_L} \tag{5.30}$$

the time at which transient conduction heat transfer becomes equal to forced liquid convection, the resulting quenching heat transfer ϕ_q is computed as:

$$\phi_q = \frac{1}{t_w + t_g} \int_0^T \frac{\lambda_L}{\sqrt{\pi \eta_L t}} \left(T_w - T_L\right) A_{sl} R_f N_{sit} dt \tag{5.31}$$

where $T = t^*$ if $t^* < t_w + t_g$ (forced convection dominates at some point during a nucleation cycle which total time is the wait time t_w plus the bubble growth time t_g) or $T = t_w + t_g$ if $t^* \geq t_w + t_g$ (transient conduction dominates over the whole nucleation cycle).

The liquid convective heat transfer is therefore:

$$\phi_{c,L} = \overline{h_{c,L}} \left(T_w - T_L\right) A_{c,L} + \overline{h_{c,L}} \left(T_w - T_L\right) A_{sl} R_f N_{sit} \left(1 - \min\left(1 \; ; \; \frac{t^*}{t_w + t_g}\right)\right) \tag{5.32}$$

with $A_{c,L} = 1 - A_{sl} R_f N_{sit}$ the wall area unaffected by bubbles.

The boiling heat flux is:

$$\phi_e = \rho_V h_{LV} \frac{\pi}{6} D_{lo}^3 R_f N_{sit} \frac{1}{t_w + t_g} \tag{5.33}$$

5.3.2 *Case 2 : Bubble Coalescence without Sliding, $D_d \geq s$*

Under higher wall superheat, the subsequent rise in the nucleation site density N_{sit} can lead to boiling regimes where bubbles coalesce with each other at early stages of their lifetime *i. e.* while still attached to their nucleation site. This situation is accounted for by Basu *et al.* in the case when $D_d \geq s$ by considering immediate lift-off of coalesced bubble at radius $D > D_{lo}$. In this case, the total density of bubbles leaving the surface is lower than N_{sit} and is thus reduced using:

$$R_f = \frac{s^3}{D_{lo}^3} \tag{5.34}$$

Under this massively coalescing regime, the entire surface will experience quenching due to bubble lift-off all over the heater. Depending on the values of t^*, we have:

$$\phi_q = \begin{cases} \dfrac{1}{t_w + t_g} \displaystyle\int_0^{t^*} \frac{\lambda_L}{\sqrt{\pi \eta_L t}} \left(T_w - T_L\right) dt & \text{if } t^* < t_w \\ \dfrac{1}{t_w + t_g} \left[\displaystyle\int_0^{t_w} \frac{\lambda_L}{\sqrt{\pi \eta_L t}} \left(T_w - T_L\right) dt + \int_0^{T} \frac{\lambda_L}{\sqrt{\pi \eta_L t}} \left(T_w - T_L\right) \left[1 - S_b N_{sit}\right] dt \right] & \text{if } t^* \geq t_w \end{cases} \tag{5.35}$$

$$\phi_{c,L} = \begin{cases} \overline{h_{c,L}} \left(T_w - T_L\right) \dfrac{t_w - t^*}{t_w + t_g} + \overline{h_{c,L}} \left(T_w - T_L\right) \left[1 - A_b N_{sit}\right] \dfrac{t_g}{t_w + t_g} & \text{if } t^* < t_w \\ \overline{h_{c,L}} \left(T_w - T_L\right) \left[1 - A_b N_{sit}\right] \dfrac{t_w + t_g - t^*}{t_w + t_g} & \text{if } t^* \geq t_w \end{cases} \tag{5.36}$$

with $A_b = \dfrac{\pi \left(Cs\right)^2}{4}$.

The boiling heat flux still expressed as Eq. 5.33.

Remark : We can note that contrary to Kurul & Podowski model, the bubble nucleation frequency is computed without neglecting the bubble growth time t_g and is thus expressed as:

$$f = \frac{1}{t_g + t_w} \tag{5.37}$$

Required closure relationships : N_{sit}, t_w, t_g, D_d, D_{lo}, $l_{sl,0}$, $h_{c,L}$.

5.4 GILMAN (2017)

A more recent HFP model dedicated to CFD simulations has been proposed in Gilman PhD work [58] and summarized in Gilman & Baglietto [59]. Among the different evolution proposed in their work, we can mention:

- A probabilistic law to account for static interaction between nucleation sites ;
- A force-balance approach to compute the bubble departure and lift-off diameters ;
- A generic law for the enhanced forced convection coefficient accounting for bubble presence ;
- The presence of a modified quenching term accounting for local wall superheat beneath a bubble dry spot.

The total heat flux is partitioned between the liquid forced convection $\phi_{c,L}$, the solid quenching $\phi_{q,s}$, the quenching due to bubble sliding $\phi_{q,sl}$ and the evaporation flux ϕ_e. Yielding:

$$\phi_w = \phi_{c,L} + \phi_{q,s} + \phi_{q,sl} + \phi_e \tag{5.38}$$

The convective term is computed in a way similar to Basu *et al.* [7] in Eq. 5.32:

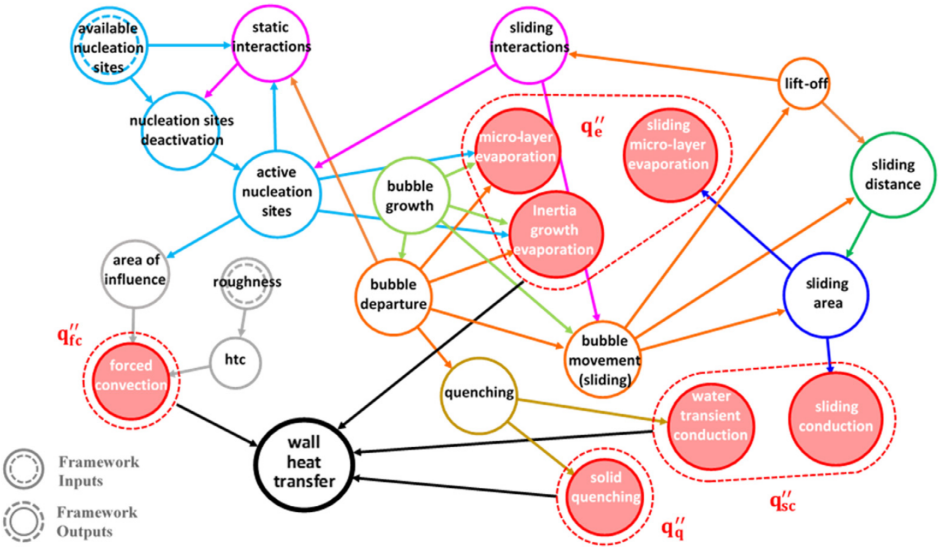

Figure 5.3: Heat Flux Partitioning mind-map description by Gilman [58] (Adapted from [59]).

$$\phi_{c,L} = h_{c,L}\left(1 - A_{sl}N_{sit,a}\right)\left(T_w - T_L\right) + \overline{h_{c,L}}A_{sl}N_{sit,a}\left(1 - \frac{t^*}{t_w + t_g}\right)\left(T_w - T_L\right) \tag{5.39}$$

where $N_{sit,a}$ is the active nucleation site density that will generate sliding bubbles, that can differ from the empirical value of available sites N_{sit} usually computed by a correlation. The time t^* is the same time as in Eq. 5.30, A_{sl} the bubble sliding area, t_w and t_g respectively the wait and bubble growth times.

The actually active nucleation site density $N_{sit,a}$ (that will generate bubbles) is considered by Gilman to be smaller than N_{sit} by considering a static interaction between the available sites *i. e.* the fact that a bubble laying on a site may be blocking nucleation from an other site laying beneath its foot. Following a so-called Complete Spatial Randomness (CSR) approach, they express the probability $\mathcal{P}$ to find a site under a growing bubble of radius R_d as:

$$\mathcal{P} = 1 - e^{-N_b \pi R_d^2} \tag{5.40}$$

where $N_b = \dfrac{t_g}{t_w + t_g}N_{sit} = t_g f N_{sit}$ is the density of bubbles covering the heated surface.
The number of active sites is then computed as:

$$N_{sit,a} = \left(1 - \mathcal{P}\right)N_{sit} = \exp\left(-\frac{t_g}{t_w + t_g}N_{sit}\pi R_d^2\right)N_{sit} \tag{5.41}$$

This value is then reduced by Gilman to obtain the density of sites generating sliding bubbles $N^*_{sit,a}$ using a reduction factor accounting for sliding bubble coalescence (similar to Basu *et al.* in Eq. 5.26):

$$N^*_{sit,a} = R_f N_{sit,a} = \frac{s}{l_{sl,0} + s}N_{sit,a} \tag{5.42}$$

where $l_{sl,0}$ is the sliding length of a single bubble and $s = 1/\sqrt{N_{sit,a}}$.
The sliding quenching term is also computed in a way similar to Basu *et al.* as:

$$\phi_{q,sl} = \frac{2\lambda_L\left(T_w - T_L\right)}{\sqrt{\pi\eta_L t^*}}t^* f A_{sl}N^*_{sit,a} \tag{5.43}$$

$$A_{sl} = \overline{D}l_{sl} = \frac{D_d + D_{lo}}{2}\left(N_{merg}s + l_{D_N \to D_{lo}}\right) \tag{5.44}$$

Regarding the boiling heat flux, Gilman splits it in two contributions respectively associated with the inception of nucleation ($\phi_{e,in}$) and liquid microlayer evaporation ($\phi_{e,ML}$) :

$$\phi_e = \phi_{e,in} + \phi_{e,ML} \tag{5.45}$$

$$= \frac{4}{3}\pi R_d^3 \rho_V h_{LV} \frac{1}{t_w + t_g} N_{sit,a} + V_{ML}\rho_L h_{LV} \frac{1}{t_w + t_g} N_{sit,a} \tag{5.46}$$

$$V_{ML} = \frac{2}{3}\pi \left(\frac{R_d}{2}\right)^3 \delta_{max} \tag{5.47}$$

where $\delta_{max} = 2$ μm is the largest bubble microlayer thickness based on experiments from Gerardi [56].

Finally, the solid quenching term is written as:

$$\phi_{q,s} = \rho_w c_{p,w} V_q \Delta T_q \frac{1}{t_g + t_w} N_{sit,a} \tag{5.48}$$

$$V_q = \frac{2}{3}\pi r_w^2 \tag{5.49}$$

with subscript w denoting the wall properties, r_w the dry patch radius and $\Delta T_q = 2$ K the extra wall superheat as suggested by Gerardi *et al.* [57].

Required closure relationships : N_{sit}, t_w, t_g, D_d, D_{lo}, $l_{sl,0}$, $h_{c,L}$, $\overline{h_{c,L}}$.

5.5 KOMMAJOSYULA (2020)

The last HFP model we will look through in this Chapter was proposed by Kommajosyula [89] in the continuation of Gilman [58] work. In particular, he proposed:

- A finer modeling of the bubble microlayer evaporation ;
- Simpler empirical correlations for closure parameters such as bubble departure diameter and wait time ;
- A modification of the probabilistic approach for the static interaction between sites.

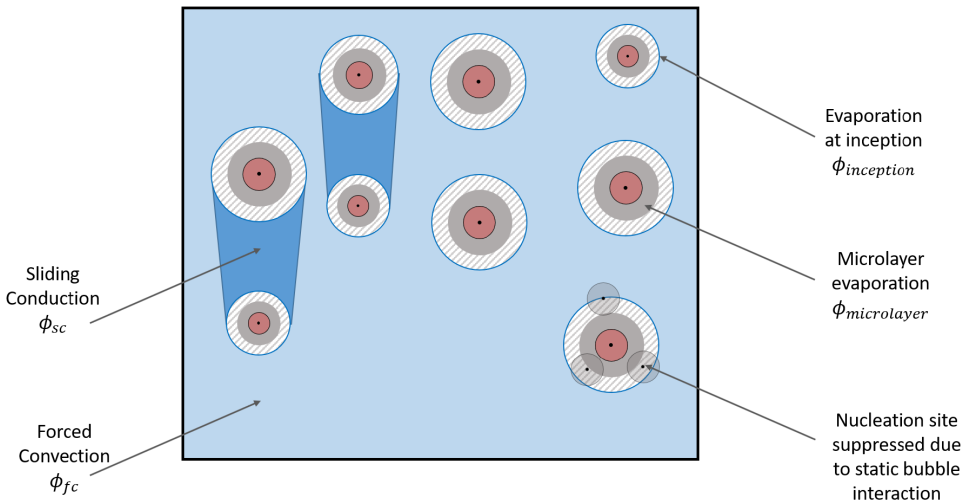

Figure 5.4: Heat Flux Partitioning considered by Kommajosyula [89].

The total heat flux is partitioned by Kommajosyula between four fluxes : the forced liquid convection $\phi_{c,L}$, the sliding conduction $\phi_{q,sl}$, the evaporation ϕ_e and a direct convective flux to the vapor ϕ_{vap}. Using the wall dry area S_{dry}, he writes:

$$\phi_w = \left(1 - S_{dry}\right)\left(\phi_{c,L} + \phi_{q,sl} + \phi_e\right) + S_{dry}\phi_{vap} \tag{5.50}$$

The liquid convective term is expressed as:

$$\phi_{c,L} = (1 - S_{sl})\, h_{c,L}\, (T_w - T_L) \tag{5.51}$$

where S_{sl} is the surface covered by sliding bubbles.

Assuming that the transient conduction during quenching operates during the time t^* (Eq. 5.30), Kommajoysula rewrites the total quenching flux using the forced-convection heat transfer coefficient as:

$$\phi_{q,sl} = 2h_{c,L} \underbrace{A_{sl} N_{sit,a} \frac{t^*}{t_g + t_w}}_{S_{sl}} (T_w - T_L) \tag{5.52}$$

$$A_{sl} = \frac{1}{\sqrt{N_{sit,a}}} \frac{D_d + D_{lo}}{2} \tag{5.53}$$

with $N_{sit,a}$ the active nucleation site density, D_d and D_{lo} respectively the bubble departure and lift-off diameters.

Note : At first glance, it seems surprising to see $h_{c,L}$ (convection coefficient) in the quenching term which is of transient conduction nature. This is due to the assumption that the quenching time is $t^* = \left(\frac{\lambda_L}{h_{c,L}}\right)^2 \frac{1}{\pi \eta_L}$ which once replaced in Eq. 5.43 under the square root at the denominator yields Eq. 5.53.

The total sliding area fraction S_{sl} is then expressed as:

$$S_{sl} = \min\left(1\ ;\ A_{sl} N_{sit,a} t^* f\right) \tag{5.54}$$

The evaporation heat flux is based on Gilman approach by splitting it between inception and microlayer evaporation:

$$\phi_e = \phi_{e,in} + \phi_{e,ML} \tag{5.55}$$

$$= \frac{4}{3}\pi \left(\frac{D_{in}}{2}\right)^3 \rho_V h_{LV} f N_{sit,a} + V_{ML} \rho_V h_{LV} f N_b \tag{5.56}$$

The microlayer terms are modeled based on the contact angle θ and the capillary number $\mathrm{Ca} = \frac{\mu_L U_b}{\sigma}$, where U_b is the bubble interface velocity, as:

$$D_{in} = D_d \max\left(1\ ;\ 0.1237 \mathrm{Ca}^{-0.373} \sin(\theta)\right) \tag{5.57}$$

$$V_{ML} = \delta_{ML} D_{ML}^2 \frac{\pi}{12} \left(2 - \left(\frac{D_{dry}}{D_{ML}}\right)^2 - \frac{D_{dry}}{D_{ML}}\right) \tag{5.58}$$

with $D_{ML} = D_{in}/2$ and $\frac{D_{dry}}{D_{ML}} = \max\left(1\ ;\ 0.1237 \mathrm{Ca}^{-0.373} \sin(\theta)\right)$.

The microlayer thickness δ_{ML} is expressed as:

$$\delta_{ML} = 4 \times 10^{-6} \sqrt{\frac{\mathrm{Ca}}{\mathrm{Ca}_0}} \tag{5.59}$$

with $\mathrm{Ca}_0 = 2.16 \times 10^{-4} \Delta T_w^{1.216}$.

The active nucleation site density $N_{sit,a}$ is computed based on the Complete Spatial Randomness approach proposed by Gilman. However, it is expressed using Lambert's W-function $\mathcal{W}$ as:

$$N_{sit,a} = \frac{\mathcal{W}\left(f t_g \pi \frac{D_d^2}{4} N_{sit}\right)}{f t_g \pi \frac{D_d^2}{4}} \tag{5.60}$$

with $\mathcal{W}$ being approximated to avoid an implicit solving of this equation.

Required closure relationships : N_{sit}, t_w, t_g, D_d, D_{lo}, $h_{c,L}$.

5.6 CONCLUSION

As we have seen, the HFP approach is widely studied since decades and is still an active field of work to hopefully reach an exhaustive and precise modeling of all the heat transfer phenomena that are at stake in wall boiling. While most models are similar to each other regarding terms such as single-phase convection or transient conduction heat transfer, they may differ in their methods to account for bubble sliding, microlayer evaporation or modeling of the bubble nucleation cycle.

Moreover, each of those approaches requires a certain number of closure laws to compute important physical parameters among which we can in particular cite:

- The nucleation site density N_{sit} ;
- The bubble nucleation period / frequency : $f = \dfrac{1}{t_g + t_w}$;
- The bubble departure and lift-off diameters D_d and D_{lo}.

In this global framework, we will propose the development of a new HFP model by first trying to have a close look at boiling bubble dynamics to propose an acceptable modeling of a bubble lifetime growing and sliding on the wall using most recent experimental and numerical results from the literature (Chapter 6). Then, we will tackle the problem of the closure laws aiming to compute important yet highly uncertain parameters (N_{sit}, t_w, etc.) before proposing a final formulation for the HFP that will be compared to experimental measurements (Chapter 7). In order to complete the description of the aforementioned models, we will highlight throughout the development when a given closure law is used in one of the presented models.

6

BOILING BUBBLE DYNAMICS

Contents

6.1 Introduction **67**
6.1.1 Experimental Insights 67
6.1.2 Existing Approaches 69
6.2 Bubble Force Balance in Vertical Flow Boiling **73**
6.2.1 Introduction 73
6.2.2 General Considerations 74
6.2.3 Buoyancy and Contact Pressure Forces 75
6.2.4 Capillary Force 75
6.2.5 Drag and Lift Forces 76
6.2.6 Inertia Force 81
6.2.7 Force Balance Summary 83
6.2.8 Liquid Velocity 84
6.3 Bubble Growth **86**
6.3.1 Introduction 86
6.3.2 Heat Diffusion in Uniformly Superheated Liquid 86
6.3.3 Microlayer Evaporation 87
6.3.4 Bubble Growth in Subcooled Flow Boiling 88
6.3.5 Analytic Approach of Bubble Growth in a Linear Thermal Boundary Layer . 90
6.3.6 Comparison with DNS Results 92
6.3.7 Comparison with Experimental Measurements 92
6.3.8 Conclusions on Bubble Growth Modeling 96
6.4 Departure by Sliding **96**
6.4.1 Non-Dimensional Analysis 96
6.4.2 Application to Experimental Data 99
6.4.3 Departure Diameter Prediction 101
6.4.4 Discussion and accounting for parameters uncertainties 103
6.5 Sliding phase **105**
6.5.1 Modeling 105
6.5.2 Low Pressure Sliding 105
6.5.3 High Pressure Sliding 105
6.5.4 Comparison of Forces in Sliding Stage 107
6.6 Bubble Lift-Off **109**
6.6.1 Introduction 109
6.6.2 Experimental Measurements of Lift-Off Diameter 111
6.6.3 Influence of the Flow Boiling Conditions 111
6.6.4 Predicting the Lift-Off with a Force Balance 113
6.6.5 A Simple Non-Dimensional Correlation 114
6.6.6 Conclusion on the Lift-Off 115
6.7 Conclusion **117**

6.1 INTRODUCTION

Dynamics of boiling bubbles is playing an important role in the Heat Flux Partitioning models. For instance, the evaporation heat flux ϕ_e is directly proportional to the bubble volume $V_b \propto R^3$ 5.16 while the quenching heat flux ϕ_q depends on the wall area visited by a bubble $A_{q,1b}$ (Eq. 5.43) which depends on the bubble sliding length l_{sl}, departure radius R_d and lift-off radius R_{lo}.

6.1.1 *Experimental Insights*

Consequently, many experimental investigations have been conducted to further understand the behavior of nucleated bubbles on a wall of a liquid flow. In the case of vertical flow boiling, a typical bubble life cycle can be described as follows:

- Beginning of nucleation, growth while attached to the nucleation site ;
- Detachment occurring when the bubble has a radius R_d, from which the bubble will start to slide and accelerate along the wall while continuing to grow ;
- Lift-off from the wall when the bubble reaches a radius R_{lo} after sliding over a length l_{sl}.

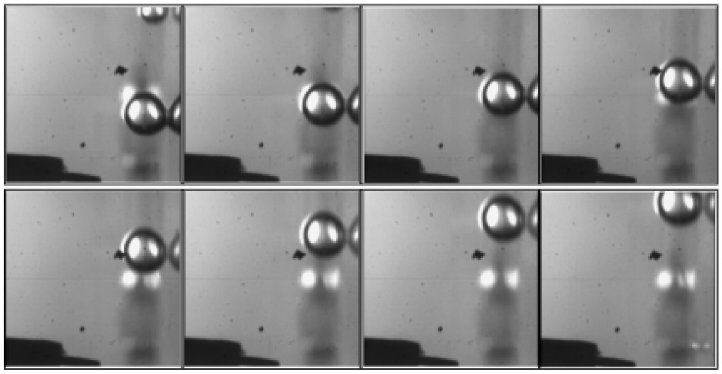

(a) Bubble sliding visualized and adapted from Maity [108] at atmospheric pressure.

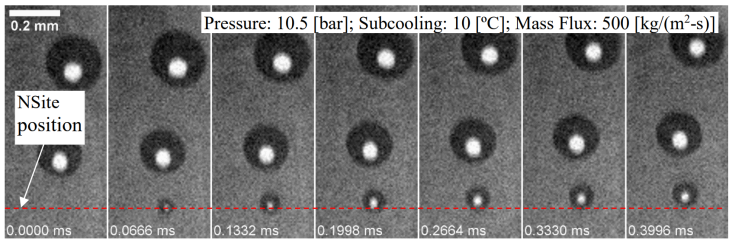

(b) Bubble sliding visualized and adapted from Kossolapov [90] at higher pressure.

Figure 6.1: Visualization of bubble sliding at various pressures.

This behavior has been supported by many experimental observations who clearly observed three stages (departure, sliding, lift-off) both at low pressure (Maity [108], Situ [148], Thorncroft [156], Prodanovic [131], Chen [22], Ren [138], etc.) and high pressure (March [110], Kossolapov [90]). Altogether, those works cover various flow conditions and operating fluids which demonstrate the dominance of this bubble behavior in vertical flow boiling. Examples from the literature of visualizations of bubble sliding at atmospheric and high pressure are reproduced on Figure 6.1.

The bubble sliding process has also been thermally studied through experiments to quantify its impact on the wall heat transfer. Estrada-Perez *et al.* [43] observed the significant thermal impact of sliding bubbles footprints. Kossolapov [90] also investigated the sliding of boiling bubbles and measured the magnitude of the transient heat transfer induced by the disruption of the liquid thermal boundary layer in the bubble's wake. Typical experimental observations from those works are reproduced on Figure 6.2

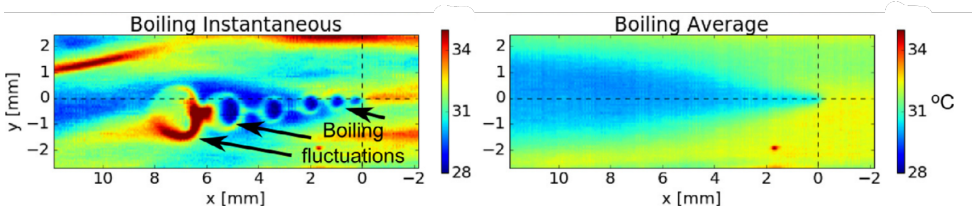

(a) Instantaneous and time-averaged wall temperature in boiling regime visualized and adapted from Estrada-Pérez *et al.* [43].

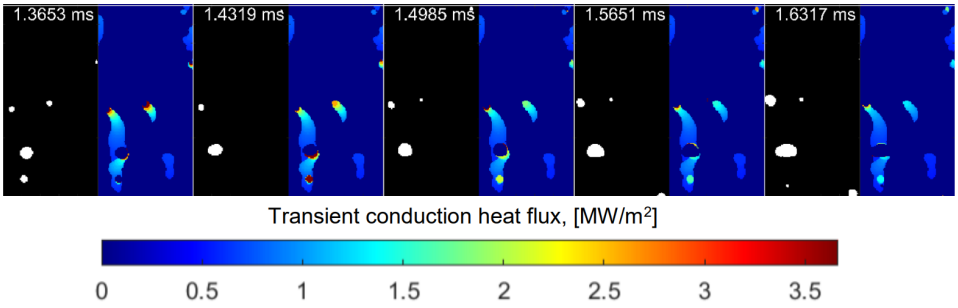

(b) Transient conduction induced by sliding bubbles visualized and adapted from Kossolapov [90].

Figure 6.2: Visualization of bubble sliding thermal impact.

Those experimental observations highlight the significant magnitude of the transient heat transfer triggered by bubble movement on the wall that can represent up to 40% of the total wall heat flux [90]. All the aforementioned observations are summed-up on Figure 6.3.

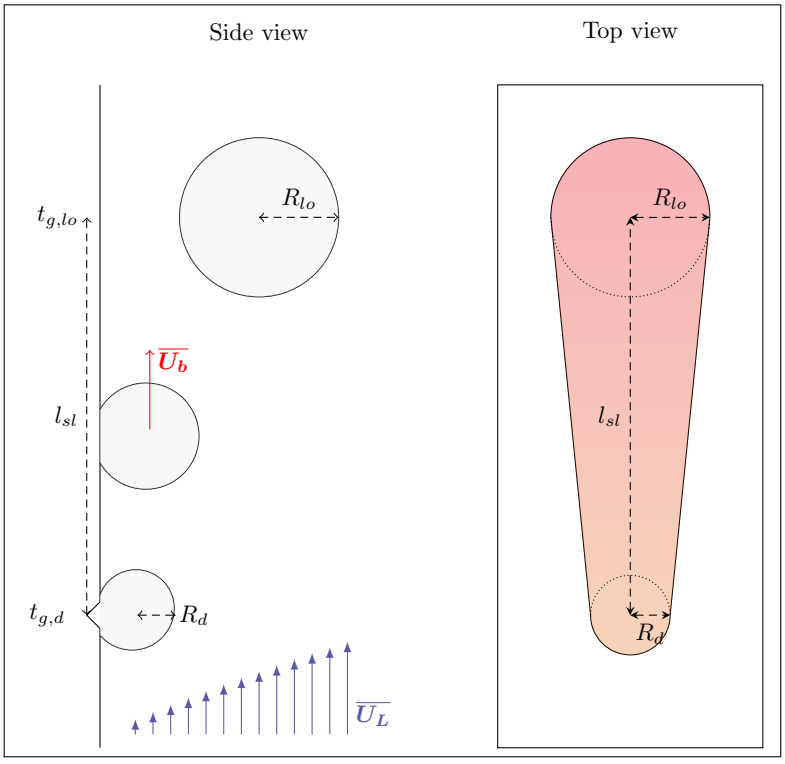

Figure 6.3: Sketch of a typical bubble lifetime in vertical flow boiling. Left depicts a typical side view of the heater with identification of departure, sliding and lift-off. Right depicts a top view of the heater, exhibiting the area that will undergo transient heat transfer.

Predicting the HFP in vertical flow boiling thus requires a description of single bubble dynamics that includes accurate estimations of bubble departure and lift-off radii R_d and R_{lo} as well as bubble sliding velocity $\overline{U_b}$ to predict the sliding length l_{sl}.

6.1.2 *Existing Approaches*

6.1.2.1 *Departure / Lift-Off Diameters*

Historically, first approaches to estimate the bubble diameter consisted of experimental-based correlations for pool boiling of horizontal surfaces through photographic studies. In those cases, departure from the nucleation site coincides with the bubble lift-off. Among the mainly used in HFP models and CFD, we can mention the law of Tolubinsky & Kostanchuk (1970)[158] that estimates the lift-off diameter D_{lo} based on the local liquid subcooling $\Delta T_L = T_{sat} - T_L$ with T_L the liquid temperature:

$$D_{lo} = D_0 \; e^{-\Delta T_L / 45}, \; D_0 = 15\text{mm} \tag{6.1}$$

On the other hand, authors such as Cole & Rohsenow (1968) (mentioned in [87]) proposed relationships including the influence of pressure through the the capillary length $L_c = \sqrt{\frac{\sigma}{g(\rho_L - \rho_V)}}$:

$$\begin{aligned} D_{lo} =& C L_c \left(\frac{\rho_L c_{p,L} T_{sat}}{\rho_V h_{LV}} \right)^{5/4} \\ C =& 1.5 \times 10^{-4} \text{ for water and } 4.65 \times 10^{-4} \text{ otherwise.} \end{aligned} \tag{6.2}$$

This equations provides a good trend for the evolution of bubble departure diameter with pressure for pool boiling as shown by Kossolapov [90].

More recently, the developments around HFP models has lead many researchers to propose dedicated correlations for bubble departure or lift-off diameter. For instance, Zhou *et al.* (2021) [179] proposed simple correlations for the departure and lift-off diameter in horizontal flow boiling at low pressure based on their experiments:

$$\frac{D_d}{L_o} = 10^{2.4086} \left(\frac{\rho_V}{\rho_L} \right)^{-0.6613} \text{Ja}_w^{*\,0.1557} \text{Ja}_L^{*\,-0.01592} \text{Re}_{L_o}^{-0.6647} \text{Pr}_L^{-1.8477} \sin(\theta_s)^{0.4} \tag{6.3}$$

$$\frac{D_{lo}}{L_c} = 10^{-1.1990} \left(\frac{\rho_V}{\rho_L} \right)^{-0.9785} \text{Ja}_w^{*\,0.1435} \text{Ja}_L^{*\,-0.0119} \text{Re}_{L_c}^{-0.5129} \text{Pr}_L^{-1.8784} \tag{6.4}$$

with the Reynolds numbers based on $L_o = \frac{\rho_L \nu_L^2}{\sigma}$ and L_c the capillary length, and $\text{Ja}^* = \frac{c_{p,L} \Delta T}{h_{LV}}$ (ΔT either the wall superheat or liquid subcooling) reduced Jakob numbers that do not include the density ratio.

In the case of vertical flow boiling, Ünal (1976)[186] derived a correlation based on a semi-analytic approach of the heat transfer mechanisms around a bubble to estimate its maximum diameter, including simultaneous influences of pressure, heater material, liquid velocity and subcooling:

$$\begin{aligned} D_{lo} =& 2.42 \times 10^{-5} P^{0.709} \frac{a}{\sqrt{b\varphi}} \\ a =& \frac{\Delta T_w \lambda_w}{2 \rho_V h_{LV} \sqrt{\pi \eta_w}} \\ b =& \frac{\Delta T_L}{2 \left(1 - \rho_V / \rho_L\right)} \\ \varphi =& \max \left(1 \; ; \; \left(\frac{U_L}{U_0} \right)^{0.47} \right), \; U_0 = 0.61 \text{ m/s} \end{aligned} \tag{6.5}$$

Ünal validated his law against several measurements from the literature covering pressures from 1 to 177 bars, liquid velocities from 0.08 to 9.15 m/s, subcooling from 3 to 86K and heat fluxes from 0.47 to 10.64 MW/m^2.

Note : The law of Ünal is used in the HFP model of Kurul & Podowski. It is also implemented in NEPTUNE_CFD and includes a correction of Borée *et al.* (Eq. 2.39) to avoid divergence in bubble diameter when reaching saturated conditions.

In the framework of their HFP model development, Basu *et al.* fitted expressions for D_d and D_{lo} based on their own measurements in vertical flow boiling at atmospheric pressure:

$$\frac{D_d}{L_c} = 1.3 \sin(\theta_s)^{0.4} \left[0.13\ e^{-1.75\times10^{-4}\mathrm{Re}_{L,D_h}} + 0.005\right] \mathrm{Ja}_w^{0.45} e^{-0.0065\mathrm{Ja}_L} \tag{6.6}$$

$$\frac{D_{lo}}{L_c} = 1.3 \sin(\theta_s)^{0.4} \left[0.2\ e^{-1.28\times10^{-4}\mathrm{Re}_{L,D_h}} + 0.005\right] \mathrm{Ja}_w^{0.45} e^{-0.0065\mathrm{Ja}_L} \tag{6.7}$$

They were validated for $14 \leq \mathrm{Ja}_w \leq 56$, $1 \leq \mathrm{Ja}_L \leq 138$, $0 \leq \mathrm{Re}_{L,D_h} \leq 7980$ and $30° \leq \theta_s \leq 90°$.

Note : Basu *et al.* use these own-developed laws in their HFP formulation to estimate bubble diameters.

Similarly, Kommajosyula[89] gathered several bubble departure and lift-off diameter measurements from the literature (both in vertical and horizontal boiling) and proposed the following reduced correlation:

$$D_d = 18.9 \times 10^{-6} \left(\frac{\rho_L - \rho_V}{\rho_V}\right)^{0.27} \mathrm{Ja}_w^{0.75} (1 + \mathrm{Ja}_L)^{-0.3} {U_{L,bulk}}^{-0.26} \tag{6.8}$$

$$D_{lo} = 1.2 D_d \tag{6.9}$$

Note : This formulation is used in Kommajosyula's HFP model. Having a proportionality between D_d and D_{lo} allows the comparison with a database gathering both departure and lift-off diameter measurements.

Although this law presents coherent trends with flow conditions, we can question the raw presence of $U_{L,bulk}$ because:

- The relationship is not dimensionless and the constant 18.9×10^{-6} must be in $\mathrm{m}^{1.26}.\mathrm{s}^{-0.26}$;
- The negative exponent will yield diverging values when reaching pool boiling conditions, which is physically inconsistent.

In order to show the spread of predicted values by the presented correlations, we plot them for water at low and high pressure on Figure 6.4.

We observe that altogether, the predicted values for both for departure and lift-off diameters spread at least over a decade, with a global decrease if pressure is increased. Correlations of Basu, Kommajosyula and Zhou seem to present pressure dependency similar to that of Cole & Rohsenow. Basu correlation however present no difference between departure and lift-off diameter at high pressure, which is inconsistent with experimental observations [90]. On the other hand, Ünal correlation appears to weakly change with pressure, its value being more controlled by the wall superheat by covering the largest range of values. Tolubinsky correlation depending solely on the liquid subcooling obviously present no variation.

6.1.2.2 *Sliding Length and Velocity*

Regarding bubble sliding phase, one of the most used correlations to predict bubble diameter evolution has been developed by Maity [108]. Based on atmospheric pressure visualization of boiling single bubbles in water, it predicts the resulting sliding diameter D_{sl} provided a sliding time t_{sl} and an arbitrary initial diameter D_{in} (not obligatorily the departure diameter) through:

$$\frac{\left(D_{sl}^2 - D_{in}^2\right)}{t_{sl}\eta_L \mathrm{Ja}_w} = \frac{1}{15\left(0.015 + 0.023\ {\mathrm{Re}_b}^{0.5}\right)\left(0.04 + 0.023\ \mathrm{Ja}_L^{0.5}\right)} \tag{6.10}$$

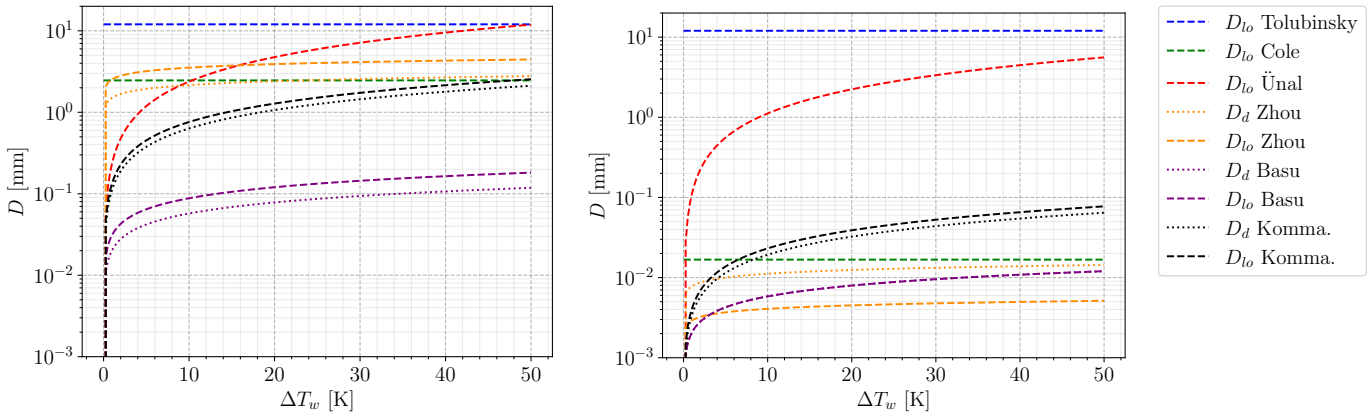

(a) $P = 1$ bar

(b) $P = 100$ bar (Basu diameters overlap each other)

Figure 6.4: Values predicted by the diameter correlations for water. $\Delta T_L = 10°C$, $G_L = 1000$ kg/m^2/s, $\theta = 40°$ and $D_h = 10$ mm.

where $\mathrm{Re}_b = \dfrac{U_L D_{in}}{\nu_L}$

Using Maity measurements of bubble sliding velocity, Basu *et al.* proposed an estimation of the sliding distance for a single bubble $l_{sl,0}$:

$$l_{sl,0} = \int_0^{t_{sl}} U_b \, \mathrm{d}t = \int_0^{t_{sl}} C_U \sqrt{t} \, \mathrm{d}t = \frac{2}{3} C_U {t_{sl}}^{3/2} \tag{6.11}$$

$$C_U = 3.2[\mathrm{s}^{-1/2}] \, U_L + 1 \tag{6.12}$$

where C_U must be in m/s$^{-3/2}$ and the multiplicative factor 3.2 is in s$^{-1/2}$.

Remark : Basu *et al.* use this correlation along with Eq. 6.10 in their model to estimate the bubble sliding and growth. The expression of C_U is yet questionable since its unit being m/s$^{-3/2}$ does not have much physical meaning here.

The estimation of the bubble sliding velocity through an explicit correlation is difficult since it varies over the bubble lifetime. Therefore, some authors simply suppose that $U_b = U_L$ such as Gilman & Baglietto who also use Eq. 6.10 for the sliding growth.

Other assumptions regarding the sliding length relies on the value of the bubble-generating site density on the heater $N_{sit,a}$. Supposing that bubbles usually lift-off after sliding a distance between two active sites gives:

$$l_{sl} = \frac{1}{\sqrt{N_{sit,a}}} \tag{6.13}$$

Note : This modeling choice is made by Kommajosyula.

6.1.2.3 *Conclusion on Correlations*

Albeit proposing coherent trend with the flow boiling conditions along with good estimations of the desired parameters on given experimental data sets, explicit correlations inherently include a limited range of application. Moreover, the constant increase of the number of works proposing data-fitted laws makes the selection of a proper relationship a complicated matter due to their potential lack of generality.

To try to overcome this drawback and come up with more generalized models, researchers have explored an alternative approach by developing mechanistic models based on a force-balance to precisely depict the external efforts experienced by the growing bubble. The goal is to compute the sum of the forces

applied to the bubble over its growing time and to detect departure and lift-off events using associated criteria such as a change in the force balance sign. This will be the subject of the next section.

As a summary, we gather the presented correlations on Table 6.1.

Bubble Departure Diameter

Author (Year)	Correlation
Basu *et al.* (2005)	$\frac{D_d}{L_c} = 1.3 \sin(\theta_s)^{0.4} \left[0.13\ e^{-1.75\times10^{-4}\mathrm{Re}_{L,D_h}} + 0.005\right] \mathrm{Ja}_w^{0.45} e^{-0.0065\ \mathrm{Ja}_L}$ $L_c = \sqrt{\frac{\sigma}{g(\rho_L - \rho_V)}}$
Kommajosyula (2020)	$D_d = 18.9\times10^{-6} \left(\frac{\rho_L - \rho_V}{\rho_V}\right)^{0.27} \mathrm{Ja}_w^{0.75} (1+\mathrm{Ja}_L)^{-0.3}\, {U_{L,bulk}}^{-0.26}$
Zhou (2021)	$\frac{D_d}{L_o} = 10^{2.4086} \left(\frac{\rho_V}{\rho_L}\right)^{-0.6613} {\mathrm{Ja}_w^*}^{0.1557} {\mathrm{Ja}_L^*}^{-0.01592} \mathrm{Re}_{L_o}^{-0.6647} \mathrm{Pr}_L^{-1.8477} \sin(\theta_s)^{0.4}$ $L_o = \frac{\rho_L \nu_L^2}{\sigma}$

Bubble Lift-Off Diameter

Author (Year)	Correlation
Tolubinsky & Kostanchuk (1970)	$D_{lo} = D_0\ e^{-\Delta T_L/45},\ D_0 = 15\mathrm{mm}$
Cole & Rohsenow (1968)	$D_{lo} = C L_c \left(\frac{\rho_L c_{p,L} T_{sat}}{\rho_V h_{LV}}\right)^{5/4}$ $C = 1.5\times10^{-4}$ (water) or 4.65×10^{-4} (other), $L_c = \sqrt{\frac{\sigma}{g(\rho_L - \rho_V)}}$
Ünal (1976)	$D_{lo} = 2.42\times10^{-5} P^{0.709} \frac{a}{\sqrt{b\varphi}},\ a = \frac{\Delta T_w \lambda_w}{2\rho_V h_{LV}\sqrt{\pi\eta_w}}$ $b = \frac{\Delta T_L}{2(1-\rho_V/\rho_L)},\ \varphi = \max\left(1\ ;\ \left(\frac{U_L}{U_0}\right)^{0.47}\right),\ U_0 = 0.61\ \mathrm{m/s}$
Basu *et al.* (2005)	$\frac{D_{lo}}{L_c} = 1.3 \sin(\theta_s)^{0.4} \left[0.2\ e^{-1.28\times10^{-4}\mathrm{Re}_{L,D_h}} + 0.005\right] \mathrm{Ja}_w^{0.45} e^{-0.0065\mathrm{Ja}_L}$ $L_c = \sqrt{\frac{\sigma}{g(\rho_L - \rho_V)}}$
Kommajosyula (2020)	$D_{lo} = 1.2\ D_d$
Zhou (2021)	$\frac{D_{lo}}{L_c} = 10^{-1.1990} \left(\frac{\rho_V}{\rho_L}\right)^{-0.9785} {\mathrm{Ja}_w^*}^{0.1435} {\mathrm{Ja}_L^*}^{-0.0119} \mathrm{Re}_{L_c}^{-0.5129} \mathrm{Pr}_L^{-1.8784}$ $L_c = \sqrt{\frac{\sigma}{g(\rho_L - \rho_V)}}$

Sliding Length, Diameter and Velocity

Author (Year)	Correlation
Maity (2000)	$\frac{\left(D_{sl}^2 - D_{in}^2\right)}{t_{sl}\eta_L \mathrm{Ja}_w} = \left[15\left(0.015 + 0.023\ {\mathrm{Re}_b}^{0.5}\right)\left(0.04 + 0.023\ \mathrm{Ja}_L^{0.5}\right)\right]^{-1}$ $\mathrm{Re}_b = \frac{U_L D_b}{\nu_L}$
Basu *et al.* (2005)	$l_{sl,0} = \frac{2}{3} C_U {t_{sl}}^{3/2},\ C_U = 3.2\ U_L + 1$
Bubble Density Average Distance	$l_{sl} = \frac{1}{\sqrt{N_{bub}}}$

Table 6.1: Summary of the presented correlations

6.2 BUBBLE FORCE BALANCE IN VERTICAL FLOW BOILING

6.2.1 *Introduction*

The derivation of the force balance over a growing bubble on a wall in a liquid flow is a very complicated problem that many researchers have tried to tackle over the past decades. Many theoretical and numerical approaches have been conducted to estimate the forces at stake in bubble dynamics and sometimes compared to experimental visualization of bubbles in movement.

Among the first propositions of the whole force-balance closure, the work of Klausner *et al.* in 1993 [84] is probably among the most referred to. They proposed a tentatively complete force-balance for a growing bubble in a boiling flow and supposed that departure from the nucleation site is reached when the force balance becomes positive either in the direction of the flow or perpendicular to the wall. They validated their approach against measurements for horizontal flow boiling of refrigerant R113.

In the same framework, many subsequent works were published such as:

- Van Helden *et al.* [164] (1995) who assessed forces coefficients using injected air bubbles in a vertical flow ;
- Thorncroft *et al.* [156, 157] (1998, 2001) who conducted experiments on horizontal and vertical flow boiling of R113 while proposing more general formulations of the force balance that were used to predict bubble diameter measurements ;
- Duhar & Colin [42] (2006) who validated a force balance on bubbles created by air injection in a shear flow. They extended their work with boiling N-pentane experiments and studied the growth and detachment of single bubbles [40] ;
- Van Der Geld (2009) [55] used potential flow theory to analytically derive the force balance for deforming bubbles near a plane ;
- Sugrue *et al.* (2014) [152] conducted measurements on boiling bubble for water at atmospheric pressure and various surface orientations. Their measurements were then used to validate a force-balance approach predicting bubble departure by sliding [151] ;
- Mazzocco *et al.* (2018) [111] gathered several measurements of bubble departure and lift-off diameters and proposed a reassessed force-balance approach including new drag coefficient and growth law to achieve predictions with a reasonable accuracy over the database ;
- Ren *et al.* (2020) [138] measured bubble departure diameter for vertical flow boiling of water up to 5 bars which they used to validate a force-balance model.

While not exhaustive, this list aims to show that force-balance modeling has become an increasingly interesting approach for authors. It is though not exempted of limitations because each force requires a proper modeling which needs sometimes to go through empirical choices as we will later discuss. This drawback is particularly noted by Bucci *et al.* [18] who points out that traditional force balances are not equal to zero when the bubble is immobile. On the other hand, they show that this is not due to the absence of unknown forces in the balance but rather associated to the computation of well-known forces such as capillary forces. Moreover, Duhar & Colin [42] managed to reach a zero total balance for their air-injected bubbles, and emphasized the interest of force modeling to deeper understand the physical phenomena behind bubble dynamics. The difficulty to close the balance of the forces in the case of a boiling bubble is due to the approximated expression of the forces which expressions are expected to be more complicated in the case of a phase change compared to air injection.

Each of the previously listed models proposed different upgrades and modifications to the force balance over the bubble. Unfortunately, they were all validated using low pressure experiments due to the lack of pressurized measurements in the literature. In addition, the mentioned common use of empirical parameters makes it difficult to reach a general validation of those models as we will see.

> **Note :** The HFP model of Gilman & Baglietto [59] is based on such a force balance for departure and lift-off prediction.

In this section, we aim to propose an update of the bubble force balance for vertical flow boiling with a reduced empiricism and to cover the whole bubble lifetime (departure, sliding, lift-off) while achieving a larger generality by including pressurized measurements up to 40 bar conducted by Kossolapov [90].

6.2.2 *General Considerations*

When trying to derive the force balance over a bubble, the first step consists of splitting the whole effort experienced by the bubble between different contributions depending on their nature. In our case, we focus on a bubble growing on a vertical wall and facing an upward flow as depicted in Figure 6.5.

The static forces are :

- The buoyancy force $\overline{F_B}$, including Archimedes force and the weight of the bubble ;
- The capillary or surface tension force $\overline{F_C}$;
- The contact pressure force $\overline{F_{CP}}$.

The hydrodynamic forces are :

- The drag and lift forces $\overline{F_D}$ and $\overline{F_L}$;
- The inertia force $\overline{F_I}$, including added-mass and Tchen force.

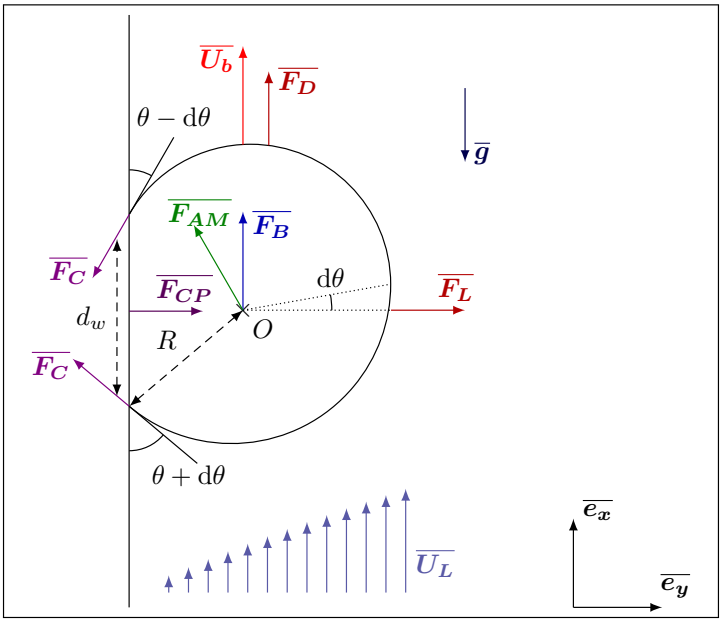

Figure 6.5: Sketch of the forces applied to the bubble facing an upward flow $\overline{U_L}$ and sliding at velocity $\overline{U_b}$

Regarding the bubble shape, we consider a quasi-spherical bubble of radius R with a circular contact area with the wall of radius $r_w = d_w/2$.

Remark : This assumption is mainly supported for high pressure boiling where bubble elongation and deformation is not observed [90]. At lower pressure, the bubble shape can somewhat deviate from a spherical shape especially before lift-off. It seems however reasonable to consider quasi-spherical bubbles at early growth stages [108].

The bubble has a static contact angle θ and is tilted under the influence of the flow by an inclination angle $\mathrm{d}\theta$ (half the total angle hysteresis). The resulting downstream and upstream contact angles are therefore $\theta_d = \theta - \mathrm{d}\theta$ and $\theta_u = \theta + \mathrm{d}\theta$. If the bubble has a shape close to a truncated sphere, we can approximate the bubble foot radius as:

$$r_w \approx R \sin\left(\frac{\theta_u + \theta_d}{2}\right) = R \sin(\theta) \tag{6.14}$$

Some authors rather take $r_w \approx \frac{1}{2}R\ (\sin(\theta_u)+\sin(\theta_d)) = R\sin(\theta)\cos(\mathrm{d}\theta)$, however this expression tends to zero when reaching $\mathrm{d}\theta \to 90°$ which is undesirable regarding the expression of forces such as Contact Pressure and Surface Tension. We suppose $V_b \approx \frac{4}{3}\pi R^3$ for the bubble volume.

6.2.3 *Buoyancy and Contact Pressure Forces*

Following the work of Thorncroft *et al.* [157] and Duhar & Colin [42], the global force balance for a bubble growing on a wall can be written as:

$$\underbrace{V_b\rho_V\overline{g}}_{\text{Bubble weight}} + \overline{F_C} - \underbrace{\int_{S_b}(P_L-\rho_L g x)\,\overline{n}\,\mathrm{d}S}_{\text{Outer liquid pressure}} - \underbrace{\int_{S_w}P_V\overline{n}\,\mathrm{d}S}_{\text{Inner vapor pressure}} + \underbrace{\int_{S_b}\overline{\overline{\tau_L}}\cdot\overline{n}}_{\text{Viscous efforts}} = \overline{0} \tag{6.15}$$

where $\overline{n}$ is the local normal unity vector, S_b is the bubble surface facing the liquid, S_w the wall-contact area and $\overline{\overline{\tau_L}}$ the deviatoric stress tensor associated to viscous effects.

Re-writing the two pressure integrals versus the liquid pressure at the wall P_0 yields:

$$\begin{aligned}
-\int_{S_b}(P_L-\rho_L g x)\,\overline{n}\,\mathrm{d}S - \int_{S_w}P_V\overline{n}\,\mathrm{d}S =& -\int_{S_b+S_w}(P_0-\rho_L g x)\,\overline{n}\,\mathrm{d}S + \int_{S_w}(P_0-\rho_L g x - P_V)\,\overline{n}\,\mathrm{d}S \\
&-\int_{S_b}(P_L-P_0)\,\overline{n}\,\mathrm{d}S \\
=& \int_{S_b+S_w}\rho_L g x\overline{n}\,\mathrm{d}S + \int_{S_w}(P_0-P_V)\,\overline{n}\,\mathrm{d}S \\
&\underbrace{-\int_{S_b}(P_L-P_0)\,\overline{n}\,\mathrm{d}S}_{=\overline{0}\text{ for a vertical wall}}
\end{aligned} \tag{6.16}$$

Summing the first term on the RHS of Eq. 6.16 with the bubble weight yields the buoyancy force:

$$\overline{F_B} = -V_b\rho_V g\overline{e_x} + \iint_{S_w+S_b}\rho_L g x\overline{n}\,\mathrm{d}S = -V_b\rho_V g\overline{e_x} + \iiint_{V_b}\overline{\nabla}(\rho_L g x)\,\mathrm{d}V \tag{6.17}$$

$$= V_b(\rho_L-\rho_V)\,g\overline{e_x} \tag{6.18}$$

The second term of Eq. 6.16 is the so-called "contact pressure force" and can be expressed versus the difference of liquid and vapor pressure at the bubble top P_L (equals to P_0 for a vertical wall):

$$\int_{S_w}(P_0-P_V)\,\overline{n}\mathrm{d}S = \int_{S_w}(P_L-P_V)\,\overline{n}\mathrm{d}S \tag{6.19}$$

$$= (P_L-P_V)\,\pi r_w^2\overline{e_y} \tag{6.20}$$

Using Laplace's pressure jump at the interface $\Delta P = 2\sigma/R_c$ yields:

$$\overline{F_{CP}} \approx \frac{2\sigma}{R_c}\pi r_w^2\ \overline{e_y} \approx \pi R\sigma\ 2\sin(\theta)^2\ \overline{e_y} \tag{6.21}$$

Here, R_c is the curvature radius of the bubble which is often assumed to be equal to $5R$ [84, 111, 151] without other explanation than avoiding an overestimation of the contact pressure force. To avoid this arbitrary choice, following the hypothesis of a nearly spherical bubble shape gives $R_c = R$.

6.2.4 *Capillary Force*

The capillary force acts at the triple contact line at the bubble's foot and is an important adhesive force maintaining the bubble attached to the wall. Its derivation can be done by integration of the effort exerted over the triple contact line. Noting Φ the polar angle around the bubble foot, we have :

$$\overline{F_C} = 2\int_0^{\pi} \sigma r_w \overline{\tau}\left(\Phi\right) \mathrm{d}\Phi \tag{6.22}$$

where $\overline{\tau}$ is the unit vector tangent to the interface and perpendicular to the contact line.
To compute the resulting components parallel and tangent to the wall, Klausner *et al.* [84] account for a contact angle difference between the upstream (receding) contact angle θ_u and downstream (advancing) contact angle θ_d. If the local contact angle is noted γ, then:

$$\overline{\tau}\left(\Phi\right) = \cos\left(\gamma\right)\cos\left(\Phi\right)\overline{e_x} + \sin\left(\gamma\right)\overline{e_y} \tag{6.23}$$

Then assuming to represent the evolution of the local contact angle γ from θ_u to θ_d using a polynomial expression of degree 3:

$$\gamma\left(\Phi\right) = \theta_d + \left(\theta_u - \theta_d\right)\left[3\left(\frac{\Phi}{\pi}\right)^2 - 2\left(\frac{\Phi}{\pi}\right)^3\right],\ 0 \leq \Phi \leq \pi \tag{6.24}$$

which verifies symmetry conditions:

$$\gamma'\left(0\right) = \theta_d,\ \gamma\left(\pi\right) = \theta_u,\ \gamma'\left(0\right) = \gamma'\left(\pi\right) = 0 \tag{6.25}$$

To obtain an analytic expression, Klausner *et al.* also consider a first order linear interpolation:

$$\gamma\left(\Phi\right) \approx \theta_d + \left(\theta_u - \theta_d\right)\frac{\Phi}{\pi} \tag{6.26}$$

This yields:

$$\overline{F_C} = -2r_w\sigma\frac{\pi\left(\theta_u - \theta_d\right)}{\pi^2 - \left(\theta_u - \theta_d\right)^2}\left(\sin\left(\theta_u\right) + \sin\left(\theta_d\right)\right)\overline{e_x} - 2r_w\sigma\frac{\pi}{\theta_u - \theta_d}\left(\cos\left(\theta_d\right) - \cos\left(\theta_u\right)\right)\overline{e_y} \tag{6.27}$$

By comparing the analytic expression of Eq. 6.27 with the values obtained by numerical integration of Eq.6.24, Klausner *et al.* introduce a correction factor of 1.25 over the x component, finally giving :

$$\overline{F_C} = -2.5r_w\sigma\frac{\pi\left(\theta_u - \theta_d\right)}{\pi^2 - \left(\theta_u - \theta_d\right)^2}\left(\sin\left(\theta_u\right) + \sin\left(\theta_d\right)\right)\overline{e_x} - 2r_w\sigma\frac{\pi}{\theta_u - \theta_d}\left(\cos\left(\theta_d\right) - \cos\left(\theta_u\right)\right)\overline{e_y} \tag{6.28}$$

$$= -\pi R\sigma\underbrace{\left[2.5\ \frac{r_w}{R}\frac{\mathrm{d}\theta}{\left(\frac{\pi}{2}\right)^2 - \mathrm{d}\theta^2}\sin\left(\theta\right)\cos\left(\mathrm{d}\theta\right)\right]}_{f_{C,x}}\overline{e_x} - \pi R\sigma\underbrace{\left[2\ \frac{r_w}{R}\sin\left(\theta\right)\frac{\sin\left(\mathrm{d}\theta\right)}{\mathrm{d}\theta}\right]}_{f_{C,y}}\overline{e_y} \tag{6.29}$$

Remark : We can see that $f_{C,x} \to 0$ and $f_{C,y} \to 2\frac{r_w}{R}\sin\left(\theta\right)$ when $\mathrm{d}\theta \to 0$. In that case, $\overline{F_C} = -\overline{F_{CP}}$.

6.2.5 *Drag and Lift Forces*

The external liquid flow over the bubble induces the well-known drag and lift forces, acting respectively in the flow direction and perpendicular to the flow. They are usually expressed using associated coefficients C_D and C_L defined by:

$$\overline{F_D} = \frac{1}{2}C_D\rho_L S_p\left|\left|\overline{U_L} - \overline{U_b}\right|\right|\left(\overline{U_L} - \overline{U_b}\right) \tag{6.30}$$

$$\overline{F_L} = \frac{1}{2}C_L\rho_L S_p\left|\left|\overline{U_L} - \overline{U_b}\right|\right|^2\ \overline{e_y} \tag{6.31}$$

with $S_p = \pi R^2$ the projected area of the bubble in the direction of the flow.

6.2.5.1 *Drag Coefficient*

Derivations of analytic expressions for the drag coefficient in an infinite fluid medium exist for more than a century, starting with Hadamard-Rybzinski (1911) [70]:

$$C_D = \frac{16}{\mathrm{Re}_b}, \text{ if } \mathrm{Re}_b < 1 \tag{6.32}$$

where $\mathrm{Re}_b = \frac{|U_{rel}|D_B}{\nu_L}$ is the bubble Reynolds number and $U_{rel} = U_L - U_b$ the relative velocity between the bubble and the surrounding fluid.
For $\mathrm{Re}_b \gg 1$, Levich (1962) [102] found for a potential flow:

$$C_D = \frac{48}{\mathrm{Re}_b} \tag{6.33}$$

For intermediate values of Re_b, traditional approaches rely on expressions of the drag force for a bubble in an infinite medium based on numerical correlations as proposed by Mei & Klausner [114], used in many different mechanistic approaches [22, 138, 151, 157, 175]:

$$C_{D,U} = \frac{16}{\mathrm{Re}_b}\left[1 + \left(\frac{8}{\mathrm{Re}_b} + \frac{1}{2}\left(1 + \frac{3.315}{\sqrt{\mathrm{Re}_b}}\right)\right)^{-1}\right] \tag{6.34}$$

Results from DNS conducted by Legendre *et al.* [99] proposed expressions of the drag and lift forces for a hemispherical bubble on a wall facing a viscous shear flow. Earlier, Legendre & Magnaudet [99] analytically derived coefficients to transpose drag and lift expressions for a particle to the case of a bubble. This was applied by Mazzocco *et al.* [111] to the Drag for a solid particle near a wall in a shear flow proposed by Zeng *et al.* [176].

In this work, we propose to rely on the recent work of Shi *et al.* [147] who conducted DNS of a shear flow over a spherical bubble of constant radius close to a wall for bubble Reynolds number between 10^{-1} and 10^3 and non-dimensional shear rates between -0.5 and 0.5. A sketch of the situation simulated by Shi *et al.* is depicted on Figure 6.6.

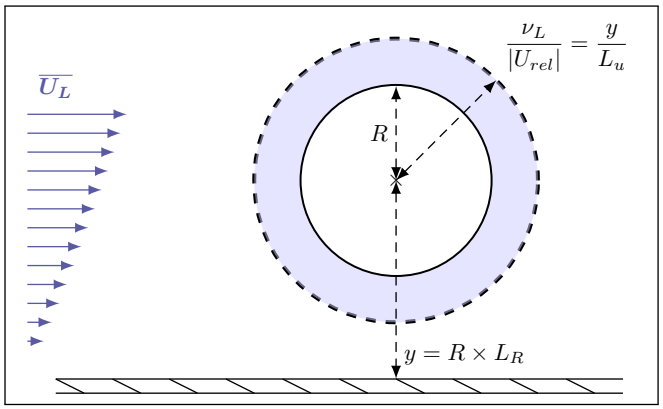

Figure 6.6: Physical situation considered by Shi *et al.* [147].

They computed the resulting drag and lift coefficients for each simulations and proposed correlations fitting their numerical results. The total Drag coefficient is expressed as a correction of the Drag coefficient for a bubble in an unbounded uniform flow $C_{D,U}$. The total drag is given by:

$$C_D = (1 + \Delta C_D)\, C_{D,U} \tag{6.35}$$

where ΔC_D accounts for both the effect of the shear flow and the wall vicinity.

To cover the whole range of bubble Reynolds numbers, correlations at low and high Re_b are smoothly connected using an exponential term.

$$\Delta C_D = \Delta C_{D,\mathrm{Re}_b = O(1)} + \left(1 - e^{-0.07\mathrm{Re}_b}\right) \Delta C_{D,\mathrm{Re}_b \gg 1} \tag{6.36}$$

Each of those corrections is computed depending on Re_b, the non-dimensional shear rate $\mathrm{Sr} = \dfrac{2\gamma R}{|U_{rel}|}$ where $\gamma = \frac{\partial U_{L,x}}{\partial y}$, the non dimensional wall distance $L_R = \dfrac{y}{R}$ ($L_R = 1$ being a spherical bubble laying on a wall) and non-dimensional viscous (or Stokes) length $L_u = \dfrac{y}{\nu_L / |U_{rel}|}$.

$$\Delta C_{D,\mathrm{Re}_b=O(1)} = \frac{1 + \tanh\left(0.012\mathrm{Re}_b^{0.8}\right) + \tanh\left(0.07\mathrm{Re}_b^{0.8}\right)^2}{1 + 0.16L_u\left(L_u + 4\right)} \times \left[\left(\frac{3}{8}L_R^{-1} + \frac{3}{64}L_R^{-4}\right)\left(1 - \frac{3}{8}L_R^{-1} - \frac{3}{64}L_R^{-4}\right)^{-1} - \frac{1}{16}\left(L_R^{-2} + \frac{3}{8}L_R^{-3}\right)\mathrm{Sr}\right] \tag{6.37}$$

$$\Delta C_{D,\mathrm{Re}_b \gg 1} = 0.47L_R^{-4} + 0.0055L_R^{-6}\mathrm{Re}_b^{3/4} + 0.002\,|\mathrm{Sr}|^{1.9}\,\mathrm{Re}_b + 0.05L_R^{-7/2}\mathrm{Sr}\mathrm{Re}_b^{1/3} \tag{6.38}$$

Figure 6.7 shows the evolution of the drag correction ΔC_D against the bubble Reynolds number for different dimensionless distances to the wall L_R and two values of Sr. We can see that as the distance between the wall and the bubble increases the drag correction logically approaches zero and that increasing the shear rate Sr increases ΔC_D for higher values of Re_b.

Shi *et al.* [147] conducted DNS for wall distances down to $L_R = 1.5$. However, Scheiff *et al.* [144] compared the values obtained for $L_R = 1$ with measured drag coefficients of bubbles sliding on a wall and observed a good agreement, which legitimates the use of this new drag correlation by extending its application to the case of a bubble laying on a wall and using the uniform drag coefficient of Eq. 6.34.

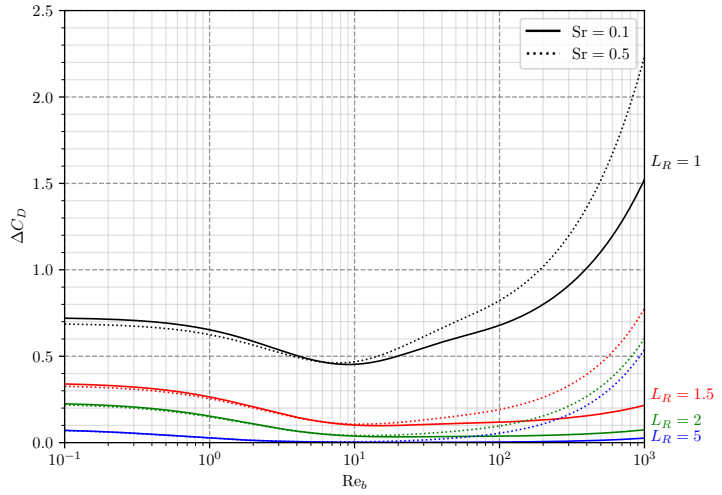

Figure 6.7: Drag correction from Shi *et al.* [147].

Remark : In PWR conditions, a static bubble of radius 0.01 mm on a wall with a bulk liquid velocity of 5 m/s leads to a non-dimensional shear rate $\mathrm{Sr} \approx 0.7$ with $\mathrm{Re}_b \approx 500$. In this case, the drag correction can reach 180% compared to the unbounded uniform flow formulation.

This also yields a bubble Weber number $\mathrm{We} \approx 0.08$ and a Capillary number $\mathrm{Ca} \approx 0.0036$ which further supports the assumption of spherical bubble shape.

6.2.5.2 *Lift Coefficient*

In 1987, Auton *et al.* [4] analytically derived the lift force for an inviscid fluid in unstationnary motion in a weak velocity gradient and found $C_L = 0.5$, with the lift force defined as:

$$\overline{F_L} = -\rho_L C_L V_b \left(\overline{U_L} - \overline{U_b}\right) \wedge \overline{\omega} \tag{6.39}$$

where $\overline{\omega}$ is the flow vorticity.

This result was enriched by Legendre & Magnaudet (1998) [99] who used numerical results to propose a dependency of C_L on the bubble Reynolds number for a sphere in an infinite medium facing a weakly sheared flows as:

$$C_L = \left(C_{L,\mathrm{Re}_b\sim 1}{}^2 + C_{L,\mathrm{Re}_b\gg 1}{}^2\right)^{1/2} \tag{6.40}$$

$$= \left(\left[\frac{6}{\pi^2} \frac{2.255\left(\mathrm{Re}_b\omega^*\right)^{-1/2}}{\left(1+0.2\frac{\mathrm{Re}_b}{\omega^*}\right)^{3/2}} \right]^2 + \left[\frac{1}{2}\frac{1+16\ \mathrm{Re}_b{}^{-1}}{1+29\ \mathrm{Re}_b{}^{-1}} \right]^2 \right)^{1/2} \tag{6.41}$$

where $\omega^* = \dfrac{2R\,|\overline{\omega}|}{|U_{rel}|}$ is the non-dimensional vorticity of the flow, equal to Sr here for the linear shear flow case.

Earlier, Mei & Klausner (1994) [113] derived the lift force induced by the shear for a spherical bubble in an unbounded flow for low Reynolds numbers, based on the expression of Saffmann [143]. By interpolating this result with the solution of Auton [4], they obtained a formulation for a large range of Re_b :

$$C_L = 2.74\sqrt{\mathrm{Sr}} \times \left[\mathrm{Re}_b^{-2} + \left(0.24\sqrt{\mathrm{Sr}}\right)^4 \right]^{1/4} \tag{6.42}$$

This expression is actually used in many mechanistic force balance [22, 84, 138, 151].

In his force-balance approach, Mazzocco *et al.* [111] used a constant lift coefficient by using the upper bound for the lift of a solid particle touching a wall in a Stokes flow, multiplied by $\dfrac{4}{9}$ as suggested by Legendre & Magnaudet [99] to transpose this value to the bubble case. This resulted in:

$$C_L = 2.61 \tag{6.43}$$

In accordance with the computation of the drag coefficient, our model will rely on the expression of the lift coefficient proposed by Shi *et al.* [147]. Their formulation includes extra parameters compared to the drag coefficient :

- The non-dimensional Saffman length $L_\omega = \dfrac{y}{\sqrt{\nu_L/\omega}}$;
- The Stokes (or Oseen) length to Saffman length ratio $\varepsilon = \dfrac{\nu_L/\,|U_{rel}|}{\sqrt{\nu_L/\omega}}$, which quantifies the origin of inertial effects being either shear ($\varepsilon > 1$) or the relative slip of the bubble ($\varepsilon < 1$).

The resulting formulation of C_L corresponds to the superposition of two contributions respectively associated to the uniform flow and the shear rate, both coupled with the wall presence.

$$C_L^W = C_{Lu}^W + C_{L\omega}^W \tag{6.44}$$

The lift associated to the uniform flow near a wall is computed as follows:

$$\begin{aligned} C_{Lu}^W = {} & e^{-0.22\ \varepsilon^{0.8} L_\omega^{2.5}} \frac{\left[1+\tanh\left(0.012\ \mathrm{Re_b}^{0.8}\right)+\tanh\left(0.07\ \mathrm{Re_b}^{0.8}\right)\right]^2}{1+0.13\ L_u\left(L_u+0.53\right)} \\ & \times \left(\frac{L_R}{3}\right)^{-2.0\ \tanh(0.01\mathrm{Re}_b)} C_{Lu}^{\text{W-in}} \\ & + \left(1-e^{-0.22\ \mathrm{Re_b}^{0.6}}\right)\left[C_{Lu,\mathrm{Re}_b\to\infty}^W + 15\ \tanh\left(0.01\ \mathrm{Re}_b\right)\mathrm{Re}_b{}^{-1} L_R^{-4}\right] \end{aligned} \tag{6.45}$$

Where:

$$C_{Lu}^{\text{W-in}} = \frac{1}{2}\left(1+\frac{1}{8}L_R^{-1}-\frac{33}{64}L_R^{-2}\right) \tag{6.46}$$

$$C_{Lu,\mathrm{Re}_b\to\infty}^W = -\frac{3}{8}L_R^{-4}\left[1+\frac{1}{8}L_R^{-3}+\frac{1}{6}L_R^{-5}\right] + O\left(L_R^{-10}\right) \tag{6.47}$$

The lift associated to the vorticity near a wall is computed as follows:

$$C_{L\omega}^{W} = \left[1 - \exp\left(-\frac{11}{96}\pi^2 \frac{L_\omega}{J_L(\varepsilon)}\left(1 + \frac{9}{8}L_R^{-1} - \frac{1271}{3520}L_R^{-2}\right)\right)\right] C_{L\omega,\mathrm{Re}_b\ll 1}^{U} \tag{6.48}$$

$$+ \left(1 - e^{-0.3\ \mathrm{Re}_b}\right)\left[1 + 0.23\ L_R^{-7/2}\left(1 + 13\ \mathrm{Re}_b{}^{-1/2}\right)\right] C_{L\omega,\mathrm{Re}_b\gg 1}^{U} \tag{6.49}$$

Where:

$$J_L(\varepsilon) = 2.254\left(1 + 0.2\varepsilon^{-2}\right)^{-3/2} \tag{6.50}$$

$$C_{L\omega,\mathrm{Re}_b\ll 1}^{U} = \frac{8}{\pi^2}\frac{\mathrm{Sr}}{|\mathrm{Sr}|}\varepsilon J_L(\varepsilon) \tag{6.51}$$

$$C_{L\omega,\mathrm{Re}_b\gg 1}^{U} = \frac{2}{3}\mathrm{Sr}\left(1 - 0.07\,|\mathrm{Sr}|\right)\frac{1 + 16\mathrm{Re}_b^{-1}}{1 + 29\mathrm{Re}_b^{-1}} \tag{6.52}$$

On Figure 6.8, we plot the values of C_L obtained by the formulation of Shi *et al.* different values of the non-dimensional wall distance L_R (extending down to $L_R = 1$) and non-dimensional shear rate Sr.

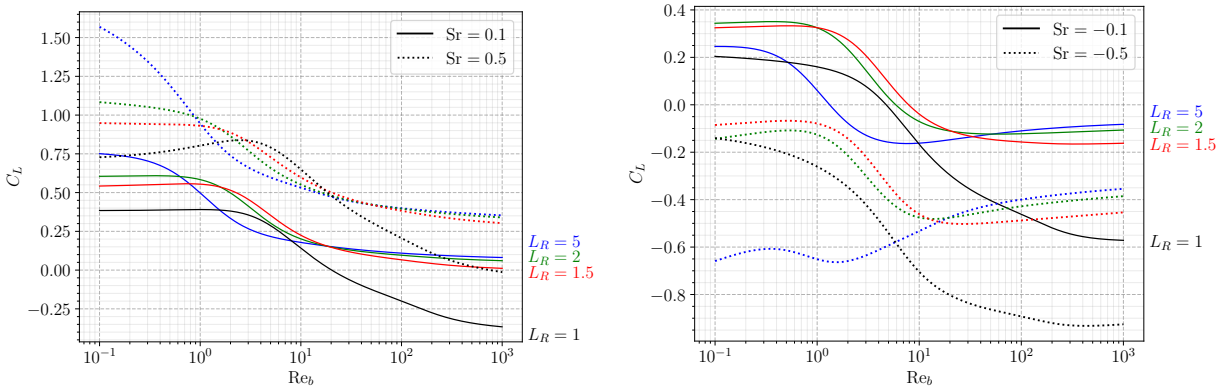

(a) Positive values of Sr

(b) Negative values of Sr

Figure 6.8: C_L computed using Shi *et al.* correlation.

We can see that the magnitude of the lift coefficient globally increases with the wall distance when $\mathrm{Sr} > 0$ and that negative lift values are easily reached when $\mathrm{Sr} < 0$. This means that correlations for unbounded medium may overestimate the lift experienced by the bubble compared to the situation with a wall.
The extension to the case $L_R = 1$ may be more questionable compared to the drag since the bubble touching the wall will stop any flow in between, leading to inertial and shear regimes that would be significantly different due to the redirection of the liquid at the bubble's foot towards the bulk. In particular, we can see that the values reached for $L_R = 1$ on Figure 6.8 are not following the general trend of simulated L_R :

- Negative values of C_L are reached with positive Sr at high Re_b while getting close to the wall seemed to tend to a value of $C_L \geq 0$ at high Re_b ;
- Magnitude of C_L with negative Sr are not coherent with the observed trend down to $L_R = 1.5$.

This observation suggest that we should include the effect of the wall using the lift of Shi *et al.* by limiting its use to $L_R = 1.5$ contrary to the drag which extension to $L_R = 1.0$ was coherent and validated.

Remark : In PWR conditions, taking $\mathrm{Sr} \approx 0.7$ with $\mathrm{Re}_b \approx 500$ for the static bubble on a wall leads to $C_L \approx 0.45$ both with Mei & Klausner (Eq. 6.42) and Shi *et al.* (Eq. 6.44). For a bubble that would slide at 90% of the local liquid velocity, this gives $\mathrm{Sr} \approx 7$ and $\mathrm{Re}_b \approx 50$ yielding $C_{L,Mei} \approx 4$ and $C_{L,Shi} \approx 2.8$.

6.2.6 *Inertia Force*

The Inertia force originates from various effects (bubble growth, free stream and bubble acceleration, etc.) and includes both added mass and Tchen forces and is expressed as presented in Magnaudet & Eames (2000) [107]:

$$\overline{F_I} = \underbrace{\rho_L V_b \left(\frac{\partial \overline{U_L}}{\partial t} + \overline{\overline{\nabla}} \left(\overline{U_L} \right) \cdot \overline{U_L} \right)}_{\text{Liquid inertia or Tchen force}} + \underbrace{\frac{\mathrm{d}}{\mathrm{d}t} \left(\rho_L C_{AM} V_b \left(\overline{U_L} - \overline{U_b} \right) \right)}_{\text{Added Mass force } \overline{F_{AM}}} \tag{6.53}$$

Since we consider a steady and quasi-parallel liquid flow, we respectively have:

$$\frac{\partial \overline{U_L}}{\partial t} = 0 \text{ and } \overline{\overline{\nabla}} \left(\overline{U_L} \right) \cdot \overline{U_L} = 0 \tag{6.54}$$

Thus only remains the added mass force to be expressed in the considered force balance. In the next subsections, we detail former approaches to tackle the added mass derivation and propose a more rigorous one to re-evaluate the added mass coefficients.

6.2.6.1 *Former Approaches*

In previous mechanistic models, the derivation of the added mass force was conducted with different approaches. In particular, some authors chose to rely on the Rayleigh-Plesset Equation (RPE) for a growing hemispherical bubble in a quiescent flow to obtain the reaction force from the liquid, oriented perpendicularly to the wall:

$$\overline{F_{AM,RPE}} = -\rho_L \pi R^2 \left[R\ddot{R} + \frac{3}{2}\dot{R}^2 \right] \overline{e_y} \tag{6.55}$$

Then, assuming a bubble inclination angle θ_i, this force was projected along the x axis to obtain an Added Mass force parallel to the wall that hinders departure. The inclination angle value is often empirical and used for data fitting [30, 111, 138, 175].

$$\overline{F_{AM,RPE}} = -\rho_L \pi R^2 \left[R\ddot{R} + \frac{3}{2}\dot{R}^2 \right] \left(\sin\left(\theta_i\right) \overline{e_x} + \cos\left(\theta_i\right) \overline{e_y} \right) \tag{6.56}$$

This approach is questionable on different aspects. First, the RPE assumes a moving boundary in a quiescent unbounded liquid, which is physically far from the real situation of a bubble growing on a wall in a boiling flow. Moreover, the subsequent projection along the different directions regarding an unknown angle is hardly reasonable if θ_i is chosen arbitrarily. Values of θ_i selected by different authors are mentioned in Table 6.2.

On the other hand, some authors [63, 84, 157] considered two distinct contributions:

- Hemispherical bubble growth in a stagnant liquid, leading to Eq. 6.56 including the inclination angle θ_i ;
- Spherical bubble growth in a uniform unbounded and inviscid liquid flow, which yields a detaching Added Mass term due to the interaction of bubble growth with the external flow:

$$\overline{F_{AM,U}} = \frac{3}{2}\rho_L V_b \frac{\dot{R}}{R} U_L \overline{e_x} \tag{6.57}$$

This last term is usually called a "bulk growth force". By including the effect of the liquid flow, this approach can be considered as closer to the reality. However, it relies on two separate derivations associated to different physical considerations.

6.2.6.2 *Proposed Approach*

To tackle the added mass derivation in a proper way, we propose to follow the approach of Lamb [94] (also presented by Milne Thomson [116] or Van Winjgaarden [166]). By solving the potential flow around a bubble and its image, we can obtain the total liquid kinetic energy E_L that corresponds to a situation where a bubble is at a given distance from a wall (represented by the line normal to the line of centers of the bubbles).

Then we can use Lagrange equation to compute the resulting forces along a given coordinate q:

$$F_{AM,q} = -\frac{\partial}{\partial t}\left(\frac{\partial E_L}{\partial \dot{q}}\right) + \frac{\partial E_L}{\partial q} \tag{6.58}$$

This method was also used by Duhar [42] who developed an asymptotic expression of E_L to compute the added mass coefficient when a growing bubble approaches the wall. Here, we express the liquid kinetic energy by relying on the work of Van Der Geld [55] who derived E_L in the case of a full or truncated spherical bubble laying on a wall and facing a uniform flow parallel to the wall of velocity U_L (Eq. 6.59). If the bubble slides at a velocity $U_{b,x} = \dot{x}$, it sees a liquid velocity $U_{rel} = U_L - \dot{x}$.

$$E_L = \frac{\rho_L V_b}{2}\left(\alpha \dot{y}^2 + \mathrm{tr}\,(\beta)\,\dot{R}^2 + \psi \dot{R}\dot{y} + \alpha_2\,(U_L - \dot{x})^2\right) \tag{6.59}$$

where (x, y) are the coordinates of the bubble's center and α, $\mathrm{tr}\,(\beta)$, ψ, α_2 are polynomials of $R/y = 1/L_R$ derived by Van Der Geld for $1 < R/y < 2$ *i. e.* $0.5 < L_R < 1$, corresponding to contact angles $0° < \theta < 60°$.

For each polynomial expression (α is used as an example), we note n its degree and write:

$$\alpha = \sum_{k=0}^{n} \alpha_k \left(\frac{R}{y}\right)^k \text{ and } \tilde{\alpha} = \sum_{k=0}^{n} k\ \alpha_k \left(\frac{R}{y}\right)^k \tag{6.60}$$

This allows to express the following derivatives:

$$\frac{\partial \alpha}{\partial y} = -\frac{1}{y}\tilde{\alpha} \text{ and } \frac{\partial \alpha}{\partial t} = \left(\frac{\dot{R}}{R} - \frac{\dot{y}}{y}\right)\tilde{\alpha} \tag{6.61}$$

Noticing that the derivatives of the polynomials along x will be 0 and injecting E_L in Eq. 6.58 allows to express the added mass force in x and y directions. If we express it using geometrical ratios $\frac{R}{y} = \frac{1}{F_1}$, $\frac{\dot{y}}{\dot{R}} = F_2$ and $\frac{\ddot{y}}{\ddot{R}} = F_3$, we can obtain:

$$F_{AM,x} = \rho_L V_b \left[\left(3\alpha_2 + \left(1 - \frac{F_2}{F_1}\right)\tilde{\alpha_2}\right)\frac{\dot{R}}{R}U_{rel} - \alpha_2 \frac{\partial U_b}{\partial t}\right] \tag{6.62}$$

$$\begin{aligned} F_{AM,y} = -\rho_L V_b \Bigg[&\left(3F_2\alpha + \frac{3}{2}\psi + \left(1 - \frac{F_2}{F_1}\right)F_2\tilde{\alpha} + \left(1 - \frac{F_2}{F_1}\right)\frac{\tilde{\psi}}{2} + \frac{F_2}{F_1}\frac{\tilde{\alpha}}{2} + \frac{1}{F_1}\frac{\mathrm{tr}\,\tilde{(\beta)}}{2} + \frac{F_2}{F_1}\frac{\tilde{\psi}}{2}\right)\frac{\dot{R}^2}{R} \\ &+ \left(F_3\alpha + \frac{\psi}{2}\right)\ddot{R} + \frac{1}{F_1}\frac{\tilde{\alpha_2}}{2}\frac{U_{rel}^2}{R}\Bigg] \end{aligned} \tag{6.63}$$

In the case of a truncated sphere, $F_1 = \frac{y}{R} = \cos(\theta) = L_R$. If we suppose that the bubble keeps a nearly constant contact angle during its lifetime, we can further write $F_1 = F_2 = F_3 = \cos(\theta) = L_R$, which simplifies the forces in:

$$F_{AM,x} = \rho_L V_b \left[3\alpha_2 \frac{\dot{R}}{R}U_{rel} - \underbrace{\alpha_2}_{C_{AM,x}} \frac{\partial U_b}{\partial t}\right] \tag{6.64}$$

$$F_{AM,y} = \rho_L V_b \left[-\left(\underbrace{3\left(L_R\alpha + \frac{\psi}{2}\right)}_{C_{AM,y1}} + \underbrace{\frac{\tilde{\alpha}}{2} + \frac{1}{L_R}\frac{\mathrm{tr}\,\tilde{(\beta)}}{2} + \frac{\tilde{\psi}}{2}}_{C_{AM,y2}}\right)\frac{\dot{R}^2}{R}\right. \tag{6.65}$$

$$\left. - \underbrace{\left(L_R\alpha + \frac{\psi}{2}\right)}_{C_{AM,y1}}\ddot{R} + \underbrace{\frac{-1}{L_R}\frac{\tilde{\alpha_2}}{2}}_{C_{AM,y3}}\frac{U_{rel}^2}{R}\right] \tag{6.66}$$

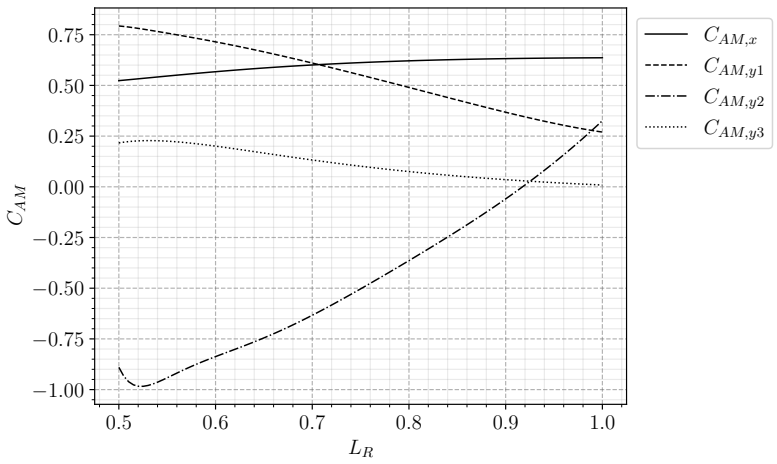

Figure 6.9: Values of the computed added mass coefficients in Eq. 6.64 and 6.66.

On Figure 6.9, we plot the values of the added mass coefficients against the values of L_R.
For the case of a spherical bubble laying on a wall ($L_R = 1$), we finally have:

$$F_{AM,x} = \rho_L V_b \left[3C_{AM,x} \frac{\dot{R}}{R} U_{rel} - C_{AM,x} \frac{\partial U_{b,x}}{\partial t} \right] \tag{6.67}$$

with $C_{AM,x} \approx 0.636$.

$$F_{AM,y} = \rho_L V_b \left[-\left(3C_{AM,y1} + C_{AM,y2}\right) \frac{\dot{R}^2}{R} - C_{AM,y1} \ddot{R} + C_{AM,y3} \frac{U_{rel}^2}{R} \right] \tag{6.68}$$

with $C_{AM,y1} \approx 0.27$, $C_{AM,y2} \approx 0.326$ and $C_{AM,y3} \approx 8.77 \times 10^{-3}$.

Parallel to the wall, the coupled term $\frac{\dot{R}}{R} U_{rel}$ in Eq. 6.67 promotes detachment and sliding of the bubble if $U_{rel} > 0$ *e. g.* if the bubble is attached to its nucleation site. This contradicts the aforementioned approach where solely projecting the RPE on both axes lead to an Added-Mass term related to bubble growth that only hinders the departure by sliding. Moreover, Eq. 6.68 exhibits a term induced by the relative velocity that acts as a lift force, which seems to rarely appear in other approaches.

Remark : The derived values of the added mass coefficients are only valid for $0.5 < L_R < 1$ as previously mentioned. When the bubble leaves the wall, added mass calculations of Duhar [41] would be more appropriate.

Those theoretical results highlight the importance of conducting a rigorous approach when possible to deriving those transient aspects of the force balance. Otherwise, some terms may be missing and lead to contradictory physical conclusions.
In the spirit of avoiding to introduce extra empirical terms, we keep the Added Mass force as presented in Eq. 6.67 and 6.68 and consider no projection along the inclination angle.

6.2.7 *Force Balance Summary*

Writing the bubble velocity $\overline{U_b} = U_{b,x}\overline{e_x} + U_{b,y}\overline{e_y}$ and applying Newton's second law, we have the total force balance over the bubble in both directions:

$$\begin{aligned} \rho_V \frac{\partial V_b U_{b,x}}{\partial t} =& -\pi R \sigma f_{C,x}(\theta, \mathrm{d}\theta) + V_b (\rho_L - \rho_V) g + \frac{1}{2} C_D \rho_L \pi R^2 \left| U_L - U_{b,x} \right| \left(U_L - U_{b,x} \right) \\ &+ \rho_L V_b \left[3C_{AM,x} \frac{\dot{R}}{R} \left(U_L - U_{b,x} \right) - C_{AM,x} \frac{\partial U_{b,x}}{\partial t} \right] \end{aligned} \tag{6.69}$$

where the relative velocity controlling the drag force is $\overline{U_L} - \overline{U_b} = U_L\overline{e_x} - U_{b,x}\overline{e_x} - U_{b,y}\overline{e_y} \approx \left(U_L - U_{b,x}\right)\overline{e_x}$ since $U_{b,y} \sim \dot{R} \ll U_L$.

$$\rho_V \frac{\partial V_b U_{b,y}}{\partial t} = -\pi R\sigma f_{C,y}\left(\theta, \mathrm{d}\theta\right) + 2\pi R\sigma \sin\left(\theta\right)^2 + \frac{1}{2}C_L\rho_L\pi R^2\left(\overline{U_L} - \overline{U_b}\right)^2 + \rho_L V_b\left[-\left(3C_{AM,y1} + C_{AM,y2}\right)\frac{\dot{R}^2}{R} - C_{AM,y1}\ddot{R} + C_{AM,y3}\frac{\left(U_L - U_{b,x}\right)^2}{R}\right] \tag{6.70}$$

Those force balances will respectively be used later to study the departure by sliding (along x) and the lift-off from the wall (along y).

On Table 6.2, we sum up some of the mentioned mechanistic approaches and their models along with the proposed force balance.

		Klausner (1993) [84]	Thorncroft (2001) [157]	Sugrue (2016) [151]
Forces	$\overline{F_B}$	$\frac{4}{3}\pi R^3\left(\rho_L - \rho_V\right)\overline{g}$	$\frac{4}{3}\pi R^3\left(\rho_L - \rho_V\right)\overline{g}$	$\frac{4}{3}\pi R^3\left(\rho_L - \rho_V\right)\overline{g}$
	$\overline{F_C}$	Eq. 6.29, $r_w = 0.045$ mm	Eq. 6.29, $r_w = R\sin\left(\theta_d\right)$	Eq. 6.29, $r_w = 0.025R$
	$\overline{F_{CP}}$	Eq. 6.21, $R_c = 5R$	Neglected	Eq. 6.21, $R_c = 5R$
	$\overline{F_D}$	$C_D = \frac{16}{\mathrm{Re}_b}\left[1 + \frac{3}{2}\left(\left(\frac{12}{\mathrm{Re}_b}\right)^n + 0.796^n\right)^{1/n}\right]$, $n = 0.65$	$C_D = \frac{16}{\mathrm{Re}_b}\left[1 + \left(\frac{8}{\mathrm{Re}_b} + \frac{1}{2}\left(1 + \frac{3.315}{\sqrt{\mathrm{Re}_b}}\right)\right)^{-1}\right]$	$C_D = \frac{16}{\mathrm{Re}_b}\left[1 + \frac{3}{2}\left(\left(\frac{12}{\mathrm{Re}_b}\right)^n + 0.796^n\right)^{1/n}\right]$, $n = 0.65$
	$\overline{F_L}$	$C_L = 2.74\sqrt{\mathrm{Sr}} \times \left[\mathrm{Re}_b^{-2} + \left(0.24\sqrt{\mathrm{Sr}}\right)^4\right]^{\frac{1}{4}}$	$C_L = 0.71\sqrt{\mathrm{Sr}} \times \left[\left(\frac{1.15\mathrm{J}(\varepsilon)}{\sqrt{\mathrm{Re}_b}}\right)^2 + \left(\frac{3\sqrt{2\mathrm{Sr}}}{8}\right)^2\right]^{\frac{1}{2}}$	$C_L = 2.74\sqrt{\mathrm{Sr}} \times \left[\mathrm{Re}_b^{-2} + \left(0.24\sqrt{\mathrm{Sr}}\right)^4\right]^{\frac{1}{4}}$
	$\overline{F_{AM}}$	$\frac{3}{2}\rho_L V_b \frac{\dot{R}}{R} U_L\overline{e_x} - \rho_L\pi R^2\left(\frac{3}{2}\dot{R}^2 + R\ddot{R}\right) \times \left(\cos\left(\theta_i\right)\overline{e_y} + \sin\left(\theta_i\right)\overline{e_x}\right)$, $\theta_i = 10°$	$2\pi\rho_L R^2\dot{R}U_L\overline{e_x} - \rho_L\pi R^2\left(\frac{3}{2}\dot{R}^2 + R\ddot{R}\right) \times \left(\cos\left(\theta_i\right)\overline{e_y} + \sin\left(\theta_i\right)\overline{e_x}\right)$, $\theta_i = 45°$	$-\rho_L\pi R^2\left(\frac{3}{2}\dot{R}^2 + R\ddot{R}\right) \times \left(\cos\left(\theta_i\right)\overline{e_y} + \sin\left(\theta_i\right)\overline{e_x}\right)$, $\theta_i = 10°$

		Mazzocco (2018) [111]	Ren (2020) [138]	Present model
Forces	$\overline{F_B}$	$\frac{4}{3}\pi R^3\left(\rho_L - \rho_V\right)\overline{g}$	$\frac{4}{3}\pi R^3\left(\rho_L - \rho_V\right)\overline{g}$	$\frac{4}{3}\pi R^3\left(\rho_L - \rho_V\right)\overline{g}$
	$\overline{F_C}$	Eq. 6.29, $r_w = R/15$	Eq. 6.29, $r_w = 0.2R$	Eq. 6.29, $r_w = R\sin\left(\theta\right)$
	$\overline{F_{CP}}$	Eq. 6.21, $R_c = 5R$	Eq. 6.21, $R_c = 5R$	Eq. 6.21, $R_c = R$
	$\overline{F_D}$	$C_D = 1.13\frac{24}{\mathrm{Re}_b}\left(1 + 0.104\mathrm{Re}_b^{0.753}\right)$	$C_D = \frac{16}{\mathrm{Re}_b}\left[1 + \frac{3}{2}\left(\left(\frac{12}{\mathrm{Re}_b}\right)^n + 0.796^n\right)^{1/n}\right]$, $n = 0.65$	$C_D = C_{D,U}\left(1 + \Delta C_D\right)$ $C_{D,U}$ by Eq. 6.34, ΔC_D by Eq. 6.36
	$\overline{F_L}$	$C_L = 2.61$	$C_L = 2.74\sqrt{\mathrm{Sr}} \times \left[\mathrm{Re}_b^{-2} + \left(0.24\sqrt{\mathrm{Sr}}\right)^4\right]^{\frac{1}{4}}$	C_L by Shi *et al.* [147]
	$\overline{F_{AM}}$	$-\frac{1}{4}\pi\rho_L K^4\left(\cos\left(\theta_i\right)\overline{e_y} + \sin\left(\theta_i\right)\overline{e_x}\right)$, $\sin\left(\theta_i\right) = 0.2$, $\cos\left(\theta_i\right) = 1$	$-\rho_L\pi R^2\left(\frac{3}{2}\dot{R}^2 + R\ddot{R}\right) \times \left(\cos\left(\theta_i\right)\overline{e_y} + \sin\left(\theta_i\right)\overline{e_x}\right)$, $\theta_i = 15°$	$\frac{F_{AM,x}}{\rho_L V_b} = C_{AM,x}\left[3\frac{\dot{R}}{R}U_{rel} - \frac{\partial U_b}{\partial t}\right]$, $C_{AM,x} = 0.636$, $F_{AM,y}$ by Eq. 6.68.

Table 6.2: Summary of different force-balance mechanistic approaches.

6.2.8 *Liquid Velocity*

In the expression of the forces, the liquid velocity is taken at a distance to the wall equal to the height of the bubble center of gravity. To compute the liquid velocity and shear rate at bubble center height, we use the wall law of Reichardt [137], which describes the velocity profile from the viscous sublayer to the logarithmic region in a single-phase flow.

$$\begin{aligned} U_L^+ =& \frac{1}{\kappa}\ln\left(1+\kappa y^+\right) + c\left(1 - e^{-y^+/\chi} + \frac{y^+}{\chi}e^{-y^+/3}\right) \\ U_L =& U_L^+ U_\tau \end{aligned} \tag{6.71}$$

with $\kappa = 0.41$, $\chi = 11$ and $c = 7.8$.

$$\begin{aligned} \frac{\partial U_L^+}{\partial y^+} =& \frac{1}{1+\kappa y^+} + \frac{c}{\chi}\left(e^{-y^+/\chi} + \left(1 - \frac{y^+}{3}\right)e^{-y^+/3}\right) \\ \frac{\partial U_L}{\partial y} =& \gamma = \frac{U_\tau^2}{\nu_L}\frac{\partial U_L^+}{\partial y^+} \end{aligned} \tag{6.72}$$

The friction velocity is computed using Mac Adams correlation [112].

$$U_\tau = \sqrt{\frac{\tau_w}{\nu_L}} \tag{6.73}$$

$$\tau_w = 0.018\ \mathrm{Re}_{D_h}^{-0.182}\ \frac{G_L^2}{\rho_L} = 0.018\ \mathrm{Re}_{D_h}^{-0.182}\ \rho_L U_L^2 \tag{6.74}$$

6.3 BUBBLE GROWTH

6.3.1 *Introduction*

In order to properly represent the bubble dynamics, it is mandatory to model the evolution of the bubble radius over time *i. e.* the bubble growth law. Since the bubble radius R and its derivatives $\dot{R}$ and $\ddot{R}$ appear in the force balance (notably in the expression of the added mass force 6.66), failing to predict the evolution of the bubble with time will definitely result in a force unbalance.

The problem of the bubble growth during its lifetime on the wall, including the sliding phase, is still an open question that aims to cover various types of heat transfer mechanisms. First, two growth regimes exist for a boiling bubble:

- Inertial growth, which occurs at the beginning of nucleation for low temperature difference between liquid and vapor. The evolution of the bubble size can be solved by the mass and momentum balances, through the solution of Rayleigh (1917) [136]. The form of the bubble growth is usually $R(t) = A \times t$ (Mikic & Rohsenow, [115]).
- Heat diffusion growth happening post the inertial phase. This type of bubble growth has been widely studied by different authors [115, 129, 146, 184] and is usually of the form $R(t) = B\sqrt{t}$, derivable using the energy balance around the bubble.

Those two regimes can be compared using the non-dimensional time t^+ defined as:

$$t^+ = \frac{A^2}{B^2} t \tag{6.75}$$

where

$$A = \sqrt{b \frac{h_{LV} \rho_V \Delta T_w}{\rho_L T_{sat}}} \text{ and } B = \sqrt{\frac{12}{\pi} \eta_L} \text{Ja} \tag{6.76}$$

with $b = \dfrac{2}{3}$ for a bubble in an infinite liquid medium and $b = \dfrac{\pi}{7}$ for a spherical bubble laying on a wall.

So that when $t^+ \ll 1$, $R(t) = At$ (inertial growth) and when $t^+ \gg 1$, $R(t) = B\sqrt{t}$ (heat diffusion growth). A general solution asymptotically covering the two regimes has been derived by Mikic & Rohsenhow:

$$R^+ = \frac{2}{3}\left[\left(t^+ + 1\right)^{3/2} + t^{+3/2} - 1\right], \; R^+ = \frac{R}{B^2/A}, \; t^+ = \frac{t}{B^2/A^2} \tag{6.77}$$

In most cases associated to wall nucleation and boiling flows, experimental observations showed that bubbles' lifetime is long enough to be mostly controlled by heat diffusion [90, 108, 181].

> **Remark :** Estimating the time t at which the diffusive growth radius equals the inertia growth radius yields:
>
> - $t \approx 0.39$ μs for water at 1 bar and $\Delta T_w = 15$ K
> - $t \approx 1.6 \times 10^{-4}$ μs for water at 150 bar and $\Delta T_w = 5$ K
>
> which insists on the validity of the nearly pure diffusive growth hypothesis.

6.3.2 *Heat Diffusion in Uniformly Superheated Liquid*

The analytic derivation of a bubble growth law in a pure heat diffusion regime has been tackled by various authors, mostly for the case of a bubble in a uniformly superheated and quiescent liquid. An reference solution is the work of Plesset & Zwick (1954) [129] who found an asymptotic solution for high values of Ja:

$$R(t) = \frac{2\sqrt{3}}{\sqrt{\pi}} \text{Ja} \sqrt{\eta_L t} \tag{6.78}$$

This result was generalized by Scriven (1959) [146] who derived whatever the value of Ja:

$$R(t) = 2\mathcal{F}(\mathrm{Ja})\,\mathrm{Ja}\sqrt{\eta_L t} \tag{6.79}$$

where $\mathcal{F}$ is implicitly defined by assuming $\frac{\rho_L}{\rho_V} \gg 1$:

$$\mathcal{F}(\mathrm{Ja}) = \frac{F}{2\mathrm{Ja}^2},\ \text{and}\ \mathrm{Ja} = F\exp\left(\frac{3}{2}F\right)\int_1^\infty \frac{1}{x^2}\exp\left(-\frac{F}{x} - \frac{F}{2}x^2\right)\mathrm{d}x \tag{6.80}$$

which falls back to $\mathcal{F}(\mathrm{Ja}) \to \frac{\sqrt{3}}{\sqrt{\pi}}$ when $\mathrm{Ja} \gg 1$.

The general formulation of $\mathcal{F}$ has been verified by Legendre *et al.* [98] with Direct Numerical Simulation of spherical bubble growth in a quiescent superheated liquid.

Usually, most authors are accepting $R(t) = K\mathrm{Ja}_w\sqrt{\eta_L t}$ for the bubble growth. With K usually expressed as $K = \frac{2b}{\sqrt{\pi}}$ with b being used as an adjustable constant depending on the flow conditions, the fluid and the heater properties, or derived analytically as presented before ($b = \sqrt{3}$ [129], $b = \frac{\pi}{2}$ [50], $1 \leq b \leq \sqrt{3}$ [184], $b = 1.56$ [174], $b = 0.24$ [172], etc.).

When the bubble presents a relative velocity with the ambient liquid, the disturbance of the thermal boundary layer around the liquid-vapor interface will impact its growth. This phenomenon has been numerically studied by Legendre *et al.* [98] who found that the ratio between the growth rate $\dot{R}$ and the relative velocity U_{rel} was controlling the growth regime as follows:

- If $\frac{\dot{R}}{U_{rel}} \gg 1$, the regime is close to the static heat diffusion and correspond to the Scriven formulation (Eq. 6.79) ;
- If $\frac{\dot{R}}{U_{rel}} \ll 1$, the relative velocity impacts the thermal boundary layer formation and leads to a growth matching the solution of Ruckenstein (1964) [141] where the Nusselt number at the liquid-vapor interface is:

  $$\mathrm{Nu} = 2\sqrt{\frac{\mathrm{Pe}(t)}{\pi}},\ \mathrm{Pe}(t) = \mathrm{Pr}_L \times \mathrm{Re}_b(t) \tag{6.81}$$

  In this case, the bubble growth is accelerated and $R \propto t^{2/3}$.

6.3.3 *Microlayer Evaporation*

In addition to the traditional heat diffusion from superheated liquid to the bubble through the liquid-vapor interface, bubble growth can also be enhanced by the evaporation of a so-called "microlayer". This term denotes a very thin layer of liquid (typically $\sim \mu$m [90]) which is trapped between the heated wall and the bubble base, as shown on Figure 6.10. The existence of this microlayer has now been supported by both experimental visualizations [24, 25, 88, 90] and numerical investigations [19, 66, 163].
Parallel to the heat diffusion approach, some authors computed the bubble growth by considering a pure microlayer evaporation regime. A well-known model of this type has been derived by Cooper & Lloyd in 1969 [31] and considers the wall thermal properties so that:

$$R(t) = 2.5\frac{\mathrm{Ja}}{\sqrt{\mathrm{Pr}_L}}\sqrt{\eta_L t}\ \text{if}\ \lambda_w \gg \lambda_L \tag{6.82}$$

$$R(t) = \frac{2}{\sqrt{\pi}}\sqrt{\frac{\lambda_w\rho_w c_{p,w}}{\lambda_L\rho_L c_{p,L}}}\ \text{if}\ \lambda_w \ll \lambda_L \tag{6.83}$$

Remark : The parameter $\sqrt{\frac{\lambda_w\rho_w c_{p,w}}{\lambda_L\rho_L c_{p,L}}}$, which is the ratio of the effusivity of the wall and the liquid, is the same used in the correlation of Ünal for the maximum bubble diameter (Eq. 6.5).

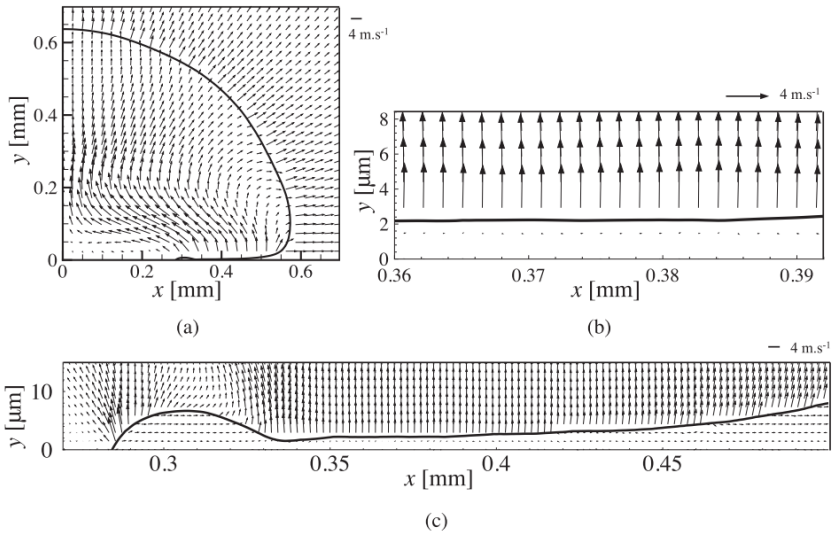

Figure 6.10: Microlayer appearing beneath the bubble in DNS conducted by and adapted from Urbano *et al.* [163].

The microlayer is also often taken into account for HFP modeling by enhancing the boiling heat flux through a computation of the microlayer volume [37, 89].

However, the presence of a liquid microlayer beneath the nucleated bubble is not assured for every boiling conditions. Indeed, experimental observations recently realized by Kossolapov [90] showed that the microlayer only existed for pressures below 3 bars when using water as working fluid. Moreover, Direct Numerical Simulations of Urbano *et al.* [163] where a full coupling between mass, momentum and energy balance was achieved managed to detect whether if the bubble grows in a contact-line regime or if a microlayer appears. They proposed a criterion based on the capillary and Jakob numbers determining the formation of a microlayer, further validated by extra Direct Numerical Simulations from Búres & Sato [19]:

$$\frac{\mathrm{JaCa}}{(\theta-\theta_0)^3} > \frac{1}{A^3},\ \theta_0 = 5°,\ A = 313 \tag{6.84}$$

Remark : Computing the capillary number using $\dot{R} = \frac{K\mathrm{Ja}}{2}\sqrt{\frac{\eta_L}{t}}$ as the interface velocity, we use Urbano *et al.* criterion to compute the time t_{max} after which the microlayer would cease to exist. Applying this to PWR conditions ($K = 1$, $\Delta T_w = 5K$) yields $t_{max} < 10^{-11}$s for $6° \leq \theta \leq 90°$, meaning that there is no time during the bubble growth during which a microlayer could grow. This agrees with the observation that increasing pressure would lead to microlayer disappearance.

Moreover, authors often consider that the whole volume of the microlayer contributes to evaporation while in reality a portion of the liquid is pushed away due to vapor recoil at the bubble foot.

We will not further detail the study of the microlayer regime since its existence is very unlikely if not impossible in the pressurized conditions typical of a PWR.

6.3.4 *Bubble Growth in Subcooled Flow Boiling*

If we consider the full problem of bubble growth in subcooled flow boiling, the analytic expressions presented above may fall out of their validation range since extra physical phenomena will be at stake. This more generic type of growth lack of proper theoretical derivations due to the complexity of the considered system (turbulence, condensation, convection, etc.). That is why authors trying to represent such complex bubble growth often combine different heat transfer mechanisms such as:

- Evaporation due to conduction from the superheated liquid near the bubble base ;
- Evaporation of the liquid microlayer ;

- Condensation on top of the bubble when it reaches subcooled liquid ;
- Convective heat transfer due to relative velocity between the bubble and the liquid.

To our knowledge, such models always consider empirical or fitted parameters. For instance Yoo *et al.* [172] wrote for a sliding bubble:

$$\frac{\partial R}{\partial t} = \underbrace{\gamma \mathrm{Pr}_L^{-0.5} \mathrm{Ja}_w \sqrt{\frac{\eta_L}{t}} \frac{A_{ML}}{A_b}}_{\text{Microlayer}} + \underbrace{(1-f)\frac{b}{\sqrt{\pi}} \mathrm{Ja}_w \sqrt{\frac{\eta_L}{t}}}_{\text{Superheated liquid}} - \underbrace{\frac{f \Delta T_L C}{1-\rho_V/\rho_L} R}_{\text{Subcooled convection}} \tag{6.85}$$

where $\gamma = \sqrt{\frac{\lambda_w \rho_w c_{p,w}}{\lambda_L \rho_L c_{p,L}}}$, $\frac{A_{ML}}{A_b} = 1.22\gamma^{-0.79}\exp\left(-0.204\mathrm{Ja}_w\right)$, $f = 0.5$, $b = 0.24$ and $C = 0.1$.

Their model was validated against low pressure sliding of boiling bubbles for different fluids (Water [108], FC87 [156], R113 [169]). They account for wall properties through the parameter γ in the microlayer term while assuming that 50% of the bubble faces subcooled liquid ($f = 0.5$) and condenses following the formulation of Levenspiel [101].

Zhou *et al.* [181] also proposed a similar modeling of the bubble growth, validated on their own measurements for boiling water at low pressure:

$$\begin{aligned}\frac{\partial R}{\partial t} = &\underbrace{\frac{1}{C}\mathrm{Pr}_L^{-0.5}\mathrm{Ja}_w\sqrt{\frac{\eta_L}{t}}}_{\text{Microlayer}} + \underbrace{\sqrt{\frac{3}{\pi}}\mathrm{Ja}_T\sqrt{\frac{\eta_L}{t}}\min\left(\frac{y_{sat}}{2R},\ 1\right)}_{\text{Superheated liquid}} \\ &\underbrace{- \frac{\eta_L}{2R}\mathrm{Ja}_L\left(2+0.6\mathrm{Re}_b^{0.5}\mathrm{Pr}_L^{0.3}\right)\max\left(\frac{H-y_{sat}}{2R},\ 0\right)}_{\text{Subcooled convection}}\end{aligned} \tag{6.86}$$

where $C = 1.45$, Ja_T is the Jakob number taken at $\min\left(\overline{T} - T_{sat},\ 0\right)$, $\overline{T}$ the average liquid temperature around the bubble, $H = R\left(1+\cos\left(\theta\right)\right)$.

While they consider a constant coefficient for the microlayer evaporation, they propose a finer modeling of the condensation term by evaluating the height y_{sat} at which $T_L = T_{sat}$ using the turbulent wall law of Kader [80]. The condensation is modeled by the Ranz & Marshall correlation [133] that accounts for the relative velocity through the bubble Reynolds number.

> **Remark :** As mentioned before, those model rely on numerous empirical parameters due to the variety of considered phenomena. In particular, microlayer evaporation is systematically considered which could be questioned regarding the observations made in Subsection 6.3.3.

Contrary to those models, Mazzocco *et al.* [111] propose to keep the radius as $K\mathrm{Ja}_w\sqrt{\eta_L t}$ and to include subcooling and microlayer influence in the value of K:

$$K = \frac{1.243}{\sqrt{\mathrm{Pr}_L}} + 1.945\chi \tag{6.87}$$

with

$$\chi = 1.55 \text{ (saturated flow) or } \chi = -0.05\frac{\Delta T_L}{\Delta T_w} \text{ (subcooled flow)} \tag{6.88}$$

> **Remark :** This approach is interesting because it keeps the simple growth law in $t^{1/2}$, but K has to be set to 0 for regimes where $\frac{\Delta T_L}{\Delta T_w}$ is very large.

6.3.5 *Analytic Approach of Bubble Growth in a Linear Thermal Boundary Layer*

In this Subsection, we propose an analytic derivation of bubble growth for a truncated sphere laying on a wall in a boundary layer with a linear temperature profile. The considered geometrical and thermal definitions are depicted on Figure 6.11.

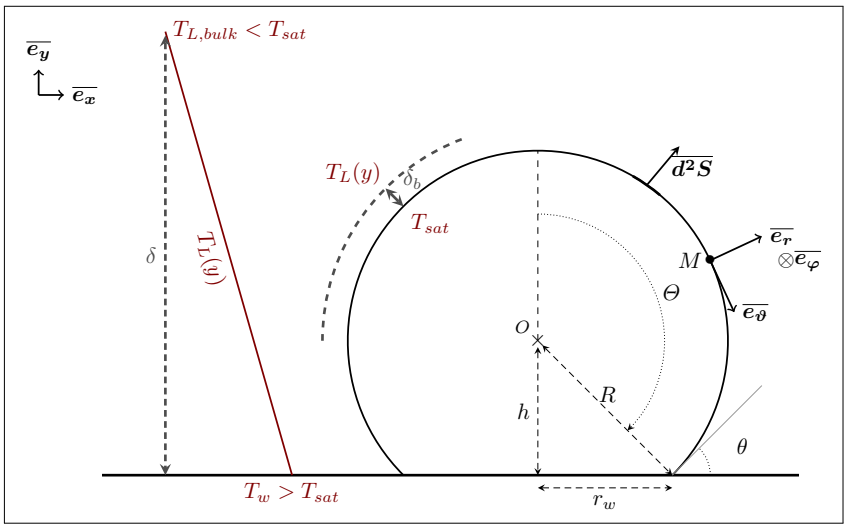

Figure 6.11: Studied geometry

We consider an established single-phase thermal boundary layer of thickness δ. When the bubble start to grow, an other boundary layer will of thickness δ_b grow between the liquid-vapor interface and the surrounding liquid which temperature depends on the wall distance y.

The liquid temperature is assumed to follow a linear profile:

$$T_L(y) = T_w + \frac{T_{L,bulk} - T_w}{\delta} y \tag{6.89}$$

Assuming that the vapor stays at a temperature close to T_{sat}, the radial component of the temperature gradient at the bubble's interface can be expressed as:

$$\overline{\nabla}(T) \cdot \overline{e_r} = \frac{\partial T}{\partial r}(R, \vartheta, \varphi) \approx \frac{T_L(y) - T_{sat}}{\delta_b} \tag{6.90}$$

Note : It is implicitly supposed that the heat flux within the vapor bubble is negligible, which is relatively reasonable since the vapor thermal conductivity is 7 to 28 times lower than that of the liquid water between 1 bar and 100 bar.

Applying Fourier's law to the liquid close to the bubble to estimate the heat flux density vector $\overline{j_Q} = -\lambda_L \overline{\nabla}(T)$. Between t and $t + dt$ the heat exchanged through d^2S is:

$$d^2Q_b \approx -\frac{\lambda_L}{\delta_b}\left[\Delta T_w R^2 \sin(\vartheta) - \frac{\Delta T_w + \Delta T_L}{\delta} R^3 \left[\cos(\vartheta) - \cos(\Theta)\right] \sin(\theta)\right] \mathrm{d}\vartheta \mathrm{d}\varphi \tag{6.91}$$

Then assuming that δ_b is constant between t and $t + dt$, the total heat flux can be expressed by integrating over the bubble's surface:

$$Q_b = \frac{2\pi\lambda_L R^2}{\delta_b}(1 + \cos(\theta))\left[\Delta T_w - \frac{R}{2\delta}(\Delta T_w + \Delta T_L)(1 + \cos(\theta))\right] \tag{6.92}$$

Writing the mass balance by considering that the heat flux contributes solely to phase change:

$$\frac{\partial V_b}{\partial t} = \frac{Q_b}{\rho_V h_{LV}} \tag{6.93}$$

$$V_b = \frac{4}{3}\pi R^3 f_V,\ f_V = \frac{1}{4}\left(2-\cos\left(\theta\right)\right)\left(1+\cos\left(\theta\right)\right)^2 \tag{6.94}$$

Writing this in terms of bubble radius:

$$\frac{\partial R}{\partial t} = \frac{\mathrm{Ja}_w \eta_L}{2\delta_b f_V}\left(1+\cos\left(\theta\right)\right)\left[1-\frac{R}{2\delta}\left(1+\frac{\mathrm{Ja}_L}{\mathrm{Ja}_w}\right)\left(1+\cos\left(\theta\right)\right)\right] \tag{6.95}$$

Which reduces to the following differential equation:

$$\frac{\partial R}{\partial t} + aR = b \tag{6.96}$$

$$a = \frac{\mathrm{Ja}_w \eta_L}{4\delta_b \delta f_V}\left(1+\frac{\mathrm{Ja}_L}{\mathrm{Ja}_w}\right)\left(1+\cos\left(\theta\right)\right)^2 \text{ and } b = \frac{\mathrm{Ja}_w \eta_L}{2\delta_b f_V}\left(1+\cos\left(\theta\right)\right) \tag{6.97}$$

Solutions of this differential equation depend on the hypothesis over δ and δ_b. If we assume that the bubble grows in a fully established liquid flow then δ can be considered as constant.
When the bubble will start to nucleate, the liquid-vapor interface will delimit a frontier through which a transient heat transfer between the vapor at constant temperature T_{sat} and liquid at $T_L\left(y\right)$ will occur. To estimate the associated local boundary layer thickness δ_b, we can rely on the solution of semi-infinite transient conduction as treated in Del Valle & Kenning [35] or Mikic & Rohsenow [115]:

$$\delta_b = \sqrt{\eta_L t} \tag{6.98}$$

The differential equation Eq. 6.96 becomes:

$$\frac{\partial R}{\partial t} + a\left(t\right)R = b\left(t\right) \tag{6.99}$$

$$a(t) = \frac{\mathrm{Ja}_w\sqrt{\eta_L}}{4\delta f_V\sqrt{t}}\left(1+\frac{\mathrm{Ja}_L}{\mathrm{Ja}_w}\right)\left(1+\cos\left(\theta\right)\right)^2 = K_a t^{-1/2} \tag{6.100}$$

$$b(t) = \frac{\mathrm{Ja}_w\sqrt{\eta_L}}{2 f_V\sqrt{t}}\left(1+\cos\left(\theta\right)\right) = K_b t^{-1/2} \tag{6.101}$$

With the initial condition $R\left(t=0\right)=0$, the solution to this differential equation is:

$$R\left(t\right) = R_\infty\left(1-e^{-2K_a\sqrt{t}}\right) \tag{6.102}$$

$$R_\infty = \frac{K_b}{K_a} = \frac{2\ \delta}{\left(1+\frac{\mathrm{Ja}_L}{\mathrm{Ja}_w}\right)\left(1+\cos\left(\theta\right)\right)} \tag{6.103}$$

This type of bubble growth presents interesting properties. First, it degenerates to the uniformly superheated liquid solution when $t \to 0$:

$$R\left(t\right) \underset{t\to 0}{\sim} \frac{1+\cos\left(\theta\right)}{f_V}\mathrm{Ja}_w\sqrt{\eta_L t} \tag{6.104}$$

with a purely geometrical growth constant depending on the contact angle, equal to 2 for the spherical case.

Moreover, this growth law accounts for the liquid subcooling and thus presents an equilibrium radius R_∞ when $t \to \infty$, corresponding to the bubble size at which the vaporization from the superheated liquid is exactly compensated by the condensation at the bubble top.

To the best of our knowledge, this simple bubble growth law has never been proposed in the literature. However, this equation has some limitations :

- It requires the knowledge of the liquid thermal boundary layer thickness δ which estimation can be tricky ;
- This law can't be applied if $T_{L,bulk} > T_{sat}$.

Remark : It is worthy to note that this solution is derived solely using the energy balance at the liquid-vapor interface. No momentum balance was used when solving this physical problem, which can be considered as a limit of the approach.

In addition, no modeling of the micro-region accounting for the specific phase change regime near the contact line have been considered.

6.3.6 *Comparison with DNS Results*

To assess the validity of Eq. 6.102, we will compare the radius time profile with DNS results by Urbano *et al.* [162] who simulated the same physical situation as depicted in Figure 6.11 for pool boiling. They also solved the heat conduction in the wall and studied the growth dynamics depending on the values of ΔT_L and ΔT_w as well as the equilibrium diameter reached by the bubble.

Note : The wall temperature in Urbano *et al.* [162] work is imposed on the outer side of the simulated wall thickness contrary to the model where it is imposed directly at the inner side.

In their analysis, Urbano *et al.* derived the same equilibrium radius as in Eq. 6.103 by equating the condensation and vaporization heat fluxes. By comparing with the equilibrium radius reached in their simulations, they found that a corrective factor $C = 1.15829$ was needed to correct Eq. 6.103. This difference could be explained by the heat conduction in the wall that is not accounted for in the theoretical approach.

DNS results obtained for three couples of subcooling ΔT_L and superheat ΔT_w are used for comparison. Results are displayed on Figure 6.12 with and without the corrective factor on R_∞ suggested by Urbano *et al.*
The analytic formulation of the bubble growth matches very well with the DNS results when the equilibrium radius is corrected. The different growth regime induced by the pairs (ΔT_L, ΔT_w) are correctly captured by the model. DNS results present different equilibrium radius values when the subcooling and superheat changes, which can not be accounted for by the model.

Remark : Those results are encouraging and validate the modeling of δ_b with the semi-infinite conduction model (Eq. 6.98).

6.3.7 *Comparison with Experimental Measurements*

6.3.7.1 *Low Pressure Measurements*

To further evaluate the proposed model, we compare the result with experimental measurements of bubble radius in vertical boiling of water at atmospheric pressure by Maity [108] in a square channel. The choice of δ is adapted to each case (best-fitting of the final radius R_∞) and $\theta = 45°$ is the average measured contact angle in the experiments.

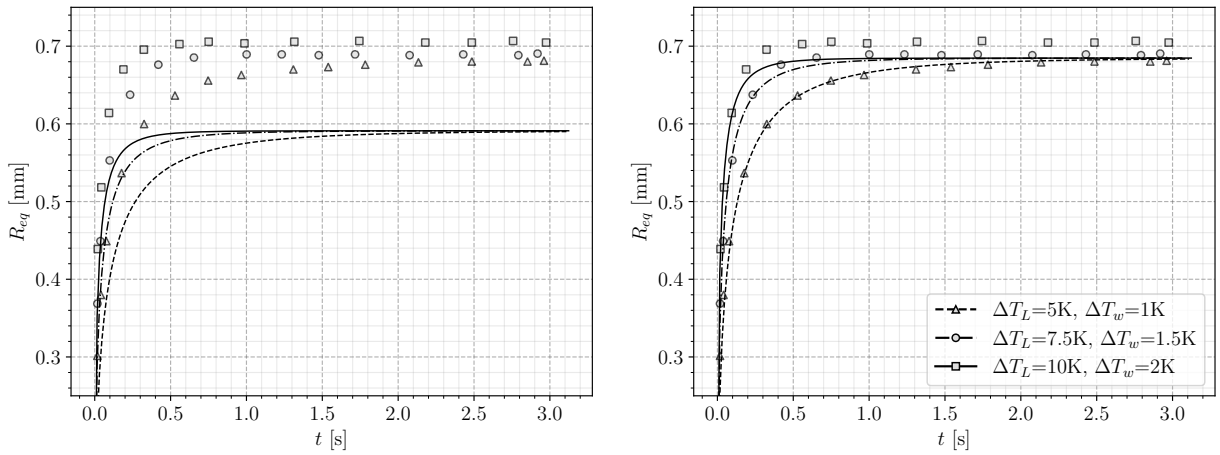

(a) Results using R_∞

(b) Results using $C \times R_\infty$, $C = 1.158$

Figure 6.12: Comparison with DNS results of Urbano *et al.* [162] ($\delta = 3$mm and $\theta = 50°$). Lines : Model predictions - Markers : DNS

In addition, we also plot the predictions by the heat diffusion solution $R = K\mathrm{Ja}_w\sqrt{\eta_L t}$ with $K = \dfrac{2b}{\sqrt{\pi}}$ and $1 \leq b \leq \sqrt{\pi}$. A solution with an optimized value of K is also represented. The models of Mazzocco and Yoo *et al.* are also compared. The results are presented on Figure 6.13.

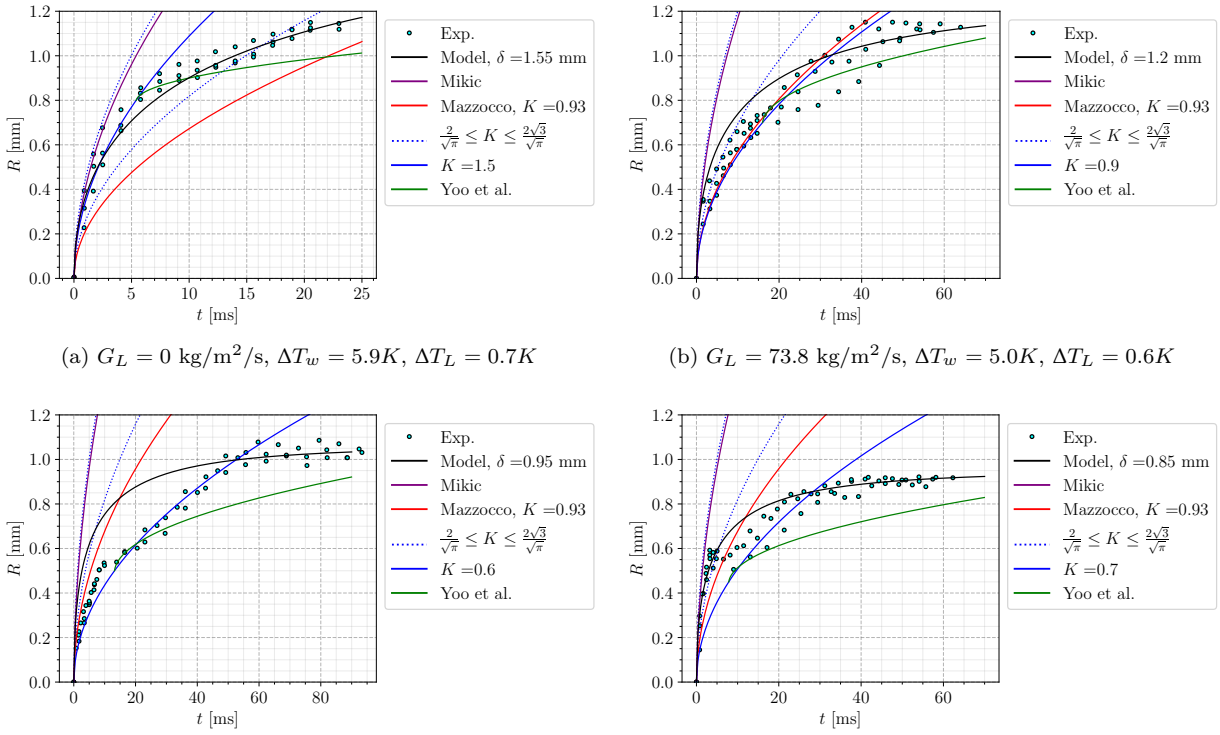

(a) $G_L = 0$ kg/m^2/s, $\Delta T_w = 5.9K$, $\Delta T_L = 0.7K$

(b) $G_L = 73.8$ kg/m^2/s, $\Delta T_w = 5.0K$, $\Delta T_L = 0.6K$

(c) $G_L = 143.8$ kg/m^2/s, $\Delta T_w = 5.9K$, $\Delta T_L = 0.3K$

(d) $G_L = 239.6$ kg/m^2/s, $\Delta T_w = 5.9K$, $\Delta T_L = 0.3K$

Figure 6.13: Comparison with experimental measurements of Maity [108].

The new formulation globally reproduces the experimental results better than the other models. In particular, the progressively damped growth rate when the bubble start to face colder liquid seems to correctly captures the nonlinear experimental growth. Values of δ needed to produce those results were between 0.85 mm and 1.55mm, which reasonably agrees with measurements of Maity in his experiment for horizontal flow giving δ roughly between 1 mm and 1.5 mm. We can note that the optimal value of δ decreases

as liquid mass flux increases, which is physically coherent as the thermal boundary layer will diminish in size with the Reynolds number.

Remark : Actually, the thermal boundary layer thickness δ depends on many parameters such as the liquid Prandtl number and mass flow rate, the heater properties and heat flux, etc.

If the total wall heat flux ϕ_w is transmitted to the liquid by conductive heat transfer in the linear boundary layer, we can write:

$$\phi_w = \lambda_L \frac{\Delta T_L + \Delta T_w}{\delta} \tag{6.105}$$

Estimating the boundary layer thickness as $\delta = \dfrac{\lambda_L}{h_{c,L}}$ with $h_{c,L}$ the convective heat transfer coefficient computed using Dittus-Boelter correlation (Eq. 3.20) yielded $\delta \approx 0.42$ mm for $G_L = 150$ kg/m^2/s, which is an acceptable order of magnitude but would be too small compared to the optimal values of δ.

On the other hand, the fitted value of K is often smaller than the lower bound $\dfrac{2}{\sqrt{\pi}}$ suggested by Zuber [184]. This is a consequence of the subcooled flow which deviates from the uniformly superheated liquid from which those values were derived. This fitted profile manages to capture some stages of bubble growth but can not predict the asymptotic behavior where bubble reaches a quasi-constant radius. We see that the model of Mikic & Rohsenow produces results that are nearly identical to the $K = 2\sqrt{3/\pi}$ solution. The growth constant computed by Mazzocco *et al.* (Eq. 6.87) is constant over the four cases and lower than $2/\sqrt{\pi}$ which is slightly better than other analytic values of K but underestimates the pool boiling case.

Finally, we see that the model of Yoo *et al.* underestimates the bubble radius. We suspect this could come from the assumption considering that half of the bubble faces subcooled liquid ($f = 0.5$, Eq. 6.85), which is hardly reasonable especially at early growth stages.

To test the sensitivity of the model to the value of δ, we plot on Figure 6.14 the Maity case at $G_L = 239.6$ kg/m^2/s for values of $\delta \pm 50\%$.

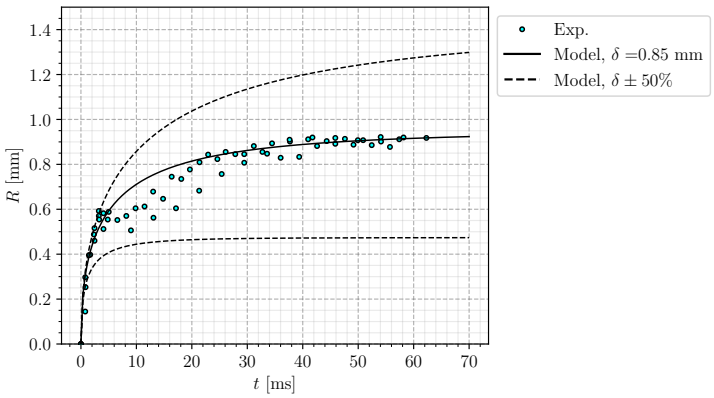

Figure 6.14: $G_L = 239.6$ kg/m^2/s, $\Delta T_w = 5.9K$, $\Delta T_L = 0.3K$

The value of δ controls the value of R_∞ and thus significantly impacts the transient growth profile. The estimation of the thermal boundary layer thickness is then an important aspect to ensure a correct prediction of the bubble growth.

6.3.7.2 *High Pressure Measurements*

The model is now compared to higher pressure measurement (20 bar and 40 bar) for water boiling by Kossolapov [90]. All the experiments are conducted with 10K of subcooling, and we take a contact angle of $\theta = 80°$ (typical for water and ITO). The range of the measured diameters over time are represented since Kossolapov observed the growth of thousands of bubbles over the heater surface. Results are presented on Figure 6.15.

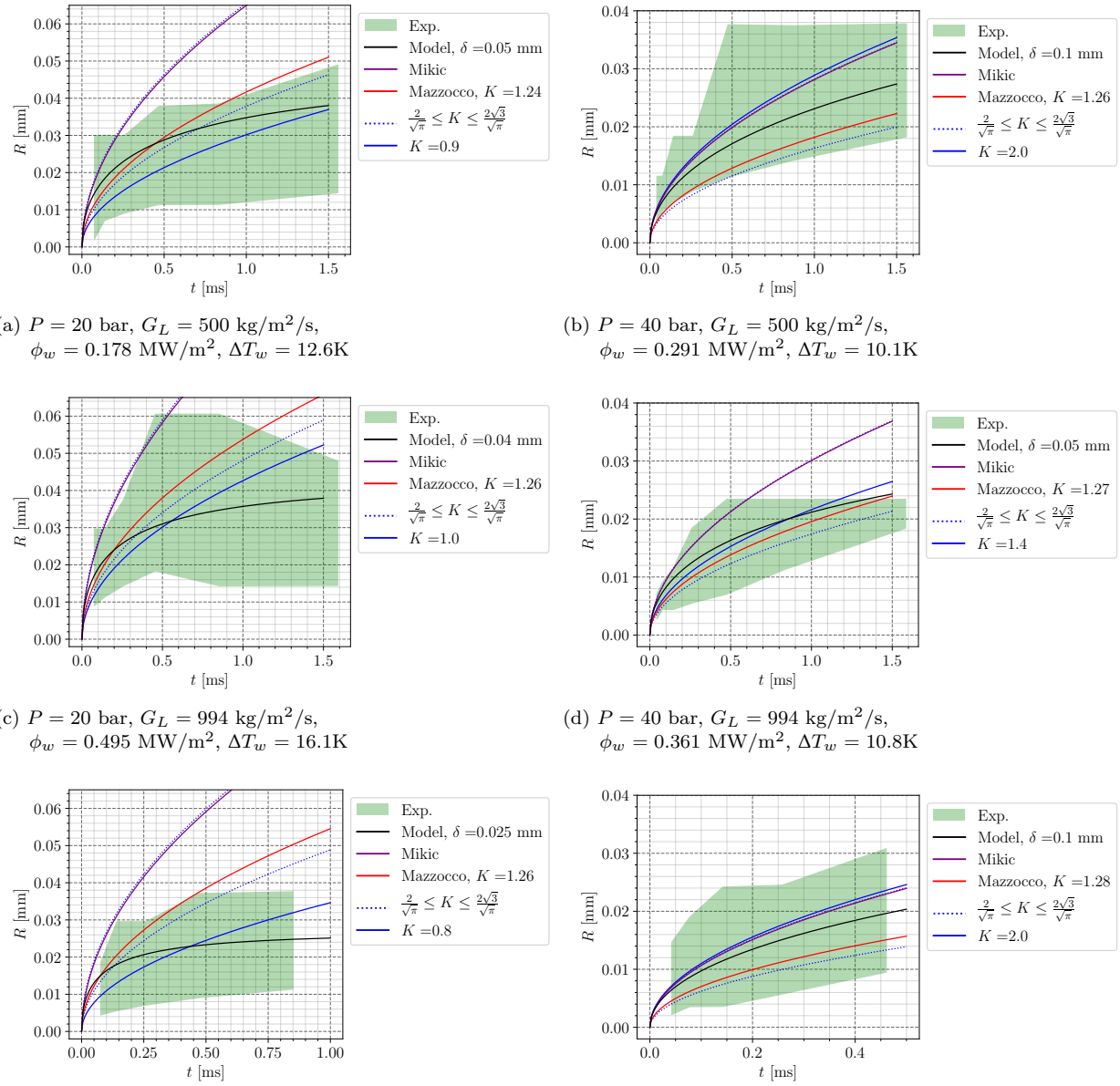

(a) $P = 20$ bar, $G_L = 500$ kg/m^2/s, $\phi_w = 0.178$ MW/m^2, $\Delta T_w = 12.6$K

(b) $P = 40$ bar, $G_L = 500$ kg/m^2/s, $\phi_w = 0.291$ MW/m^2, $\Delta T_w = 10.1$K

(c) $P = 20$ bar, $G_L = 994$ kg/m^2/s, $\phi_w = 0.495$ MW/m^2, $\Delta T_w = 16.1$K

(d) $P = 40$ bar, $G_L = 994$ kg/m^2/s, $\phi_w = 0.361$ MW/m^2, $\Delta T_w = 10.8$K

(e) $P = 20$ bar, $G_L = 1504$ kg/m^2/s, $\phi_w = 0.487$ MW/m^2, $\Delta T_w = 16.2$K

(f) $P = 40$ bar, $G = 1504$ kg/m^2/s, $\phi_w = 0.613$ MW/m^2, $\Delta T_w = 12.2$K

Figure 6.15: Comparison with experimental measurements of Kossolapov [90]. ΔT_w values are recalculated from analytic growth profiles fitted by the author.

The values of δ needed to match the experimental measurements using Eq. 6.102 are much smaller than the low pressure case, with $\delta \leq 0.1$ mm. The higher mass fluxes in Kossolapov measurements could explain lower values of δ, nevertheless they do not follow a particular trend with G_L.

Contrary to low pressure measurements, the Plesset & Zwick solution with $\frac{2}{\sqrt{\pi}} \leq K \leq \frac{2\sqrt{3}}{\sqrt{\pi}}$ provides an acceptable estimation of the bubble radius. This is probably due to the smaller bubble size in pressurized boiling (roughly 10 times smaller compared to atmospheric pressure).

Remark : The non-dimensional positions of the center of gravity of the bubble $R^+ = \frac{Ru_\tau}{\nu_L}$ rise up to 40 for Maity cases and 20 for Kossolapov cases while having larger liquid mass fluxes. This supports the fact that bubbles at higher pressure are less likely to be impacted by subcooled liquid, spending most of their lifetime between the viscous and buffer layer.

Note that this assumptions is true if the thermal and hydrodynamic boundary layers are close, which is often assumed in numerical simulations under the assumption of a unity turbulent Prandtl number $\mathrm{Pr}_T \approx 1$ (Eq. 2.43).

6.3.8 *Conclusions on Bubble Growth Modeling*

- Recent experimental and numerical research have shown that the presence of a liquid microlayer contributing to the bubble growth strongly depends on the boiling conditions. In particular, disappearance of this microlayer at pressures higher than 3 bar has been observed by Kossolapov [90]. This microlayer should thus not be systematically taken into account.
- A new formulation derived from the heat diffusion in a linear temperature profile has been proposed (Eq. 6.102). Provided a correct value of the thermal boundary thickness δ, validation both on DNS and low pressure measurements shows that the model better captures the growth regime of bubbles in subcooled boiling compared to traditional models. However, this improvement appears limited at higher pressure when bubbles are smaller, where the Plesset & Zwick treatment also proposes an acceptable estimation of the bubble growth.
- Mechanistic models that includes several heat transfer mechanisms require a certain number of empirical closures that limits the model generality, making them unsuitable for application to any boiling conditions.
- Whatever the conditions, a proper choice of the growth constant K in the $R = K\mathrm{Ja}_w\sqrt{\eta_L t}$ solution for a uniform liquid superheat can yield reasonable results. Moreover, it presents interesting mathematical properties such as the time independence of the products $R\dot{R}$ and $R^3\ddot{R}$ that appear in the bubble force balance (Eq. 6.70).

All things considered, it seems that the proposed new growth law of Eq. 6.102 can be of greater interest for low pressure subcooled boiling since the associated larger bubbles are more likely to be impacted by the bulk flow, contrary to high pressure bubbles. Although it provides finer physical representation of bubble radius evolution, its application is limited by the estimation of δ to which the model is strongly sensitive. Moreover, it could benefit from an association with a microlayer evaporation term which would be of greater physical consistency for low pressure boiling. **On the other hand, less precise yet acceptable predictions of bubble growth are achieved using the $t^{1/2}$ law with a growth constant K close to unity.**

6.4 DEPARTURE BY SLIDING

The question of departure by sliding being central for bubble dynamics in vertical flow boiling, we will tackle the problem by starting with a non-dimensional analysis before moving to predictions of experimental measurements of departure diameters.

6.4.1 *Non-Dimensional Analysis*

To study the departure by sliding, we rely on force balance parallel to the wall (Eq. 6.69). Before departure, the bubble grows on its nucleation site while staying immobile, thus with a sliding velocity $U_b = \frac{\partial U_b}{\partial t} = 0$. The force balance parallel to the wall becomes:

$$-\pi R\sigma f_{C,x} + \frac{4}{3}\pi R^3\left(\rho_L - \rho_V\right)g + \frac{1}{2}C_D\rho_L\pi R^2U_L^2 + \frac{4}{3}\pi R^3\rho_L\ 3C_{AM,x}\frac{\dot{R}}{R}U_L = 0 \tag{6.106}$$

We can note that in this equation, departure by sliding is promoted by the buoyancy, the drag and the added mass forces. Only the capillary force keeps the bubble attached to its nucleation site, which will be discussed later. As discussed in the previous section, the bubble growth is modeled as:

$$R\left(t\right) = K\mathrm{Ja}_w\sqrt{\eta_L t} \tag{6.107}$$

with K as an adjustable constant.

Re-writing Eq. 6.106 in non-dimensional form by dividing the LHS by the added mass force yields:

$$-\frac{1}{2}\frac{f_{C,x}}{K^2 C_{AM,x}}\frac{1}{\mathrm{Ca}}\frac{\mathrm{Pr}_L}{\mathrm{Ja}_w^2} + \frac{1}{3}\frac{1}{K^2 C_{AM,x}}\frac{\mathrm{Re}_b}{\mathrm{Fr}}\frac{\mathrm{Pr}_L}{\mathrm{Ja}_w^2} + \frac{1}{8}\frac{C_D}{K^2 C_{AM,x}}\mathrm{Re}_b\frac{\mathrm{Pr}_L}{\mathrm{Ja}_w^2} + 1 = 0 \tag{6.108}$$

where we have the following non-dimensional numbers:

$$\mathrm{Re}_b = \frac{2RU_L}{\nu_L}\ ;\ \mathrm{Fr} = \frac{\rho_L U_L^2}{\left(\rho_L - \rho_V\right)gR}\ ;\ \mathrm{We} = \frac{\rho_L U_L^2 R}{\sigma}\ ;\ \mathrm{Eo} = \frac{\left(\rho_L - \rho_V\right)gR^2}{\sigma}\ ;$$
$$\mathrm{Ja}_w = \frac{\left(T_w - T_{sat}\right)\rho_L c_{P,L}}{\rho_V h_{LV}}\ ;\ \mathrm{Pr}_L = \frac{\nu_L}{\eta_L}\ ;\ \frac{\dot{R}}{U_L} = \frac{K^2\mathrm{Ja}_w^2}{\mathrm{Pr}_L\mathrm{Re}_b}\ ;\ \mathrm{Ca} = \frac{\mu_L U_L}{\sigma}$$

Eq. 6.108 exhibits terms that can be used to compare the magnitude of each detaching forces and obtain the following conditions:

$$\text{Added mass force greater than drag if: } \frac{\mathrm{Ja}_w^2}{\mathrm{Pr}_L} > \frac{1}{8}\frac{C_D}{C_{AM,x}}\frac{1}{K^2}\mathrm{Re}_b \tag{Bd. 1}$$

$$\text{Added mass greater than buoyancy if: } \frac{\mathrm{Ja}_w^2}{\mathrm{Pr}_L} > \frac{1}{3}\frac{1}{C_{AM,x}K^2}\frac{\mathrm{Re}_b}{\mathrm{Fr}} \tag{Bd. 2}$$

$$\text{Drag greater than buoyancy if: } \mathrm{Fr} > \frac{8}{3}\frac{1}{C_D} \tag{Bd. 3}$$

Those three conditions can be seen as boundaries in a $\left(\mathrm{Ja}_w^2/\mathrm{Pr}\ ;\ \mathrm{Re}_b\right)$ plane. With a given fluid and bubble diameter $D = 2R$, we can represent the different regimes of force dominance by plotting those three boundaries simultaneously on a regime map. Eq. Bd. 3 corresponds to a vertical line in the plane since $C_D \sim \frac{1}{\mathrm{Re}_b}$. An example of such a map is presented on Figure 6.16.

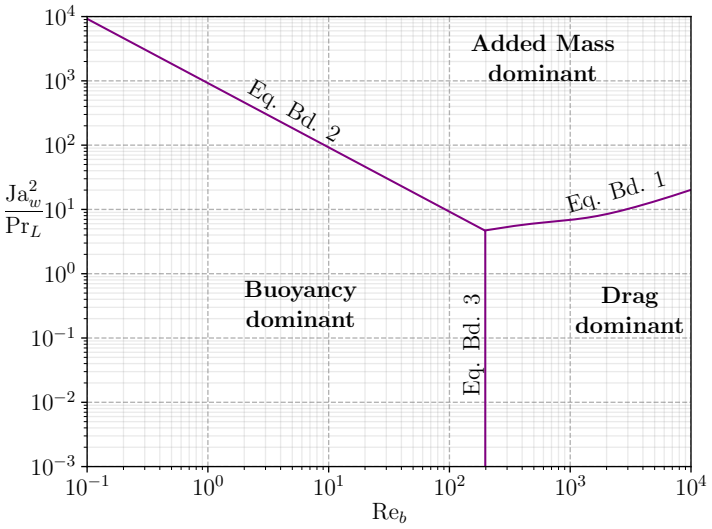

Figure 6.16: Regime map regarding departure by sliding. Boundaries plotted for water at 1 bar and $D_d = 0.5$mm. ($K = 2$)

This allows to visualize the operating conditions under which each of the detaching forces will be dominant. Logically, buoyancy dominates for low Fr numbers, thus low Re_b regimes contrary to drag. Added mass dominates when values of $\mathrm{Ja}_w^2/\mathrm{Pr}_L$ are high *i. e.* when bubble grows rapidly.

6.4.1.1 *Influence of Pressure*

On Figure 6.17, we draw the regime map for 3 different pressures and associated orders of magnitude of bubble departure diameter [87].

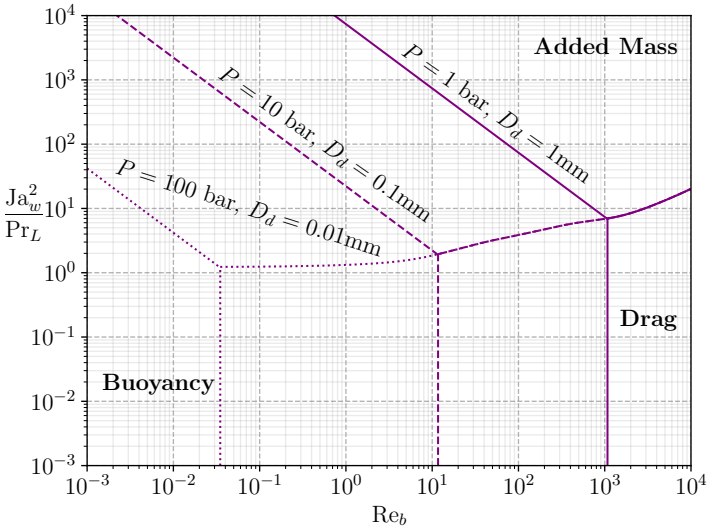

Figure 6.17: Regime map plotted for water at different pressures and bubble departure diameters. ($K = 2$)

The impact of pressure is mostly seen through the decrease of bubble departure diameter. As pressure increases, buoyancy force decreases while drag and added mass forces display much larger dominance zones. The competition between those two terms mainly relies on the competition between liquid flow velocity and wall superheat or heat flux.

6.4.1.2 *Comparison between Fluids*

On Figure 6.18, we compare the dominance zones for R12 at 26 bar and water at 155 bar. Moderately pressurized R12 (10 to 30 bar) has often been used as a simulating fluid to mimic water in PWR since it has the same density ratio and Weber number for instance (see Chapter 3 related to the DEBORA experiments).

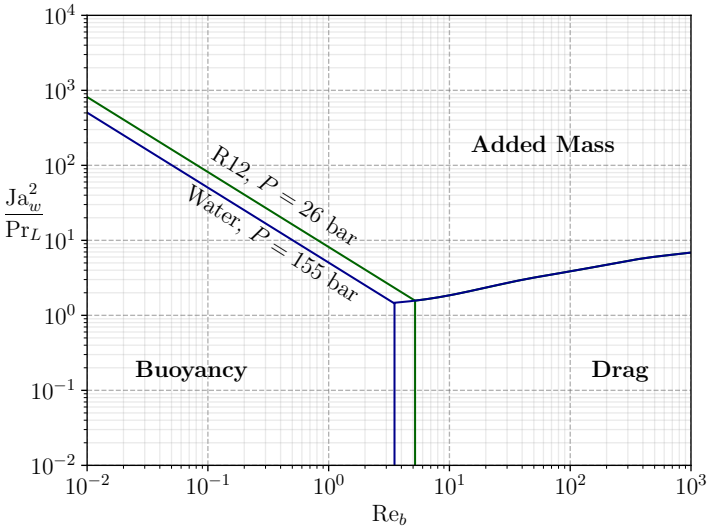

Figure 6.18: Regime map for R12 as simulating fluid for PWR. $D_d = 0.05$mm is chosen according to R12 measurements from Garnier *et al.* [53] who observed bubbles of ~ 0.1mm diameter after lift-off. The same value is taken for water. ($K = 2$)

Assuming that the conservation of Weber and Boiling numbers may lead to similar bubble departure diameters, we can observe that the boundaries between the two fluids are very close. This qualitatively

indicates that R12 shall present bubble departure by sliding mechanisms similar to what happens in PWR.

Remark : This approach could easily be applied to comfort the confidence one may have in extrapolating the observations done using a simulating fluid to industrial applications.

6.4.2 *Application to Experimental Data*

Now we want to apply this non-dimensional approach to experimental measurement in order to determine the actual bubble departure by sliding regimes. We rely on 7 experiments in which bubble departure diameters in vertical flow boiling were measured. The operating conditions are gathered in Table 6.3.

Author	Fluid	D_h [mm]	P [bar]	G_L [kg/m^2/s]	ΔT_L [K]	ϕ_w [kW/m^2]	ΔT_w [K]	D_d [mm] (N_{mes})
Thorncroft [156] (1998)	FC-87	12.7	N.A.	0 - 319	0.99 - 3.27	2.83 - 11.8	0.54 - 6.89	0.094 - 0.237 (10)
Maity [108] (2000)	Water	20	1.01	0 - 239.6	0.3 - 0.7	N.A.	5 - 5.9	0.788 - 1.71 (9)
Chen [22] (2012)	Water	3.8	1.2 - 3.35	214 - 702	14.5 - 30.3	83.6 - 334	N.A.	0.549 - 2.255 (22)
Sugrue [151] (2014)	Water	16.6	1.01	250 - 400	10 - 20	50 - 100	2 - 6	0.229 - 0.391 (16)
Guan [63] (2014)	Water	9	1.01	87.3 - 319.2	8.5 - 10.5	68.2 - 104	4.5 - 8.5	0.62 - 1.85 (12)
Ren [138] (2020)	Water	3.8	2 - 5.5	488.4 - 1654	28.7 - 51	160.7 - 643.2	N.A.	0.045 - 0.111 (42)
Kossolapov [90] (2021)	Water	11.8	19.9 - 39.8	500 - 1500	10	178 - 613	10.1 - 16.2	0.01 - 0.047 (11)

Table 6.3: Bubble departure diameters data sets in vertical flow boiling

If the value of ΔT_w is not available in the considered data-set, we estimate it ΔT_w using Frost & Dzakowic correlation [51]:

$$\Delta T_w = \mathrm{Pr}_{L,sat}\sqrt{\frac{8\sigma\phi_w T_{sat}}{\lambda_L \rho_V h_{LV}}} \tag{6.109}$$

To place experimental measurements on the non-dimensional map, we need a bubble detachment diameter value D_d to plot the dominance zones. Since measured D_d vary significantly in each experiment, we draw the boundaries for the maximum and minimum values of D_d as shown on Figure 6.19a. If the considered data covers different pressures, boundaries for each pressure are plotted to exhibit its impact (Figures 6.19d, 6.19e and 6.19f). We chose a value of $K = 1$ to draw the boundaries.

The Figure 6.19 shows that for most of the low pressure experiments, the detaching forces are the added mass and the buoyancy. Smaller bubbles are mainly detached under the effect of the added mass force (Figures 6.19c, 6.19d and 6.19e). When the bubbles detach at higher diameters, the impact of the buoyancy force naturally increases and is comparable to the added mass force (Figures 6.19a and 6.19b).

When the pressure increases, we observe that the experimental measurements gradually move towards the drag dominant zone as seen on Figures 6.19e and 6.19f. This main difference in the dynamic regime when bubble departs by sliding arises from multiple effects:

- The decrease of ρ_L/ρ_V with pressure, thus reducing Ja_w and the impact of the detaching added mass term ;
- The higher liquid mass fluxes in Kossolapov experiments, increasing the impact of the drag ;

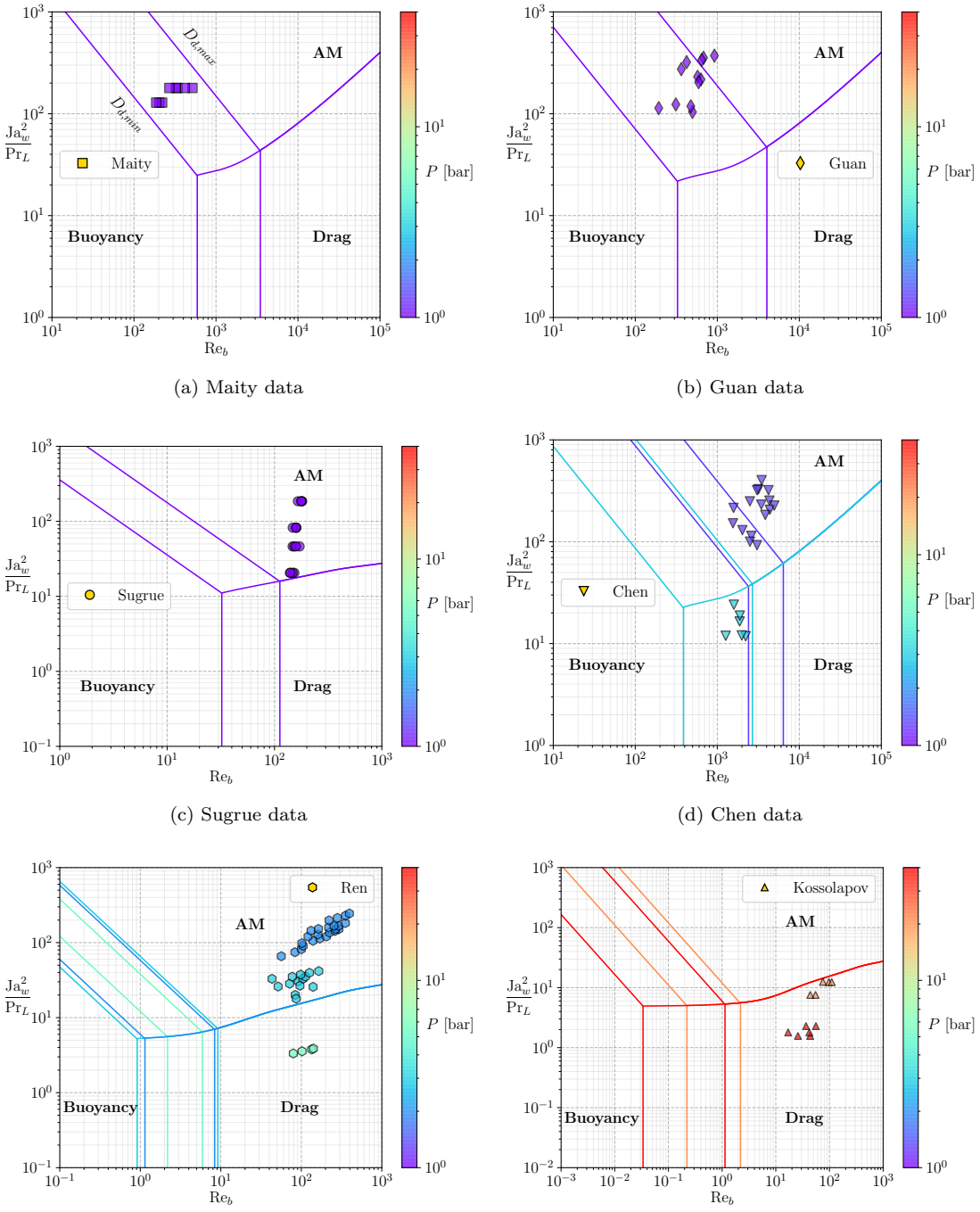

(a) Maity data

(b) Guan data

(c) Sugrue data

(d) Chen data

(e) Ren data

(f) Kossolapov data

Figure 6.19: Regime maps for each water data sets from Table 6.3.

- The decrease of D_d with pressure, reducing the magnitude of buoyancy.

However, we see that some measurements lie close to the added mass / drag boundary (Figure 6.19f), indicating that the added mass force still plays a significant role for bubble detachment. This means that regardless of the operating pressure, the detaching term associated to the coupling between bubble growth and outer liquid flow should not be neglected in the force balance (Eq. 6.106).

6.4.3 *Departure Diameter Prediction*

6.4.3.1 *About the Use of Empiricism*

As previously mentioned, the case of bubble detachment in vertical flow boiling is particular since only one force maintains the bubble attached to its nucleation site: the capillary force (Eq. 6.106). Its expression depends on the contact angle θ, the half-angle of hysteresis $\mathrm{d}\theta$ and the bubble foot radius r_w (or ratio to bubble diameter r_w/R) and is thus very sensitive to those values.
Paradoxically, those terms are among the least precisely known due to the difficulty of measurement and associated uncertainties. For instance, conducting precise evaluations of the contact angle near the bubble base through optical techniques can be challenging because of the strong temperature gradients close to the heated surface leading to a strong deformation of the bubble image.

Consequently, empirical choices have to be made in order to set a value to those parameters, often by relying on data-fitting or approximate measurements in other conditions. For instance, contact angles are often taken as arbitrary average values [138] or measurements in room conditions [151] and applied over a whole set of experiments. This is questionable since contact angle is unlikely to remain unchanged over different operating conditions and surfaces with varying roughness, properties and wall superheat. [149].

However, no better information except those given by the authors can be used to evaluate the capillary force since no generic model exist to compute the contact angle and hysteresis. In this work, admitting a significant uncertainty (typically 5°, as in Guan [63]), we will use the following values for the contact angles :

- $\theta_u = 25.3°$ and $\theta_d = 6.6°$ for Thorncroft data (measured values for FC-87 on nichrome [157]) ;
- $\theta_u = 50°$ and $\theta_d = 40°$ for Maity data (measured average contact angles for each bubble during its lifetime [108]) ;
- $\theta_u = 130°$ and $\theta_d = 65°$ for Chen data (chosen values in their study following measurements for water on stainless steel at high temperature by Kandlikar *et al.* [82]) ;
- $\theta_u = 91°$ and $\theta_d = 8°$ for Sugrue data (measured values at room temperature [153]) ;
- $\theta_u = 75°$ and $\theta_d = 30°$ for Guan data (measured average value through experimental visualizations [63]) ;
- $\theta_u = 45°$ and $\theta_d = 36°$ for Ren data (chosen values in their study [138]) ;
- $\theta = 80°$ for Kossolapov data (typical contact angle for water on ITO [90]) and $\mathrm{d}\theta = 1°$ assuming that the very small bubbles at high pressure are nearly not tilted.

Similarly, the bubble foot radius r_w is often empirically assumed to be either constant [84] proportional to the bubble radius [111, 151] or to follow a linear or logarithmic law of R [63, 181]. That is why we chose to use the truncated sphere hypothesis (Eq. 6.14) to compute r_w using R and θ.
Finally, we would like to acknowledge that the empiricism to evaluate those parameters represents one of the biggest flaws of the force-balance approach. Indeed, such a model aims to detect small sign changes in a sum of a few μN of forces that are decades larger as pointed out by Bucci *et al.* [18]. Mechanistic models are thus strongly sensitive to any extra parameter included in the modeling of the forces.

6.4.3.2 *Growth Constant Value*

As discussed in Section 6.3, a value close to one or lower for the constant K in the bubble growth rate usually provides reasonable approximation of the bubble radius. In particular, subcooled flow boiling may need smaller values of K, as well as fluids with high Prandtl numbers.

To avoid a systematic overestimation of the added mass term which could lead to strong underestimations of the departure diameter in cases that would present strong subcooling, liquid velocity or working fluids with low thermal conductivity, we will use:

$$K = \frac{2b}{\sqrt{\pi}},\ b = 0.24 \tag{6.110}$$

as proposed by Yoo *et al.* [172] to model the superheated liquid diffusion growth term.

6.4.3.3 *Predictions*

We consider the non-dimensional force balance before departure.

$$C_{AM,x}K^2\frac{\mathrm{Ja}_w^2}{\mathrm{Pr}_L}+\frac{1}{3}\frac{\mathrm{Re}_b}{\mathrm{Fr}}+\frac{1}{8}C_D\mathrm{Re}_b=\frac{1}{2}\frac{f_{C,x}}{\mathrm{Ca}} \tag{6.111}$$

Since we only have the capillary term hindering departure as a first approach, we can suppose that departure is reached when:

$$C_{AM,x}K^2\frac{\mathrm{Ja}_w^2}{\mathrm{Pr}_L}+\frac{1}{3}\frac{\mathrm{Re}_b}{\mathrm{Fr}}+\frac{1}{8}C_D\mathrm{Re}_b>\frac{1}{2}\frac{f_{C,x}}{\mathrm{Ca}} \tag{6.112}$$

which is similar to considering that the other forces overcome the capillary force.

On Figure 6.20, we show the predictions obtained with the proposed modeling and those obtained with Mazzocco's recent model [111] (see Table 6.2).

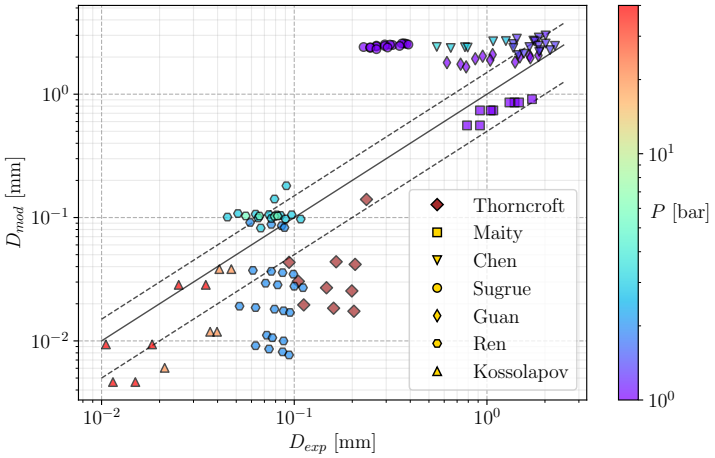

(a) Proposed model without accounting for contact angle uncertainties

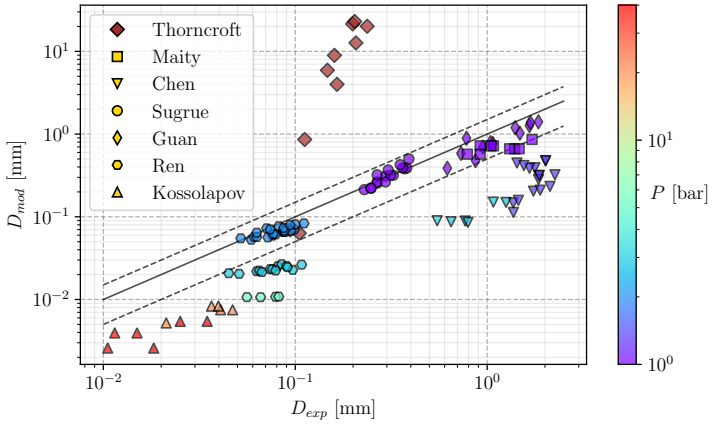

(b) Mazzocco model

Figure 6.20: Predicted bubble departure diameters. ±50% error bars are indicated.

The model has an acceptable trend on some experimental sets, but strong overestimation occur on the cases of Sugrue. Moreover, we observe significant underestimations on the data of Ren at 2 bar and Thorncroft.
Mazzocco's model provides a good accuracy on the data of Sugrue, Guan, Maity and Ren (2 bar). However, we observe very large overestimation over Thorncroft's measurements and significant underestimation on Chen, Ren (3 and 5 bar) and Kossolapov measurements.

6.4.4 *Discussion and accounting for parameters uncertainties*

The aforementioned errors observed for the proposed model may originate from various reasons:

- The contact angle proposed for Sugrue cases is high with a large hysteresis, suggesting strongly deformed and flattened bubbles under the truncated sphere hypothesis. Based on images from Sugrue's work [152], a comparison between a real bubble with the assumed shape is presented on Figure 6.21. This shows a huge difference which indicates that the contact angle and hysteresis values may be overestimated. Using the available images, the ratio of the bubble diameter to the apparent bubble foot would lead to an average contact angle $\theta \approx 20°$ for a truncated sphere. Noting that a larger inclination is observed for the bubbles under higher mass fluxes leads us to suppose a value $\mathrm{d}\theta \approx 15°$. This represent a similar inclination to contact angle ratio ($\mathrm{d}\theta/\theta$) compared to the initially proposed values. The resulting new shape is also presented on Figure 6.21 and seem to better represent the actual bubble.

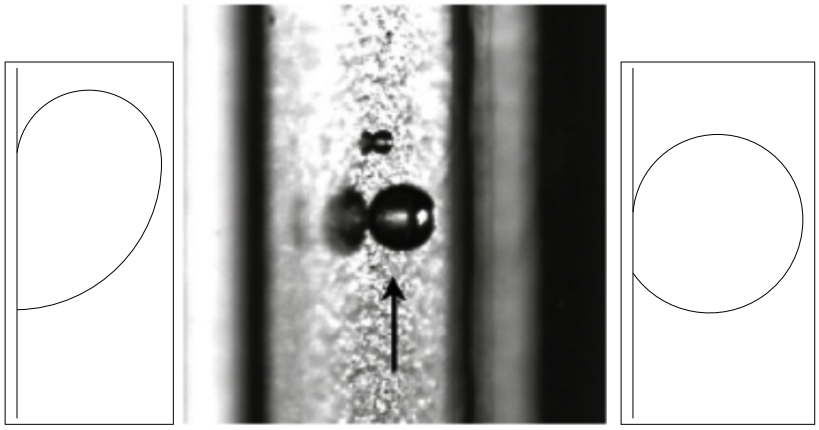

Figure 6.21: Initially assumed, real and reassessed bubble shape for Sugrue cases (picture adapted from [152]).

- For cases where limited under and overestimation is observed, we may allow to account for an uncertainty as high as 5° for the average contact angle θ and half-hysteresis $\mathrm{d}\theta$.
- As mentioned earlier, applying the same contact angle and hysteresis over a wide range of measurements is a strong assumption, especially for cases where different pressures and bubble diameter variations are observed. Thus, we may slightly distinguish the applied values of θ and $\mathrm{d}\theta$ for different pressures within a given experiment, keeping a change no larger than 5°.
- Kossolapov cases at $G_L = 500$ kg/m^2/s are better predicted. Cases under higher mass fluxes (1000 and 1500 kg/m^2/s) present underestimation that could come from the value of $\mathrm{d}\theta$. At such mass fluxes, the Weber number can be up to a decade higher and bubbles may thus accept a larger inclination before detachment.
- Cases of Ren and Chen rely on chosen values for θ and $\mathrm{d}\theta$ and not on measured ones. They are therefore subject to strong uncertainties. We can note that the values for Chen cases are significantly high.
- The proposed growth law is still rather simple and may miss significant information, especially regarding bubble size and fluid properties such as the Prandtl number.
- Errors on Thorncroft cases may be linked to uncertainties regarding FC-87 properties. Indeed, we use the values given at $T_{sat} = 29°$ at 1 bar in his work [156]. However, the saturation temperature indicated in his test matrix is close to 40° which means that measurements were conducted at a higher pressure, for which we do not have FC-87 properties.

Therefore, using modified values of θ and $\mathrm{d}\theta$ among experimental data sets with no more than a 5° change (except for Sugrue cases reassessed values) leads to predictions on Figure 6.22.

The predictive capacity of the model is significantly enhanced, especially on Sugrue's cases which tends to indicate that the contact angle reassessment was justified under the truncated sphere hypothesis. Table 6.4 summarizes the average errors obtained with the present model and Mazzoco's one.

Author	θ [°]	dθ [°]
Thorncroft	21	14
Maity	45	10
Chen	92.5	27.5
Sugrue	20	15
Guan	47.5	17.5
Ren (2 bar)	45.5	7.5
Ren (3 bar)	37.5	3.5
Ren (5 bar)	35.5	3.5
Koss. (500 kg/m^2/s)	80	0.5
Koss. (1000 kg/m^2/s)	80	1
Koss. (1500 kg/m^2/s)	80	1.5

(a) Modified contact angle and hysteresis values.

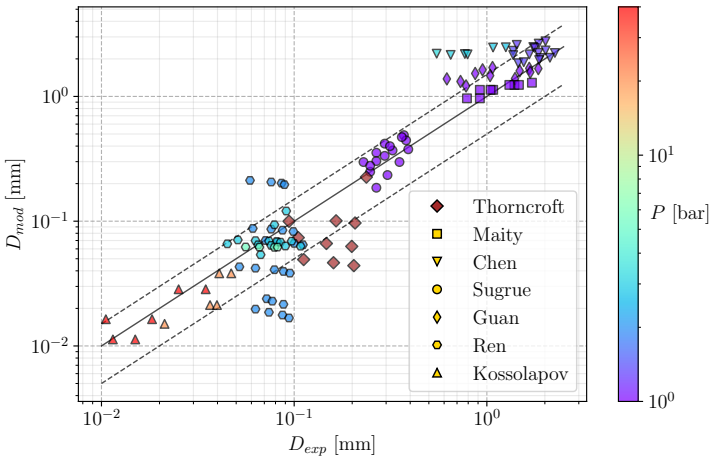

(b) Predicted bubble departure diameters.

Figure 6.22: Proposed model performance while accounting for contact angle uncertainties

The proposed model achieves an overall better predictive capability even when excluding measurements from Thorncroft on which Mazzocco's model strongly overestimates the departure diameter. Mazzocco's model is still better on Sugrue and Guan cases since it was built and validated using those measurements. It better predicts results from Ren but only for the 2 bar cases while it underestimates the departure diameter for higher pressures. Those results are a coupled effect of his optimized growth law along with the imposed value of r_w/R and the use of the inclination angle to hinder departure as mentioned in 6.2.6.

Author	Mazzocco	Present model
Thorncroft	4874%	46.2%
Maity	39.7%	13.8%
Chen	83.8%	73.6%
Sugrue	9.73%	21%
Guan	25.5%	44.5%
Ren	40.32%	47%
Kossolapov	78.3%	24.2%
Total (without Thorncroft)	46.58%	43.3%

Table 6.4: Average relative error reached by the models.

The approach demonstrated the importance and the strong influence of the contact angle and hysteresis. A small change of their value (staying in the uncertainty range of 5°) allowed to reach reasonable predictions over a large range of bubble departure diameters with the proposed model, using a reduced number of empirical parameters.

6.5 SLIDING PHASE

6.5.1 *Modeling*

After departure, bubbles slide over a distance l_{sl} which scales the impact of the sliding phenomenon over the wall heat transfer. Achieving good prediction of bubble sliding velocity is then important if one wishes to correctly quantify its impact. Following the force balance framework presented in Section 6.2, we can write Newton's second law parallel to the wall for the sliding bubble.

$$\begin{aligned}\rho_V \frac{\mathrm{d}\left(V_b U_b\right)}{\mathrm{d}t} =& -\pi R \sigma f_{C,x} + \frac{4}{3}\pi R^3 \left(\rho_L - \rho_V\right) g + \frac{1}{2} C_D \rho_L \pi R^2 U_L^2 \\ &+ \frac{4}{3}\pi R^3 \rho_L \left[3 C_{AM,x} \frac{\dot{R}}{R} U_{rel} - C_{AM,x} \frac{\mathrm{d}U_b}{\mathrm{d}t}\right]\end{aligned} \tag{6.113}$$

This equation can be re-written to express the bubble acceleration.

$$\begin{aligned}\left(1 + \frac{\rho_L}{\rho_V} C_{AM,x}\right) \frac{\mathrm{d}U_b}{\mathrm{d}t} =& \left(\frac{\rho_L}{\rho_V} - 1\right) g + \frac{3}{8} \frac{C_D}{R} \frac{\rho_L}{\rho_V} \left(U_L - U_b\right) \left|U_L - U_b\right| \\ &+ 3 \frac{\dot{R}}{R} \left[C_{AM,x} \frac{\rho_L}{\rho_V} \left(U_L - U_b\right) - U_b\right] - \frac{3}{4} \frac{\sigma}{\rho_V} \frac{f_{C,x}}{R^2}\end{aligned} \tag{6.114}$$

Then, we numerically solve this equation from the moment when $R \geq R_d$ using a first order Euler scheme for a duration close to the experimental sliding time. To assess the validity of Eq 6.114, we modify the growth constant K in order to roughly match experimental radius measurements. The goal is to verify if the force balance allows a good prediction of bubble velocity provided a correct bubble growth. Next sections compare obtained results against low and high pressure data.

6.5.2 *Low Pressure Sliding*

Maity [108] provided simultaneous measurements of bubble radius and velocity over time in vertical boiling for three liquid mass fluxes near saturation conditions. The contact angles were kept the same as in 6.4.3 since Maity provided average values over the bubble lifetime.

Results are displayed on Figure 6.23. The model seems to fairly good predict bubble sliding velocity for the 3 cases. The moment of departure is a bit underestimated as previously observed (Figure 6.20).

The biggest discrepancy is observed for the case at $G_L = 143.8$ kg/m^2/s. The slope of the velocity profile is close to the experiments, but the bubble reaches a nearly constant acceleration too rapidly which yields an approximately constant overestimation of 0.1 m/s.

The case with $G_L = 239.6$ kg/m^2/s is well predicted regarding the velocity. However, the growth profile was difficult to match since measurements exhibit significant changes in growth regime after departure, which is probably due to the bubble being large enough to be impacted by the bulk flow. We can note that values of K between 0.5 and 1 were used to better fit the bubble radius time profile.

Regarding the relative velocity between the bubble and the surrounding liquid, the ratio $\frac{U_b}{U_L}$ greatly overcomes 1 which means the bubble slides much faster than the liquid. This is a consequence of both the low values of G_L along with the large bubble sizes inducing a great acceleration by the buoyancy force.

6.5.3 *High Pressure Sliding*

In his work, Kossolapov [90] conducted measurements of radius and sliding length over thousands of individual bubbles and then provided the associated statistical distributions. To compare our model with his measurements, we took the upper and lower bounds of R and l_{sl} over time and plotted the associated bands of measured values as shown on Figure 6.24 and 6.25.

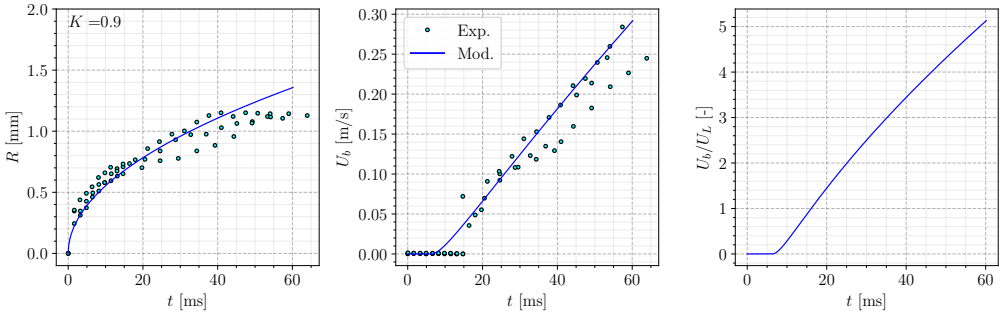

(a) $\Delta T_w = 5.0°C$, $G_L = 73.8$ kg/m^2/s

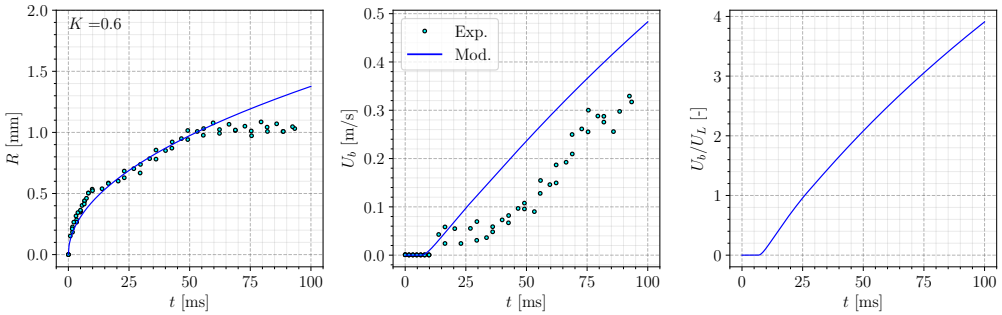

(b) $\Delta T_w = 5.9°C$, $G_L = 143.8$ kg/m^2/s

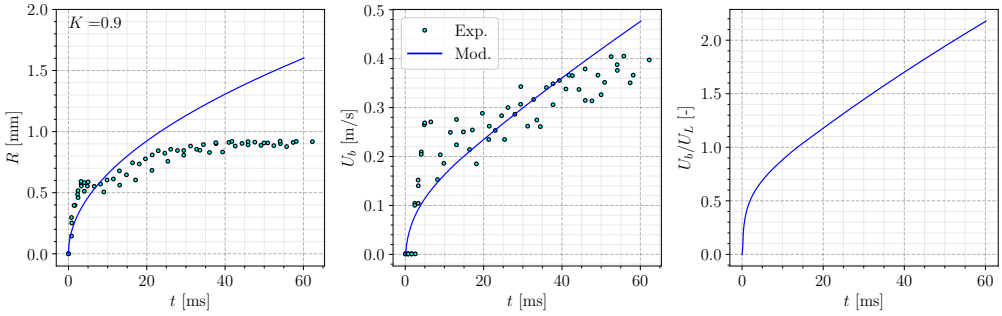

(c) $\Delta T_w = 5.9°C$, $G_L = 239.6$ kg/m^2/s

Figure 6.23: Bubble sliding velocity predictions on Maity cases

Comparisons were done for cases at 20 bar and 40 bar and 3 different values of G_L. The value of dθ for the simulations was kept really small (2° at 20 bar and 0.5° at 40 bar) since bubble tilt is supposed to reduce during sliding because the relative velocity regarding the liquid flow is diminishing. Moreover, higher pressure means smaller bubbles that are even more unlikely to present a significant contact angle hysteresis. We also want to mention that neglecting the capillary term in Eq. 6.114 had a minor impact over the results except that the bubble accelerates a little bit faster.

The obtained results are in good agreement with the sliding length profile vs. time, which means bubble sliding velocity is well predicted for those cases. Values of K between 0.8 and 2 were needed to match the bubble radius measurements.

We see that bubbles are rapidly reaching sliding velocities between 80% and 95% of the local liquid velocity. Only the 20 bar case at $G_L = 500$kg/m^2/s where the bubble departs slightly later, reaching approximately 55% of the liquid velocity.

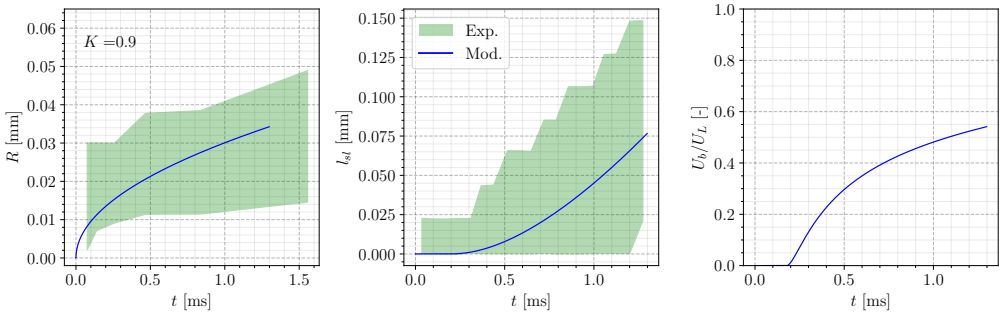

(a) $\phi_w = 0.178$ MW/m^2, $\Delta T_w = 12.6$K, $G_L = 500$ kg/m^2/s

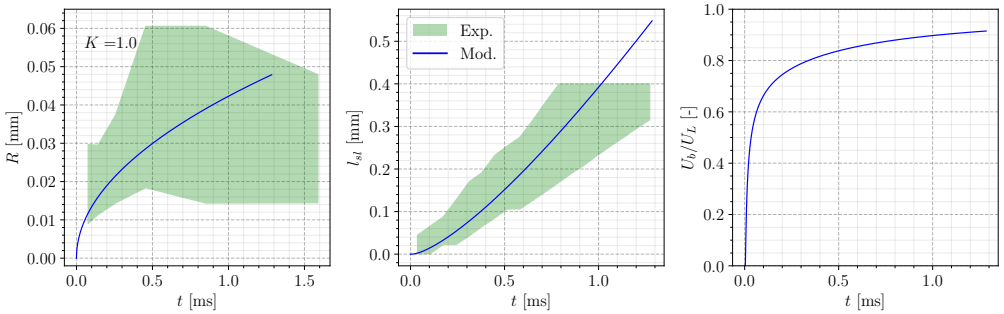

(b) $\phi_w = 0.495$ MW/m^2, $\Delta T_w = 16.1$K, $G_L = 994$ kg/m^2/s

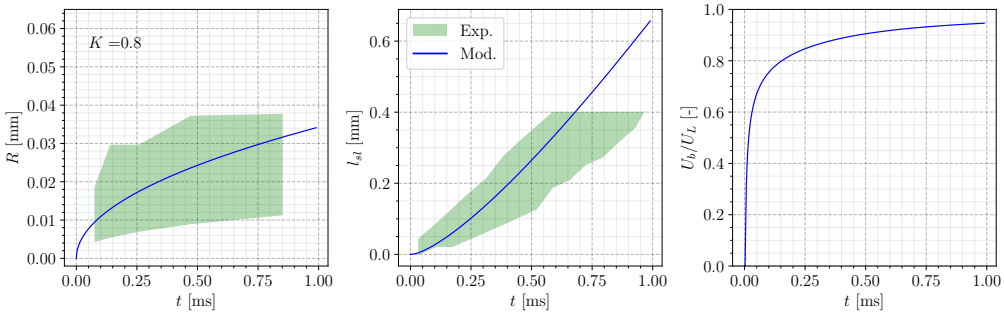

(c) $\phi_w = 0.487$ MW/m^2, $\Delta T_w = 16.2$K, $G_L = 1504$ kg/m^2/s

Figure 6.24: Bubble sliding length predictions on Kossolapov cases - $P = 20$ bar

6.5.4 *Comparison of Forces in Sliding Stage*

In order to identify the main accelerating forces, we compare the amplitude of the forces during the sliding phase for one low pressure case of Maity and one high pressure case of Kossolapov (Figure 6.26).

It appears that at high pressure and liquid velocity, the drag force is the main driving force and stays positive since the bubble do not slide faster than the rapid surrounding liquid (reaching approximately 80% of the local liquid velocity). On the other hand, larger bubbles observed at low pressure and liquid velocity are accelerated by buoyancy due to their larger volume, with a nearly negligible Drag force. In both cases, the added mass force can not be neglected especially when bubble velocity rises by limiting its acceleration induced by the larger force (buoyancy or drag in the presented cases). This further emphasizes the importance of a proper derivation of the added mass force regardless of the boiling conditions. The capillary force seem to be a limited but constant slowing term in both cases. Finally, the amplitude of the forces involved can span from roughly 10×10^{-4} N at low pressure (much greater than the rate of change of bubble momentum laying around 10^{-9} N) down to a few nN at higher pressure (same order of magnitude as the rate of change of bubble momentum), especially due to the bubble size.

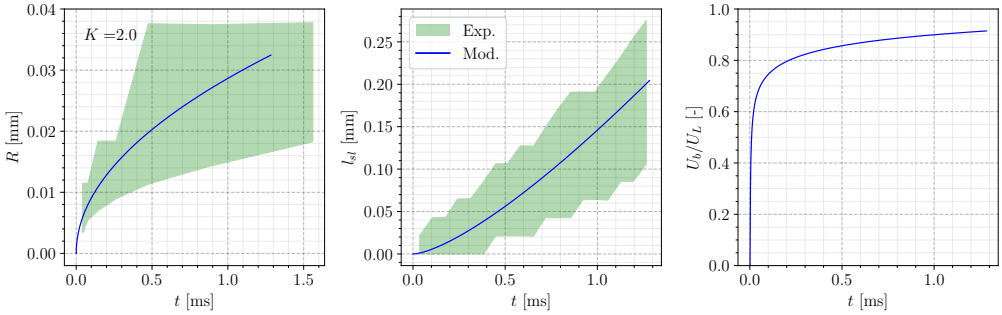

(a) $\phi_w = 0.291$ MW/m^2, $\Delta T_w = 10.1$K, $G_L = 500$ kg/m^2/s

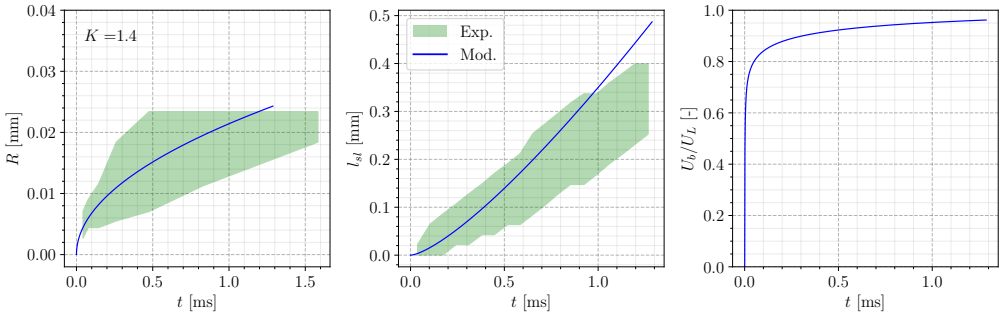

(b) $\phi_w = 0.361$ MW/m^2, $\Delta T_w = 10.8$K, $G_L = 994$ kg/m^2/s

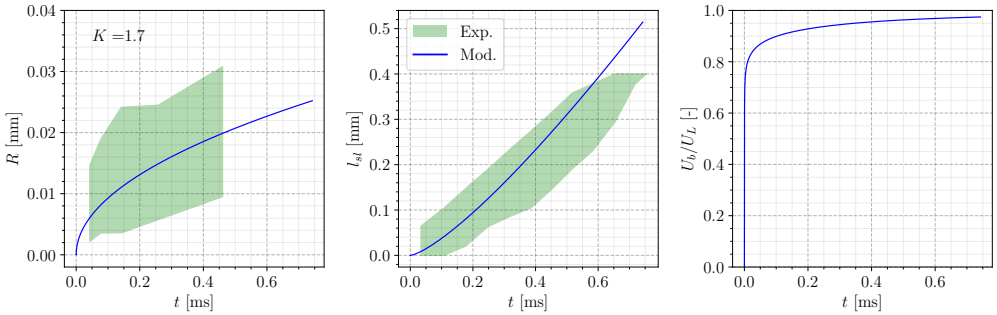

(c) $\phi_w = 0.613$ MW/m^2, $\Delta T_w = 12.2$K, $G_L = 1504$ kg/m^2/s

Figure 6.25: Bubble sliding length predictions on Kossolapov cases - $P = 40$ bar

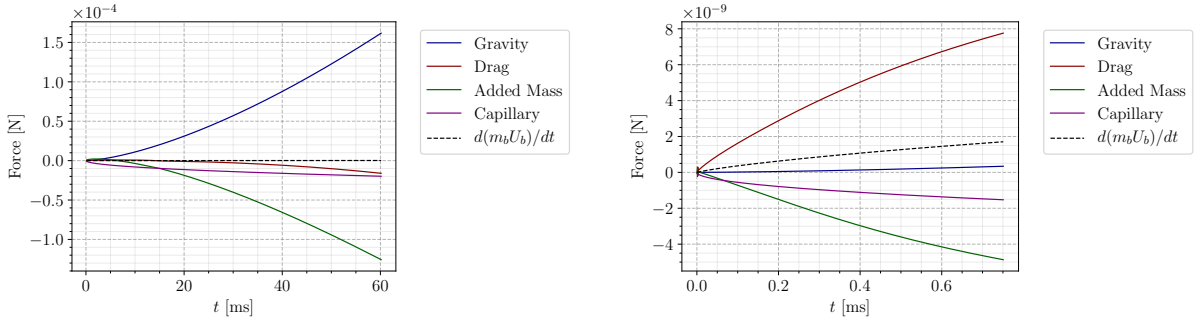

(a) Maity : $\Delta T_w = 5.9°$ C, $G_L = 239.6$ kg/m^2/s

(b) Kossolapov : $P = 40$ bar, $\phi_w = 0.613$ MW/m^2, $G_L = 1504$ kg/m^2/s

Figure 6.26: Amplitude of each force during sliding

This comparison highlights the fact that the proposed model is able to represent different forces hierarchy depending on the flow conditions and to acceptably predict the associated bubble sliding velocity, which is an encouraging point regarding its generality.

6.6 BUBBLE LIFT-OFF

6.6.1 *Introduction*

The question of lift-off for a single bubble in vertical boiling is trickier than for horizontal boiling. Indeed, in horizontal boiling, lift-off is ensured thanks to the buoyancy force that will continuously increase as the bubble grows. It can also be promoted by the lift force if the bubble slides slower than the liquid. This facilitates the identification of the moment when bubble leaves the surface (Figure 6.27).

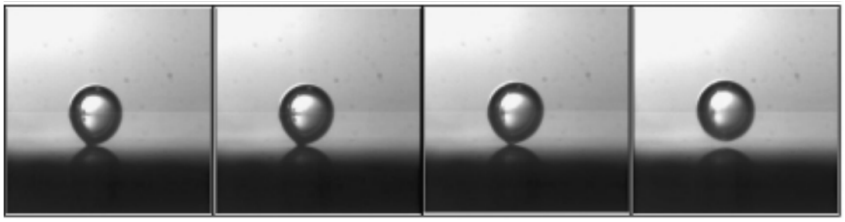

Figure 6.27: Visualization of bubble lift-off in horizontal boiling conducted by and adapted from Maity [108]. The detachment the the bubble base from the surface is clear in the last frame.

However, in vertical boiling, the lift-off from the surface only results of the competition between the added mass force and lift force (capillary force and contact pressure compensating each other for a truncated sphere). The added mass force keeps the bubble attached and the lift force which can either promote lift-off or push the bubble against the wall depending on the value of the lift coefficient C_L. As seen in Subsection 6.2.5, the lift coefficient can become negative when reaching negative relative velocity U_{rel}, yielding negative non-dimensional shear rates Sr in Eq. 6.44. In this case, the force balance perpendicular to the wall (Eq. 6.70) will never become positive and thus never predict bubble lift-off using criterion based on the force balance sign.
In addition, those two forces are difficult to precisely evaluate since they rely on complex phenomena such as the bubble growth (R, $\dot{R}$, $\ddot{R}$) and the fine hydrodynamics of a bubble attached to a wall. A small error on the evaluation of one of those forces can therefore lead to erroneous predictions of the lift-off phenomenon.

On the experimental side, different behavior for boiling bubbles in vertical boiling have been observed. Single bubble experiments such as those of Maity [108] and Situ *et al.* [148] observed bubble lift-off for single bubble at atmospheric pressure as shown on Figure 6.28.

Although bubble lift-off is observed for those single bubble cases, the exact moment of lift-off is complicated to identify since the bubbles sometimes stay very close to the wall and can even re-attach to the wall, presenting a bouncing motion while moving close to the wall as in Yoo *et al.* [170].

Contrary to those observations, other authors who realized experimental visualizations of vertical flow boiling of surfaces with numerous bubbles saw that single bubbles did not leave the wall by themselves. For instance, Scheiff [145] observed different possible behaviors in highly subcooled liquid:

- Bubble growth up to an equilibrium diameter while sliding on the wall and keeping the same size.
- Rapid sudden growth of bubbles can enlarge them up to the subcooled liquid, yielding to condensation while sliding on the wall.
- Bubble lift-off under application of a high heat flux (rapid growth) or after coalescence with an other bubble on its path.

Similar behaviors of bubbles sliding along the wall and not leaving it until a coalescence occurs have also been reported for vertical flow boiling by Prodanovic *et al.* [131] or Thorncroft *et al.* [156]. In particular, Prodanovic *et al.* mentioned that bubbles that would detach from the wall by themselves cannot be interpreted as typical bubble behavior in those conditions since there were very few of them. Typical experimental visualizations of this nature are presented on Figure 6.29.

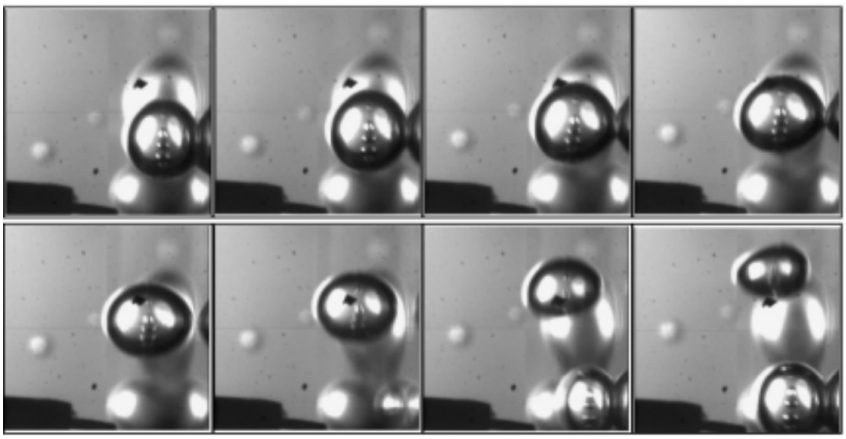

(a) Lift-off observed in Maity experiment [108]

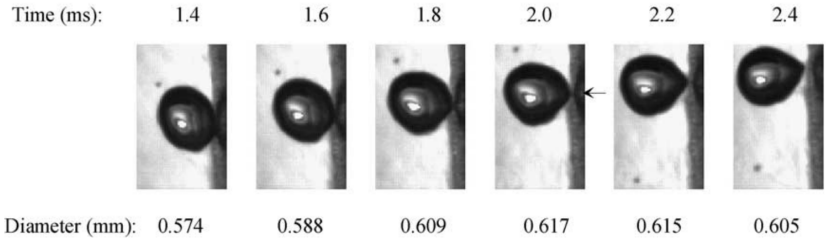

(b) Lift-off observed in Situ experiment [148]

Figure 6.28: Visualization of bubble lift-off in vertical boiling. The moment when bubble leaves the surface appears less clearly than for horizontal boiling.

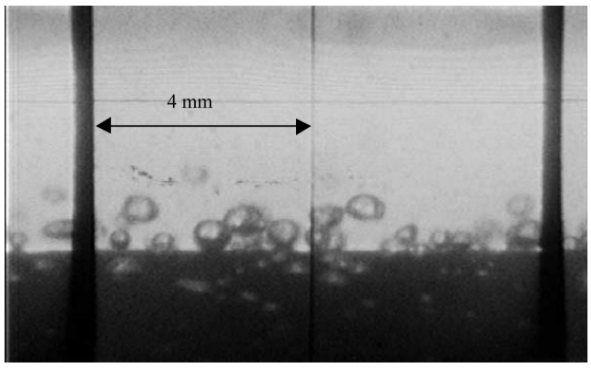

(a) Boiling visualization by and adapted from Prodanovic *et al.* [131] in the region where bubble coalescence started to occur.

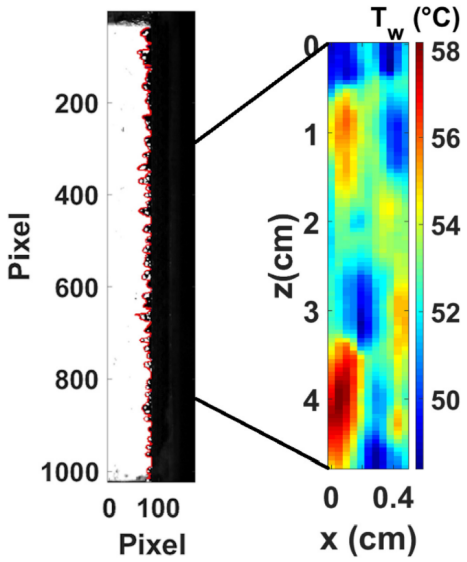

(b) Boiling visualization by and adapted from Scheiff *et al.* [144], highlighting the observed layer of sliding bubbles.

Figure 6.29: Visualization of boiling surfaces in vertical boiling, where single bubble lift-off is not systematically observed.

Generally speaking, it seems that single bubbles in vertical boiling are not likely to present a lift-off behavior by themselves in every flow conditions that could be explored. **As concluded by Okawa *et al.* [127] and discussed in Yoo *et al.* [170], it seems that a more general trigger for bubble**

lift-off would be either associated to strong deformation / elongation of the bubble shape (inducing a change in the lift coefficient) or to a coalescence event between two bubbles.

> **Note :** Such a lift-off mechanism is considered by Gilman & Baglietto [59] who consider lift-off when the Eotvös number of the bubble reaches 0.1.

To further discuss this question, we will nevertheless try to consider the bubble lift-off as a single event and therefore try to attribute a given lift-off diameter D_{lo} based on available experimental measurements.

6.6.2 *Experimental Measurements of Lift-Off Diameter*

Observations and measurements of bubble diameter in various flow conditions have been conducted by numerous authors since the middle of the XX$^{\text{th}}$ century. Although recent experimental techniques allow to identify the moment at which bubble diameter is measured (departure from nucleation site, lift-off, etc.), older experiments could not ensure the nature of the bubbles that were observed.

For instance, the work of Ünal [186] measured the maximum bubble diameter and used other experimental results (Gunther [68], Griffith [61], Treshchev [161] and Tolubinsky [158]) to build a correlation. However, it can not be clearly stated that those measurements were single bubbles lifting off the surface or bubbles resulting of coalescence.

> **Remark :** As explained by Ünal, their measurements (detailed in De Munk [120]) are based on enlarged photographic observations of the bubble population near the boiling surface from which they extracted the maximum diameter, meaning there is no evidence that it was actually a lift-off diameter of a single bubble.

This was also pointed out by Kossolapov [90] who showed that at very high pressure, old measurements of bubble diameter were larger for flow boiling compared to pool boiling, which is intuitively nonphysical. This could be explained as mentioned above if those measurements were actually coalesced bubbles which would naturally exhibit larger diameters than single bubbles at lift-off.

However, those measurements can still be interesting since their evolution with the operating conditions should present trends similar to single bubble experiments. To do so, we gathered several experimental data sets of maximum / lift-off diameter from the literature for vertical subcooled flow boiling of water. The experimental conditions of the data set are presented on Table 6.5.

6.6.3 *Influence of the Flow Boiling Conditions*

To evaluate the influence of the flow boiling conditions over the various experimental measurements, we have represented the values of the non-dimensional lift-off diameter $\dfrac{D_{lo}}{L_c}$ (L_c is the capillary length) versus 6 dimensionless flow parameters:

- The reduced Jakob numbers of superheat and subcooling Ja_w^* and Ja_L^*. With $\text{Ja}^* = \dfrac{c_{p,L}\Delta T}{h_{LV}}$ which excludes the impact of pressure through the density ratio.
- The density ratio $\rho^* = \dfrac{\rho_L}{\rho_V}$, scaling the operating pressure.
- The saturated liquid Prandtl number Pr_L, quantifying the liquid thermal properties.
- The local wall Reynolds number $\text{Re}_\tau = \dfrac{\rho_L U_\tau L_c}{\mu_L}$, evaluating the impact of the liquid flow, with U_τ the shear friction velocity as in Eq. 6.73.
- The capillary number Ca which can be related to bubble deformation under viscous effects.

Author	Fluid	D_h [mm]	P [bar]	G_L [kg/m^2/s]	ΔT_L [K]	ϕ_w [kW/m^2]	ΔT_w [K]	D_{lo} [mm] (N_{mes})
Gunther [68] (1951)	Water	6.92	1 - 1.7	1492 - 6070	33 - 86	2.3 - 10.64	N.A.	0.32 - 1.02 (12)
Griffith [61] (1958)	Water	12.7	34.5 - 103	4651 - 7593	11 - 80	3.25 - 8.53	N.A.	0.081 - 0.146 (6)
Treshchev [161] (1969)	Water	10.18	5 - 50	1643 - 1789	30 - 62	1.4 - 2.9	N.A.	0.12 - 0.26 (3)
Tolubinsky [158] (1970)	Water	10	1 - 10	72.6 - 198.4	5 - 60	0.47	N.A.	0.19 - 1.24 (9)
Ünal [186] (1976)	Water	8	139 - 177	2082 - 2171	3 - 5.9	0.38 - 0.55	N.A.	0.11 - 0.18 (7)
Maity [108] (2000)	Water	20	1.01	0 - 239.6	0.3 - 0.7	N.A.	5 - 5.9	1.8 - 2.4 (4)
Prodanovic [131] (2002)	Water	9.3	1.01 - 3	76.7 - 815.8	10 - 60	0.1 - 1.2	N.A.	0.366 - 2.68 (44)
Situ [148] (2005)	Water	19.1	1.01	471.8 - 910.8	1.5 - 20	0.06 - 0.2	N.A.	0.145 - 0.605 (90)
Chu [20] (2010)	Water	22.25	1.45	301 - 702	3.4 - 22.6	0.135 - 0.201	N.A.	0.51 - 1.71 (14)
Ahmadi [1] (2012)	Water	13.3	0.96 - 1.13	169 - 497	8.4 -20.6	0.16 - 0.318	11.4 - 18.4	0.12 - 3.9 (13)
Okawa [128] (2018)	Water	14	1.27 - 1.86	252 - 490	10 - 39	0.161 - 0.487	N.A.	0.64 - 0.188 (10)

Table 6.5: Bubble lift-off diameters data sets in vertical flow boiling

The results are presented on Figure 6.30.

The experimental values of $\frac{D_{lo}}{L_c}$ display the following trends:

- Increase with Ja_w^* ;
- Decrease with Ja_L^* ;
- Increase with ρ^* ;
- Increase with Pr_L ;
- Decrease with Re_τ and Ca.

A great range of D_{lo} values at low pressure (for which we have the larger number of measurements) are reached in the experiments. This further indicates the complicated behavior of bubble lift-off, for which similar flow conditions can lead to very different bubble diameters.

Remark : This variation could be associated to the heater material and surface morphology, which are not quantified here.

Moreover, we can observe that measurements from Ünal do not follow the general tendency of other data as on Figure 6.30c, with values of D_{lo}/L_c above the trend, further supporting the assumption that those experimental values were actually those of coalesced bubbles.

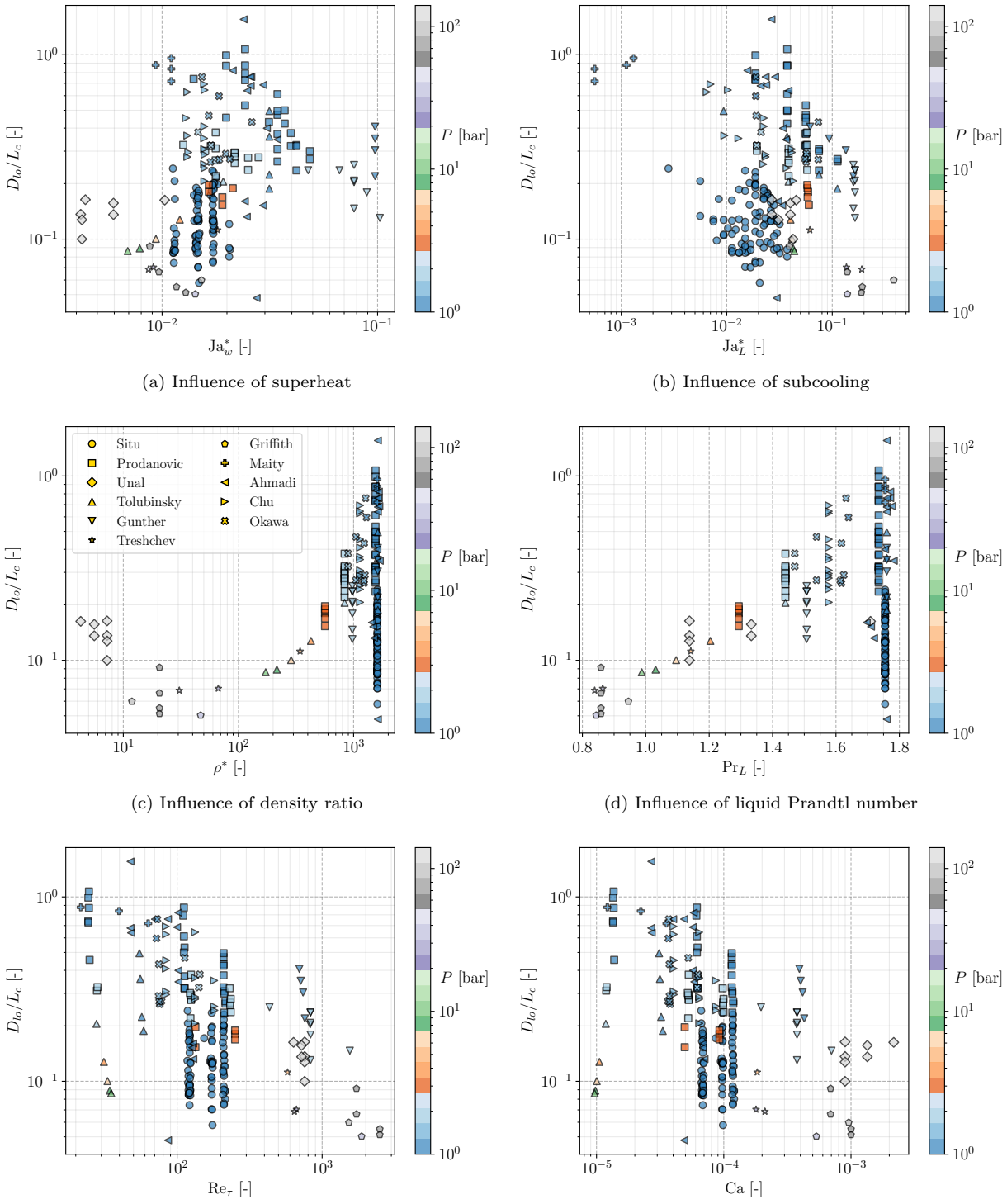

(a) Influence of superheat

(b) Influence of subcooling

(c) Influence of density ratio

(d) Influence of liquid Prandtl number

(e) Influence of Reynolds number

(f) Influence of capillary number

Figure 6.30: Evolution of D_{lo}/L_c depending on the flow conditions.

6.6.4 *Predicting the Lift-Off with a Force Balance*

As previously discussed, the prediction of the lift-off using the force balance perpendicular to the wall (Eq. 6.70) is complicated because:

- The spherical shape without tilt ($\mathrm{d}\theta = 0$) leads to exact compensation between contact pressure force and capillary force. Leaving only the added mass force and lift force to predict the lift-off.

- Those two forces can both be directed towards the wall depending on the flow conditions, making it impossible for a single bubble to lift-off by itself.
- The estimation of those forces rely on complicated description of thermal and hydrodynamic phenomena, making any uncertainty a source of large errors on lift-off prediction.

This difficulty has already been pointed out by Montout [119] who faced difficulties in consistently using the force balance perpendicular to the wall for bubble lift-off. Depending on the flow conditions, the force balance would sometimes predict an immediate lift-off right after or even before departure by sliding, which is in contradiction with aforementioned experimental observation.

Following a similar approach to the departure diameter (Section 6.4), we can rearrange Eq. 6.70 into the following non-dimensional force balance perpendicular to the wall, supposing that $U_{b,y} = \dot{R}$:

$$\underbrace{\rho^* \left(\frac{C_L}{8} + \frac{C_{AM,y3}}{3} \right)}_{\text{Promotes lift-off}} - \underbrace{\frac{1}{3} \left[\rho^* \left(2C_{AM,y1} + C_{AM,y2} \right) + \frac{2}{3} \right] \left(\frac{K^2 \mathrm{Ja}_w^2}{\mathrm{Pr}_L \mathrm{Re}_b} \right)^2}_{\text{Hinders lift-off}} > 0 \tag{6.115}$$

This formulation sums up the competition between the lift-off promoted by the first term on the LHS combining effect of the lift force and the added mass force due to the external flow versus the growth terms that will hinder the lift-off by pushing the bubble against the wall.

Remark : Eq. 6.115 mathematical formulation present some coherent trend with physical observations:

- The hindering term will increase with bubble growth rate (*i. e.* Ja_w increase) thus increasing R_{lo} ;
- The hindering term will reduce with the liquid velocity (*i. e.* Re_τ or Re_b increase), thus reducing R_{lo}.

Other influence of the flow parameters are less directly possible to anticipate.

The solving of the equation of bubble departure (Eq. 6.106) and sliding (Eq. 6.114) while checking when Eq. 6.115 detects lift-off can be performed to estimate the lift-off diameter D_{lo}. Applied over the experimental database of Table 6.5, this yields the predictions of Figure 6.31.

First, it is important to note that among every experimental data used for comparisons, many points did not converge to a lift-off diameter value, Eq. 6.115 failing to become positive at any moment of the simulated bubble lifetime. As a consequence, 61 measurements (27 from Prodanovic, 5 from Tolubinsky, 3 from Maity, 13 from Ahmadi, 6 from Chu, 7 from Okawa) out of 211 could not be compared to the force balance approach.
For the converged cases, this yields an acceptable order of magnitude at low pressure especially for Situ data. On the contrary, high pressure measurements are greatly underestimated with lift-off diameters lower than 1μm.

At last, even though the force-balance approach presents many interests for modeling grounds, its application to lift-off prediction in vertical boiling seems a bit tricky contrary to the departure by sliding. The sole competition based on fine hydrodynamics (lift and added mass) and the bubble growth (for which a proper complete modeling is still unavailable) makes it a very complicated solution to address the lift-off diameter estimation problem.

6.6.5 *A Simple Non-Dimensional Correlation*

Alternatively, in case it would prove to be necessary to define a lift-off diameter value for the HFP model, we propose a simple direct correlation based on non-dimensional parameters characterizing the boiling conditions. We chose to model the value of the non-dimensional lift-off diameter D_{lo}/L_c using the liquid Prandtl number Pr_L at saturation, the density ratio $\rho^* = \rho_L/\rho_V$, the reduced Jakob numbers Ja_w^* and

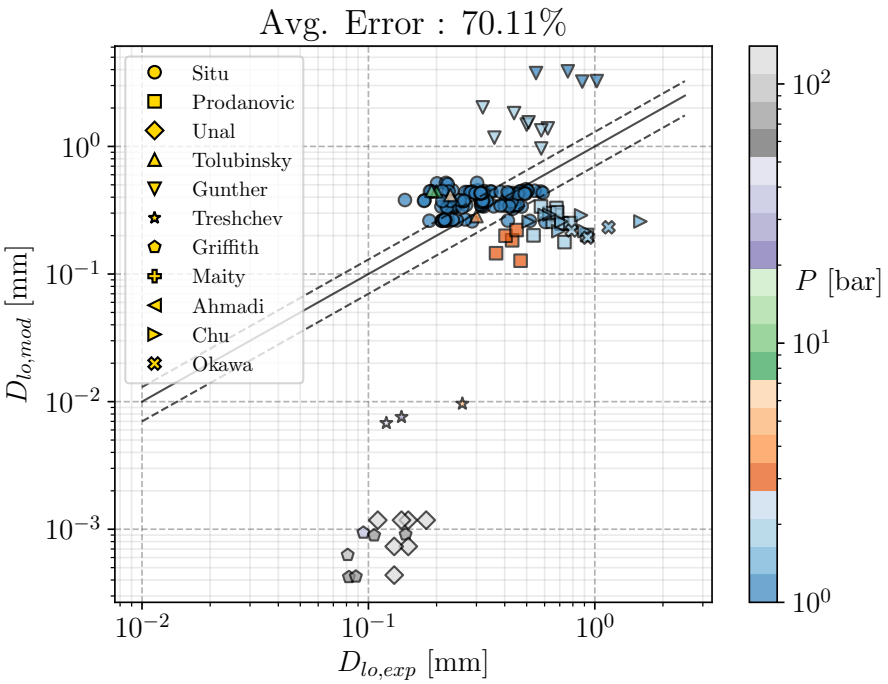

Figure 6.31: Prediction of Eq. 6.115 versus data from Table 6.5. Value of $K = 0.24$ (same as in Figure 6.22) was used and only converged points are presented.

Ja_L^* and the wall Reynolds number Re_τ. Using the `sklearn` module to estimate the value of the coefficient for the multilinear regression over the data of Table 6.5 yields:

$$\frac{D_{lo}}{L_c} = e^{8.43}\mathrm{Pr}_L^{-0.005}\left(\frac{\rho_L}{\rho_V}\right)^{-0.36}\mathrm{Ja}_w^{*\,1.15}\left(1+\mathrm{Ja}_L^*\right)^{-6.68}\left(1+\mathrm{Re}_\tau\right)^{-0.53} \tag{6.116}$$

We chose to correlate $(1+\mathrm{Ja}_L)$ and $(1+\mathrm{Re}_\tau)$ so that the formulation degenerates those terms to 1 for saturated and pool boiling conditions. This simple care is often forgotten in similar approaches [89, 180] where the resulting correlations either diverges or tend to 0 when reaching those conditions.

The correlation is compared to Kommajosyula's correlation [89] on Figure 6.32.
The proposed formulation, though simple, allows to reach an average error of approximately 45% over the whole data set versus approximately 94% of error for Kommajosyula's formulation. Even if the approach may lack of detailed physical modeling, it seems appropriate to obtain an acceptable order of magnitude of the lift-off (or maximum observed) bubble diameter over various flow conditions including high pressure.

Remark : The use of Re_τ instead of the bulk liquid velocity of Reynolds number allows the correlation to be more easily applied in CFD computations where obtaining bulk quantities from wall cells can be tricky depending on the geometry.

6.6.6 *Conclusion on the Lift-Off*

As discussed in this section, the question of the bubble lift-off in vertical flow boiling is very complicated and can not be answered in a straightforward way. First, we saw that the lift-off is not always observed for individual bubbles that can slide for a very long time before leaving the surface as a result of a coalescence by colliding with an other bubble. This difficulty was also experienced when using the force-balance approach to predict the lift-off diameter, with bubble lifetime and sliding simulations that would not converge, *i. e.* yield a positive force balance perpendicular to the wall that would detach the bubble.

Moreover, existing database, though diverse, are lacking of high pressure measurements using recent experimental techniques. The existing high-pressure data present a qualitative uncertainty regarding the nature of the measured bubbles that can result of coalescence events.

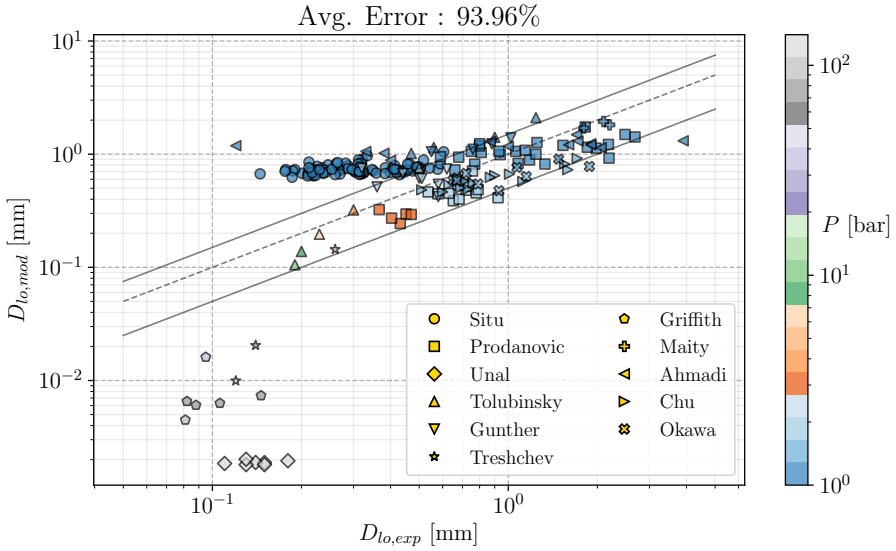

(a) Prediction with Kommajosyula correlation [89]

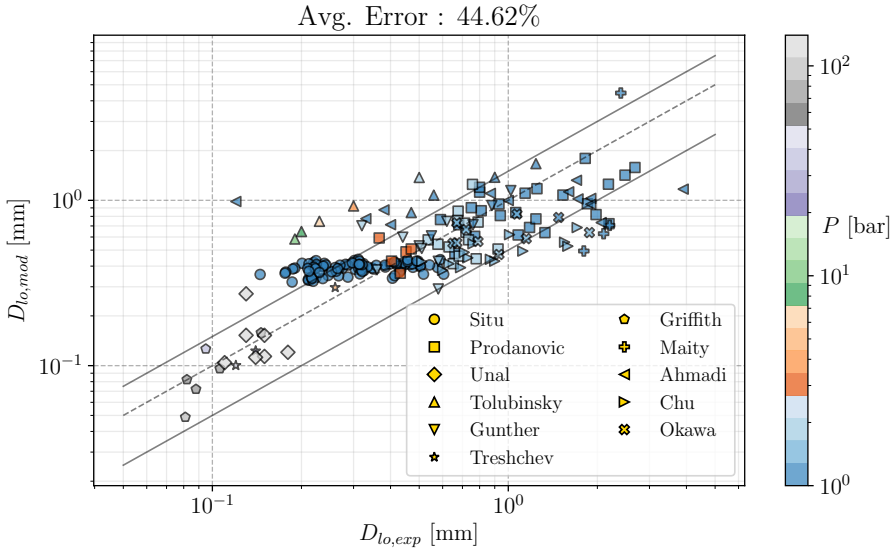

(b) Prediction using Eq. 6.116

Figure 6.32: Comparison of simple direct correlations with data from Table 6.5

Finally, the question of lift-off in the framework of the HFP model can be answered in three ways:

1) No lift-off diameter value is attributed to single bubbles. It is thus computed by solving the bubble sliding until it collides and coalesces with an other bubble growing on its nucleation site. This approach is likely to be the most representative of the general behavior of bubbles in vertical boiling according to experiments. However, it may lead to very large, if not nonphysical, values of sliding length at low heat fluxes values where the average distance between bubbles would increase greatly.

2) Same as above 1) but the lift-off is considered when a non-dimensional number representative of bubble deformation reaches a critical value. Several bubble coalescence can thus occur until that moment occurs.

3) A lift-off / maximum diameter is attributed for single bubble behaviors and sliding is computed between the fixed values of D_d and D_{lo}, with coalescence that can be considered between those two events and trigger earlier lift-off. This choice would be in fewer concordance with experimental observations but would allow to consider distinct bubble lifetime scenario including full single bubbles.

6.7 CONCLUSION

In this chapter, we discussed the different aspects of boiling bubble dynamics in vertical flow boiling. This is a pivotal aspect of the HFP to reach modeling representative of the boiling phenomenon. However, the great variety of both experimental observations and existing models demonstrate the high complexity of the physics at stake here. At last, we can conclude that:

- The problem of bubble growth in complicated conditions (external flow, subcooling, wall presence) remains an open question that could benefit from new experimental insights trying to account for those effects. A new model based on simple heat diffusion accounting for subcooling was proposed and could achieve better predictions compared to traditional model when using a correct value of the thermal boundary layer thickness δ. However, a general precise estimation of δ is complicated and simpler model of the form $R = K\mathrm{Ja}_w\sqrt{\eta_L t}$ can also propose reasonable predictions provided an optimal choice of K.
- Modeling the bubble dynamics through a force balance faces modeling uncertainties that still have to be leveraged, especially regarding wall-related effects (contact angle, thermal properties, etc.). Nonetheless, the development of a simpler force balance with less empiricism and enhanced forces expressions allowed to reach acceptable predictions of the departure by sliding diameter D_d over a large database in vertical boiling.
- The same force balance was also able to propose good estimations of the bubble sliding velocity along the wall, both at low and high pressure.
- A similar approach was more complicated to apply for lift-off predictions due to the high sensitivity of the force balance perpendicular to the wall. Moreover, single bubble lift-off can not be considered as a general bubble behavior in vertical boiling according to many experimental observations.
- The many different correlations for bubble dynamics predictions are tied to their establishment range and can lack of generality or present undesirable mathematical behavior (*e. g.* divergence or tending to 0 in pool boiling or saturated conditions). A direct correlation was proposed to estimate the bubble lift-off diameter (or maximum bubble diameter for a single bubble) based on a large experimental database in vertical boiling. The use of terms in the form $(1 + \mathrm{Ja}_L^*)^a$ and $(1 + \mathrm{Re}_\tau)^b$ that degenerates to 1 in pool or saturated boiling allow the correlation to be applied in any flow conditions.

7

CLOSURE LAWS AND CONSTRUCTION OF A NEW HEAT FLUX PARTITIONING MODEL

Contents

7.1 Introduction **118**
7.2 Single-Phase Heat Transfer Coefficient **119**
7.3 Nucleation Site Density **121**
7.3.1 Existing Correlations 122
7.3.2 Comparison with Experimental Measurements 124
7.4 Growth time **126**
7.5 Waiting Time **126**
7.5.1 Existing Models 126
7.5.2 Experimental Measurements 128
7.5.3 Evaluation of the Models 130
7.6 Considerations on Bubble Interactions and Nucleation Sites Deactivation **131**
7.6.1 Nucleation Site Distribution 131
7.6.2 Static Deactivation 133
7.6.3 Static Coalescence 134
7.6.4 Sliding Coalescence 135
7.7 Bubble Sliding Length **136**
7.8 Single Bubble Quenching Area **139**
7.9 Assembling a New Heat Flux Partitioning **140**
7.9.1 Liquid Convective Heat Flux 140
7.9.2 Static Coalescence Evaporation Heat Flux 141
7.9.3 Sliding Coalescence Evaporation Heat Flux 141
7.9.4 Quenching Heat Flux 141
7.9.5 Vapor Convective Heat Flux 142
7.9.6 Liquid Convection Area 142
7.9.7 Model Summary 142
7.10 Conclusion **145**

7.1 INTRODUCTION

When constructing a Heat Flux Partitioning model, different modeling steps have to be followed:

- Definition of the heat transfer mechanisms to be accounted for ;
- Identification of the physical parameters requiring a specific computation ;
- Conduct analytic approaches or correlation selection to choose dedicated closure laws.

In this work, we want to account for four different heat fluxes:

- The liquid convective heat-flux :
- The evaporation heat flux ;
- The transient conduction / quenching heat flux including the impact of sliding bubbles ;

- The vapor convective heat flux located at dry spot locations beneath bubble footprints.

The evaluation of those different heat fluxes requires to model a certain number of parameters, namely:

- The single-phase heat transfer coefficient toward the liquid phase $h_{c,L}$;
- The nucleation site density N_{sit}, representing the number of cavities per unit of area where bubbles will be allowed to nucleate ;
- The different times involved in the bubble nucleation cycle, *i. e.* the growth time until bubble departure by sliding $t_{g,d}$ and the waiting time between two nucleation events on a site t_w ;
- The bubble dynamics at the wall, including bubble departure radius R_d, sliding velocity U_b, lift-off (discussed in Chapter 6), sliding length l_{sl} and area $A_{q,1b}$;
- Possible interactions between bubbles (coalescence) or nucleation sites (deactivation).

In this Chapter, we will go through each physical parameter and discuss their modeling in the light of experimental measurements when possible. Finally, a new model formulation for the Heat Flux Partitioning is proposed in Section 7.9.

7.2 SINGLE-PHASE HEAT TRANSFER COEFFICIENT

The choice of a proper correlation to compute the single-phase heat transfer coefficient is a first but unavoidable step to build a HFP model. Indeed, if the single-phase convection term is badly computed, the resulting boiling model will fail to predict the wall temperature. For instance, if the liquid convective HTC is overestimated, it would result in a delayed increase of the boiling and quenching heat fluxes which would in turn lead to an overprediction of the wall temperature.

To assess existing correlations for the single-phase HTC, we will use wall temperature measurements extracted from experimental boiling curves for water where $T_w \leq T_{sat}$. They correspond to the single-phase part of the experimental data later used to assess the HFP model. As discussed before, good prediction of the single-phase HTC is very important in the frame of boiling heat transfer, which means achieving good wall temperature predictions prior to the Onset of Nucleate Boiling. The chosen data are presented on Table 7.1.

Author	D_h [mm]	P [bar]	G_L [kg/m^2/s]	ΔT_L [K]	ϕ_w [MW/m^2]	$T_{sat} - T_w$ [K]	N_{mes} [-]
Kossolapov [90] (2021)	12	10.5	500 - 2000	10	0.1 - 0.6	0.22 - 9.5	12
Richenderfer [139] (2018)	15	1 - 5	1000 - 2000	10-20	0.1 - 0.63	1 - 18.7	13
Jens-Lottes [78] (1951)	5.74	137.9	2617.5	53.3 - 92.2	0.91 - 2.37	0.33 - 44.1	15
Kennel [83] (1948)	4.3 - 13.2	2 - 6.2	284 - 10 577	11.1 - 83.3	0.035 - 1.89	0.35 - 69	52

Table 7.1: Experimental data range of wall temperature measurements from the single-phase part of boiling curves. N_{mes} is the number of measurements of each data set.

On Figure 7.1, we compare the results of wall temperature prediction in the single-phase region obtained with the correlation of Dittus-Boelter (Eq. 3.20) and Gnielinski (Eq. 3.21).

Note : The Gnielinski correlation is used in Kommajosyula's HFP model to compute the liquid heat transfer coefficient.

The two correlations are of similar efficiency regarding wall temperature predictions over the considered data sets. They both have very good agreement with Kennel data and clear overestimation of ΔT_w on Richenderfer and Kossolapov measurements. The slope difference compared to the parity implies that the correlations are predicting too small Nusselt numbers for those cases. Regarding Jens-Lottes data, both models underestimate the wall temperatures, with better results achieved by Gnielinski correlation.

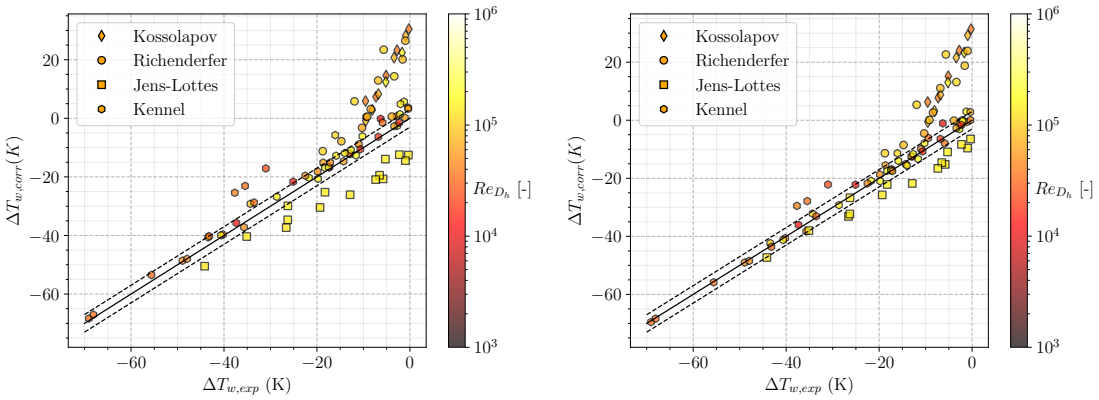

(a) Dittus-Boelter correlation

(b) Gnielinski correlation

Figure 7.1: Predictive capability of wall temperature by single-phase heat transfer correlations. $\pm 3K$ error bars indicated.

Remark : Different friction factor were tested along with different values of wall roughness in the Gnielinski correlation and observed a negligible impact on the overall results. This allows to stay with a simple formulation for the friction coefficient.

The error obtained on Richenderfer and Kossolapov data can partly be explained by the definition of the HTC computed by Gnielinski correlation. Indeed, Gnielinski correlated a Nusselt number associated to a forced convection coefficient $h_{fc,Gniel}$ in the case of a internal flow with a completely heated wall. However, only one side of the channel is heated in Richenderfer ans Kossolapov experiments. If S_{heat} denotes this actual heated surface, then Gnielinski correlation estimates the HTC for a surface $4S_{heat}$. With the same imposed total heat power Φ_w and bulk liquid temperature T_L, we have:

$$h_{fc,Gniel} = \frac{\Phi_w}{\left(T_{w,Gniel} - T_L\right) 4S_{heat}} \tag{7.1}$$

$$h_{fc,exp} = \frac{\Phi_w}{\left(T_{w,exp} - T_L\right) S_{heat}} \tag{7.2}$$

Writing $T_{w,Gniel} = T_{w,real}$ then yields:

$$h_{fc,exp} = 4h_{fc,Gniel} \tag{7.3}$$

Remark : This correction can be interpreted as using the thermal diameter instead of the hydraulic diameter, which is 4 times smaller when only one side of the channel is heated.

Moreover, it should be noted that the experiments of Kossolapov and Richenderfer correspond to developing thermal boundary layers, for which larger heat transfer coefficients are expected. For instance, testing the Al-Arabi correlation [2] for those experiments shows a 20% to 40% enhancement of the heat transfer coefficient compared to a fully developed flow. This further explains the initially observed overestimation of the wall temperature.

On Figure 7.2 we display the predictions of Gnielisnki correlation including this correction by a factor 4 on the HTC for Richenderfer and Kossolapov cases. On the same Figure, we also present predictions achieved with the local HTC estimation implemented in NCFD (Eq. 2.35), using a value of $y^+ = 100$.

The NCFD approach yields predictions similar to the 1D correlations (Figure 7.1) with larger underestimations on Jens-Lottes measurements, confirming its correct behavior for single-phase flows as observed on DEBORA simulations (Chapter 4). On the other hand, we see that applying a constant correction to

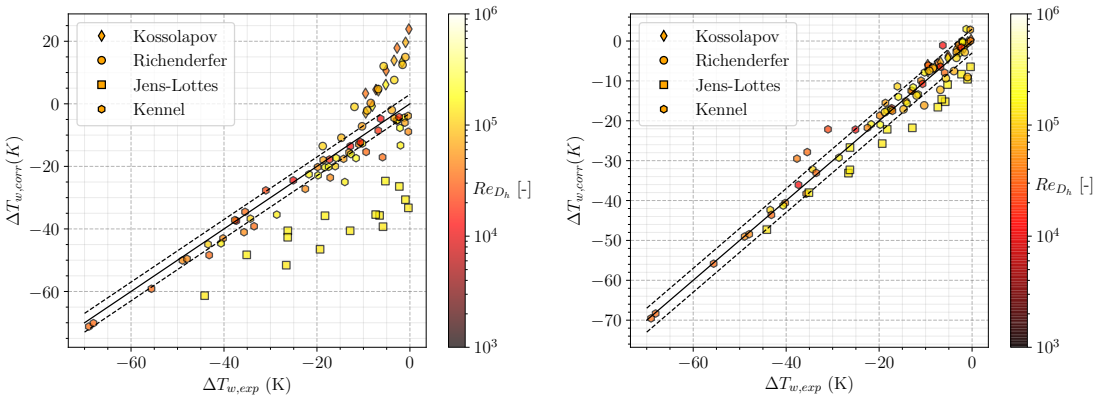

(a) NCFD law

(b) Corrected Gnielinski correlation. We multiply the HTC by 4 on Richenderfer and Kossolapov cases.

Figure 7.2: Predictive capability of wall temperature by NCFD law and Gnielinski correlation including corrections. $\pm 3K$ error bars indicated (dashed lines).

the Gnielinski correlation (4 for Kossolapov and Richenderfer cases) suffices to yield accurate predictions on the whole range of wall temperature measurements.

Remark : The NCFD law was tested without running CFD simulations. Eq. 2.33 was re-written in python to allow its testing outside of the whole code. The use of $y^+ = 100$ as well as the Mac Adams correlation (Eq. 6.73) for the friction velocity U_τ may induce a difference with the predictions that could be achieved by running a complete CFD computation of the considered cases since liquid temperature may not be equal to bulk temperature at this wall distance.

The average errors obtained with each model are summed up on Table 7.2

Model	Kossolapov err. [K]	Richenderfer err. [K]	Jens-Lottes err. [K]	Kennel err. [K]
Dittus-Boelter [38]	19.67	15.07	10.09	3.13
Gnielinski [60]	20.31	14.06	6.09	1.74
NCFD law [65]	15.52	9.25	23.69	3.36
Corrected Gnielisnki	1.34	3.08	6.09	1.74

Table 7.2: Average errors achieved by the considered models on each data sets.

Recalling that Gnielinski correlation was also providing good results on the DEBORA cases with R12 (Chapter 3) further indicates it as a proper choice regarding single-phase HTC estimation in the HFP model.

Note : We will later allow the use of the correction factor when needed to ensure a proper representation of the single-phase part when trying to assess the models associated to boiling.

7.3 NUCLEATION SITE DENSITY

The Nucleation Site Density is among the most influencing parameters over the HFP models predictions, particularly regarding wall temperature [49]. Indeed, its value directly controls the density of bubbles generated at the heater and therefore impacts both the boiling (ϕ_e) and quenching (ϕ_q) heat fluxes to

the first order. Being able to come up with correct predictions of the NSD is thus critical if one wishes to properly capture the thermal behavior of the boiling surface.

In particular, a distinction has to be made between the density of sites or cavities over the surface, which is an intrinsic property of the material, versus the active sites density, *i. e.* the cavities that will actually reach thermal-hydraulics conditions to allow nucleation, which usually depends on the cavity radius R_c. The smallest cavities are less likely to be flooded by the liquid due to capillary effects and can thus become a place where a vapor bubble will grow.

The active nucleation site density, noted N_{sit}, is the one of interest when trying to model wall boiling since it control the density of bubbles that can be generated on the heater. Its value is actually influenced by many parameters being either linked to thermal-hydraulics (wall temperature, pressure, operating fluid) or the heater material (roughness, wettability, thermal conductivity, diffusivity, etc.). That is why it is often estimated through empirical correlations, for which many different expression have been proposed over the years since the end of the XX$^{\text{th}}$ century as discussed below.

7.3.1 *Existing Correlations*

One of the firstly identified behavior of the NSD was its power dependency with the wall superheat ($N_{sit} \propto \Delta {T_w}^m$), which is form adopted in the correlation of Lemmert & Chawla [100] :

$$N_{sit} = \left[210\left(T_w - T_{sat}\right)\right]^{1.8} \tag{7.4}$$

> **Note :** This law is used in the HFP model of Kurul & Podowski and NEPTUNE_CFD to compute N_{sit}.

However, such an expression misses the influence of other parameters such as pressure, which has been proven to be strongly impacting the range of active cavities that can generate bubbles as shown on Figure 7.3 and induces a larger bubble density over the heater.

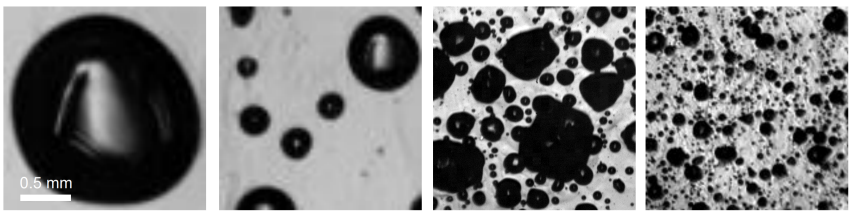

Figure 7.3: HSV Visualization of bubble density at various pressures adapted from Kossolapov [90] (left to right: 1.01 bar, 3 bar, 19.8 bar, 75.8 bar).

Moreover, experimental measurements such as in Borishanskii [13] showed that the power dependency on the wall superheat changes by increasing both with pressure and the superheat value itself. This was accounted for by Hibiki & Ishii in 2003 [73] who came up with a new correlation that requires an estimation of the minimum activated cavity radius R_c :

$$N_{sit} = N_0\left(1 - \exp\left(-\frac{\theta^2}{8\mu^2}\right)\right)\left[\exp\left(\mathrm{f}\left(\rho^+\right)\frac{\lambda'}{R_c}\right) - 1\right] \tag{7.5}$$

$$R_c = \frac{2\sigma\left(1 + \dfrac{\rho_V}{\rho_L}\right)/P}{\exp\left(\dfrac{h_{LV}\Delta T_w}{\dfrac{R_g}{M}T_w T_{sat}}\right) - 1} \tag{7.6}$$

$$\mathrm{f}\left(\rho^+\right) = -0.01064 + 0.48246\rho^+ - 0.22712{\rho^+}^2 + 0.05468{\rho^+}^3 \tag{7.7}$$

with θ the contact angle, R_c the cavity radius, σ the surface tension, h_{LV} the latent enthalpy of vaporization, P the operating pressure, T_w and T_{sat} the wall and saturation temperature in Kelvins, $R_g = 8.314$ J/-mol/K the perfect gas constant, M the molar mass of the fluid (18 g/mol for water), $N_0 = 4.72 \times 10^5$ m^{-2}, $\mu = 0.722$ rad, $\lambda' = 2.5 \times 10^{-3}$ m and $\rho^+ = \log_{10}\left(\frac{\rho_L - \rho_V}{\rho_V}\right)$.

Note : This law is used in the HFP model of Gilman & Baglietto [59] and Kommajosyula [89].

We can note that it also includes the value of the static contact angle θ which can be used as a parameter to accounts for wall properties, since it is dependent on the wall roughness, wettability and the operating fluid. Indeed, a high-wetting material (low values of θ) will allow smaller cavities to be flooded by the surrounding liquid, thus hindering non-condensable gases to be captured inside and become a potentially active nucleation site (Figure 7.4).

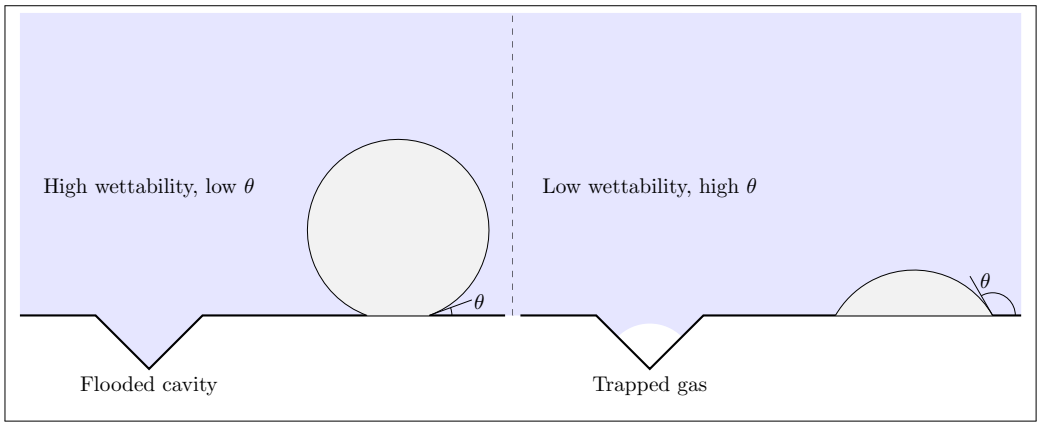

Figure 7.4: Sketch of the link between bubble contact angle and wettability / cavity flooding

This influence of the contact angle on the NSD was confirmed by experimental observations of Basu *et al.* [7] and was also included in a law correlated on their own measurements :

$$N_{sit} = \begin{cases} 0.34\left[1 - \cos\left(\theta\right)\right]{\Delta T_w}^2 & \text{if } \Delta T_{w,ONB} < \Delta T_w < 15\ K \\ 3.4 \times 10^{-5}\left[1 - \cos\left(\theta\right)\right]{\Delta T_w}^{5.3} & \text{if } \Delta T_w > 15\ K \end{cases} \tag{7.8}$$

Similarly, Zhou *et al.* [181] correlated their measurements, including an influence of the pressure:

$$N_{sit} = N_0\left(1 - \cos\left(\theta\right)\right)\left[\exp\left(\mathrm{f}\left(P\right)\Delta T_w\right) - 1\right] \tag{7.9}$$

$$\mathrm{f}\left(P\right) = 0.218\ \ln\left(\frac{P}{P_0}\right) + 0.1907 \tag{7.10}$$

with $N_0 = 55\ 395.26$ m^{-2} and $P_0 = 1.01$ bar.

Finally, one of the most recent NSD correlation has been proposed by Li *et al.* in 2018 [103] and validated over a large range of measurements by including a more realistic power law for ΔT_w. It avoids the divergence of N_{sit} observed in Hibiki & Ishii law (Eq. 7.5) when reaching high pressure and superheat. It also includes the impact of pressure and contact angle and its evolution with temperature *e. g.* its decrease close to 0 ° when approaching the critical temperature [149]:

$$N_{sit} = N_0 e^{\mathrm{f}(P)}{\Delta T_w}^{A\Delta T_w + B}\left(1 - \cos\left(\theta\right)\right) \tag{7.11}$$

$$\mathrm{f}\left(P\right) = 26.006 - 3.678e^{-2P} - 21.907e^{-P/24.065} \tag{7.12}$$

$$A = -2 \times 10^{-4}P^2 + 0.0108P + 0.0119 \tag{7.13}$$

$$B = 0.122P + 1.988 \tag{7.14}$$

$$1 - \cos\left(\theta\right) = \left(1 - \cos\left(\theta_0\right)\right)\left(\frac{T_c - T_{sat}}{T_c - T_0}\right)^{\gamma} \tag{7.15}$$

with P in MPa, θ_0 the contact angle at room temperature T_0, and default value being for water $\theta_0 = 41.37°$, $T_c = 374°C$ $T_0 = 25°C$, $\gamma = 0.719$.

Remark : We can question the absence of bulk liquid velocity and temperature in the presented law since they should logically influence the nucleation process. However, this impact is rather limited as observed in experimental measurements of Zhou *et al.* [181] and Kossolapov [90].

7.3.2 *Comparison with Experimental Measurements*

In order to assess existing NSD correlations and choose the most pertinent to include in a HFP model, we gather NSD measurements from 4 different authors. The different operating conditions of the chosen data sets are gathered on Table 7.3.

Author	Fluid	P [bar]	G_L [kg/m^2/s]	ΔT_L [K]	ΔT_w [K]	θ_0 [°]	N_{mes} [-]
Zhou [181] (2020)	Water	1.21 - 3.12	482.7 - 1930.6	8 - 15	6.7 - 20.2	51	60
Richenderfer [139] (2018)	Water	1.01	500 - 1000	10	21.7 - 42.8	80	49
Kossolapov [90] (2021)	Water	1.01 - 75.8	500 - 2000	80	10	80°	63
Borishanskii [13] (1966)	Water	1.01 - 198	N.A.	N.A.	1.75 - 17.3	45	132

Table 7.3: Nucleation Site Density data in flow boiling

We then compare the predictions achieved by the model of Lemmert & Chawla (Eq. 7.4), Hibiki & Ishii (Eq. 7.5), Zhou *et al.* (Eq. 7.9) and Li *et al.* (Eq. 7.11). The comparison with measurements are presented on Figure 7.5.
The Lemmert & Chawla model appears to fail in predicting the NSD at high pressures. This is a logical drawback of its sole dependence on the wall superheat. More importantly it increasingly underestimates the NSD as pressure increases, which makes it a clearly unsuitable correlation to compute N_{sit} particularly for pressurized flows such as in PWR.

Although the model of Zhou *et al.* includes a pressure term, its partial calibration on data covering a low range of pressure may explain the large error observed when compared to higher pressure measurements.

On the contrary, models from Hibiki & Ishii and Li *et al.* seem to better reproduce the different trends with flow conditions, especially with pressure. The model from Li *et al.* achieves better predictions by avoiding to reach nonphysically high values of N_{sit} at higher wall superheat compared to Hibiki & Ishii. This behavior is clear over Kossolapov data at high pressure, where both model lead to overestimation, the strongest discrepancy being associated to Hibiki & Ishii model.

Overall, the model of Li *et al.* is the most efficient with an acceptable agreement on most of the data of Borishanskii and Zhou *et al.*. The measurements of Richenderfer and Kossolapov fail to be precisely reproduced, but it shows a coherent trend and the most limited error when compared to other correlations.

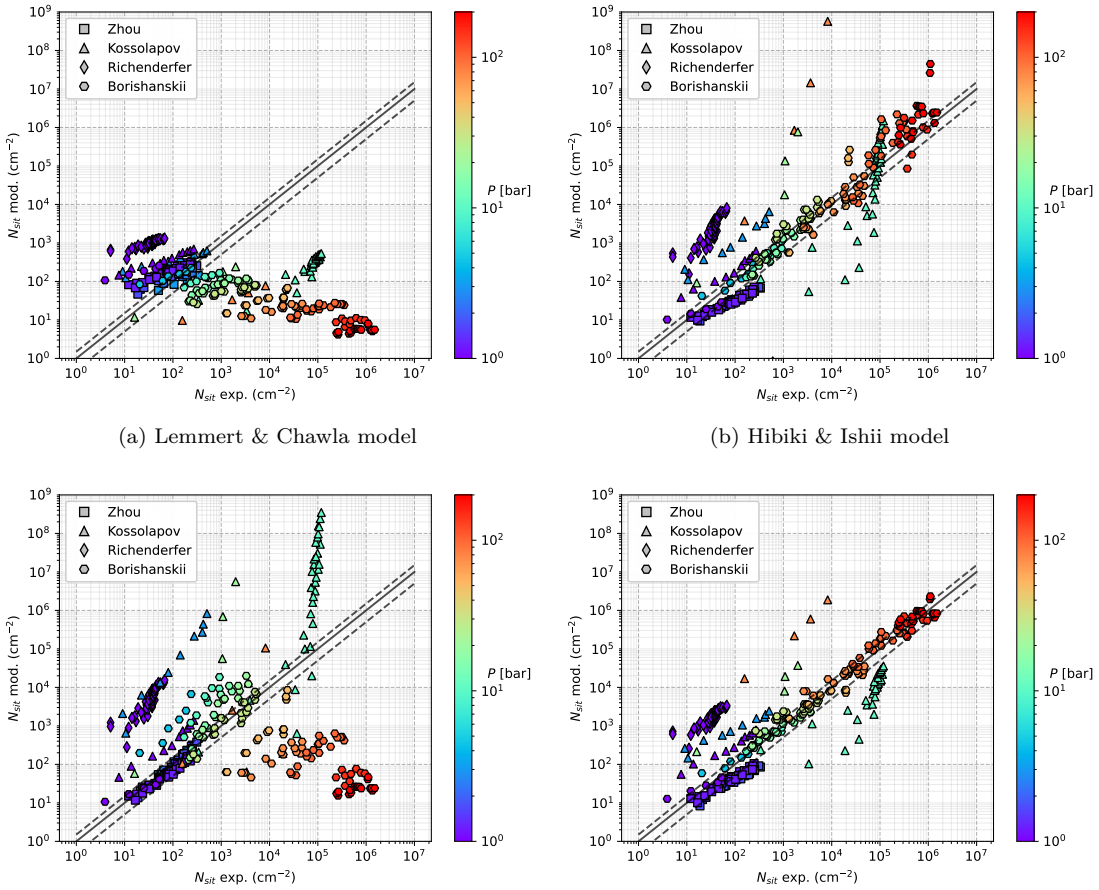

(a) Lemmert & Chawla model

(b) Hibiki & Ishii model

(c) Zhou *et al.* model

(d) Li *et al.* model

Figure 7.5: Predictions of the chosen models against the experimental data of Table 7.3 with ±50% error bars. The contact angles

Remark : The coherency of NSD predictions is hard to ensure since we do not know the exact contact angle and boiling surface morphology in the experiments. This was pointed out by Richenderfer [139] who observed significant variation in the NSD value depending on the heater, though keeping the same material (ITO). For instance, this may explain the fact that the NSD measured by Kossolapov at 10.5 bar is higher than any other pressure on his experiment, leading to both underestimations and overestimations of the model of Li *et al.* depending on the pressure.

Moreover, we must keep in mind that Richenderfer and Kossolapov experiments are conducted on non-prototypical surfaces, which usually display much lower nucleation site densities compared to metallic surfaces. This could explain the systematic overestimation on Richenderfer data observed on Figure 7.5.

All things considered, those comparisons show that the Nucleation Site Density remains among the most difficult quantity to evaluate because of its very large variations over experiments, boiling surfaces and flow conditions. Dedicated correlations are hardly precise outside of their establishment databases. However, it remains the best yet only way to compute N_{sit}. **In that regard, the NSD correlation of Li *et al.* appears to be the most coherent choice.**

Note : It seems important to note that Li *et al.* correlation is validated on data established using water as working fluid. Its extension to other fluids must be carefully done, in particular regarding value of the critical temperature T_c in Eq. 7.11.

7.4 GROWTH TIME

As discussed in Section 6.3, the bubble growth can be acceptably modeled as:

$$R\left(t\right) = K\mathrm{Ja}_w\sqrt{\eta_L t} \tag{7.16}$$

with value of K laying roughly between 0.1 and 2 depending on the boiling conditions.

With a given departure radius R_d, the bubble growth time until departure from nucleation site $t_{g,d}$ can be estimated as:

$$t_{g,d} = \left(\frac{R_d}{K\mathrm{Ja}_w}\right)^2 \frac{1}{\pi\eta_L} \tag{7.17}$$

Note : This formulation is used in Gilman [58] and Kommajosyula [89] HFP models, with their own choice of value for K.

By correlating their own growth time measurements, Basu *et al.* [7] propose the following relationship including an influence of the liquid subcooling:

$$\frac{D_d^2}{\eta_L \mathrm{Ja}_w t_{g,d}} = 45e^{-0.02\mathrm{Ja}_L} \tag{7.18}$$

which is naturally used in their HFP model to compute the bubble growth time.

Remark : If precise estimations of the thermal boundary layer thickness is achievable, the new analytic expression of the bubble growth proposed in Eq. 6.102 can be used to express the growth time:

$$t_{g,d} = \left[\frac{1}{K_a}\ln\left(1-\sqrt{1-\frac{R_d}{R_\infty}}\right)\right]^2 \tag{7.19}$$

with K_a defined as in Eq. 6.101 and R_∞ in Eq. 6.102.

This formulation requires $R_d < R_\infty$ the equilibrium radius in subcooled pool boiling. Though this condition seems logical physically speaking, it can't be ensured numerically due to the range of values attainable using correlations or other mechanistic models to estimate R_d.

7.5 WAITING TIME

The waiting time t_w between two nucleation events on an active site corresponds to the time needed for the thermal boundary layer to reconstruct after its disruption due to bubble departure from the nucleation site. This process is then intrinsically related to the heater properties and the transient heat transfer with the external liquid flow.

7.5.1 *Existing Models*

7.5.1.1 *Analytic Approaches*

Traditional approaches of the wait time estimation rely on the analytic solution to the transient heat transfer in a semi-infinite medium. Assuming that after bubble departure liquid at $T_{L,bulk}$ is displaced towards the wall at T_w, one can solve the conductive heat transfer problem at the wall with the initial and boundary conditions:

$$\frac{\partial T_L}{\partial t} = \eta_L \frac{\partial^2 T_L}{\partial y^2} \tag{7.20}$$

$$T_L\left(y,0\right) = T_{L,bulk},\ \forall y > 0 \tag{7.21}$$

$$T_L\left(0,t\right) = T_w,\ \forall t \geq 0 \tag{7.22}$$

The solution of this heat transfer problem if given by:

$$T_L\left(y,t\right) = T_{L,bulk} + \left(\Delta T_w + \Delta T_L\right) \text{erfc}\left(\frac{y}{2\sqrt{\eta_L t}}\right) \tag{7.23}$$

For instance, Mikic & Rohsenow [115] combine this solution with the assumption that a new nucleation will occur over a cavity of radius R_c when the vapor temperature reaches:

$$T_{V,nuc} = T_{sat} + \frac{2\sigma T_{sat}\left(\frac{1}{\rho_V} - \frac{1}{\rho_L}\right)}{R_c h_{LV}} \tag{7.24}$$

The wait time is then assumed to be the time needed for the transient temperature field to reach $T_{V,nuc}$ at height $y = R_c$, *i. e.* $T_L\left(R_c, t_w\right) = T_{V,nuc}$. Combining Eq. 7.23 and 7.24 allow to write:

$$t_w = \frac{1}{4\eta_L}\left[\frac{R_c}{\text{erfc}^{-1}\left(\frac{\Delta T_L}{\Delta T_L + \Delta T_w} + T_{sat}\left(\frac{1}{\rho_V} - \frac{1}{\rho_L}\right)\frac{2\sigma}{\left(\Delta T_w + \Delta T_L\right) h_{LV} R_c}\right)}\right]^2 \tag{7.25}$$

$$\approx \frac{1}{\pi\eta_L}\left[\frac{\left(\Delta T_w + \Delta T_L\right) R_c}{\Delta T_w - T_{sat}\left(\frac{1}{\rho_V} - \frac{1}{\rho_L}\right)\frac{2\sigma}{R_c h_{LV}}}\right]^2 \tag{7.26}$$

Using the same approach, Han & Griffith [26] use the same expression of the transient liquid temperature field but consider $T_L\left(\frac{3}{2}R_c, t_w\right) = T_{V,nuc}$, which yields a wait time that is $\frac{9}{4}$ times Eq. 7.26.

Later, Yeoh *et al.* [168] followed a similar derivation to propose an expression of the wait time that accounts for the contact angle value:

$$t_w = \frac{1}{\pi\eta_L}\left[\frac{\left(\Delta T_L + \Delta T_w\right) C_1 R_c}{\Delta T_w - \frac{2\sigma T_{sat}}{C_2 \rho_V h_{LV} R_c}}\right]^2 \tag{7.27}$$

$$C_1 = \frac{1 + \cos\left(\theta\right)}{\sin\left(\theta\right)}\ ;\ C_2 = \frac{1}{\sin\left(\theta\right)} \tag{7.28}$$

All those analytic approaches present one pivotal parameter: the activated cavity radius R_c. It is a very complicated parameter to evaluate since it can vary by decades depending on the flow conditions and the boiling surface morphology.

Among existing expressions of R_c, we can mention:

$$R_c = \frac{2\sigma T_{sat}}{\rho_V h_{LV} \Delta T_w},\ \text{used by Han \& Griffith [26]} \tag{7.29}$$

$$R_c = \sqrt{\frac{1}{C_1 C_2}\frac{2\sigma T_{sat}\lambda_L}{\rho_V h_{LV}\phi_w}},\ \text{used by Yeoh } \textit{et al.} \text{ [168]} \tag{7.30}$$

$$R_c = \frac{2\sigma\left(1 + \frac{\rho_V}{\rho_L}\right)/P}{\exp\left(h_{LV}\frac{\Delta T_w}{R_g T_w T_{sat}}\right)},\ \text{used by Hibiki \& Ishii [73]} \tag{7.31}$$

Remark : Those analytic expressions do not include the influence of an external liquid velocity, which could have an impact over the wait time since it modifies the hydrodynamics controlling the reconstruction of the thermal boundary layer. In particular, turbulent flows could induce a larger mixing effect between the bulk and the wall thus increasing the time needed to reach sufficient superheat to allow a new nucleation to occur.

7.5.1.2 *Empirical Correlations*

Alternatively, other authors considered the wait time estimation through empirical correlations based on data-fitting on given measurements. For instance, Basu *et al.* [7] proposed:

$$t_w = 139.1 \Delta T_w{}^{-4.1} \tag{7.32}$$

based on low pressure and low liquid velocity experiments.

Note : This expression of t_w is used in Basu *et al.* HFP model [7].

More recently, Kommajosyula [89] included the effect of the liquid subcooling through the liquid Jakob number Ja_L as:

$$t_w = 0.061 \frac{\mathrm{Ja}_L{}^{0.63}}{\Delta T_w} \tag{7.33}$$

Remark : : This expression, used in Kommajosyula's HFP model, will yield $t_w = 0$ for saturated boiling conditions, which is hardly reasonable since a non-zero wait time exists between two nucleation events even at saturation [57].

7.5.2 *Experimental Measurements*

To try to assess the proposed expressions of the bubble wait time, we rely on some experimental measurements available in the literature from Basu *et al.* [7], Richenderfer [139] and Kossolapov [90]. The boiling conditions of the data are summed up on Table 7.4.

Author	Fluid	P [bar]	G_L [kg/m^2/s]	ΔT_L [K]	ϕ_w [MW/m^2]	ΔT_w [K]	t_w [ms] (N_{mes})
Basu *et al.* [7] (2005)	Water	1.01	346.0	8.35 - 46.5	N.A.	9.83 - 17.5	0.797 - 13.3 (19)
Richenderfer [139] (2018)	Water	1 - 2	1000 - 2000	5 - 20	0.74 - 7.13	N.A.	0.914 - 6.02 (259)
Kossolapov [90] (2021)	Water	10.5	500 - 2000	10	N.A.	0.12 - 25.9	6.13 - 85.9 (33)

Table 7.4: Bubble wait time data in vertical flow boiling. Wall superheat values for Richenderfer data are estimated using Frost & Dzakowic correlation (Eq. 6.109).

The experimental data are all using water as working fluid. We can see at first glance that values measured by Kossolapov are nearly a decade larger compared to the other experiments. This may be an effect of pressure due to:

- The bubbles that are smaller and depart nearly right after nucleation, leaving wait time as the main part of the nucleation cycle ;
- The wall Jakob number values that are smaller ;
- The heterogeneity in nucleation sites behavior (their number increasing with pressure), with sites exhibiting very large wait time due to their very low nucleation frequency versus very active sites that contributes much more to the overall nucleation. This can partially be explained by the local

decrease in wall temperature when a bubble nucleates (acting locally as a heat sink), potentially deactivating the neighboring sites. Averaging over those events as done by Kossolapov [90] may result in a large wait time.

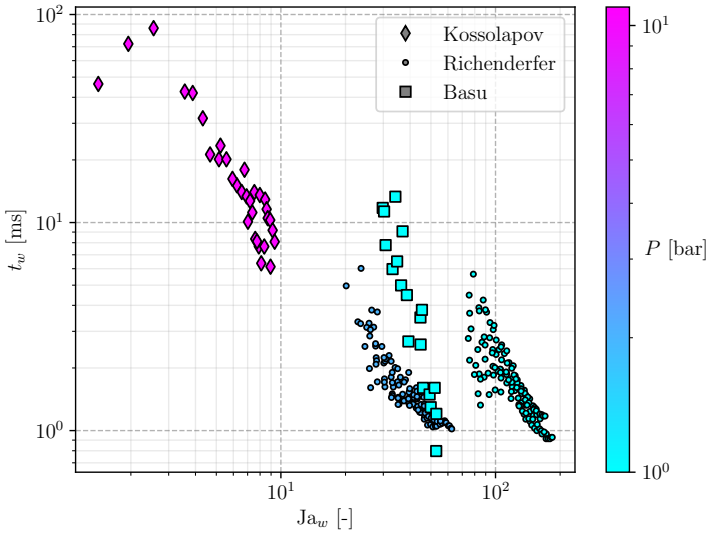

Figure 7.6: Evolution of the wait time values with the wall Jakob number.

On Figure 7.6, we show the evolution of the measured wait times with the wall Jakob number. We can see that the low values of Jakob number actually correspond to high wait times, which seems to confirm the previous assumptions.

Moreover, we see that there is a steep decrease of the wait time with Ja_w. The slope however changes depending on the data set, which would logically depend on the heater thermal properties as well as on the operating fluid. It seems that the slope followed by Kossolapov data at 10 bar seem to align with that of Richenderfer data at 2 bar, which would exhibit a sort of coherency between those two data sets.
On the contrary, values at 1 bar from Basu do not clearly match with Richenderfer data at 1 bar.

The data sets from Kossolapov and Richenderfer also give the associated frequency to each wait time measurement. This allows to plot the product $t_w \times f$ to evaluate the proportion of the nucleation cycle occupied by wait time. The value of $t_w \times f$ would physically be expected to tend to 1 when $\Delta T_w \to 0$ (highly reduced nucleation) and to 0 when $\Delta T_w \to \infty$ due to the intense nucleation and increased transient heat transfer under the high temperature gradient between the wall and the fluid. Experimental values are plotted on Figure 7.7 versus the reduced Jakob number $\mathrm{Ja}_w^* = \dfrac{c_{p,L}\Delta T_w}{h_{LV}}$ values to regroup the values by excluding the influence of the density ratio ρ_L/ρ_V.
We can see that for lower values of Ja_w^*, the product $t_w \times f$ starts to tend to 1. For higher values, a linear decrease seem to be the general trend of the measurements. However, it can't decrease linearly forever, which is why the trend on Figure 7.7 extrapolated to higher values of Ja_w^* looks like a sigmoid in order to approach zero for large superheat. Nevertheless, we clearly lack of measurements at larger values of Ja_w^* to confirm this supposed trend.

Remark : The range of values attained by the product $t_w \times f$ can vary from 1 down to 0.5 on the chosen experimental data. This clearly shows that the relation between the wait time and the growth time is not straightforward as assumed in some works who neglects the growth time or suppose a constant relationship such as $t_w = 3t_g$[26].

Moreover the boiling conditions range covered by the data are not that exhaustive, leaving room for even larger ranges of $t_w \times f$ with different fluids and heater material for instance.

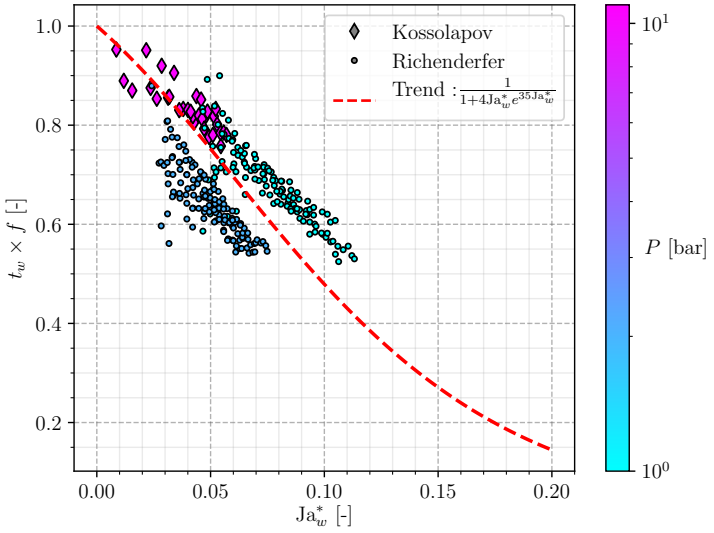

Figure 7.7: Evolution of the product $t_w \times f$ with the reduced Jakob number.

7.5.3 *Evaluation of the Models*

Using the data of Table 7.4 to evaluate the different approaches presented above, we obtain the results presented on Figures 7.8 and 7.9.

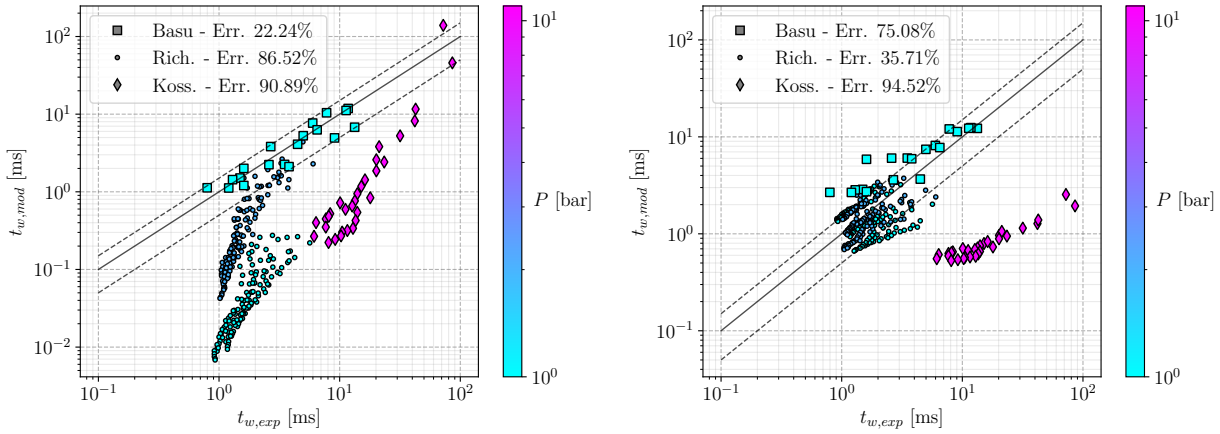

(a) Basu *et al.* correlation

(b) Kommajosyula correlation

Figure 7.8: Predictions using the correlations. ±50% dashed lines are represented.

The correlation of Basu *et al.* naturally performs well on their own data but largely underestimates the wait time for Richenderfer and Kossolapov data. Kommajosyula's formulation produces better results on the low pressure cases, particularly on Richenderfer cases. However, it fails to capture the increase in t_w for Kossolapov data and largely underestimates them.

When testing the analytic formulations of the wait time, we tested different combinations of (t_w, R_c) expressions. Overall, we saw that the results were strongly dependent on the value of the cavity radius with values that can change by decades depending on the chosen formulation.

At last, it appeared that choosing the Yeoh *et al.* expression of t_w (Eq. 7.27) along with the cavity radius of Han & Griffith (Eq. 7.29) resulted in good results in average over the three chosen data sets. As we can see on Figure 7.9, it produces overall better results compared to the correlation. Moreover, we used contact angle values that were representative of each experimental conditions according to each author:

- $\theta = 31°$ for Basu *et al.* data [6] (metallic surface) ;

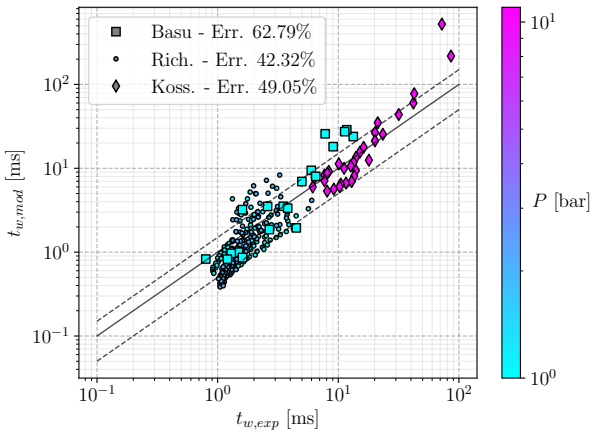

Figure 7.9: Yeoh *et al.* formulation of t_w with Han & Griffith cavity radius. ±50% dashed lines are represented.

- $\theta = 72°$ for Richenderfer data [139] (ITO on sapphire) ;
- $\theta = 80°$ for Kossolapov data [90] (ITO on sapphire).

Remark : Obviously, since the wait time results from a transient heat transfer between the wall and the liquid after the bubble departure, it should strongly depend on the wall thermal properties (*e. g.* its effusivity). However, they are not accounted for in the analytic expressions, with solely the contact angle being related to the wall material.

The fact that the analytic expression is able to correctly predict the large range of t_w values from the different experiments is encouraging since it is based on a physical approach contrary to correlations which mainly relies on data-fitting.

To conclude, it seems appropriate to use the wait time formulation of Yeoh *et al.* along with expressing cavity radius using Han & Griffith estimation. We must though keep in mind that the model is sensitive to the value of the contact angle θ, which has to be evaluated in order to make a proper use of the analytic expressions.

7.6 CONSIDERATIONS ON BUBBLE INTERACTIONS AND NUCLEATION SITES DEACTIVATION

7.6.1 *Nucleation Site Distribution*

NSD correlations actually estimate the total number of sites where bubbles can nucleate on a surface. However, experimental observations showed that nucleation sites exhibit largely heterogeneous behaviors. For instance, Figure 7.10 shows experimental observations from Kossolapov [90] that demonstrate the variety of nucleation frequency measured for each site on a boiling surface.

This large difference in nucleation frequency between the different sites indicates that a minority of sites contribute to most of the total phase change process. Those differences may originate from different interactions such as:

- Thermal deactivation: a bubble nucleating at a site gathers the energy in the wall to use it for phase change, which in turns locally decreases the temperature and will hinder nucleation to occur at neighboring sites.
- Static deactivation: given a number of active sites, distributing a number of bubbles of radius R_d over them can lead to overlapping that can not geometrically be accommodated on the wall. This effect was notably considered by Gilman & Baglietto [59].
- Sliding deactivation: if a bubble slides and swipes a given area, sites laying on its path may experience quenching even before holding a nucleating bubble. This consequently will impact their nucleation frequency and may lead to partial deactivation under the sliding effect.

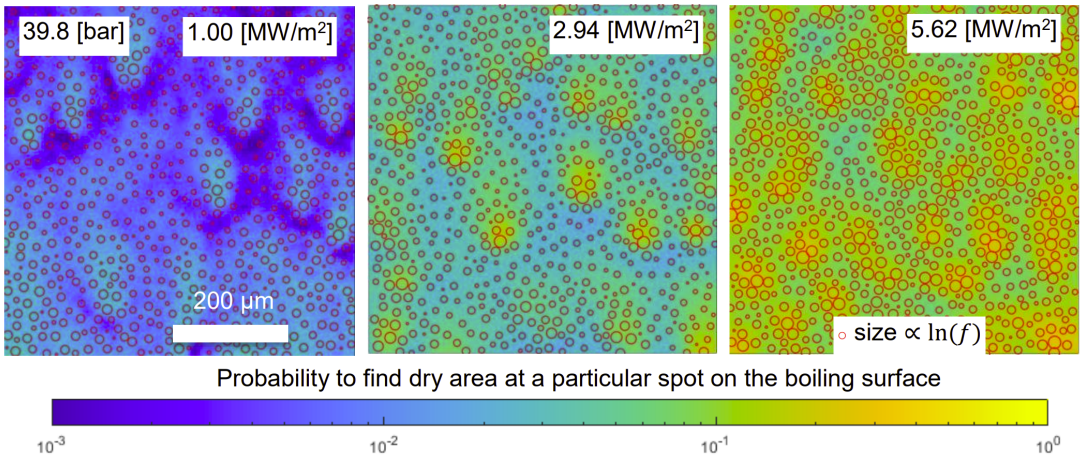

Figure 7.10: Nucleation site distribution by and adapted from Kossolapov [90]. Red circles represent the active sites positions with diameter increasing with the site's nucleation frequency.

In order to consider such interactions between nucleation sites, we need to know their spatial distribution over the boiling surface. Usual approaches considered that the nucleation sites followed an homogeneous spatial Poisson process *i. e.* the probability of finding a site in an area A only depends on the value of A and not on its location over the boiling surface.

This has been supported by different experimental observations such as those of Gaertner [52] or Sultan [154] for pool boiling who found an agreement between site distribution and Poisson process by studying sites populations in subdivisions of the boiling surface. It was also confirmed for flow boiling by Del Valle & Kenning [35] who observed site distribution at different heat fluxes. However, they noticed that the increase in nucleation site with the heat flux did not come from an additive effect of new sites since some active sites at low heat fluxes became inactive at higher heat fluxes before sometimes reactivating later (see Figure 7.11a). This further highlights that the interactions and deactivation processes originate from complex physics that simultaneously include wall morphology and thermal behavior, external flow influence and bubble presence.

More recent observations also show a random distribution of the sites such as in Zhou *et al.* [180] (Figure 7.11b).

Considering an homogeneous spatial (two-dimensional) Poisson process with an event density (*i. e.* average number of events per unit of area) λ, then the probability that the number of events N in an area A is equal to $n \in \mathbb{N}$ is [34]:

$$\mathcal{P}\left(N\left(A\right)=n\right)=\frac{\left(\lambda A\right)^{n}}{n!}e^{-\lambda A} \tag{7.34}$$

Then, one can express the probability density function of the nearest-neighbor, depending on the distance r between two events as:

$$f\left(r\right)=2\lambda\pi re^{-\lambda\pi r^{2}} \tag{7.35}$$

This special case of Poisson point-processes is also called "Complete Spatial Randomness".

Remark : Although observations of the boiling surface presented random distributions of sites close to a Poisson process, Del Valle & Kenning [35] found that the measured nearest-neighbor distance distribution was deviating from Eq. 7.35 for low values of r.

Eq. 7.35 allows to compute the average distance s between two events:

$$s=\int_{0}^{+\infty}rf\left(r\right)\mathrm{d}r=2\frac{\sqrt{\pi}}{4\sqrt{\lambda\pi}}=\frac{1}{2\sqrt{\lambda}} \tag{7.36}$$

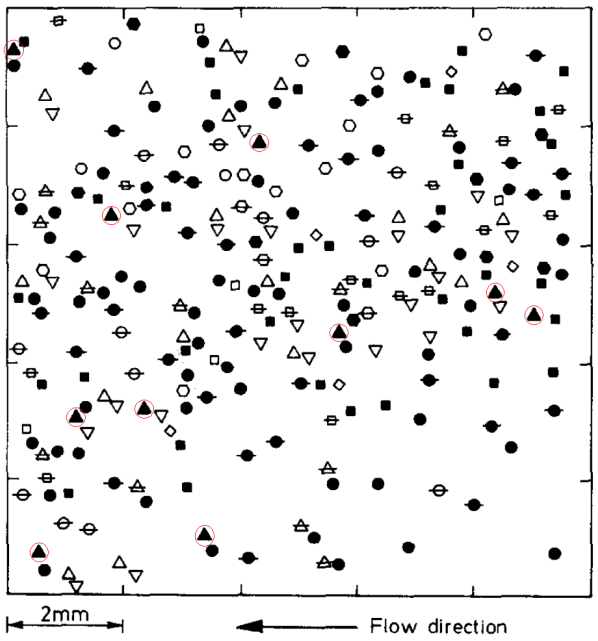

(a) Nucleation site distribution in flow boiling from Del Valle & Kenning [35], each symbol represent a family of active nucleation site observed at different heat fluxes. Black triangles circled in red are sites that deactivate when the heat flux exceeded 70% of the CHF.

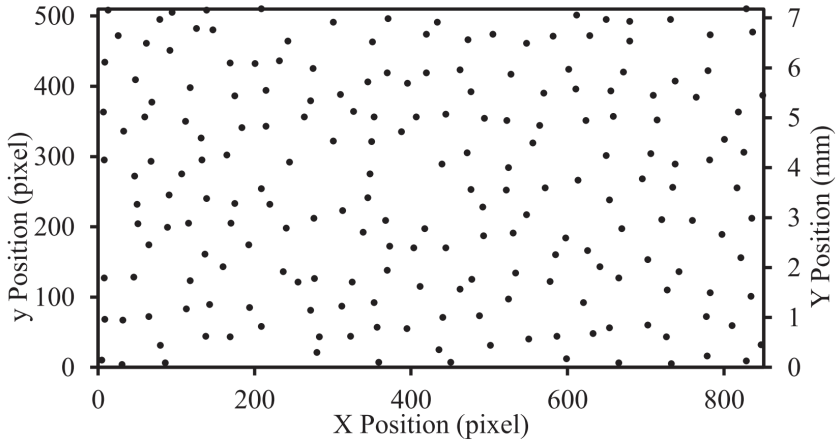

(b) Nucleation site distribution at 3 bar by and adapted from Zhou *et al.* [181].

Figure 7.11: Examples of experimental nucleation sites distribution in flow boiling.

Note : In the case of boiling physics, the word "event" can refer to active nucleation sites or bubbles on the surface.

From those mathematical expressions, we can then model different type of interactions between sites by choosing proper event densities λ. Further subsections propose treatments of a few of them.

7.6.2 *Static Deactivation*

Note : This calculation has originally been conducted by Gilman [59] and continued by Kommajosyula [89].

Let us consider the nucleation site density N_{sit} computed by a correlation as in Section 7.3. As mentioned earlier, if we distribute a given number of bubbles of radius R_d over the different sites, we have no

guarantee that the correlation avoids too large values of N_{sit} that would lead to geometrical overlapping as shown on Figure 7.12.

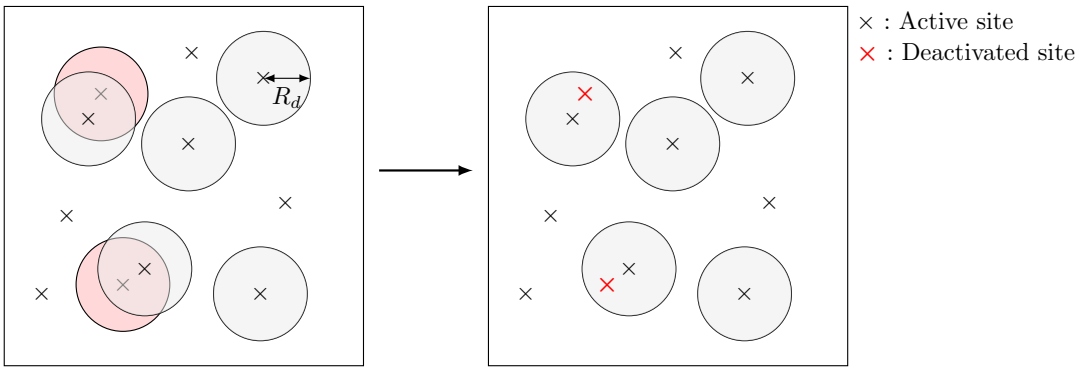

Figure 7.12: Sketch of the geometrical overlapping leading to static deactivation. Bubbles in red can not be accommodated on the surface due to their site laying below an existing bubble.

Thus, we need a correction of N_{sit} to obtain the actual number of active sites $N_{sit,a}$ that can geometrically fit on the surface regarding the nucleation parameters. Given a bubble growth time before departure $t_{g,d}$ and an average nucleation frequency f, we can estimate the actual number of bubbles growing attached to their sites on the boiling surface as:

$$N_b = t_{g,d} \times f \times N_{sit,a} \tag{7.37}$$

If N_b is used as an event density in the Poisson process, we can estimate the probability to have an undesired overlapping *i. e.* two simultaneous bubbles of radius R_d on neighboring sites at a distance $r \leq R_d$:

$$\mathcal{P}\left(r \leq R_d\right) = 1 - \underbrace{\mathcal{P}\left(N\left(\pi R_d^2\right) = 0\right)}_{\text{No bubble nucleates within } \pi R_d^2} = 1 - e^{-N_{sit,a} t_{g,d} f \pi R_d^2} = \mathcal{P} \tag{7.38}$$

This overlapping probability $\mathcal{P}$ can then be used to ponderate the number of sites given by the NSD correlation, yielding:

$$N_{sit,a} = \left(1 - \mathcal{P}\right) N_{sit} \tag{7.39}$$

$$\Leftrightarrow N_{sit,a} t_{g,d} f \pi R_d^2 e^{N_b t_{g,d} f \pi R_d^2} = N_{sit} t_{g,d} f \pi R_d^2 \tag{7.40}$$

$$\Leftrightarrow N_{sit,a} = \frac{\mathcal{W}\left(N_{sit} A_{sit}\right)}{A_{sit}} \tag{7.41}$$

where $A_{sit} = t_{g,d} f \pi R_d^2$ and $\mathcal{W}$ is Lambert's W-function (reciprocal of $x \to x e^x$).
The evaluation of $\mathcal{W}$ can easily be achieved with a few iterations of a bisection method. Otherwise, Kommajosyula proposed an approximation to allow its direct computation [89].

On Figure 7.13 we show the impact of the correction of Eq. 7.41 on NSD correlations of Hibiki & Ishii (Eq. 7.5) and Li *et al.* (Eq. 7.11).

Li *et al.* correlation present a significant correction for larger wall superheat due to its formulation that damps the exponential growth of the NSD at high superheat. On the contrary, the well-known drawback of Hibiki & Ishii correlation which yields too large N_{sit} value at high superheat is strongly ponderated by the static deactivation correction.

7.6.3 *Static Coalescence*

Now that the actual number of bubble-generating sites have been identified, we can consider other interaction phenomena that can occur on the boiling surface. For instance, if two bubbles are simultaneously

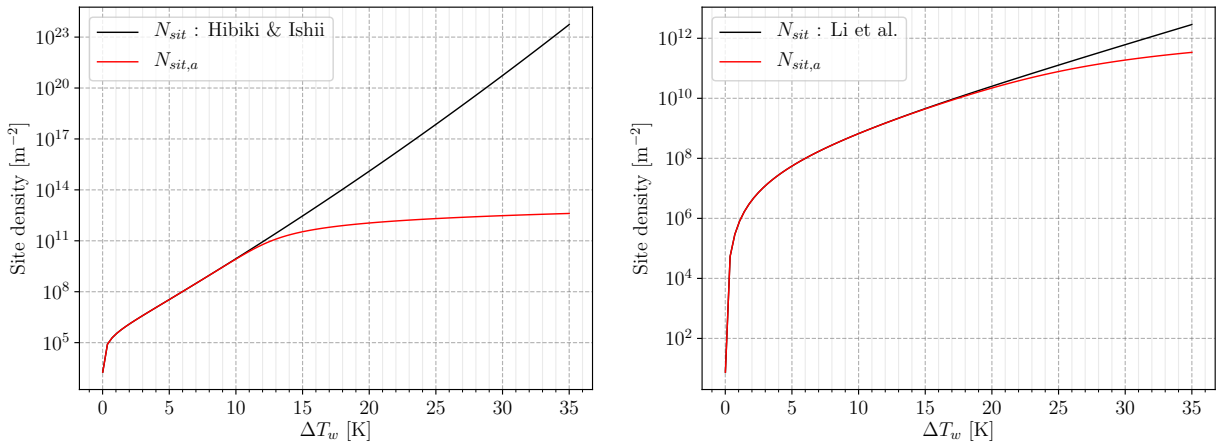

(a) Hibiki & Ishii correlation (Eq. 7.5)

(b) Li *et al.* correlation (Eq. 7.11)

Figure 7.13: Static deactivation correction tested with Hibiki & Ishii and Li *et al.* correlations for water at 40 bar, $f = 200$ Hz, $t_{g,d} = 0.1$ ms, $\theta = 80°$ and $R_d = 0.01$ mm.

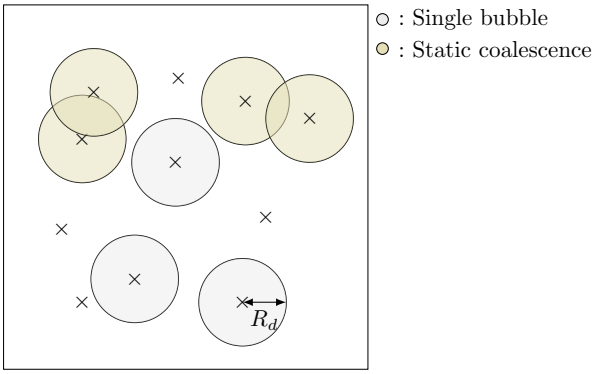

Figure 7.14: Sketch of the static coalescence phenomenon.

growing on sites at a distance lower than $2R_d$, the bubbles will coalesce while growing up to the detachment diameter (Figure 7.14).
Using the bubble density N_b (Eq. 7.37) as the event density in Eq. 7.35, the probability of static coalescence is:

$$\mathcal{P}\left(r \leq 2R_d\right) = \int_0^{2R_d} f\left(r\right) \mathrm{d}r = 1 - e^{-N_b \pi (2R_d)^2} = \mathcal{P}_{coal,st} \tag{7.42}$$

The density of bubble-generating sites that will lead to a static coalescence can then be estimated as :

$$N_{coal,st} = \mathcal{P}_{coal,st} N_{sit,a} \tag{7.43}$$

Figure 7.15 the evolution of $\mathcal{P}_{coal,st}$ with the wall superheat for two departure radius values, using the same conditions as in Figure 7.13.

7.6.4 *Sliding Coalescence*

The question of sliding coalescence is partly addressed by Basu *et al.* [7] (Section 5.3) by comparing the computed sliding distance of a single bubble $l_{sl,0}$ with the average distance between two active nucleation sites $s = 1/\sqrt{N_{sit,a}}$ (twice the value obtained if we use the Poisson distribution Eq. 7.36). They suppose that if $l_{sl,0} > s$ bubble coalescence will occur during the sliding phase and reduces the number of sites generating sliding bubbles.

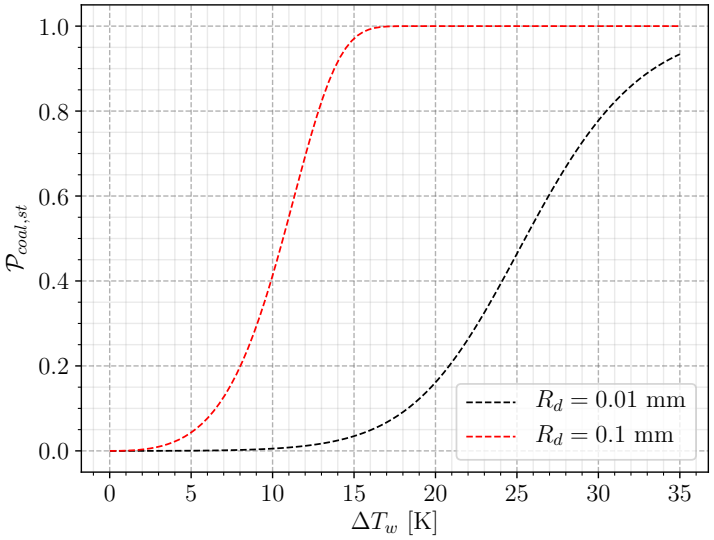

Figure 7.15: Static coalescence probability with corrected Li *et al.* for water at 40 bar, $f = 200$ Hz, $t_{g,d} = 0.1$ ms and $\theta = 80°$.

Remark : Their approach is based on the distribution of active nucleation sites $N_{sit,a}$ and not on the bubble density N_b which could better represent the average distance between two bubbles actually living on the surface.

Using the spatial distribution, if the total area covered by a single sliding bubble is $A_{q,1b}$ and the number of sites generating sliding bubbles N_{sl}, we can estimate:

- The probability of finding no growing bubbles in area $A_{q,1b}$, meaning no sliding coalescence (NC): $\mathcal{P}_{NC} = \exp\left(-N_{sit,a} t_{g,d} f A_{q,1b}\right)$
- The number of sites generating sliding bubbles without coalescence : $N_{sl,NC} = N_{sl} \times \mathcal{P}_{NC}$
- The number of sites generating sliding bubbles that will coalesce with others: $N_{sl,C} = N_{sl} \times (1 - \mathcal{P}_{NC})$
- The number of sites, present in sliding bubbles path, that will not be holding growing bubbles : $N_{nob} = N_{sit,a} \times N_{sl,NC} \times A_{q,1b}$

Those types of calculations are interesting if one wishes to further distinguish many different types of bubble behavior, and particularly *if we dispose of a sliding length for single bubbles $l_{sl,0}$ meaning that single bubble lift-off would be considered.* This point being questionable in vertical flow boiling as discussed in Section 6.6.

7.7 BUBBLE SLIDING LENGTH

Estimation of the bubble sliding length is critical for the evaluation of the quenching term since it acts as an enhancing factor of the wall area that will undergo transient heat transfer.

As discussed in Section 6.6, if we consider that bubble lift-off occurs when a sliding bubble coalesces with an other bubble growing on its site, the sliding length l_{sl} shall be close to the average distance between two nucleation bubbles on the boiling surface. This value has been derived in Section 7.6:

$$l_{sl} = s_b = \frac{1}{2\sqrt{N_b}} \tag{7.44}$$

with N_b the bubble density from Eq. 7.37.

To assess the validity of this assumption, we compare on Figure 7.16 values of sliding length obtained using either the bubble density N_b or the active site density $N_{sit,a}$ (Eq. 7.41). Since their expression depend on the values of f, $t_{g,d}$ and R_d, we take:

- $R_d = 0.015$ mm at 40 bar and $R_d = 0.02$ mm at 20 bar (see Table 6.3) ;
- $ft_{g,d} = 0.1$ or $ft_{g,d} = 0.01$ since bubble departure by sliding becomes nearly instantaneous after nucleation as pressure increases [90].

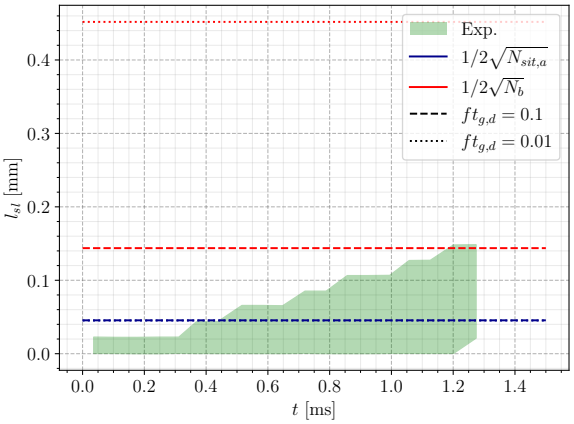

(a) $P = 20$ bar, $G = 500$ kg/m^2/s

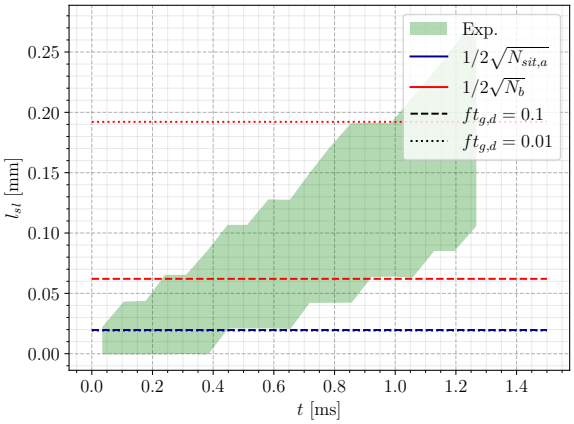

(b) $P = 40$ bar, $G = 500$ kg/m^2/s

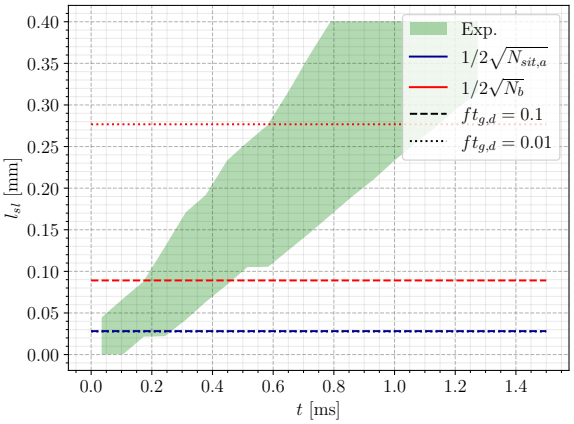

(c) $P = 20$ bar, $G = 1000$ kg/m^2/s

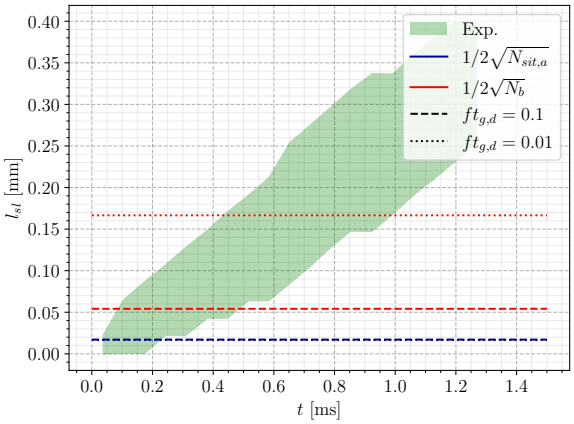

(d) $P = 40$ bar, $G = 1000$ kg/m^2/s

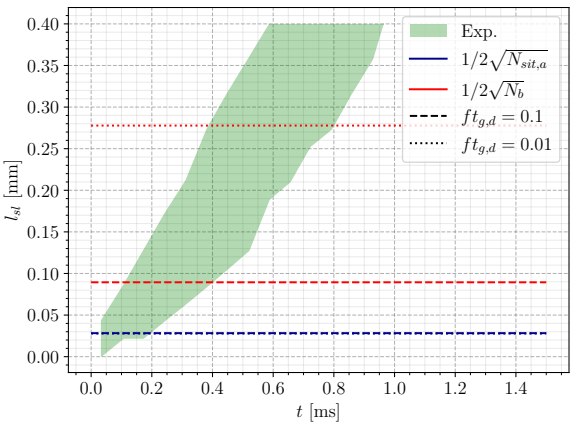

(e) $P = 20$ bar, $G = 1500$ kg/m^2/s

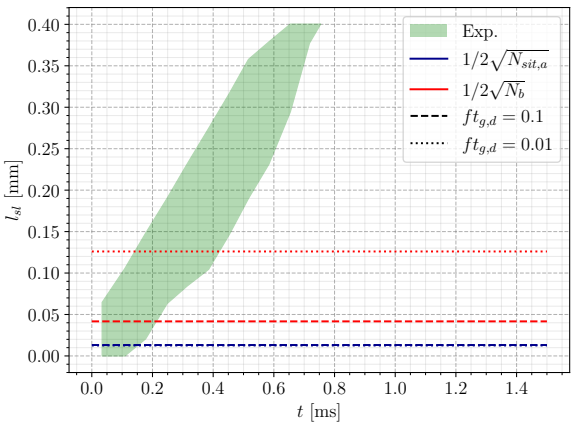

(f) $P = 40$ bar, $G = 1500$ kg/m^2/s

Figure 7.16: Comparison of sliding distance estimations with Kossolapov measurements [90]. NSD was estimated using Li *et al.* correlation (Eq. 7.11).

First, we must acknowledge that the ranges of measured sliding length by Kossolapov include bubbles that do not slide to the longest observed distance. When looking at the statistical distribution provided in his work [90], bubbles seem to averagely slide around half the longest distance measured in the experiments.

The evaluation using the average distance between two active sites is always clearly underestimating the sliding distance. This seems natural due to the heterogeneity and temporal asynchronism between active sites regarding their nucleation behavior. On the contrary, estimating the distance using the bubble density with very low values of $ft_{g,d}$ seem to better approach the actual sliding length. Only a clear overestimation is observed for the $P = 20$ bar and $G = 500$ kg/m^2/s case for which we can speculate that values of $ft_{g,d}$ may be larger.

7.8 SINGLE BUBBLE QUENCHING AREA

When computing the quenching heat flux, we need to provide the total wall area visited by a single bubble $A_{q,1b}$ that will undergo quenching. In wall boiling model that do not consider bubble sliding [65, 92, 130] the impacted area at bubble lift-off is often considered as :

$$A_{q,1b} = F_A \pi R_{lo}^2 \tag{7.45}$$

with F_A being an enhancement factor that accounts for the the possibility that the bubble will induce quenching over a surface larger than its projected area. For instance, we remind that Kurul & Podowski used $F_A = 4$ in their model [92].

Remark : This question of bubble influence area has been discussed by different authors. Yoo *et al.* [171] experimentally found enhancement factor up to 14 for small sliding bubbles. On the contrary, Kossolapov [90] observed that the area undergoing quenching was exactly the surface covered by the bubble footprint that can be even smaller that the bubble projected area. This aspect seems still open to discussions and may need extra experimental observations to reach a solid conclusion. **In this work, we will simply consider that the bubble induces transient heat transfer over its projected area.**

Otherwise, models that account for bubble sliding [7, 59, 89, 168] compute the quenching area using the sliding length l_{sl} as:

$$A_{q,1b} = l_{sl} \left(R_d + R_{lo} \right) \tag{7.46}$$

However, depending on the relationship between l_{sl}, R_d and R_{lo}, the quenching area induced by a single sliding bubble without coalescence can have different shapes as pictured in Figure 7.17.

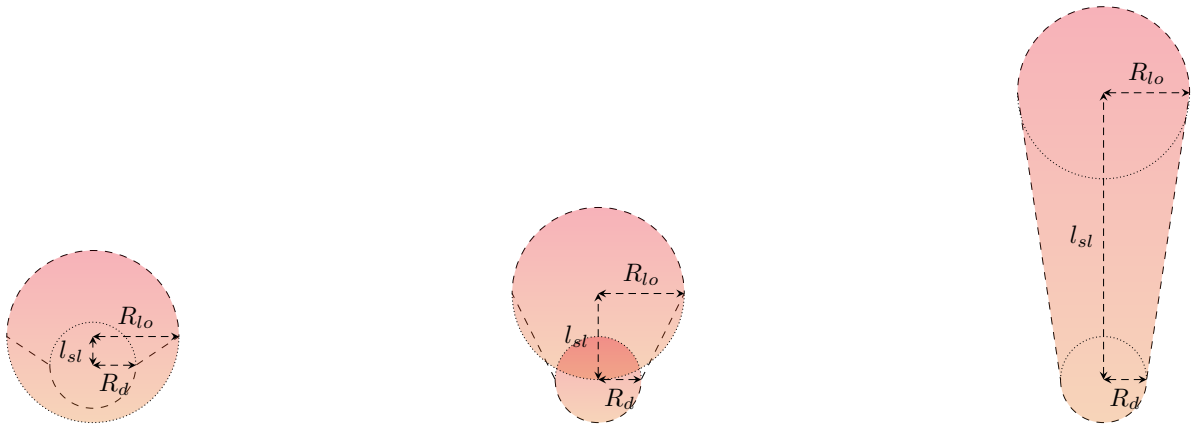

(a) $l_{sl} < R_{lo} - R_d$

(b) $R_{lo} - R_d \leq l_{sl}$ and $l_{sl} \leq R_{lo} + R_d$

(c) $l_{sl} > R_{lo} + R_d$

Figure 7.17: Quenching area shape depending on the relation between R_d, R_{lo} and l_{sl}, if the bubble do not experience multiple coalescence while sliding.

Based on Figure 7.17, we can then write:

$$A_{q,1b} = \begin{cases} \pi R_{lo}^2 & \text{if } l_{sl} \leq R_{lo} - R_d \\ \frac{1}{2}\pi R_d^2 + l_{sl}\left(R_d + R_{lo}\right) + \frac{1}{2}\pi R_{lo}^2 & \text{if } l_{sl} \geq R_{lo} + R_d \end{cases} \tag{7.47}$$

Which can be re-expressed by defining ${l_{sl}}^* = \dfrac{l_{sl}}{R_{lo}}$ and ${A_{q,1b}}^* = \dfrac{A_{q,1b}}{\pi R_{lo}^2}$

$$A_{q,1b}{}^{*} = \begin{cases} 1 & \text{if } l_{sl}{}^{*} \leq 1 - \dfrac{R_d}{R_{lo}} \\ \dfrac{1}{2}\left(1 + \left(\dfrac{R_d}{R_{lo}}\right)^2\right) + \dfrac{l_{sl}{}^{*}}{\pi}\left(1 + \dfrac{R_d}{R_{lo}}\right) & \text{if } l_{sl}{}^{*} \geq 1 + \dfrac{R_d}{R_{lo}} \end{cases} \tag{7.48}$$

and we linearly interpolate those two expressions for the region where $1 - \dfrac{R_d}{R_{lo}} \leq l_{sl}{}^{*} \leq 1 + \dfrac{R_d}{R_{lo}}$.

7.9 ASSEMBLING A NEW HEAT FLUX PARTITIONING

Based on all the discussions conducted in Chapter 6 and in previous Sections of this Chapter, we will now propose a formulation for the HFP model.

In our approach, we consider the following partitioning (Figure 7.18):

- A liquid convective heat flux $\phi_{c,L}$ associated to forced convection ;
- An evaporation heat flux based on static coalescence between adjacent bubbles nucleating on very close sites $\phi_{e,coal,st}$;
- An evaporation heat flux based on sliding coalescence between a sliding bubble and a growing bubble on its site $\phi_{e,coal_{sl}}$;
- A quenching heat flux due to transient conduction following bubble departure, sliding and lift-off ;
- A vapor convective heat flux $\phi_{c,V}$ that accounts for the portion of the wall directly in contact with vapor under a bubble footprint.

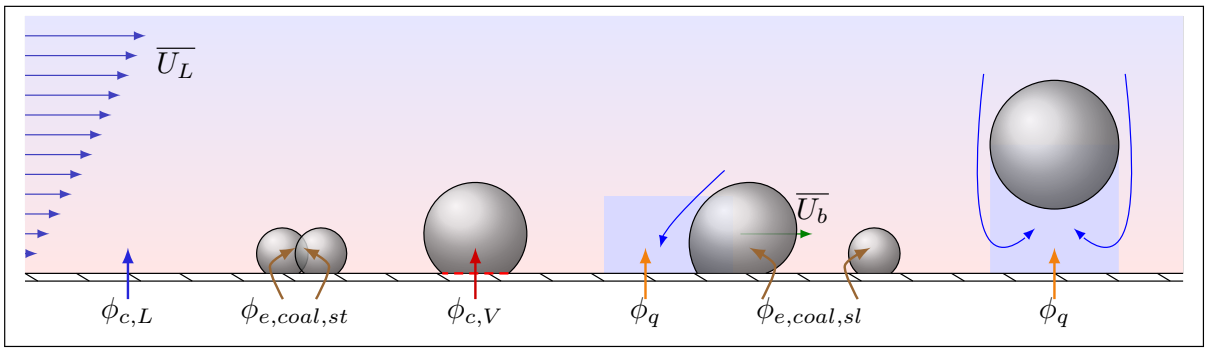

Figure 7.18: Sketch of all the considered heat transfers for the new HFP model.

The total wall heat flux then writes:

$$\phi_w = \phi_{c,L} + \phi_{e,coal,st} + \phi_{e,coal,sl} + \phi_q + \phi_{c,V} \tag{7.49}$$

7.9.1 *Liquid Convective Heat Flux*

The liquid convective heat flux $\phi_{c,L}$ is naturally computed as:

$$\phi_{c,L} = A_{c,L} h_{c,L} \left(T_w - T_L\right) = h_{c,L} \left(\Delta T_w + \Delta T_L\right) \tag{7.50}$$

where $A_{c,L}$ is the proportion of the wall area that is affected by liquid forced convection.

The liquid heat transfer coefficient $h_{c,L}$ is computed using Gnielinski correlation (Eq. 3.21) that has proven to be efficient for wall temperature predictions in single-phase regimes both for R12 and water (3.5.2 and 7.2).

7.9.2 *Static Coalescence Evaporation Heat Flux*

The static coalescence arises from the calculation of the probability for two bubbles to nucleate at a distance lower than $2R_d$ (Eq. 7.42) which gives the proportion of active nucleation sites that will produce this type of bubble (Eq. 7.43).

Assuming that the bubbles will merge at a radius close to R_d, we can compute the associated evaporation heat flux:

$$\phi_{e,coal,st} = N_{coal,st} f \rho_V h_{LV} \frac{4}{3} \pi R_d^3 \tag{7.51}$$

This heat flux can also be expressed using the resulting radius of the coalescence:

$$\phi_{e,coal,st} = \frac{N_{coal,st}}{2} f \rho_V h_{LV} \frac{4}{3} \pi R_{coal,st}^3 \tag{7.52}$$

$$R_{coal,st} = \left(R_d^3 + R_d^3\right)^{1/3} = 2^{1/3} R_d \tag{7.53}$$

7.9.3 *Sliding Coalescence Evaporation Heat Flux*

Since we identified the active sites that will lead to static coalescence, we consider that the remaining sites will generate bubbles for which lift-off occurs under sliding coalescence. Meaning that half of the sites will generate a sliding bubble and the other half a static bubble that will coalesce with the sliding one. This results in a bubble of diameter:

$$R_{coal,sl} = \left(R_{sl}^3 + R_d^3\right)^{1/3} \tag{7.54}$$

Where R_{sl} is the diameter of the sliding bubble after a distance $l_{sl} = \frac{1}{2\sqrt{N_b}}$ (Eq. 7.44). The sliding part is solved following the bubble dynamics model that has been developed in Section 6.5 after departure at radius R_d computed using Eq. 6.108.

We can thus write:

$$\phi_{e,coal,sl} = \frac{N_{coal,sl}}{2} f \rho_V h_{LV} \frac{4}{3} \pi \left(R_{sl}^3 + R_d^3\right) \tag{7.55}$$

7.9.4 *Quenching Heat Flux*

The quenching heat flux is split in two parts:

- Quenching from static coalescing bubbles, each of them having a projected area of πR_d^2 ;
- Quenching from sliding coalescing bubbles, for which the total swiped area can be expressed using Eq. 7.47 with a lift-off radius being the resulting coalescence radius (Eq. 7.54).

The time during which the transient heat transfer will take place depends on the relationship between the total wait time t_w and the theoretical time t^* at which the heat transfer coefficient of transient conduction and forced convection are equal:

$$h_{c,L} \left(\Delta T_w + \Delta T_L\right) = \frac{\lambda_L \left(\Delta T_w + \Delta T_L\right)}{\sqrt{\pi \eta_L t^*}} \tag{7.56}$$

$$\Leftrightarrow t^* = \left(\frac{\lambda_L}{h_{c,L}}\right)^2 \frac{1}{\pi \eta_L} \tag{7.57}$$

If the wait time t_w is lower than t_*, then transient conduction dominates during the whole period between two nucleation and the quenching time t_q is thus equal to t_w.
Otherwise, if $t_w > t^*$ the wait time will consist of transient heat transfer during t^* before being dominated by forced convection up to t_w. The quenching time t_q in this case is then t^*.

Then, using the transient heat transfer solution (mentioned in Section 7.5, also derived by Del Valle [35]), we can write the total quenching flux as:

$$\phi_q = A_q t_q f \frac{2\lambda_L \left(\Delta T_w + \Delta T_L\right)}{\sqrt{\pi \eta_L t_q}} \tag{7.58}$$

$$A_q = N_{coal,st} \pi R_d^2 + \frac{N_{coal,sl}}{2} A_{q,1b} \tag{7.59}$$

$$t_q = \min\left(t_w, t^*\right) \tag{7.60}$$

where $A_{q,1b}$ is computed using Eq. 7.47 with $R_{coal,sl}$ as the lift-off radius.

7.9.5 *Vapor Convective Heat Flux*

Assuming that the vapor is at saturation temperature, we can write:

$$\phi_{c,V} = A_{c,V} h_{c,V} \left(T_w - T_{sat}\right) = A_{c,V} h_{c,V} \Delta T_w \tag{7.61}$$

where $A_{c,V}$ is the portion of the wall area in direct contact with vapor.

The vapor heat transfer coefficient is estimated simply based on a conductive transfer over a bubble radius:

$$h_{c,V} = \frac{\lambda_V}{\langle R \rangle} \tag{7.62}$$

For a truncated spherical bubble, the vapor contact area is its foot area : $\pi \left(R \sin\left(\theta\right)\right)^2$. Since the bubbles are supposed to grow following a $\sqrt{t}$ law (Section 6.3), the average radius for a bubble over its growth time t_g is:

$$\langle R \rangle = \frac{1}{t_g} \int_0^R r \, \mathrm{d}r = \frac{1}{t_g} \int_0^{t_g} K \mathrm{Ja}_w \sqrt{\eta_L t} \, \mathrm{d}t = \frac{1}{t_g} K \mathrm{Ja}_w \frac{2}{3} \sqrt{\eta_L} \, t_g^{3/2} = \frac{2}{3} R \tag{7.63}$$

Distinguishing between the bubbles that coalesce while growing up to R_d on their site and sliding bubbles that reaches R_{sl}, we have:

$$A_{c,V} = \left(N_{coal,st} + \frac{N_{coal,sl}}{2}\right) \pi \left(\frac{2}{3} R_d \sin\left(\theta\right)\right)^2 + \frac{N_{coal,sl}}{2} \pi \left(\frac{2}{3} R_{sl} \sin\left(\theta\right)\right)^2 \tag{7.64}$$

The time-averaged surface proportion occupied by bubble footprints is then:

$$\overline{A_{c,V}} = \left(N_{coal,st} + \frac{N_{coal,sl}}{2}\right) \pi \left(\frac{2}{3} R_d \sin\left(\theta\right)\right)^2 \times t_{g,d} f + \frac{N_{coal,sl}}{2} \pi \left(\frac{2}{3} R_{sl} \sin\left(\theta\right)\right)^2 \times t_{g,lo} f \tag{7.65}$$

7.9.6 *Liquid Convection Area*

Using the expressions of A_q and $A_{c,V}$, we can deduce the remaining unaffected area $A_{c,L}$:

$$A_{c,L} = 1 - A_q t_q f - A_{c,V} \tag{7.66}$$

7.9.7 *Model Summary*

On Tables 7.5 and 7.6, we gather the formulations and closure laws of the proposed Heat Flux Partitioning model.

In the end, we can see that to fully close the model, we need to set 3 parameters values being:

- The contact angle θ which should be chosen in reasonable ranges regarding the heater surface and working fluid. As discussed earlier, usual uncertainties for contact angle measurements usually lie around 5° to 10° [63].

- The contact angle hysteresis dθ of the tilted bubble. It plays a role in determining the capillary term in the non-dimensional approach (Chapter 6). Although precise measurements and its dependency on flow parameters are clearly lacking, it seems that value higher than 10° are acceptable for low pressure flows (larger bubbles) and decrease down to a few degrees when reaching higher pressures such as 40 bar.
- The bubble growth constant K which value has been discussed earlier (Section 6.3). Its value should roughly lie between 0.1 and 2 depending on the flow conditions. It appeared that for subcooled low pressure flow match with values of $K < 1$ while at higher pressures $1 \leq K \leq 2$ better represent the bubble growth regime.

Remark : Since the contribution of the microlayer was not directly accounted for in this work, we can mention that its impact can be included in the value of K in the bubble growth term for low pressure cases (as done by Mazzocco *et al.* [111]).

Closure Laws

Physical Parameter	Modeling
Liquid Convective Heat Transfer Coefficient $h_{c,L}$	$\mathrm{Nu}_L = \dfrac{h_{c,L}\lambda_L}{D_h} = \dfrac{\dfrac{C_f}{2}\left(\mathrm{Re}_{D_h} - 1000\right)\mathrm{Pr}}{1 + 12.7\sqrt{\dfrac{C_f}{2}}\left(\mathrm{Pr}^{2/3} - 1\right)}$, $C_f = 0.036\mathrm{Re}_{D_h}^{-0.1818}$
Departure Radius R_d	$C_{AM,x}K^2\dfrac{\mathrm{Ja}_w^2}{\mathrm{Pr}_L} + \dfrac{1}{3}\dfrac{\mathrm{Re}_b}{\mathrm{Fr}} + \dfrac{1}{8}C_D\mathrm{Re}_b > \dfrac{1}{2}\dfrac{f_{C,x}(\theta, \mathrm{d}\theta)}{\mathrm{Ca}}$ $C_{AM,x} = 0.636$, $C_D = (1 + \Delta C_D)\, C_{D,U}$ (See Eq. 6.36)
Sliding Velocity U_b	$\left(1 + \dfrac{\rho_L}{\rho_V}C_{AM,x}\right)\dfrac{\mathrm{d}U_b}{\mathrm{d}t} = \left(\dfrac{\rho_L}{\rho_V} - 1\right)g + \dfrac{3}{8}\dfrac{C_D}{R}\dfrac{\rho_L}{\rho_V}(U_L - U_b)\lvert U_L - U_b\rvert + 3\dfrac{\dot{R}}{R}\left[C_{AM,x}\dfrac{\rho_L}{\rho_V}(U_L - U_b) - U_b\right] - \dfrac{3}{4}\dfrac{\sigma}{\rho_V}\dfrac{f_{C,x}}{R^2}$
Bubble Growth Law & Times t_g	$R(t) = K\mathrm{Ja}_w\sqrt{\eta_L t}$, $t_g = \left(\dfrac{R}{K\mathrm{Ja}_w}\right)^2\dfrac{1}{\eta_L}$
Bubble Wait Time t_w	$t_w = \dfrac{1}{\pi\eta_L}\left[\dfrac{(\Delta T_L + \Delta T_w)\, C_1 R_c}{\Delta T_w - \dfrac{2\sigma T_{sat}}{C_2\rho_V h_{LV} R_c}}\right]^2$, $C_1 = \dfrac{1 + \cos(\theta)}{\sin(\theta)}$, $C_2 = \dfrac{1}{\sin(\theta)}$ $R_c = \dfrac{2\sigma T_{sat}}{\rho_V h_{LV}\Delta T_w}$
Nucleation Frequency f	$f = \dfrac{1}{t_{g,d} + t_w}$
Nucleation Site Density N_{sit}	$N_{sit} = N_0 e^{\mathrm{f}(P)}{\Delta T_w}^{A\Delta T_w + B}(1 - \cos(\theta))$ $\mathrm{f}(P) = 26.006 - 3.678e^{-2P} - 21.907e^{-P/24.065}$ $A = -2\times10^{-4}P^2 + 0.0108P + 0.0119$, $B = 0.122P + 1.988$ $1 - \cos(\theta) = (1 - \cos(\theta_0))\left(\dfrac{T_c - T_{sat}}{T_c - T_0}\right)^{\gamma}$, $\gamma = 0.719$ P in MPa, θ_0 contact angle at room temperature. (Eq. 7.11)
Active Nucleation Site Density $N_{sit,a}$	$N_{sit,a} = \dfrac{\mathcal{W}(N_{sit}A_{sit})}{A_{sit}}$, $A_{sit} = t_{g,d}f\pi R_d^2$, $\mathcal{W}$ is Lambert's W-function
Nucleating Bubbles Density N_b	$N_b = t_{g,d}fN_{sit,a}$
Average Sliding Distance l_{sl}	$l_{sl} = \dfrac{1}{2\sqrt{N_b}}$
Static & Sliding Coalescing Site Density $N_{coal,st}$ & $N_{coal,sl}$	$N_{coal,st} = \mathcal{P}_{coal,st}N_{sit,a}$, $N_{coal,sl} = (1 - \mathcal{P}_{coal,st})N_{sit,a}$ $\mathcal{P}_{coal,st} = 1 - \exp\left(-N_b\pi(2R_d)^2\right)$
Static & Sliding Coalescence Radiuses $R_{coal,st}$ & $R_{coal,sl}$	$R_{coal,st} = 2^{1/3}R_d$, $R_{coal,sl} = \left(R_d^3 + R_{sl}^3\right)^{1/3}$, R_{sl} sliding diameter after l_{sl}

Table 7.5: Summary of the HFP model closure laws

Mathematical Formulation

Physical Parameter	Modeling
Liquid Convective Heat Flux $\phi_{c,L}$	$\phi_{c,L} = A_{c,L} h_{c,L} \left(\Delta T_w + \Delta T_L\right)$ $A_{c,L} = 1 - A_q - A_{c,V} + A_q \max\left(0, \frac{t_w - t_q}{t_q}\right)$
Static Coalescence Evaporation Heat Flux $\phi_{e,coal,st}$	$\phi_{e,coal,st} = N_{coal,st} f \rho_V h_{LV} \frac{4}{3} \pi R_d^3$
Sliding Coalescence Evaporation Heat Flux $\phi_{e,coal,sl}$	$\phi_{e,coal,sl} = \frac{N_{coal,sl}}{2} f \rho_V h_{LV} \frac{4}{3} \pi \left(R_{sl}^3 + R_d^3\right)$
Quenching Heat Flux ϕ_q	$\phi_q = A_q t_q f \frac{2\lambda_L \left(\Delta T_w + \Delta T_L\right)}{\sqrt{\pi \eta_L t_q}}$ $A_q = N_{coal,st} \pi R_d^2 + \frac{N_{coal,sl}}{2} A_{q,1b}$ $A_{q,1b} = \pi R_{coal,sl}^2 \times A_{q,1b}^*$ with $A_{q,1b}^*$ by Eq. 7.48
Vapor Convective Heat Flux $\phi_{c,V}$	$\phi_{c,V} = A_{c,V} h_{c,V} \Delta T_w$ $h_{c,V} = \frac{\lambda_V}{\langle R \rangle}$ $A_{c,V} = \left(N_{coal,st} + \frac{N_{coal,sl}}{2}\right) \pi \left(\frac{2}{3} R_d \sin\left(\theta\right)\right)^2 + \frac{N_{coal,sl}}{2} \pi \left(\frac{2}{3} R_{sl} \sin\left(\theta\right)\right)^2$

Table 7.6: Summary of the HFP model formulation

.

7.10 CONCLUSION

In this Chapter, we covered different aspects related to the construction of the HFP model, including the evaluation of closure laws required to complete the mathematical model.

At last, we can remember that:

- Single phase heat transfer coefficient is well predicted using Gnielinski correlation, with errors on the wall temperature below 3K for single-phase water flows in various conditions. A corrective factor of 4 had to be used for cases where only one side of the channel is heated to account for geometry difference regarding the correlation establishment.
- Nucleation site density using existing correlations have been assessed using different experiments with water. Covering a large range of pressure, it appeared that Li *et al.* [103] formulation was better at predicting the experimental nucleation site density. In particular, the influence of pressure is very significant and must be accounted for. However, we must keep in mind that although the nucleation site density is critical for wall boiling modeling, its value depends on very fine details of the boiling surface which are not always accessible.
- The bubble wait time has been studied using some existing experimental measurements. Its strong decrease with the wall superheat makes it accounting between nearly 100% down to 50% of the total nucleation period. Comparison of wait time values predictions showed that analytic approaches could perform better than correlations, though this requires an estimation of the active cavity radius which can be very tricky depending and surface-dependent.
- Considering sites and bubble interactions can be achieved under the hypothesis that they both follow an homogeneous spatial Poisson point-process. The mathematical formulations can then be used to account for events such as nucleation site suppression and bubble static coalescence.
- Bubble sliding length was found to be in reasonable agreement with the average distance between two nucleating bubbles on the wall, which can be associated to the fact that bubble leave the surface when coalescing with another one.

- A new heat flux partitioning model was finally proposed in which the boiling flux is computed based on coalescence event avoiding the need of a particular closure law for the lift-off diameter D_{lo}, which estimation for single bubbles was questionable as discussed in Section 6.6. Moreover, the departure and sliding includes the detailed force balance approach developed in Chapter 6.

Next chapter will be dedicated to the validation of the new HFP model through comparisons with wall temperature measurements in vertical flow boiling.

8

VALIDATION OF THE HEAT FLUX PARTITIONING MODEL

Contents

8.1 Detailed Comparison and Assessment of the Heat Flux Partitioning **147**
8.1.1 Active Nucleation Site Density 148
8.1.2 Wait Time, Growth Time, Quenching Time and Nucleation Frequency 148
8.1.3 Single Bubble Area and Total Bubble Area 149
8.1.4 Flux Proportions and Wall Superheat 151
8.2 Wall Temperature Predictions **152**
8.2.1 Kossolapov Data 152
8.2.2 Jens-Lottes Data 155
8.2.3 Kennel Data 158
8.3 Validation for DEBORA Experiment **159**
8.4 Conclusions **159**

In this Chapter, we want to assess the validity of the new Heat Flux Partitioning formulation proposed in Chapter 7. To do so, we will conduct two different validations:

- The first part will be dedicated to validation on a single experimental subcooled boiling case at 10.5 bar from Kossolapov [90] for which numerous physical parameters have been measured. This will ensure that the mathematical formulation and the closure laws propose an acceptable physical modeling of the boiling parameters.

- The second part will consist on wall temperature predictions for vertical subcooled flow boiling of water in various conditions, including pressure. Experimental database from Jens & Lottes [78], Kennel [83] and Kossolapov [90]. Comparison with other HFP models from Kurul & Podowski, Basu and Kommajosyula will be performed.

8.1 DETAILED COMPARISON AND ASSESSMENT OF THE HEAT FLUX PARTITIONING

In this section, we compare our results to those obtained by Kossolapov [90] in vertical subcooled flow boiling. At a pressure of 10.5 bar, he realized measurements of many relevant parameters regarding the Heat Flux Partitioning:

- Active nucleation site density $N_{sit,a}$;
- Bubble nucleation frequency f ;
- Bubble wait time t_w ;
- Transient heat transfer (quenching) time t_q ;
- Average bubble growth time t_g ;
- Average area visited by a bubble $A_{q,1b}$;
- Proportion of the heater area impacted by bubbles $A_{b,tot}$
- Liquid single-phase heat flux proportion $\frac{\phi_{c,L}}{\phi_w}$;

- Quenching heat flux proportion $\frac{\phi_q}{\phi_w}$;
- Wall superheat ΔT_w.

The only lacking parameters to conduct a full evaluation of the model would be the average bubble departure diameter R_d, sliding length l_{sl} and lift-off diameter / coalescence diameter.
The values provided by Kossolapov are an average conducted over all the observed nucleation events during the time of the experiment. Such data are representative of what we want to achieve using a HFP model since we represent average values of the boiling parameters for the considered boiling surface.

All those variables were measured for a subcooling $\Delta T_L = 10°C$ at three different liquid mass fluxes $G_L = 500$, 1000 and 2000 kg/m^2/s.

In next Subsections, we present the results obtained by comparison with the case at $G_L = 2000$ kg/m^2/s for each of those variables. The simulations using the HFP model were conducted using a contact angle $\theta = 85°$ (usual contact angle for water and ITO [90]), an hysteresis $\mathrm{d}\theta = 2°$ and a growth constant $K = 0.8$

8.1.1 *Active Nucleation Site Density*

On Figure 8.1, we compare the values obtained for the active nucleation site density. The Li *et al.* correlation used in the model (Eq. 7.11) propose a reasonable prediction of the measured values of $N_{sit,a}$ with an underestimation of less than a decade. The correlation correctly reproduce the experimental trend where we observe a sort of saturation in the nucleation site density for higher wall superheat.

To better match the asymptotic value of the experiment, we correct the Li *et al.* correlation for this case by a factor $\Delta T_w^{2-0.3\Delta T_w^{0.5}}$ which better fits the measurements for $\Delta T_w > 10$ K but yields a small overestimation before.

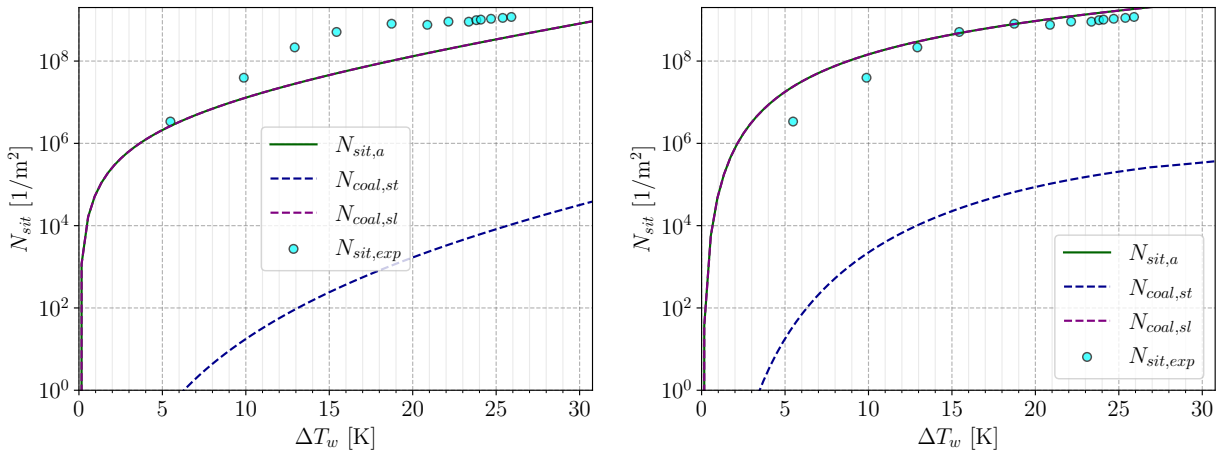

(a) $N_{sit,a}$ predictions by Li *et al.* correlation

(b) $N_{sit,a}$ predictions with corrected Li *et al.* correlation

Figure 8.1: Comparison of active nucleation site density with and without a correction for Li *et al.* formulation.

Note : Following comparisons are conducted using the corrected value of $N_{sit,a}$ to limit the impact of the nucleation site density prediction over the other parameters.

8.1.2 *Wait Time, Growth Time, Quenching Time and Nucleation Frequency*

Figure 8.2 compares the different times involved in the boiling physics and the bubble nucleation frequency. As seen in Section 7.5, the wait time is quite fairly reproduced along with the nucleation frequency. Actually, the bubble departure is nearly instantaneous and the nucleation cycle is mainly composed of the wait period, which means a good estimation of t_w leads to a reasonable estimation of f for this case.

The average bubble growth time is overestimated by nearly a decade for low superheat and is better predicted for larger superheat. Its evolution seem coherent with a decrease up to 15 K and a stabilization afterwards. However, the experimental measurements show an increase in the growth time for large superheat which could be associated to bubble diameter increase with the wall Jakob number as previously observed in Section 6.6. This could be in partial contradiction with the single coalescence hypothesis for the lift-off since the average distance between bubbles in likely to decrease with wall superheat, thus decreasing the average growth time. On the other hand, the growth time overprediction may be associated to sliding length overestimation, especially at low wall superheat.

A very good approximation of the quenching time t_q is achieved using the time t^* (Eq. 7.57). This indicates that for this experimental case, the large value of the wait time implies that the transient conduction will be limited to a duration t^* and that the remaining wait time will be governed by forced convection.

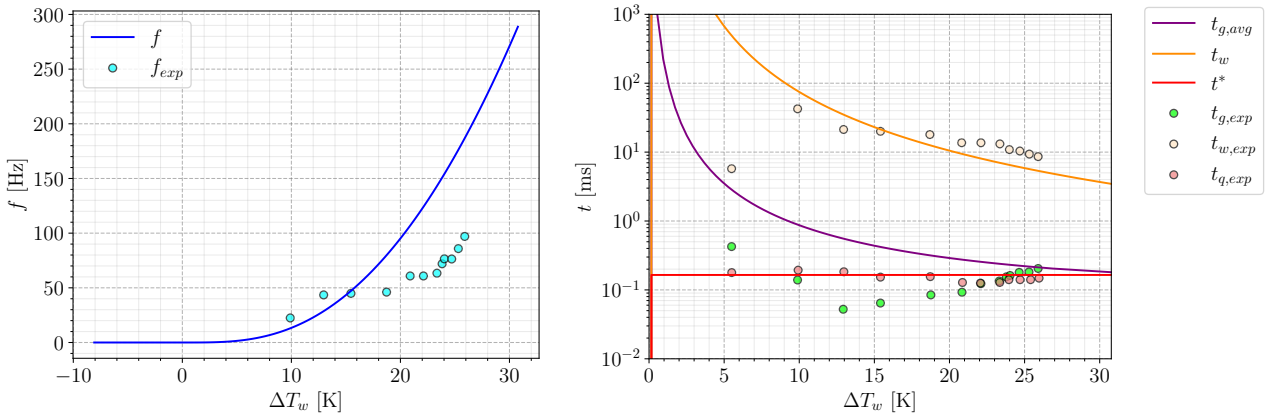

(a) Bubble nucleation frequency

(b) Bubble wait time, growth time and quenching time

Figure 8.2: Comparison of bubble nucleation frequency, wait time, average growth time and quenching time.

8.1.3 *Single Bubble Area and Total Bubble Area*

Figure 8.3 shows that the total area visited by a bubble $A_{q,1b}$ is largely overestimated for the whole boiling curve. It only achieves a reasonable order of magnitude at high wall superheat ($\Delta T_w > 23$ K). This could question the usual hypothesis that supposes a sliding length l_{sl} equal to the average distance between bubbles $s_b = 0.5/\sqrt{N_b}$. The sole projected area of the bubbles is in average better for the visited area, but underpredicts the largest values of $A_{q,1b}$ when bubbles start sliding over significant lengths.

Moreover, both values do not reproduce the experimental trend where the visited area regularly increases with the wall superheat. Further experimental insights regarding the behavior of the bubble sliding length could allow a better modeling of l_{sl} depending on the bubble lift-off process as discussed in Section 6.6.

Those results naturally lead to an overprediction of the wall area fraction impacted by bubbles but shows an coherent increasing trend with wall superheat.

On Figure 8.4, we indicatively show the values of sliding length l_{sl}, departure diameter R_d and sliding diameter R_{sl} when sliding over l_{sl}. The small values of R_d are coherent with nearly immediate departure by sliding, with sliding radiuses close to 0.1 mm.

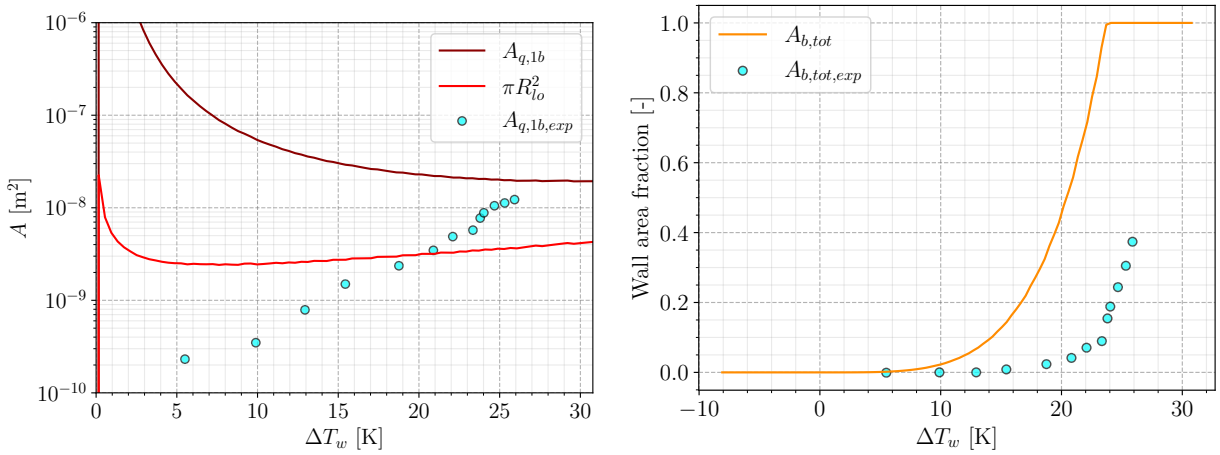

(a) Single bubble area

(b) Total wall area impacted by bubbles

Figure 8.3: Comparison of average area visited by a bubble and total wall fraction area impacted by bubbles (footprint or transient conduction).

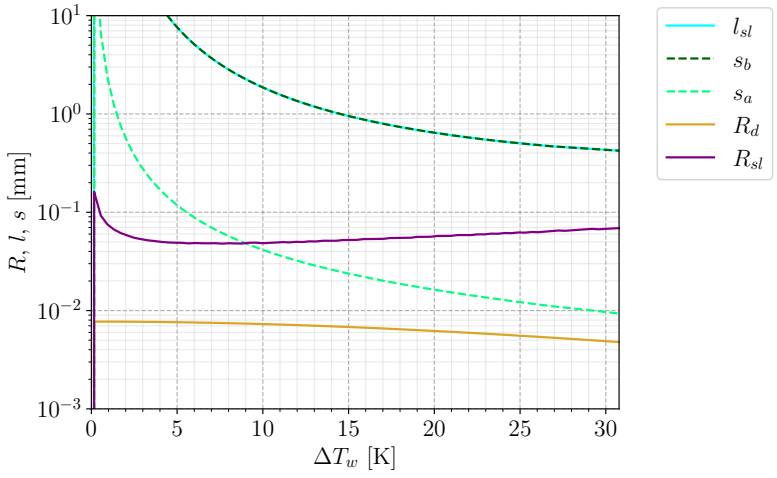

Figure 8.4: Bubble radiuses, sliding length and distances between sites.

8.1.4 *Flux Proportions and Wall Superheat*

Figure 8.5 finally compares the fraction of single-phase convection and quenching over the total heat flux ϕ_w along with the boiling curve. The evolution of the single-phase flux reasonably agrees with the experiment and becomes 0 at a superheat similar to the measurement. However, the quenching heat flux is logically overestimated due to the significant overestimation of the area visited by a single bubble.

On the other hand, the boiling curve is pretty well predicted except for the last experimental measurement where an increase in wall temperature starts, which could correspond to conditions close to the CHF that can't yet be detected by the HFP model.

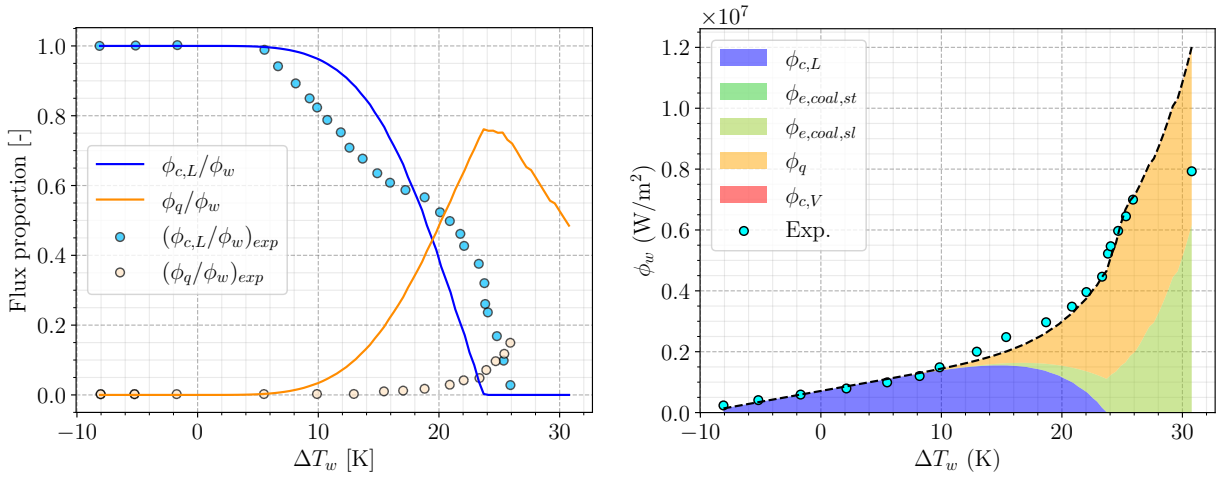

(a) Single-phase and quenching heat fluxes proportions

(b) Global boiling curve of the experiment

Figure 8.5: Comparison of the resulting heat flux partitioning along with the boiling curve.

8.2 WALL TEMPERATURE PREDICTIONS

In this section, we want to evaluate the model's capability to predict wall temperature in boiling regimes for different flow conditions. To do so, we gather boiling curves data from the literature for water that covers a large range of flow conditions as detailed in Table 8.1.

Author	D_h [mm]	P [bar]	G_L [kg/m^2/s]	ΔT_L [K]	ϕ_w [MW/m^2]	ΔT_w [K]	N_{mes} [-]
Kossolapov [90] (2021)	11.78	1.12 - 75.8	500 - 2000	10	0.23 - 7.93	1.55 - 30.77	81
Jens-Lottes [78] (1951)	5.74	137.9	2617.5	53.3 - 92.2	2.15 - 3.63	1.81 - 4.16	38
Kennel [83] (1948)	4.3 - 13.2	2 - 6.2	284 - 10 577	11.1 - 83.3	0.053 - 6.35	1.64 - 49.7	172

Table 8.1: Experimental data range of wall temperature measurements in the boiling region.

The following sub-sections compare the results for wall superheat predictions obtained using four models: Kurul & Podowski (Section 5.2), Basu *et al.* (Section 5.3), Kommajosyula (Section 5.5) and the new formulation (Section 7.9).

In order to propose consistent choices required closing parameters for the new formulation, we will discuss the values attributed to the contact angle θ, bubble inclination dθ and constant value in bubble growth rate K.

8.2.1 *Kossolapov Data*

The boiling curves from Kossolapov's work [90] are among the most recent available data and notably include various operating pressures. The experimental setup consists of a heated flat plate of ITO in vertical flow boiling in a rectangular channel.

As stated by Kossolapov, the contact angle for water and ITO usually lies between 80° and 90° [90]. The bubble tilt is likely to be very low for high pressure cases (see Sec. 6.4) and the bubble growth rate coefficient K shall be closer to 1.5 / 2 at high pressure while it can be lower than 1 for low pressure cases. The chosen values are then:

- $\theta = 85°$;
- d$\theta = 1°$ for $P > 5$ bar and d$\theta = 5°$ otherwise ;
- $K = 1.5$ for $P > 5$ bar and $K = 1.0$ otherwise.

Figure 8.6 shows two typical boiling curves along with the heat flux partitioning obtained using the new formulation for Kossolapov cases at 19.8 bar and 75.8 bar. Comparisons are also made with Kurul & Podowski (Section 5.2) and Kommajosyula (Section 5.5) models.

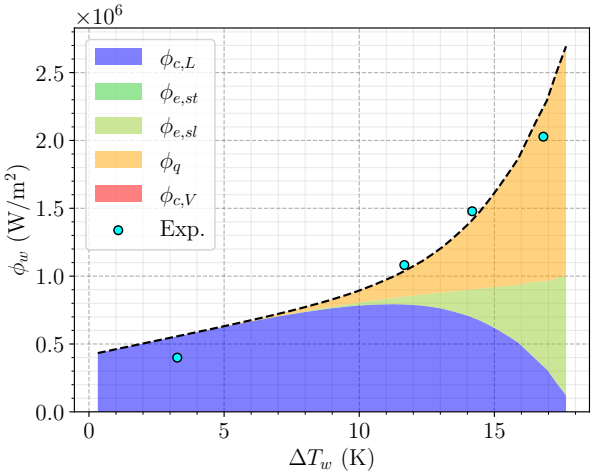

(a) New model, $P = 19.8$ bar

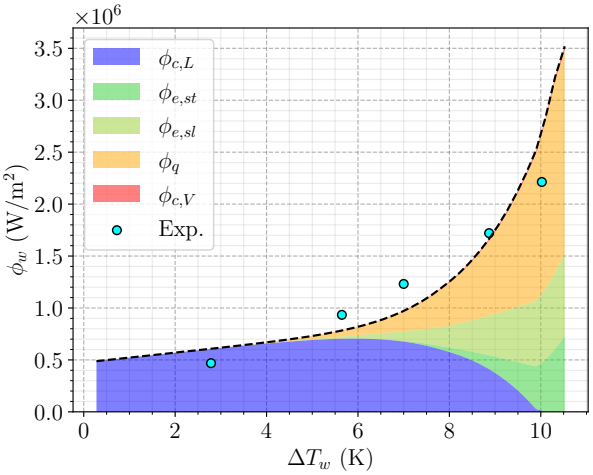

(b) New model, $P = 75.8$ bar

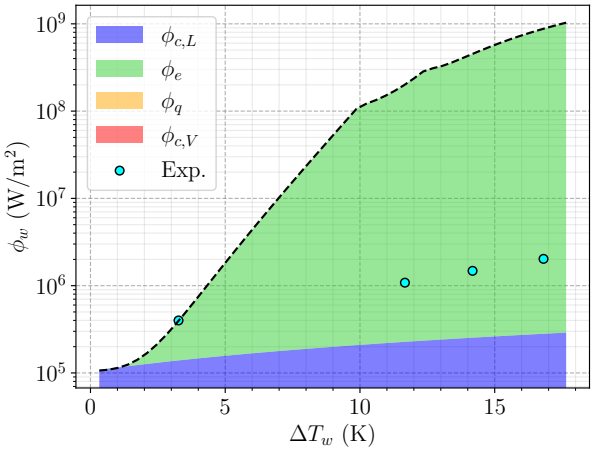

(c) Kommajosyula model, $P = 19.8$ bar

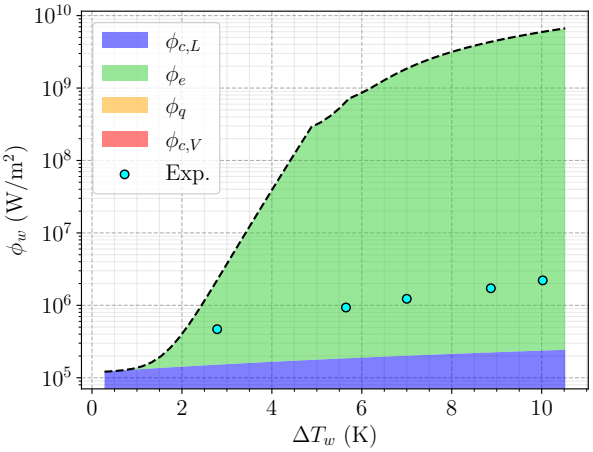

(d) Kommajosyula model, $P = 75.8$ bar

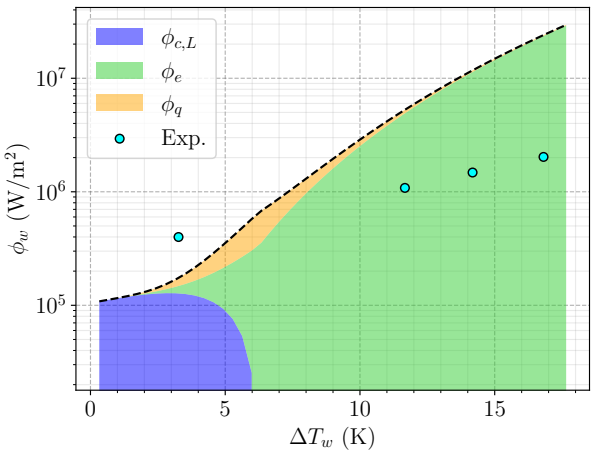

(e) Kurul & Podowski model, $P = 19.8$ bar

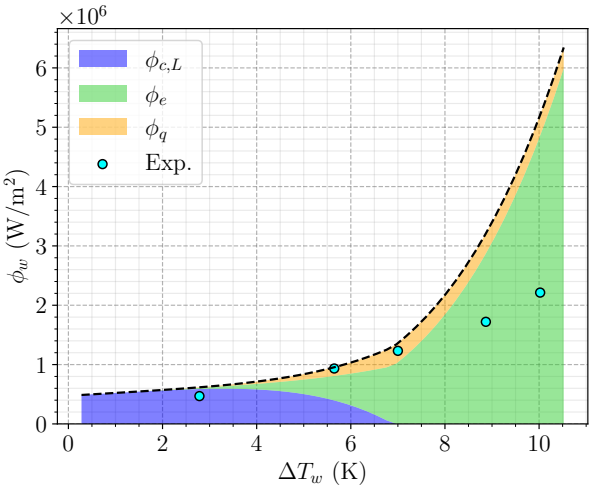

(f) Kurul & Podowski model, $P = 75.8$ bar

Figure 8.6: Comparison with measured boiling curves from Kossolapov [90]. $\Delta T_L = 10$°C and $G_L = 1000$ kg/m^2/s. ϕ_w axis is sometimes set to logarithmic scale if a HFP model largely overcomes the experiment.

We can observe that experimental profiles are quite fairly reproduced in both cases with the new model. It shows different types of heat flux partitioning with the case at 75.8 bar starting to have a significant proportion of static coalescence evaporation flux. This is probably a consequence of both the high pressure and large wall superheat resulting in a very large nucleation site density and increasing the probability for two bubbles to coalesce early in their lifetime.
However, we can see that the results drastically diverge from one HFP model to another, with Kommajosyula model finding extremely large evaporation heat fluxes and rapidly overcoming the measurements. A large evaporation heat flux is also computed by Kurul & Podowski model who is yet a bit closer to the experiments for the 75.8 bar case.

Figure 8.7 shows the wall temperature predictions achieved with the different HFP models on Kossolapov database.

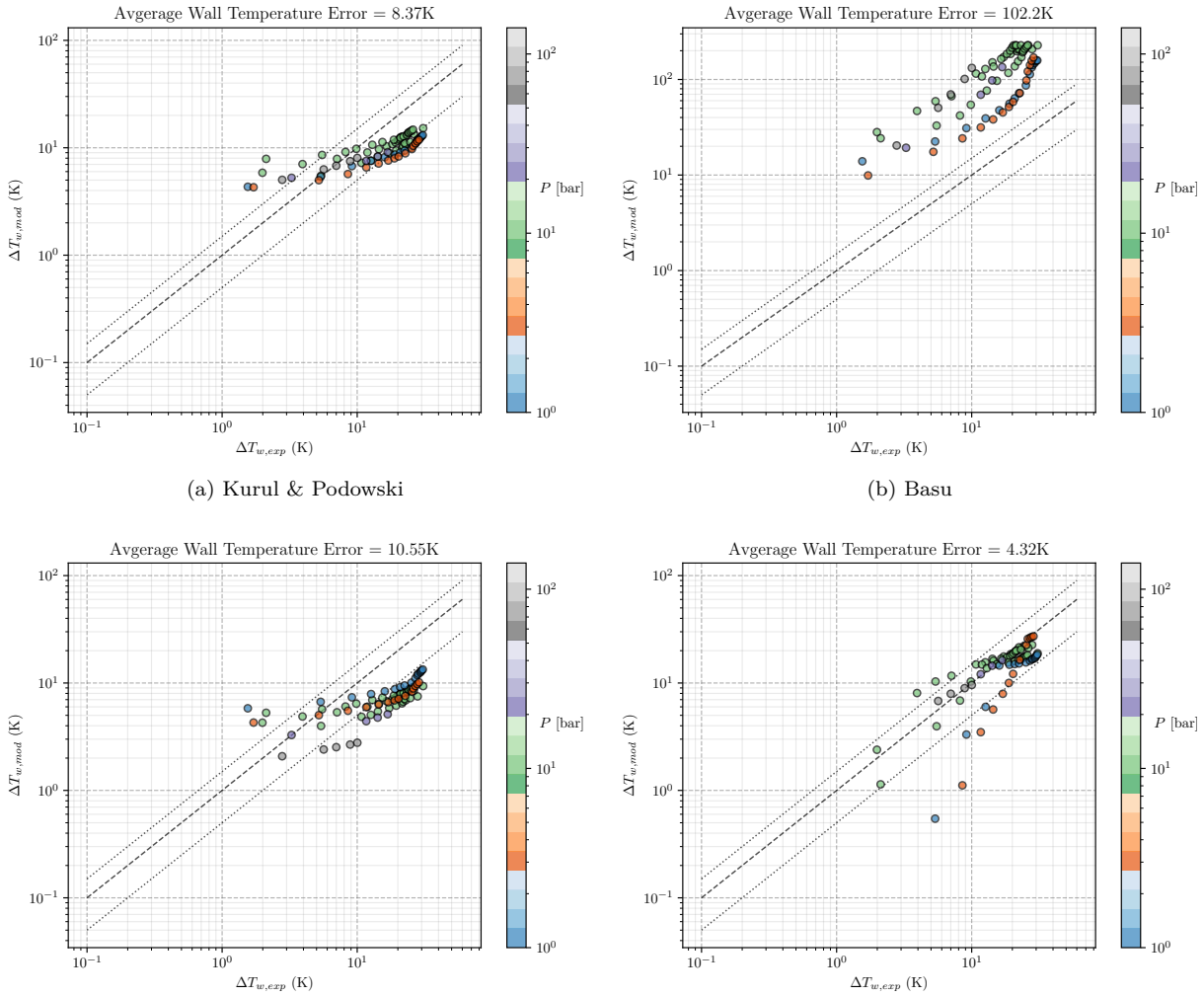

(a) Kurul & Podowski

(b) Basu

(c) Kommajosyula

(d) New Model

Figure 8.7: Wall temperature predictions achieved by the different HFP models on Kossolapov data. ±50% error bars in dashed lines.

We can note that the new formulation generally better agrees with experimental measurements but yields significant underestimation of low wall superheat values for low pressure cases. The predictions achieved by Kurul & Podowski and Kommajosyula models seem similar while Basu *et al.* formulation largely overestimates the wall temperature with an average error above 100 K.

8.2.2 *Jens-Lottes Data*

The data of Jens & Lottes are of particular interest for the HFP validation since they were obtained in conditions close to PWR ones, with an operating pressure of 138 bar, liquid mass flux above 2500 kg/m^2/s and high inlet liquid subcooling. The experiment consisted of an integrally heated metallic circular pipe. Precise evaluation of the contact angle in those conditions is tricky but, according to the work of Song & Fan [149], the water contact angle on metallic surfaces (*e. g.* stainless steel) at large pressure present a very large decrease when reaching surface temperatures above 200°C. Since saturation temperature of water at 138 bar if $T_{sat} \approx 335$°C, the boiling measurements lie largely in the low contact angle zone. Therefore, we will assume:

- $\theta = 20°$;
- $\mathrm{d}\theta = 1°$ (very high pressure leading to nearly non-tilted bubbles) ;
- $K = 2.0$ (very high pressure and low Jakob numbers).

Figure 8.8 shows a typical boiling curve obtained for an experimental case of Jens & Lottes with the new model, Kommajosyula and Kurul & Podowski models.

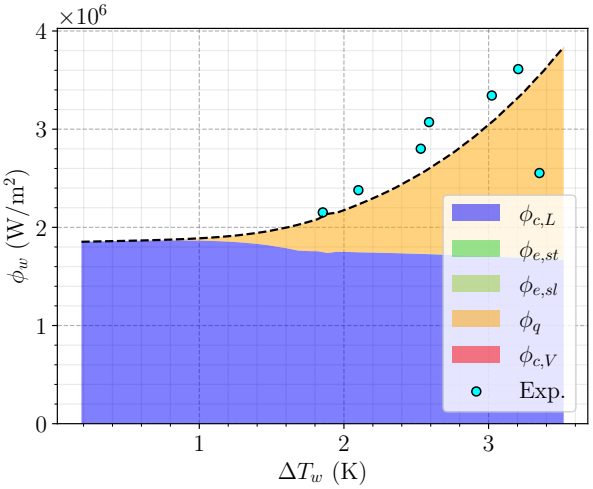

(a) New model

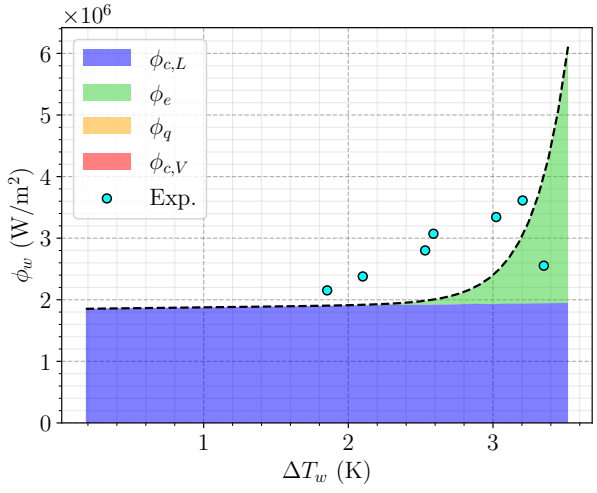

(b) Kommajosyula model

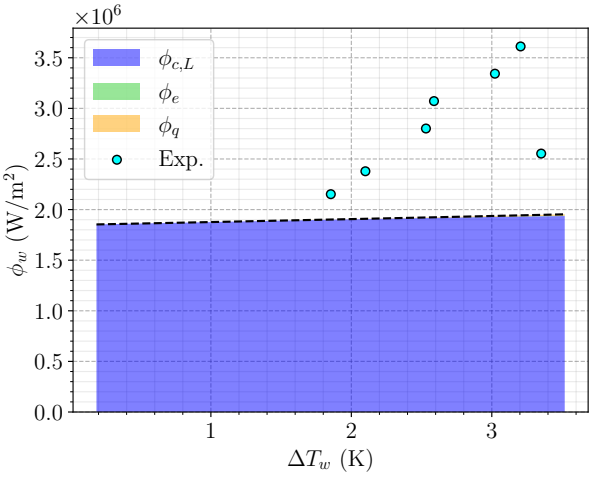

(c) Kurul & Podowski model

Figure 8.8: Comparison with measured boiling curve by Jens & Lottes [78]. $P = 138$ bar, $G = 2600$ kg/m^2/s, $\Delta T_L = 64$°C.

We can observe that, with the new model, in this region where wall superheat are low ($\Delta T_w < 5$ K), the quasi-entirety of the wall heat flux is evacuated through liquid convection and transient conduction

through quenching . This is likely to be a consequence of the very high pressure conditions under which nucleation site density is very large but bubbles become extremely small ($R \sim \mu$m). Evaporation heat flux is then relatively small but the large number of bubbles and their sliding induce a strong quenching effect over the heater surface.
Similar to Kossolapov cases (Figure 8.6),other HFP models provide strikingly different results. While having fair wall temperature predictions, Kommajosyula model predicts a nearly constant liquid convective heat flux before rapidly producing a large evaporation heat flux. On the other hand, Kurul & Podowski model is still in his single-phase zone with only liquid convection.

Remark : We can wonder why Komajosyula's model always yields a negligible quenching flux, with a resulting partitioning composed solely of evaporation and liquid convection. This may actually be a consequence of the quenching area estimation (Eq. 5.53) where it is computed as $A_q = \frac{1}{\sqrt{N_{sit,a}}} \frac{D_d + D_{lo}}{2} = \frac{1.1\ D_d}{\sqrt{N_{sit,a}}}$ since he considers $D_{lo} = 1.2\ D_d$. We can see that reaching very large active nucleation site densities (as in high pressure conditions) will drastically reduce the quenching area.

This highlights the interest of simple, though important, discussions over the quenching area as discussed in Section 7.8. Considering the constant "circular part" under the bubble ($\sim \pi R_d^2$) in addition to the "linear part" associated to sliding may avoid to reach so low quenching heat fluxes which are not expected in those conditions.

All in all, those comparisons of the resulting partitioning using different models points out that achieving good wall temperature predictions does not ensure at all the general validity of the underlying heat flux partitioning, which can vary by decades from one model to another.

Figure 8.9 shows the wall temperature predictions achieved with the different HFP models for the whole Jens-Lottes database.

Both the new formulation and Kommajosyula model achieve good predictions of the wall temperature in those high pressure conditions. However, Kurul & Podowski and Basu models do not seem to capture properly the wall superheat evolution, with large relative overestimation ($\sim 200\%$).

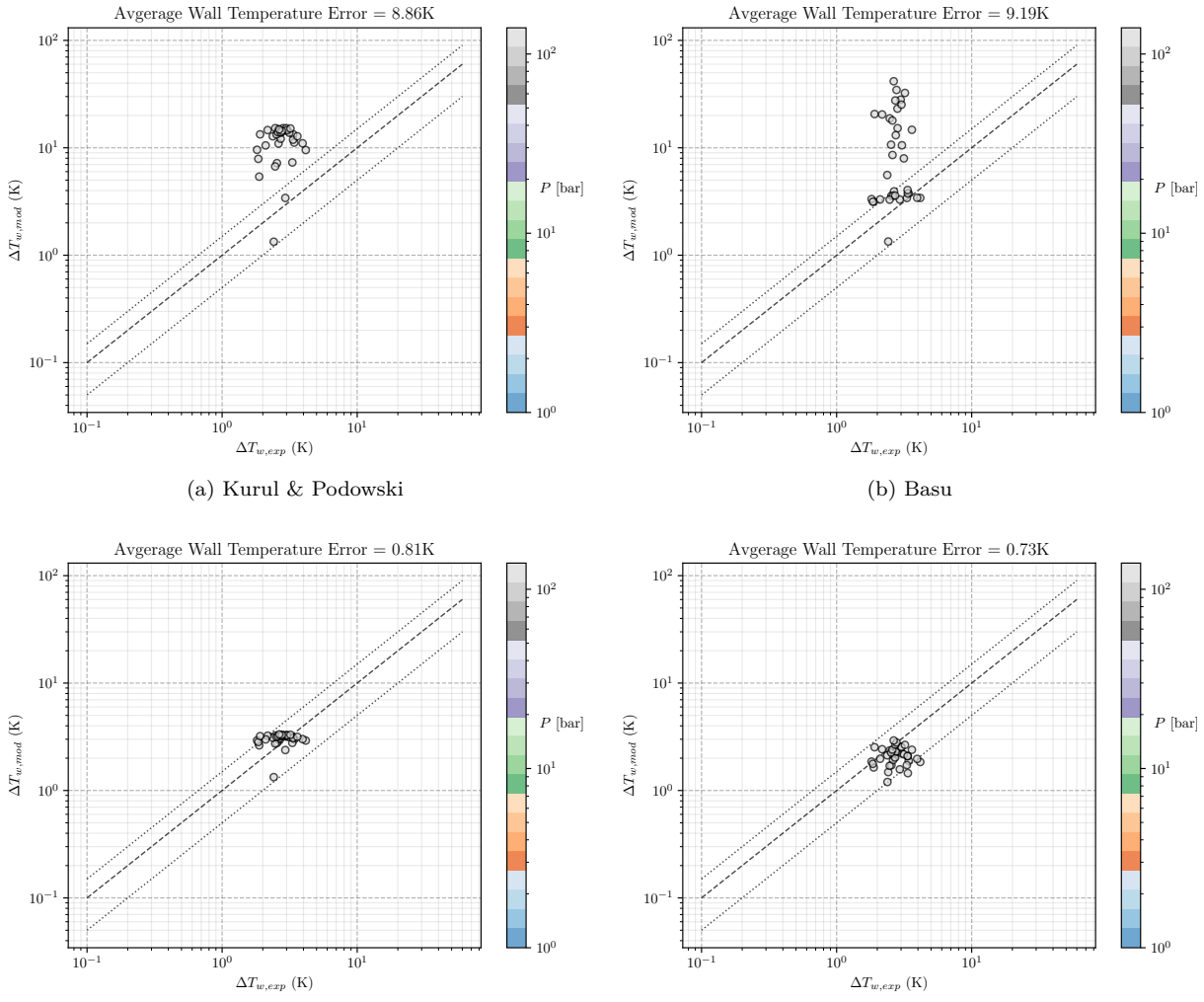

(a) Kurul & Podowski

(b) Basu

(c) Kommajosyula

(d) New Model

Figure 8.9: Wall temperature predictions achieved by the different HFP models on Jens data. ±50% error bars in dashed lines.

8.2.3 *Kennel Data*

Kennel measurements are of similar nature to those of Jens & Lottes since they were conducted for a uniformly heated vertical circular metallic pipe. However, the experiments were operated at pressures lower than 6 bar and various inlet liquid mass fluxes and subcooling. In those conditions, the evaluation of the constant K in the bubble growth profile can be very tricky since the larger bubbles at low pressure are more impacted by the bulk flow, implying potentially large variations of K that can become much lower than 1. Regarding the contact angle, its value can also be roughly estimated using Song & Fan review [149] showing that metallic surfaces at low and moderate pressure also show a contact angle decrease with temperature, with values roughly lying between 40° and 60° when $T_w \sim T_{sat}$. Therefore, we assume:

- $\theta = 50°$;
- $\mathrm{d}\theta = 5°$ (larger and deformable bubbles at low pressure) ;
- $K = 0.3$ (larger impact of bulk subcooling on bubble growth).

Figure 8.10 shows the wall temperature predictions achieved with the different HFP models.

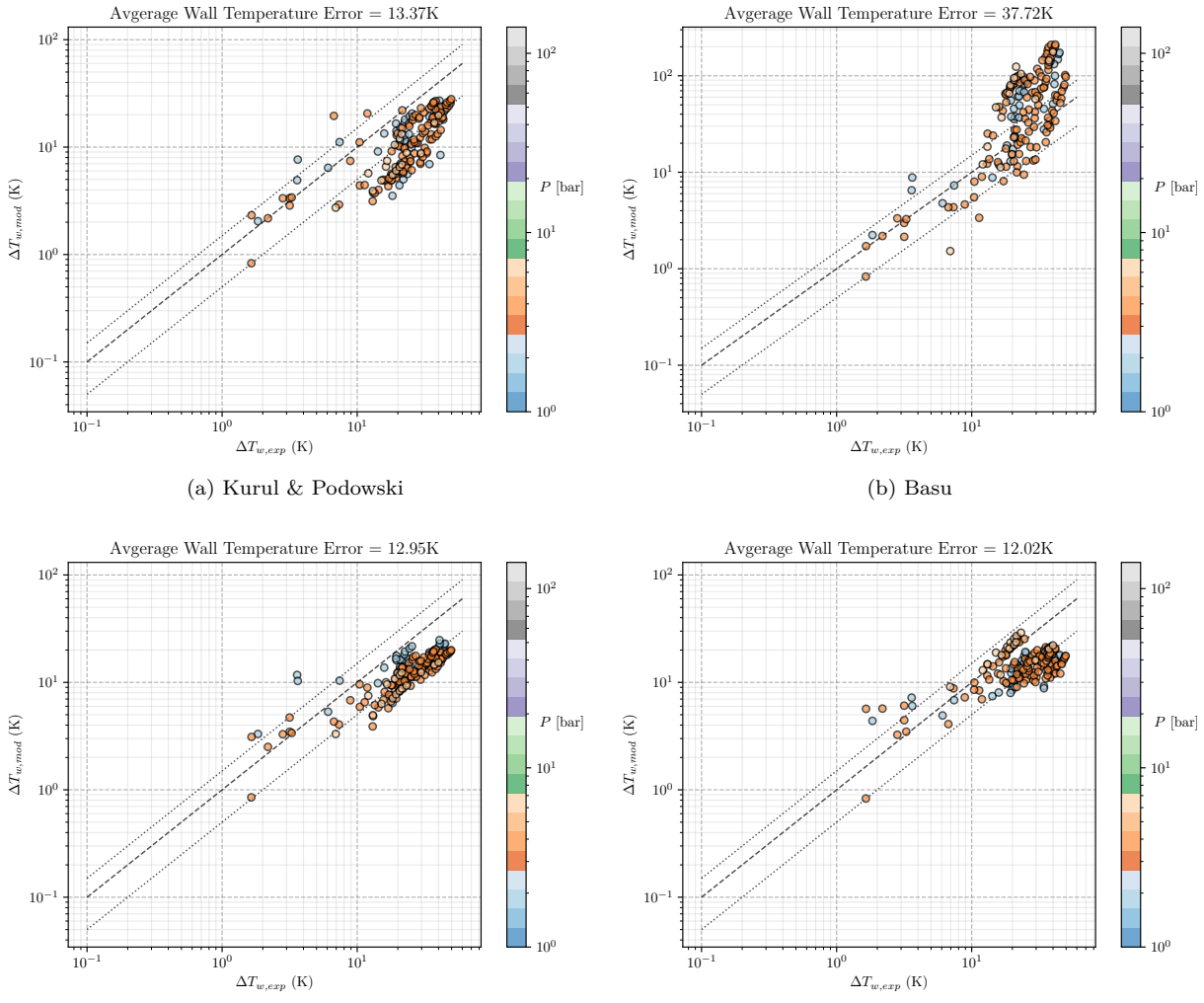

(a) Kurul & Podowski

(b) Basu

(c) Kommajosyula

(d) New Model

Figure 8.10: Wall temperature predictions achieved by the different HFP models on Kennel data. ±50% error bars in dashed lines.

Achieving a good quality of wall superheat predictions for the cases of Kennel appears more complicated. Indeed, the new formulation and Kommajoysula model obtain the best results but still present an average

underestimation of approximately 50%. The very large range of conditions associated to the low pressure may invalidate the assumption of constants values for $\mathrm{d}\theta$ and K.

Remark : In his work, Kommajosyula [89] presented better wall temperature predictions on Kennel data with his model (average error between 3 K and 5 K). We only managed to achieve similar results using a much lower contact angle ($\theta \leq 20°$) which could be questioned regarding the operating conditions.

8.3 VALIDATION FOR DEBORA EXPERIMENT

In order to try a further validation of the proposed HFP model, we will test it under conditions that are representative of the DEBORA cases for the G2P26W16 campaign (Chapter 3):

- R12 as operating fluid ;
- $P = 26.2$ bar ;
- $G_L = 2000$ kg/m^2/s ;
- $\phi_w = 73.9$ kW/m^2.

Since refrigerant are usually known to have low contact angle and recalling that wall temperature in this case is less than 20°C lower than R12 critical temperature ($T_{crit,R12} \approx 380$ K), we suppose $\theta = 5°$. The operating pressure being experimentally chosen to match high-pressure water similarity, we thus choose $\mathrm{d}\theta = 1°$ and $K = 2$ in accordance with the choices made for Jens & Lottes cases.

A one-dimensional simulation of the 8G2P26W16Te44.9 DEBORA case is conducted to compare the wall temperature results obtained by the different HFP models and the NCFD simulation (Chapter 4).

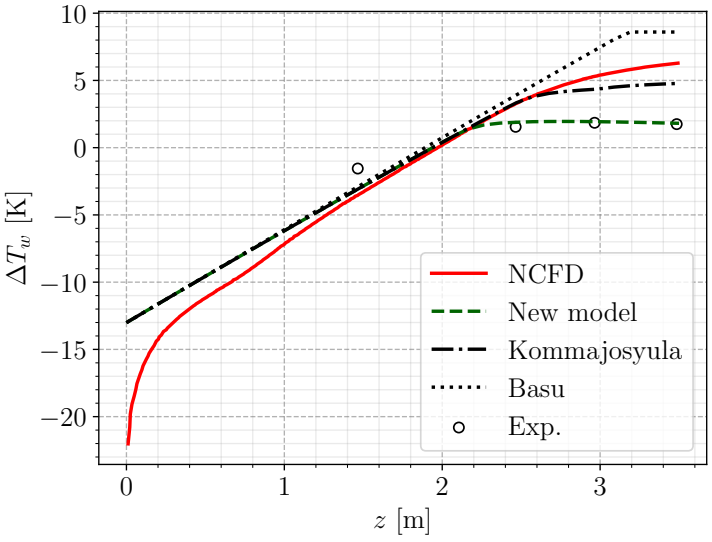

Figure 8.11: Comparison of different HFP and NCFD simulation on the 8G2P26W16Te49 DEBORA case.

We see that the models perform in very different ways for the DEBORA conditions. Basu *et al.* formulation largely overestimates the experimental value while Kommajosyula's model finds a wall temperature slightly lower than the NCFD computation. On the other hand, the new formulation provides a wall temperature much closer to the experimental measurements, which is probably an effect mainly due to the large quenching combined with the pressure dependency of the nucleation site density.

8.4 CONCLUSIONS

In this Chapter, we proposed different aspects of validation regarding the proposed Heat Flux Partitioning model developed in Section 7.9. All in all, we can conclude that:

- The evolution of most physical parameters included in the model are coherent with detailed measurements conducted by Kossolapov [90] (Section 8.1), namely the nucleation site density, the bubble departure frequency, waiting time and quenching time.
- The quenching seems overestimated with a probably too large sliding length. Meaning that the proposed modeling (*i. e.* average distance between two nucleating bubbles, Section 7.7) is likely to be an upper bound of the actual sliding length. Bubbles may actually slide over shorter length, which would require dedicated investigations when reaching boiling regimes with large bubble density on the wall.
- The formulation seems able to capture different nature of heat flux partition, with high-quenching regimes at high pressure and low superheat (Figure 8.8), regimes with both static and sliding coalescence at high pressure and high superheat (Figure 8.6), or mixed between quenching and sliding coalescence at low to moderate pressure and high superheat (Figure 8.6).
- Wall temperature predictions (Section 8.2) using the new formulation along with reasonable values for the closing parameters (θ, $\mathrm{d}\theta$, K) yields better results in average compared to older models. In particular, it seems capable of enhancing the wall temperature predictions on the DEBORA case as shown on Figure 8.11.
- It is however important to note that HFP models presenting similar performances in terms of wall temperature predictions may actually hide truly different flux partitioning as we saw on Figures 8.6 and 8.8. This indicates the difficulty of achieving a globally validated modeling framework due to the spread of predictions produced by the different formulations.

9

PERSPECTIVES TOWARDS CRITICAL HEAT FLUX PREDICTION

Contents

9.1 Previous Modeling of the Boiling Crisis **161**
9.1.1 Empirical Approaches 161
9.1.2 Physical Phenomenology Approaches 161
9.2 Recent Approaches and Advances for CHF Prediction **164**
9.2.1 Dry Patch Formation 164
9.2.2 Model of Baglietto, Demarly & Kommajosyula [5] : Stability of the Heat Flux Partitioning 165
9.2.3 Model of Zhang, Seong & Bucci [178]: Bubble Interaction and Scale-Free Footprint distribution 165
9.3 Simple test of the Zhang Criterion **166**
9.4 Conclusions **167**

In this last Chapter of this Part dedicated to the modeling of wall boiling, we briefly discuss historical approaches to represent the Boiling Crisis and propose a perspective use of Heat Flux Partitioning models as a mean to estimate the Critical Heat Flux.

9.1 PREVIOUS MODELING OF THE BOILING CRISIS

Historically, since the pioneering observations of Nukiyama [126] who identified the maximum boiling heat flux, the question of explaining the triggering of the Boiling Crisis has been thoroughly investigated by many researchers who attempted to propose various physical explanations and modelings aimed to estimate the value of the CHF.

9.1.1 *Empirical Approaches*

As a direct way of estimating the CHF, empirical approaches have remained the preferred solution for engineering problems to tackle the Boiling Crisis issue. Indeed, according to Groeneveld [62], more than 1000 dedicated CHF correlations for water and heated tubes were reported in 2007. As mentioned in the Introduction (Chapter 1), current safety analyses in the nuclear industry actually rely on specific correlations tied to a given core / fuel assembly geometry and usually depend on the pressure P, the mass flux G, the inlet quality $x_{eq,in}$ and geometry through the thermal /heated diameter D_{th} and distance between the mixing grids L_g. For instance, Westinghouse company developed the so-called "Tong-67" correlation [160] based on data-fitted optimization.

Following the huge number of CHF experimental tests that were conducted over the past decades, Groeneveld *et al.* [62] proposed to simply gather a very large number of measurements in order to come up with a "Look-Up Table", which directly tabulates the CHF values depending on the operating conditions. Though computationally efficient, this approach is not extendable to any other conditions except those covered by the table data. As a result, their work is limited to external upward flow of water around circular tubes (*e. g.* fuel rods).

9.1.2 *Physical Phenomenology Approaches*

In 1948, Kutateladze [93] proposed a dimensional analysis to tackle the question of the boiling crisis. Stating that near CHF, the concept of single bubbles / nucleation sites behaviors is lost, he considered

the boiling crisis to come from the destruction of stability of two-phase flow existing near the wall. Based on the interaction of three "energetic scales" respectively associated to surface tension force, gravity and turbulence, he derived:

$$\phi_{w,CHF} = C_K h_{LV} \rho_V \left(\frac{\sigma \left(\rho_L - \rho_V \right) g}{\rho_V^2} \right)^{1/4} \tag{9.1}$$

where $C_K = 0.16$ was obtained from experiments.

This formulation of the CHF found a true success due to its analytic nature and its good performance for moderate to high pressure measurements. The coherent behavior of Kutateladze law has been once more recently confirmed by Kossolapov [90] whose CHF measurements dependency with pressure were fairly reproduced.

Kutateladze approach was further developed by Zuber [183] who proposed a physical interpretation of the Boiling Crisis as an hydrodynamic instability. Considering vapor columns coming out of the heated surface (Figure 9.1), he supposed that the Boiling Crisis was triggered under a combination of Rayleigh-Taylor and Kelvin-Helmoltz instabilities. Assuming the vapor columns were regularly spaced by a distance equal to the Rayleigh-Taylor instability wavelength, the Boiling Crisis is supposed to be triggered by the merging of those vapor columns due to the emergence of Kelvin-Helmholtz instabilities. He then could analytically derive:

$$\phi_{w,CHF} = \frac{\pi}{24} h_{LV} \rho_V \left(\frac{\sigma \left(\rho_L - \rho_V \right) g}{\rho_V^2} \right)^{1/4} \left(\frac{\rho_L}{\rho_L + \rho_V} \right)^{1/2} \tag{9.2}$$

which degenerates to Kutateladze formulation when $\rho_L \gg \rho_V$ with the constant value $C_K = \pi/24 \approx 0.131$.

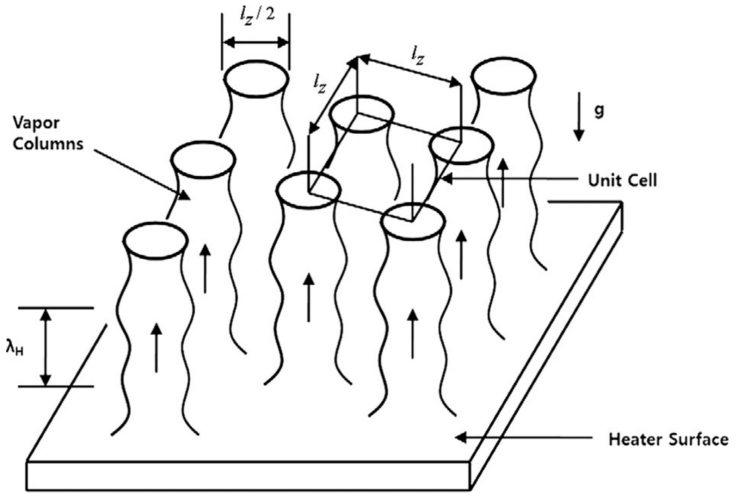

Figure 9.1: Sketch of the boiling crisis description by Zuber [183]. l_z and λ_H are respectively the Rayleigh-Taylor and Kelvin-Helmholtz instability wavelengths.

Note : The formulations of Kutateladze and Zuber were both derived for horizontal pool boiling.

Other approaches are based on different physical mechanism. For instance, Lee & Mudawar [96] propose to describe the boiling crisis phenomenon as the evaporation of a very thin liquid layer trapped between the wall and an elongated slug of vapor (Figure 9.2), following experimental observations

The idea that the boiling crisis is associated to rapid dynamics of bubble base evaporation was also explored by Nikolayev & Beysens [122] who considered the force exerted by the vapor recoil at the bubble base during boiling. They found that this force could trigger a change in bubble shape through a change of the apparent contact angle, leading to the irreversible growth of the dry area. This was further confirmed at low-gravity conditions for liquid helium near the critical temperature [123, 124].

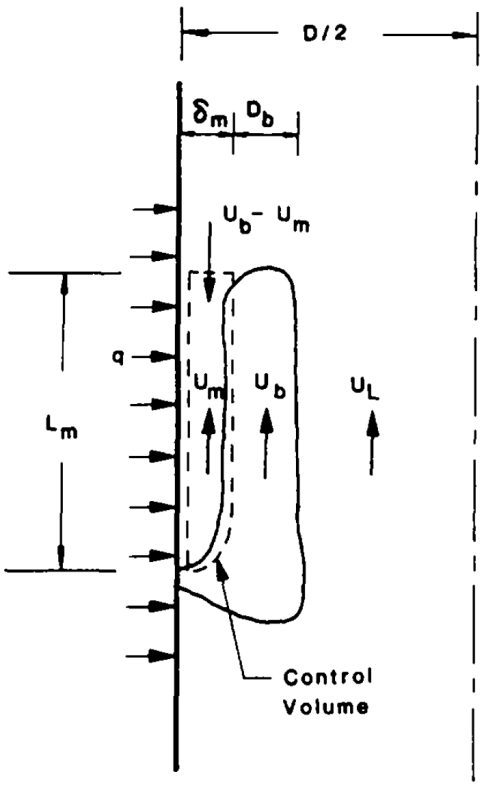

Figure 9.2: Sketch of the boiling crisis description by Lee & Mudawar. Here, the boiling crisis is supposed to be triggered when the evaporation rate of the sublayer exceeds the entering liquid flux (*i. e.* when velocity $U_b - U_m$ approaches 0).

On the other hand, Weisman & Pei [165] proposed that the boiling crisis was due to lack of turbulent transport of the bubbles from the wall towards the bulk, resulting in a bubble layer close to the wall (Figure 9.3) that will trigger coalescence near the heater and isolating it from the liquid phase.

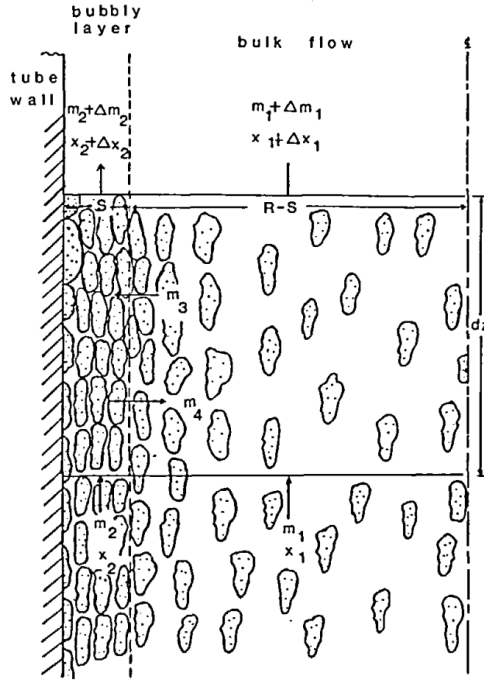

Figure 9.3: Sketch of the boiling crisis description by Weisman & Pei

Assuming bubbles were of ellipsoidal shapes at CHF, they considered that boiling crisis occurred when the maximum packing density was reached, *i. e.* having a wall void fraction:

$$\alpha_{CHF} = 0.82 \tag{9.3}$$

Although this criterion is very suitable for CMFD applications [104, 117], the critical void fraction close to the wall can vary in large ranges (down to 30% at high subcooling) according to experimental observations [17].

Remark : This criterion is the baseline for other CHF detection methods in CFD computations. For instance, NEPTUNE_CFD model uses the 4$^{\text{th}}$ flux towards vapor (Section 2.5) to represent the temperature excursion. This redirection of the heat flux to the vapor phase is controlled by a function depending on critical values of α, which finally resembles to Weisman & Pei criterion.

We can also cite Liu *et al.* [104] who do not use a constant α_{CHF} but rather a fitted pressure and mass flux dependent expression : $\alpha_{CHF}(P, G)$.

9.2 RECENT APPROACHES AND ADVANCES FOR CHF PREDICTION

The question of the boiling crisis occurrence and CHF value is still a topic of active research nowadays. Recently, new experimental observations have allowed the access to wall-related boiling measurements [12, 90, 139] and permitted to better understand the phenomenology behind the trigger of the boiling crisis.

9.2.1 *Dry Patch Formation*

As detailed by Kossolapov [90], a significant number of different experiments studying the wall boiling at CHF have demonstrated that the occurrence of the boiling crisis was similar at various pressures and associated to the formation of an irreversibly growing dry patch [90, 139]. Such observations are leveraging mechanistic behavior of bubbles right before the CHF. First attempts of modeling this phenomenon were proposed by Ha & No [69], prior to the aforementioned experimental observations. Based on a random distribution of the bubbles on the heater surface (similar to the Poisson distributions discussed in Section 7.6), they proposed that a dry patch is created when a bubble crowding hindering rewetting is reached, which was translated as:

$$\phi_w = \phi_{1b} N_{sit,a} \left(1 - \mathcal{P}\left(N \geq N_c\right)\right) \tag{9.4}$$

where $\mathcal{P}(N \geq N_c)$ is the probability to find more than N_c bubbles in the area of influence of a single bubble and $\phi_{w,1b}$ is the heat flux removed by a single bubble.

They noted that this ponderation of the total heat flux allowed to reach reasonable predictions of the maximum heat flux when $N_c = 5$ (Figure 9.4).

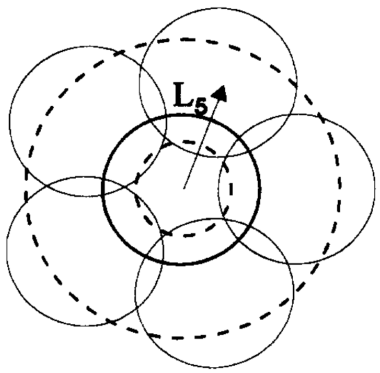

Figure 9.4: Sketch of the dry patch formation mechanism by and adapted from Ha & No [69].

This model was recently re-used by Dong & Gong for low pressure cases [39].

9.2.2 *Model of Baglietto, Demarly & Kommajosyula [5] : Stability of the Heat Flux Partitioning*

In the framework of Heat Flux Partitioning modeling of Kommajosyula [89] and Demarly [37], Baglietto *et al.* [5] proposed a modeling of the wall area in direct contact with vapor (corresponding to $A_{c,V}$ in Section 7.9). By accounting for bubble interactions, the dry area below the bubbles gets enhanced and result in a total dry area fraction S_{dry}:

$$S_{dry} = ft_{g,d} N_{sit,a} \pi \left(\zeta \underbrace{e^{ft_{g,d} N_{sit,a} \pi R_d^2}}_{\text{Bubble interaction}} \sin(\theta) R_d \right)^2 \tag{9.5}$$

where $\zeta = 0.15$ based on data-fitting of Richenderfer [139] experiments.
The total heat flux is finally written as:

$$\phi_w = \left(1 - S_{dry}\right) \left(\phi_{c,L} + \phi_e + \phi_q\right) + S_{dry} \phi_{dry} \tag{9.6}$$

where ϕ_{dry} is the heat flux through the dry area, which is nearly negligible versus the other heat fluxes.

This modeling allows to impose a decrease of the total heat flux by gradually enhancing the growth of the dry area, thus inducing a decrease of ϕ_w when covering a whole boiling curve (Figure 9.5).

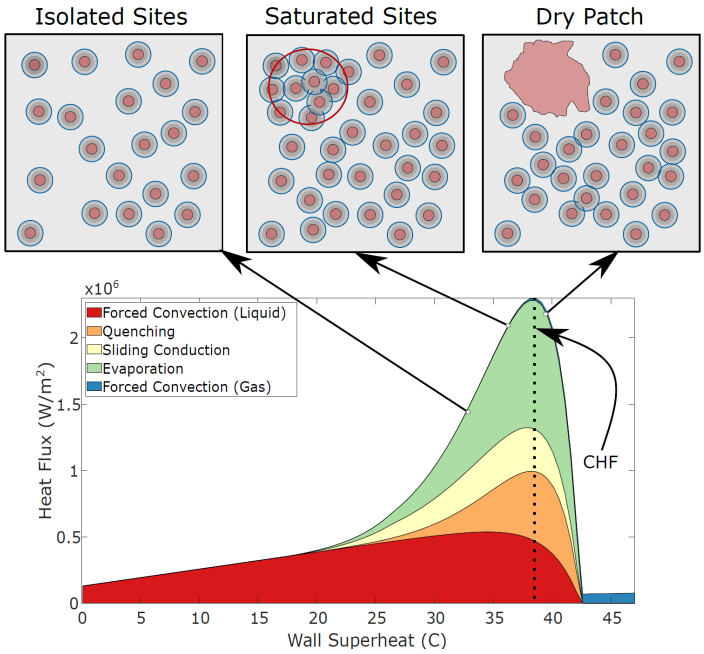

Figure 9.5: Illustration of CHF prediction by Baglietto *et al.* [5].

This model was applied for both low and high pressure cases by Demarly [37] and predicted most CHF values within a ±30% error.

> **Remark :** Since this model detects the CHF as the maximum value reached for ϕ_w on the boiling curve, its application requires to compute the heat flux partitioning for a large enough range of wall superheat and then extract the maximum ϕ_w resulting from the computation.
>
> For CFD applications, this requires to apply this procedure in each cell to obtain the local value of the CHF, which would result in the possibility of estimating the local DNB ratio (Section 1.5) in a way similar to current industrial approaches.

9.2.3 *Model of Zhang, Seong & Bucci [178]: Bubble Interaction and Scale-Free Footprint distribution*

Based on experimental observations, Zhang *et al.* [178] have observed that the boiling crisis behaved as a scale-free phenomenon, *i. e.* probability density function of parameters such as the bubble footprint area

A follows a power law (PDF $\propto 1/A^{\gamma}$, $\gamma > 0$). In particular, they noted that bubble clustering on the surface could be used as an indicator for boiling crisis occurrence: when following the size of the two largest clusters of bubbles, CHF was attained when the second largest cluster reached its maximum size.

Moreover, they managed to reproduced the bubble footprint power-law distribution with a simple Monte-Carlo stochastic simulation (Figure 9.6), using measured physical inputs being the average bubble radius $\langle R \rangle$, active nucleation site density $N_{sit,a}$ and probability of finding a bubble on the surface $t_g f$.

Remark : This power-law for the probability density function of bubble dry area distribution, becoming critical near CHF, has been further confirmed by Kossolapov [90] who found same distributions at various pressures up to 75 bar.

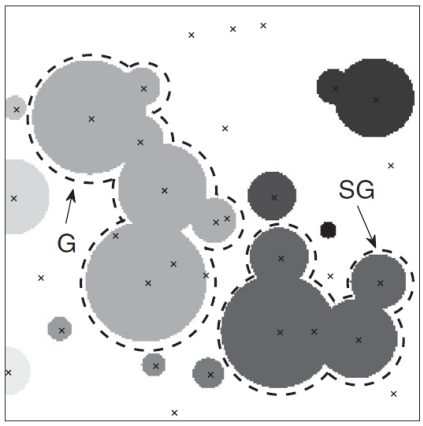

Figure 9.6: Example of Monte-Carlo simulation of the bubble clustering process, by and adapted from [178]. G and SG respectively denote the largest and second largest bubble clusters.

Further investigating these findings, Zhang [177] concluded that the computed CHF was mostly controlled by the values of the three physical input parameters: $\langle R \rangle$, $N_{sit,a}$ and $t_{g,d} f$. Her idea was then to suppose that the boiling crisis could be detected based only on this so-called "triplet". This has been further confirmed through the work of Ravichandran *et al.* [134, 135] who used neural-networks for real-time processing of boiling experiments. While trying to tentatively anticipate the CHF value in given operation conditions, they showed that most of the information regarding the CHF prediction with the neural-network was contained in the three values $\langle R \rangle$, $N_{sit,a}$ and $t_{g,d} f$ by reaching nearly 90% of prediction accuracy.

Experiments presented in Zhang PhD [177] finally demonstrated this capacity of CHF anticipation. By covering 11 different heater material / fluid combinations in both pool and flow boiling, boiling crisis occurred every time when:

$$N_{sit,a} \pi \langle R \rangle^2 t_g f \sim 1 \tag{9.7}$$

This dimensionless relationship physically means that non-interacting bubbles cover in average the entire boiling surface, which seems reasonable when approaching the boiling crisis.

9.3 SIMPLE TEST OF THE ZHANG CRITERION

The criterion proposed by Zhang in the last sub-section presents a particular interest in the frame of HFP models. Indeed, it relies on physical parameters that are all computed in the Heat Flux Partitioning process, namely the average bubble radius $\langle R \rangle$, the bubble-generating sites density $N_{sit,a}$, the bubble growth time t_g and nucleation frequency f.

Regarding CFD application, this results in a very simple value to compute in every wall boiling cells in order to estimate the local proximity to the boiling crisis. As a prospective test, we computed this value

using the original NEPTUNE_CFD HFP formulation (Section 2.5) on a DEBORA case relatively close to CHF (Figure 9.7).

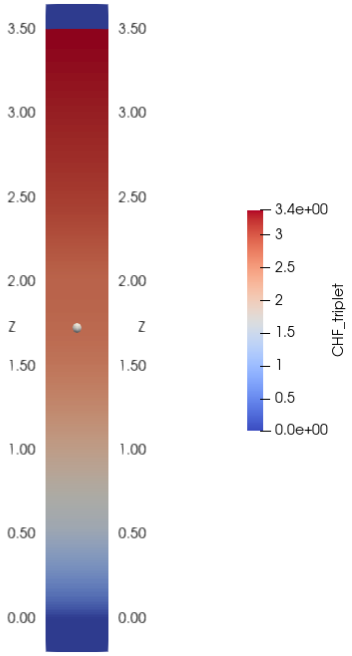

Figure 9.7: Value of the CHF triplet for the DEBORA case 30G2P26W16Te70 (Chapter 4). The heat flux applied corresponds approximately to 90% of the CHF in those conditions [47] and the wall void fraction approaches 40% (Figure 3.7a).

First, we must acknowledge that the values of the CHF criterion $N_{sit,a}\pi \langle R \rangle^2 t_g f$ are not calibrated to reach of value around 1 at the CHF since the initial HFP model of NEPTUNE_CFD presents obsolete closure laws (Chapter 7). However, we can qualitatively study the evolution of the criterion value by logically considering that the higher the CHF triplet, the closer we locally are to the boiling crisis.

From that, we can observe that for the simple DEBORA case, the value of the criterion progressively rises as we move upwards the heating length. Qualitatively, it indicates that the longer we heat the closer we are to the boiling crisis, which is physically expected.

At first glance, this criterion thus seems to present a reasonable qualitative behavior and may be more relevant than local wall temperature (which is nearly constant in the whole boiling region) or void fraction (strongly depending on the mesh size if taken at the wall cell).

Remark : Testing this criterion with new HFP model at outlet conditions for this case ($\Delta T_L \approx 0$) yielded $N_{sit,a}\pi \langle R \rangle^2 t_g f \approx 0.8$ which falls better in the range of [0, 1] found by Zhang.

9.4 CONCLUSIONS

In this prospective Chapter, we presented former approached for CHF estimation and discussed the possibility of achieving boiling crisis prediction using the Heat Flux Partitioning Modeling framework. Finally, we can note that:

- Recent experimental observation from various authors are starting to reach a general agreement regarding the physics of Departure from Nucleate Boiling, where wall boiling measurements showed that boiling crisis coincides with the formation of an irreversible dry patch
- The modeling of the dry wall area has thus been studied by Baglietto *et al.* [5] who managed to display a maximum wall heat flux by accounting for bubble interactions.

- Further experimental studies of Zhang *et al.* [178], Zhang [177] and Kossolapov [90] showed that the boiling crisis seems intrinsically linked to bubble footprint distribution becoming critical at CHF.
- Zhang [177] and Ravichandran *et al.* [135] showed that those latter observations were strongly depending on the physical triplet $(\langle R \rangle, N_{sit,a}, t_g f)$ which proved to be sufficient to predict boiling crisis occurrence when $N_{sit,a} \pi \langle R \rangle^2 t_g f \sim 1$.
- Test of this last criterion was very suitable for CFD application using Heat Flux Partitioning approach and showed a coherent qualitative behavior on a simple tube case from the DEBORA database.

Part III

TOWARDS THE INDUSTRIAL GEOMETRY

10

TUBE WITH MIXING VANES : DEBORA-PROMOTEUR AND AGATE-PROMOTEUR EXPERIMENTS

Contents

10.1 Introduction 170
10.2 DEBORA-Promoteur 170
10.2.1 Test Section and Experimental Campaigns 170
10.3 AGATE-Promoteur 172
10.4 Analysis of the DEBORA-Promoteur Experimental Measurements 173
10.4.1 Estimation of the Bubble Diameter 175
10.5 Conclusions 177

10.1 INTRODUCTION

In PWR cores, the industrial geometry is tremendously complex compared to traditional experimental setup usually consisting of simple tubes such as in the DEBORA experiment (Chapter 3). Although simple geometries are absolutely mandatory for verification and validation of the multiscale physics modeling involved in boiling two-phase flows, it would hardly suffice to be perform a full scaling of the industrial configurations.

To that extent, there is a need for experimental measurements both in representative flow conditions **and** geometry. This implies reproducing test sections including complicated shapes such as grids inducing significant transverse flow and turbulent mixing.

In this Chapter, we focus on such a dedicated experiment called DEBORA-Promoteur and propose some analyses of its experimental measurements. Its single-phase counterpart called AGATE-Promoteur is also presented.

10.2 DEBORA-PROMOTEUR

10.2.1 *Test Section and Experimental Campaigns*

In 2003, the wish to investigate boiling flows in complex geometries similar to those of PWR fuel assembly motivated CEA and EDF to perform modifications of the DEBORA facility [47]. In order to mimic the turbulent mixing induced by the grids holding the fuel rods, a mixing device equipped with blades was built with respect to the geometrical properties of the mixing vanes of the PWR grids (Figure 10.1).

This mixing device was then welded into the DEBORA test section, thus named DEBORA-Promoteur. Its position upstream the end of the heating length was meant to induce a strong rotation in the flow in order to quantify the impact of the mixing regarding:

- Bubble re-condensation for subcooled boiling ;
- Void redistribution for saturated cases ;
- Critical Heat Flux value compared to the naked pipe case.

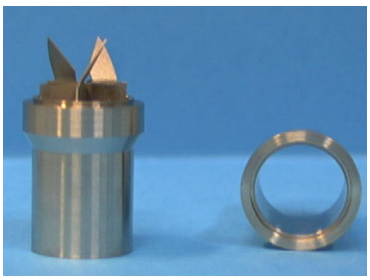

Figure 10.1: Picture of the mixing device. (Adapted from [46])

Figures 10.2a and 10.2b present the position of the measurement radius along with a sketch of the experiment, defining the position of the mixing vanes (MV) upstream the measurements section at a distance L_{MV}.

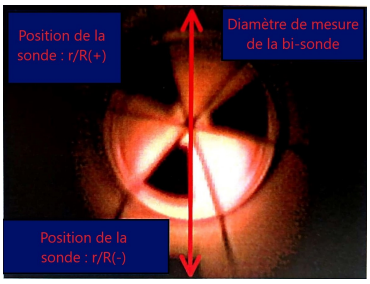

(a) Measurement radius. (Adapted from [47])

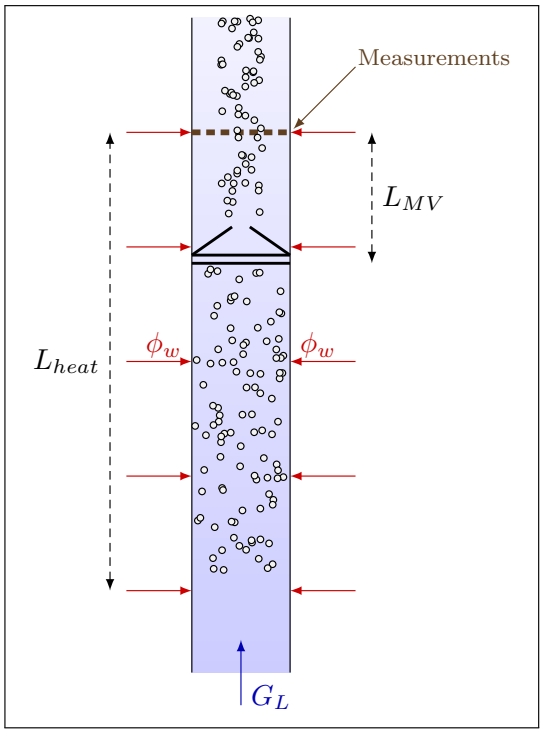

(b) Sketch of the DEBORA-Promoteur test section.

Figure 10.2: Description of the DEBORA-Promoteur experiment.

The same measurement instrumentation as the DEBORA C3000 cases (bi-optical probe, Figure 3.6) was used to study the flow topology in the DEBORA-Promoteur experiment. In that regard, two measurements campaign were conducted:

- Campaign C4800 where the mixing vanes were placed at $L_{MV} = 23.5\ D_h$ (≈ 0.45 m)upstream the end of the heating length [47] ;

- Campaign C5200, where the mixing vanes were placed $L_{MV} = 10\ D_h$ (≈ 0.19 m) upstream the end of the heating length [48].

> **Note :** Unfortunately, no thermal measurement campaign was conducted on the DEBORA-Promoteur facility.

The different cases of the DEBORA-Promoteur experiment follow the same nomenclature as the DEBORA ones (Section 3.4). A total of three test series were conducted:

1. Series 48G3P26WA ;
2. Series 52G3P26WA ;
3. Series 52G3P26WB.

where $B > A$ are the total power applied in the test section, which order of magnitude lies around those of Table 3.4.

> **Note :** The values of the applied heat flux for those data sets are not given in this document due to confidentiality reasons.

Regarding the available data for each test, bi-optical probes allow the measurements of the void fraction but also bubble diameter using the vapor (or interfacial) velocity as explained in Subsection 3.3.2. However, the measurement of the vapor velocity is reliable if:

1) The flow is mainly one-directional and aligned with the probes ;
2) Vapor phase is composed of spherical bubbles ;
3) Velocity gradient and center density gradient are small along a distance equal to the bubble diameter.

Since the mixing vanes introduce a strong mixing and rotational effect, hypothesis 1) is, at first glance, impossible to verify and ensure that measurements of vapor velocity are correct. For each data set, the available experimental file contains:

- 48G3P26WA: Void fraction α and interference frequency ν value for each probe (1 and 2)
- 52G3P26WA & 52G3P26WB: void fraction α and interference frequency ν value for each probe (1 and 2) plus the estimated (potentially uncertain) vapor velocity $U_{V,z}$.

10.3 AGATE-PROMOTEUR

Following the DEBORA-Promoteur tests, experimental findings lead CEA and EDF to investigate the single-phase liquid velocity profile in the mixing vanes geometry, resulting in the development of an experiment called AGATE-Promoteur.

The AGATE-Promoteur experiments consist of LDV (Laser Doppler Velocimetry) measurements of the liquid velocity and turbulent intensity in both axial and radial direction. The test in conducted using the very same geometry and mixing vanes as the DEBORA-Promoteur case and consists of a single set of measurements for water at 2 bar flowing at a mass flow rate $G_L \approx 3000$ kg/m^2/s (same mass flux as the DEBORA-Promoteur cases) and $T_L \approx 40$°C, resulting in an hydraulic Reynolds number $\mathrm{Re}_{D_h} \approx 8.5 \times 10^4$. Measurements are then operated at several axial positions (18) and diameters (6). Figure 10.3 details the different positions where measurements were conducted.

Each diameter has 24 points of measurements, with a total of 108 diameters covered in the whole test both upstream and downstream of the mixing vanes.

For each data point, we have the local axial velocity, radial velocity (signed positive or negative depending on its direction relative to the measured diameter), axial and radial turbulent intensities. Later, we will prefer reconstructing the values of the local RMS (Root Mean Square) of the velocity:

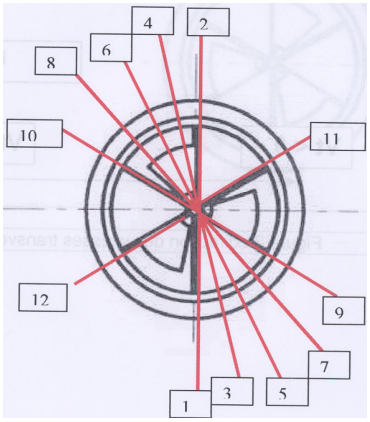

(a) Radial measurements diameters. (Adapted from [46])

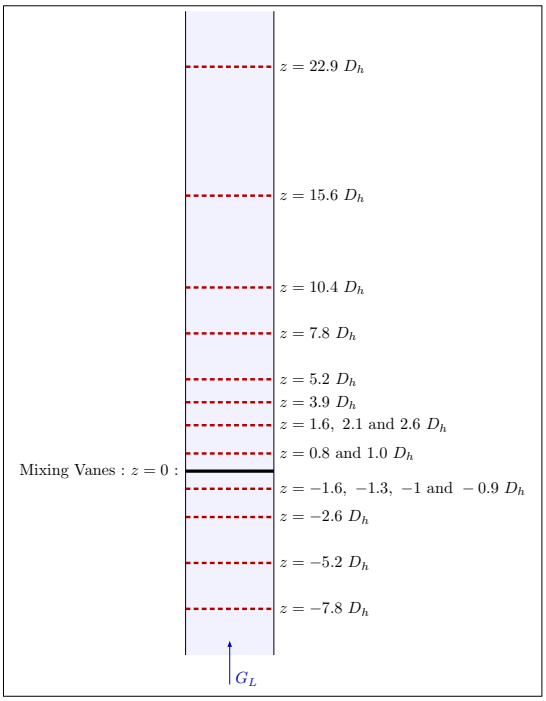

(b) Axial positions of measurements.

Figure 10.3: Covered measurements positions in AGATE-Promoteur experiment.

$$RMS_i := \sqrt{\langle U_i' U_i' \rangle} = I_{T,i} \times \langle U_i \rangle \tag{10.1}$$

where $i = A,\ R$ for axial or radial direction, $U = \langle U \rangle + U'$ the velocity decomposed between time-average and fluctuation, and I_T the measured turbulent intensity.

10.4 ANALYSIS OF THE DEBORA-PROMOTEUR EXPERIMENTAL MEASUREMENTS

On Figures 10.4, 10.5 and 10.6, we plot respectively the void fraction and interference frequency (averaged for the two probes) for campaigns 48G3P26WA, 52G3P26WA and 52G3P26WB.

10.4.0.1 *48G3P26WA cases*

The first immediate observation is the position of the void fraction peak positioned at the center of the tube (Figure 10.4a), strongly differing from the naked tube (Figure 3.7a). This is a direct consequence of the mixing vanes inducing a rotational flow that will gather the vapor at the center. Except for lowest

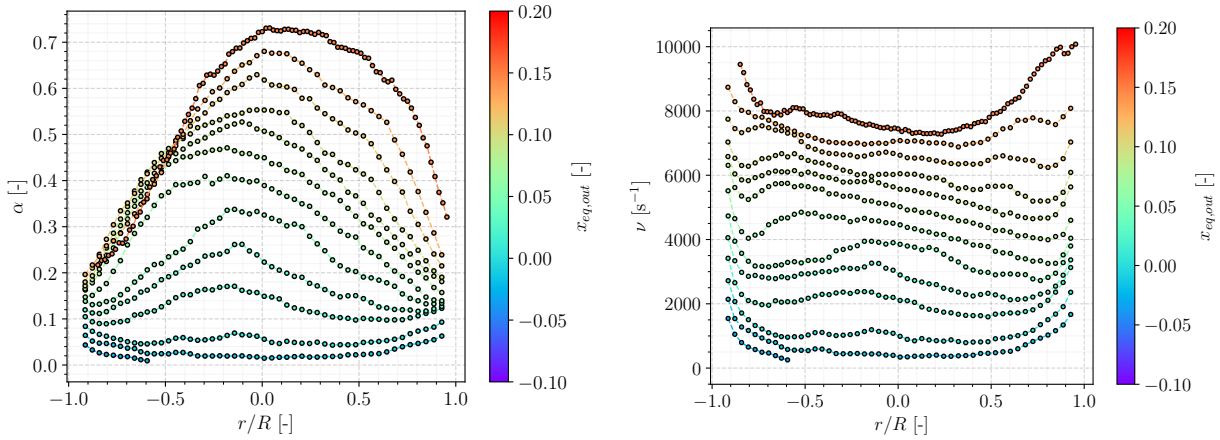

(a) Void fraction

(b) Interference frequency

Figure 10.4: Experimental results from the 48G3P26WA series.

quality cases, the void fraction at the wall is the minimum value along the measurement radius, which insists on the inversion of the void fraction profile under the mixing vanes effect.
Moreover, the profile is not perfectly symmetrical with a void peak progressively shifting towards positive values of r/R. This could be expected since the mixing vanes do not present any axisymmetry.

Analyzing the interference frequency (Figure 10.4b), *i. e.* the number of interface detection per second, allow to qualitatively determine whether if the measured void fraction at a given point is the result of a large number of small bubbles or a small number of large bubbles going through the probes. We note for hottest cases that the interference frequency reaches its maximum at the wall where the void fraction is the lowest, while its minimum is at the center where void fraction is maximal. This means that fewer bubbles at the center lead to a larger void fraction compared to the wall, which is likely to indicate the effect of coalescence increasing the average bubble size.

10.4.0.2 *52G3P26WA and WB cases*

The main difference between the C5200 and C4800 cases is the position of the mixing vanes that are closer to the end of the mixing length in the C5200 campaigns (10 D_h versus 23.5 D_h).

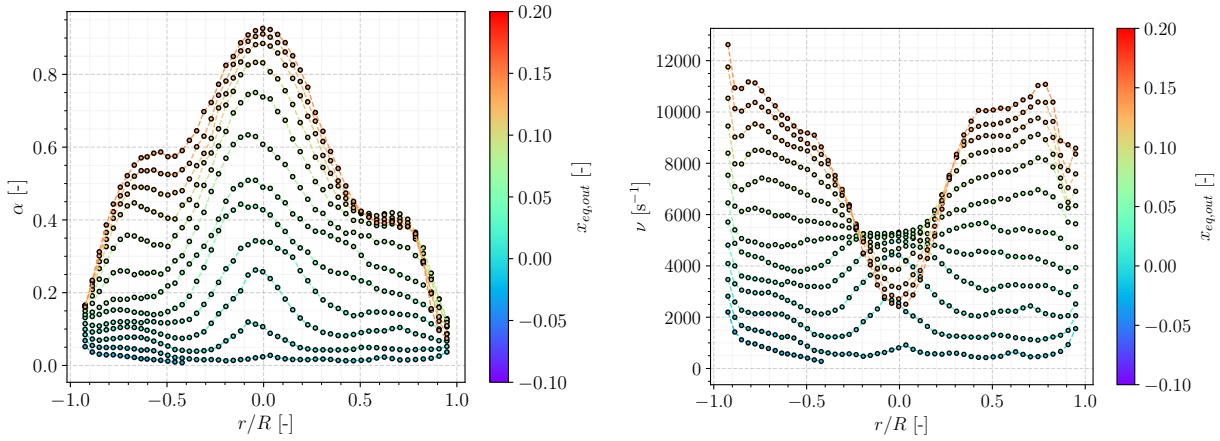

(a) Void fraction

(b) Interference frequency

Figure 10.5: Experimental results from the 52G3P26WA series.

Similar to C4800 cases, we observe a void fraction peak at the center and minimum at the wall (Figures 10.5a and 10.6a). However, the shape of the measurements largely differs by presenting local maximum values around $r/R = \pm 0.6$ for hottest cases. The void fraction peaks are also higher than for C4800 cases, with values up to 90%. This is probably an effect of the MV positions since moving the vanes

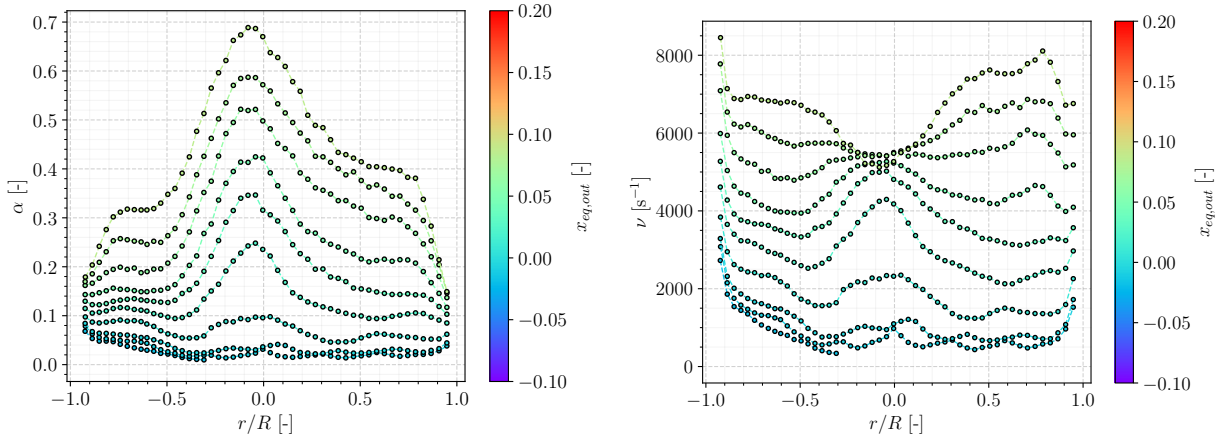

(a) Void fraction

(b) Interference frequency

Figure 10.6: Experimental results from the 52G3P26WB series.

downwards means that the flow will be mixed later, leaving a shorter distance for the flow to fall back to a traditional single tube profile. The amount of vapor suddenly brought to the center will increase as the distance between the vanes and the measurement section reduces.

Remark : Such an effect may be assimilated to the so-called "history effect", meaning that the distance to such a mixing device has an impact over the two-phase flow properties.

Interference frequencies (Figures 10.5b and 10.6b) profiles are also differing from C4800 cases. The interference peak is initially located at the center for low quality cases, meaning that there is a larger number of bubbles at the center compared to the wall. However, the shape reverses as the outlet quality increases (and thus the core void fraction), with a huge decrease of the bulk interference frequency which significantly points towards predominant coalescence effects. Noting that this change happens roughly when $x_{eq,out} \leq 0$ (saturation is reached) indicates that it may originates from the absence of condensation.

Remark : The considerations over condensation are though speculative and would largely benefit from liquid temperature measurements in such a configuration, which could both quantify the impact of mixing on the liquid phase and correlate interference frequencies to local subcooling values.

10.4.1 *Estimation of the Bubble Diameter*

Since values of vapor velocity measurements are given for the C5200 cases, one may be interested in exploiting them to try to extract information about the bubble size distribution in the flow. However, we have to be able to tell whether those measurements were largely erroneous due to the rotation effects or not *i. e.* if the bubbles were moving in the direction of the probes.

To do so, we propose two arguments:

- Analyzing the difference between the measured interference frequencies for each probe, which could help to quantify if the number of bubbles detected largely differ between them. If so, it means a strong rotation made bubbles flowing through only one probes. On the contrary, this would support the fact that, locally, bubbles were globally flowing in the direction of the probes.
- Quantifying the importance of the radial velocity compared to the axial velocity in the measurement section.

On Figure 10.7, we plot the relative difference of interference frequency between the two probes for each C5200 campaign.

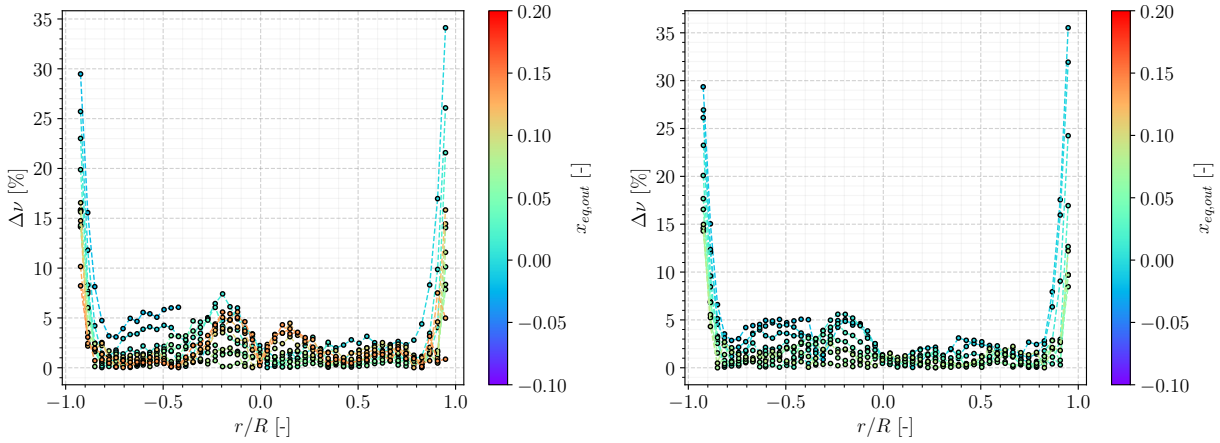

(a) 52G3P26WA series

(b) 52G3P26WB series

Figure 10.7: Relative difference of interference frequency for the two probes.

We see that, close to the wall, the interface detection of the probes differ by up to 35%, which clearly indicates a vapor phase moving radially. However, as we approach the center ($-0.75 \leq r/R \leq 0.75$), the difference in interference frequency globally falls below 5%, potentially showing that bubbles at those locations were having mostly axial velocities.

To quantify the importance of the radial velocity at the measurement section ($z \approx 10\ D_h$ after the grids), we rely on the AGATE-Promoteur experimental results (Section 10.3). Based on the different measured diameters at each axial position, we can compute the average value of the ratio between radial and axial velocities U_R/U_A depending on the height z. The results are shown on Figure 10.8

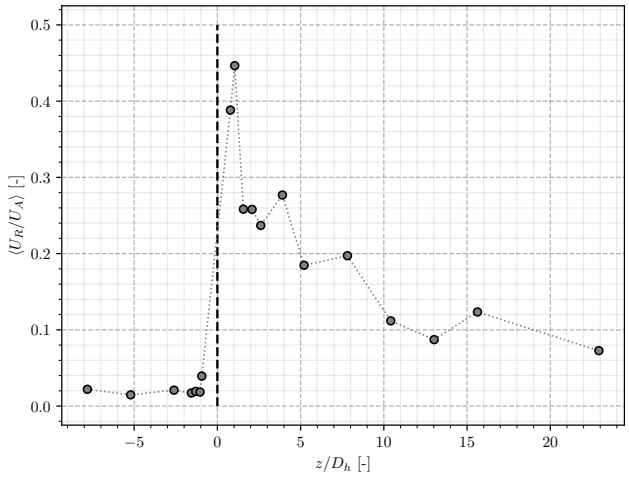

Figure 10.8: Average relative importance of radial velocity to axial velocity in AGATE-Promoteur experiment. Black dotted lines denotes the position of the MV.

The mixing effect on liquid velocity is clear: the average induced rotation velocity can reach up to 45% of the axial velocity in the section right after the MV. The importance of the radial velocity then naturally fades with the distance to the MV, becoming of the order of 10% at $z \approx 10\ D_h$.

At the position corresponding to the measurements in the C5200 campaign, the radial velocity then is approximately 10 times smaller than the axial velocity. This comforts the fact that the flow direction is mainly axial when the measurement using the bi-optical probe is conducted.

Altogether, those two analyses both support the fact that the hypothesis of a flow aligned with the probes at $z = 10\ D_h$ downstream the MV is reasonable. Therefore, we allow ourselves to use the measured values of the vapor velocity $U_{V,z}$ **between** $r/R = -0.75$ **and** $r/R = 0.75$ in the C5200 cases to propose **an estimation** of the bubble diameter in DEBORA-Promoteur measurements:

$$D_V \approx \frac{6\alpha U_{V,z}}{4\nu} \tag{10.2}$$

Resulting values are presented on Figure 10.9.

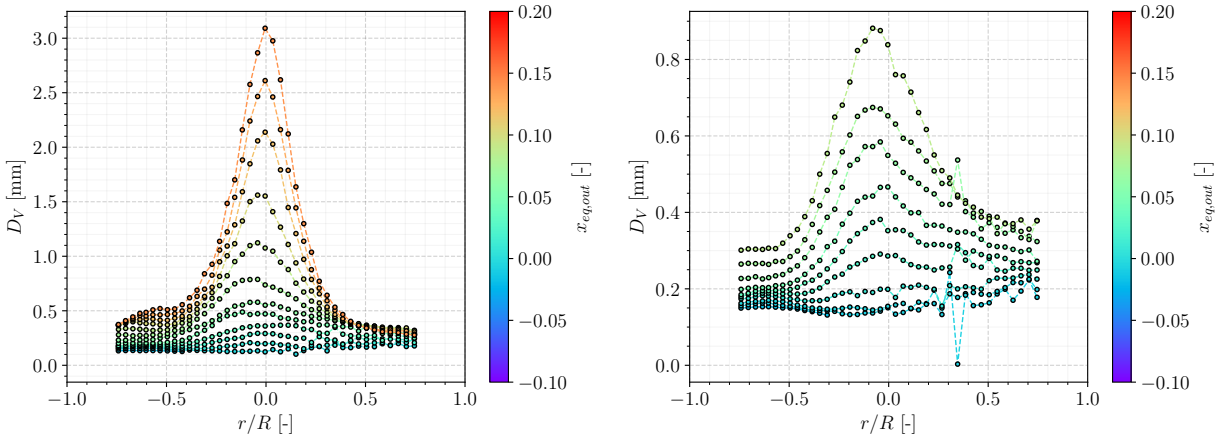

(a) 52G3P26WA series

(b) 52G3P26WB series

Figure 10.9: Estimation of bubble diameter on C5200 measurements series.

First, we notice that the values attained closer to the wall mostly lie between 0.1 mm and 0.5 mm which is coherent with the values observed in the naked tube case (Figure 3.7c).

When approaching the center of the pipe for high quality cases, the bubble diameter sharply increase with values that can reach up to 3 mm. In those conditions, such a diameter is the result of an important coalescence along with negligible condensation effects. Although very large void fractions are reached, those bubble diameters are still an order of magnitude lower than the tube diameter meaning we are not in presence of a slug or annular flow at the center. The resulting flow regime at high void fractions is likely looking like a foam composed of several millimeters bubbles separated by thin layers of liquid.

Remark : In such two-phase flow conditions, the dispersed approach is unlikely to be representative of the real physics at stake. Strong interaction between the bubbles can be expected.

Moreover, the optimal packing for non-overlapping spheres of same sizes is mathematically capped at 74% [167], bubbles at void fraction $\alpha > 74\%$ then must have, at least partially, non-spherical shapes. Which is also supported by Weber number value We ~ 0.1 and Eötvös value Eo ~ 1 in those conditions.

10.5 CONCLUSIONS

The analysis of the DEBORA-Promoteur experiment allowed to qualitatively qualify the two-phase flow in a geometry including mixing vanes. So far, we can remember that:

- The mixing vanes have a clear impact on the vapor distribution, gathering it at the center of the tube thus reversing the radial void fraction profile.
- The axial distance to the mixing vanes appears to have a significant influence over the vapor distribution, further enlightening the presence of a "history effect".
- An estimation of the bubble diameter in those conditions was achievable and showed very important coalescence effects with bubble diameters increasing up to 10 times larger when moving from the

wall to the center. **This constitutes a new element of analysis of the DEBORA-Promoteur tests.**

- Void fraction can reach very high values with peaks at the center up to 90%, which combined with the bubble diameter value indicates that the flow may look like a foam composed of vapor bubbles with thin layers of liquid between them.

In the next chapter, we perform numerical simulations of the DEBORA-Promoteur and AGATE-Promoteur experiments to assess NEPTUNE_CFD capacity on such geometries.

11

NEPTUNE_CFD SIMULATIONS OF DEBORA-PROMOTEUR AND AGATE-PROMOTEUR CASES

Contents

11.1 NEPTUNE_CFD simulations of DEBORA-Promoteur cases **179**
11.1.1 Simulation Setup 179
11.1.2 Results 180
11.2 NEPTUNE_CFD simulations of AGATE-Promoteur cases **182**
11.2.1 Simulation Setup 182
11.2.2 Results 184
11.3 Regarding CHF Detection in Mixing Vanes Geometry **188**
11.4 Conclusions **190**

In this Chapter, we conduct NEPTUNE_CFD simulations of the DEBORA-Promoteur and AGATE-Promoteur experiments. The results are presented as a prospective study of the capacity of the code to handle complex geometries approaching the industrial configuration.

11.1 NEPTUNE_CFD SIMULATIONS OF DEBORA-PROMOTEUR CASES

11.1.1 *Simulation Setup*

Contrary to the DEBORA simulations (Chapter 4), the physics involved in the DEBORA-Promoteur case are intrinsically three-dimensional. Therefore, the problem can not be reduced to 2D-axisymmetric computations. The computational domain is thus a 4m long vertical tube of radius $R = 9.6$ mm, with base of the mixing blades positioned at the axial height $z = 0$. The heated section is translated axially to adapt the simulation for each position of the mixing vanes (23.5 D_h for C4800 and 10 D_h for C5200), giving the following boundary conditions:

- Uniform wall heat flux for -3.055 m $\leq z \leq 0.445$ m (C4800) or -3.318 m $\leq z \leq 0.182$ m (C5200) ;
- Adiabatic wall for remaining wall faces ;
- Uniform outlet pressure ;
- Uniform liquid inlet velocity and temperature.

A mesh sensitivity conducted to use the mesh presented on Figure 11.1 which contains a total of 3 487 267 cells.

We simulated 3 cases per series 48G3P26WA and 52G3P26WA, covering the two MV positions and different outlet quality ($x_{eq,out}$) :

- 48G3P26WATe65 & 52G3P26WATe65 with $x_{eq,out} \approx 0\%$
- 48G3P26WATe69 & 52G3P26WATe69 with $x_{eq,out} \approx 5\%$
- 48G3P26WATe75 & 52G3P26WATe75 with $x_{eq,out} \approx 12.5\%$

Note : The computational times was ensured to be long enough to reach time-average convergence of the simulations.

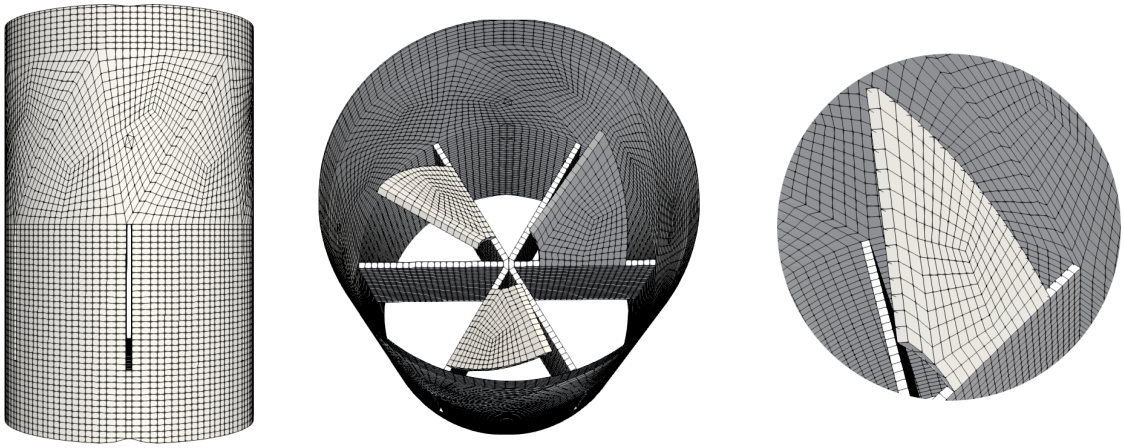

Figure 11.1: Meshing of the mixing vanes region.

Results are compared to the experimental measurements *i. e.* only void fraction for C4800 cases and void fraction, bubble diameter and vapor velocity for C5200 cases.

Remark : Following the discussions regarding vapor velocity and bubble diameter estimation for C5200 cases (Chapter 10), comparison with the CFD results will rather be of qualitative nature since we can't ensure the accuracy of the measurements.

11.1.2 *Results*

Results are presented on Figure 11.2.

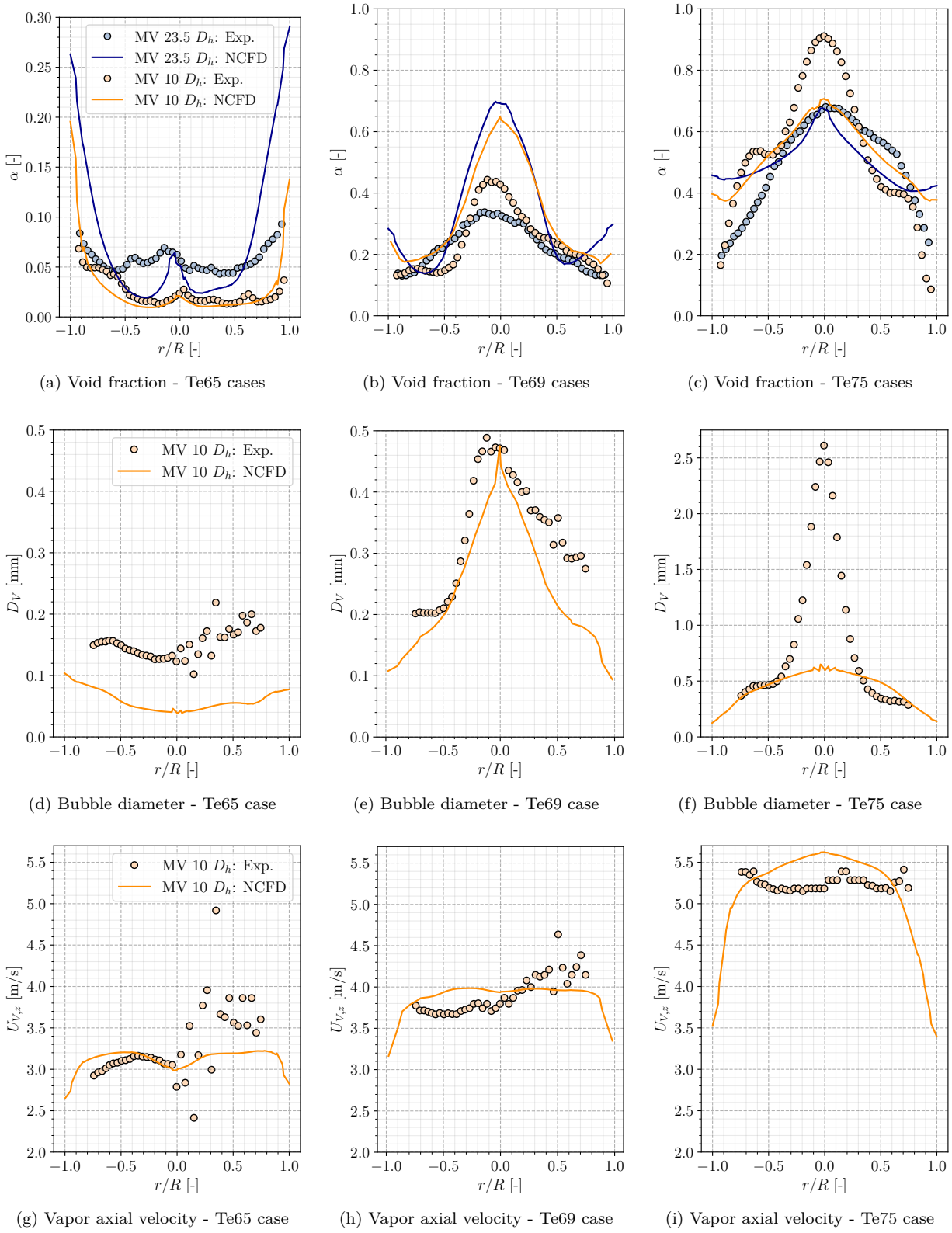

(a) Void fraction - Te65 cases

(b) Void fraction - Te69 cases

(c) Void fraction - Te75 cases

(d) Bubble diameter - Te65 case

(e) Bubble diameter - Te69 case

(f) Bubble diameter - Te75 case

(g) Vapor axial velocity - Te65 case

(h) Vapor axial velocity - Te69 case

(i) Vapor axial velocity - Te75 case

Figure 11.2: NCFD results on the DEBORA-Promoteur cases. MV at 23.5 D_h and 10 $D_h$respectively correspond to C4800 and C5200 cases.

Quantitatively speaking, it seems that NEPTUNE_CFD reproduces the effect of vapor accumulation at the center under the pressure gradient generated by the swirl induced by the mixing vanes. The radial position of the core void fraction peak correctly matches the experimental one. The Te65 cases (Figure 11.2a) are reasonably predicted with void fractions values at the center close to the measurements, with the C5200 simulation much closer to the experimental profile. However, Te69 and Te75 cases (Figures 11.2b and 11.2c) are showing much larger discrepancies with the experiments. The core void fraction peak appears largely overestimated for $T_{L,in} = 69°C$ with $\alpha\,(r/R = 0) \approx 70\%$ and do not change when moving to $T_{L,in} = 75°C$ where the void fraction profile rather flattens. Such a behavior strongly differs from the experiments where a large increase in core void fraction when inlet temperature increases. Moreover, the particular shape of 52G3P26WATe75 case where local maximum for α are observed at $r/R \approx \pm 0.6$.

Remark : The computed void fraction seems unable to go above 70% in this case, which is in contradiction with the experiments. However, a sensitivity test showed that removing all the interfacial forces except the drag (Eq. 2.20) allowed the bulk void fraction to reach 90% as presented on Figure 11.3.

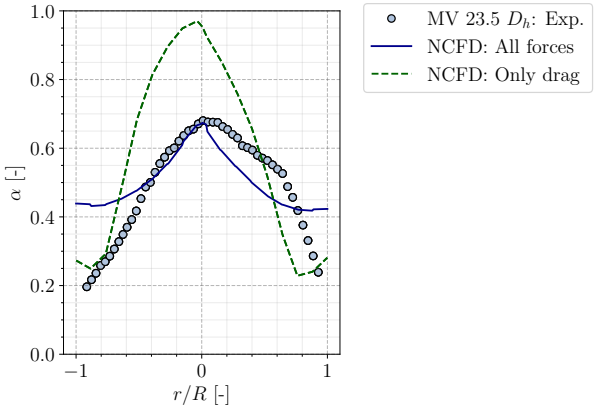

Figure 11.3: Sensitivity test on case 48G3P26WATe75 leaving only the drag force in the interfacial momentum closure.

Regarding C5200 cases, bubble diameter profiles appear coherent with the experimental estimations for Te65 and Te69 cases (Figure 11.2d and 11.2e). In particular, the growth towards the center due to coalescence is fairly reproduced in Te69 case. On the contrary, the very large estimated values for Te75 case ($D_V \sim 2$ mm) are completely missed by the simulation (Figure 11.2f).

Remark : As discussed in the analysis of the experimental results (Subsection 10.4.1), the flow regime encountered in the 52G3P26W3Te75 case is very likely deviate from a dispersed flow (very large void fractions), explaining the inability of the simulations to reproduce this behavior.

Finally, the order of magnitude of predicted vapor velocities increases with the inlet temperature (Figures 11.2g, 11.2h, 11.2i) similarly to the experimental estimations.

To further investigate the mixing vanes geometry and understand the large discrepancies on the void fraction profiles (Figures 11.2b and 11.2c), we perform simulations of the single-phase AGATE-Promoteur case in next Section.

11.2 NEPTUNE_CFD SIMULATIONS OF AGATE-PROMOTEUR CASES

11.2.1 *Simulation Setup*

Simulations of the AGATE-Promoteur case are done using *code_saturne* 7.0, the single-phase counterpart of NEPTUNE_CFD. The computational domain is 0.7 m long (shorter than DEBORA-Promoteur case since we don't need to apply the 3.5m heating) with the mixing blades positioned at $z = 0$. Using the

same meshing used for the DEBORA-Promoteur cases (Figure 11.1), the total mesh contains 1 905 357 cells.

Two simulations are performed using the turbulence model $R_{ij} - \varepsilon$ SSG with a smooth wall two-scale turbulent law and with a rough wall turbulent law (average roughness $\epsilon = 10^{-5}$ m fixed arbitrarily as a sensitivity test). The usual wall law in *code_saturne* is a two friction velocity scales law [185], with the roughness inducing a shift in the logarithmic term of the non-dimensional velocity:

$$u^+ = \frac{1}{\kappa} \ln\left(\frac{y+\epsilon}{\epsilon}\right) + C_{log} \tag{11.1}$$

with $C_{log} = 5.2$ and y the absolute distance to the wall.

Note : Before comparisons with experiments, we made sure that NEPTUNE_CFD two-phase solver and *code_saturne* single-phase solver produced similar results when simulating a single-phase flow using the $R_{ij} - \varepsilon$ SSG model.

To test the sensitivity to turbulence modeling, we also realize a Large Eddy Simulation (LES) using the LES WALE (Wall-Adapting Local Eddy-Viscosity) model [121]. For this simulation, we use a more refined mesh (Figure 11.4) containing a total of 121 942 848 cells.

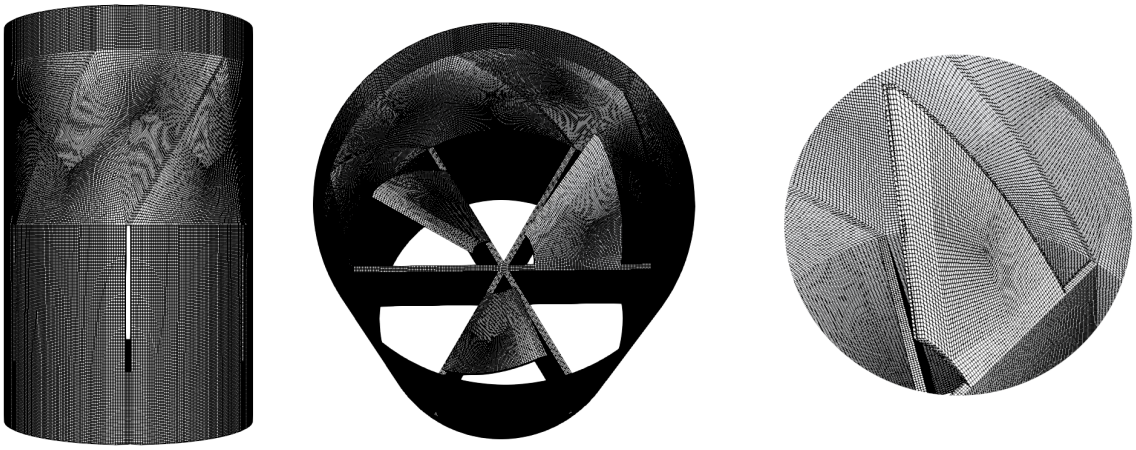

Figure 11.4: Fine meshing of the mixing vanes region for the LES calculation.

In this configuration, we achieve an average wall distance $y^+ \approx 13$ in the whole domain (while $y^+ \approx 50$ for the other mesh), which is too large to numerically resolve the boundary layer meaning a wall-law will be used to evaluate the liquid velocity in the wall cell.

Note : A stable time-convergence of all the variables is achieved for the LES computation after 10 s of simulated physical time.

Finally, we want to compare the results of the simulations with measurements of the RMS of the velocity fluctuations (Eq. 10.1), meaning that we have to reconstruct those values from the CFD computations. Since we perform Unsteady-RANS (URANS) simulations (using the $R_{ij} - \varepsilon$ SSG model), fluctuations of the velocity field are both modeled in the components of the Reynolds Stress Tensor and partly simulated due to the potential time-oscillations of the average velocity field $\langle \overline{U} \rangle$. Therefore, the RMS for URANS simulations is computed using the modeled components of the Reynolds Stress Tensor $R_{ij,mod}$:

$$RMS_{A,URANS} = \sqrt{R_{zz,mod} + \left\langle \left(\tilde{U} \otimes \tilde{U}\right)_{zz} \right\rangle} \tag{11.2}$$

where $\tilde{U} = \langle \overline{U} \rangle - \overline{U}$ is the instantaneous difference between the velocity field and its time average *i. e.* the simulated fluctuations of the URANS computation.

Regarding the LES computation, the fluctuations of the velocity field are mainly simulated and are thus only contained in the instantaneous velocity field $\overline{U}$. Therefore, they are computed as:

$$RMS_{A,LES} = \sqrt{\langle (\tilde{U} \otimes \tilde{U})_{zz} \rangle} \tag{11.3}$$

The same operation is conducted for the radial RMS, which involves the components xx, yy and xy.

11.2.2 *Results*

In this section, we discuss results obtained at three different heights : 0.8 D_h, 10 D_h and 23 D_h downstream the mixing vanes.

11.2.2.1 0.8 D_h *After the Mixing Vanes*

Figure 11.5 shows the results less than a hydraulic diameter after the mixing vanes. As mentioned in previous Section, a sensitivity to the wall modeling is realized by performing an extra simulation including a wall roughness.

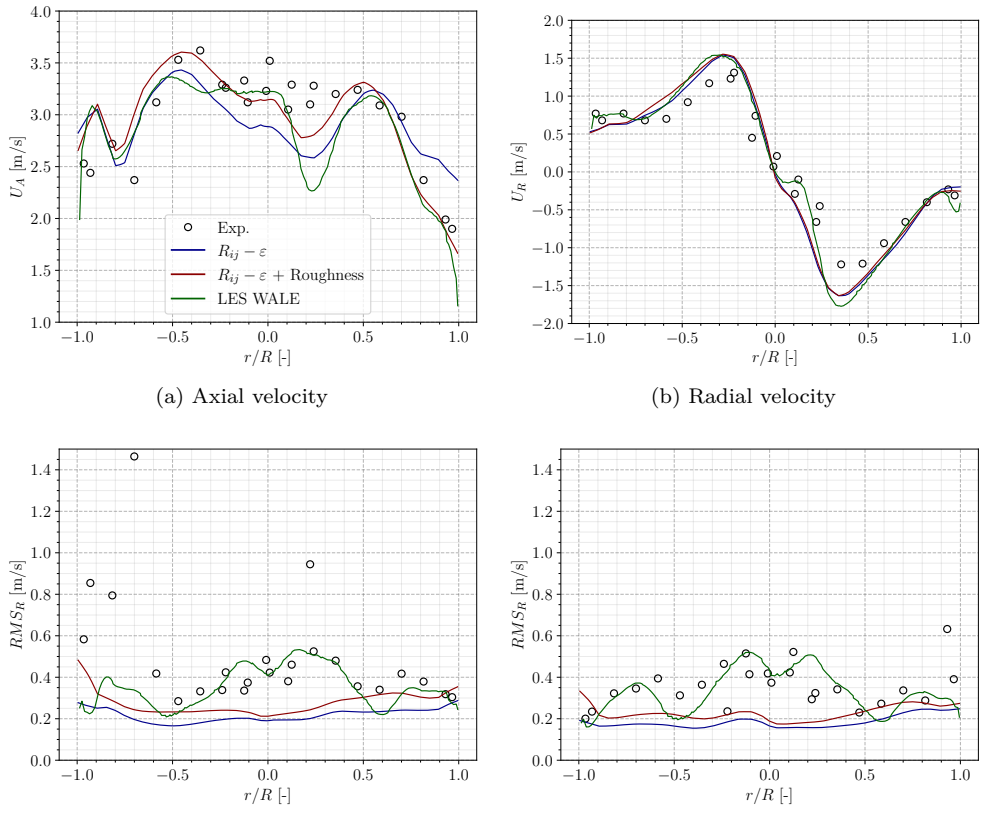

(a) Axial velocity

(b) Radial velocity

(c) Axial RMS

(d) Radial RMS

Figure 11.5: Results for $z = 0.8\ D_h$

The three simulations correctly match the experiments for the axial and radial velocities (Figures 11.5a and 11.5b). However, the velocity RMS (Figures 11.5c and 11.5d) are underestimated by the $R_{ij} - \varepsilon$ model, with the rough law use yielding slightly higher values. On the contrary, the LES simulation better reproduce the core velocity fluctuations especially near the center of the pipe.

Figure 11.6 shows the ratio of radial to axial velocity 1 D_h after the vanes for the LES computation.

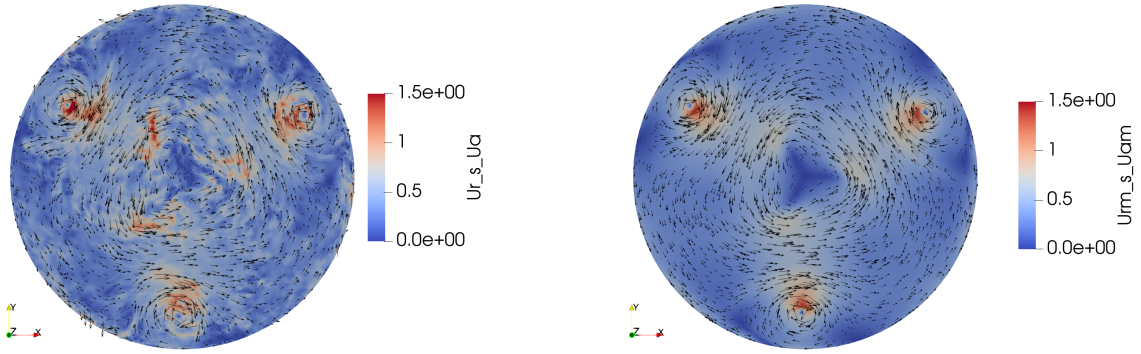

(a) Instantaneous values

(b) Time-averaged values

Figure 11.6: Visualization of the radial velocity field and ratio between radial and axial velocity obtained with the LES, $z = 1\ D_h$ downstream the MV.

11.2.2.2 10 D_h *After the Mixing Vanes*

Figure 11.7 shows the results at 10 D_h downstream the mixing vanes, which corresponds to the distance at which two-phase flow measurements of the DEBORA-Promoteur C5200 campaign was conducted (Section 10.2.

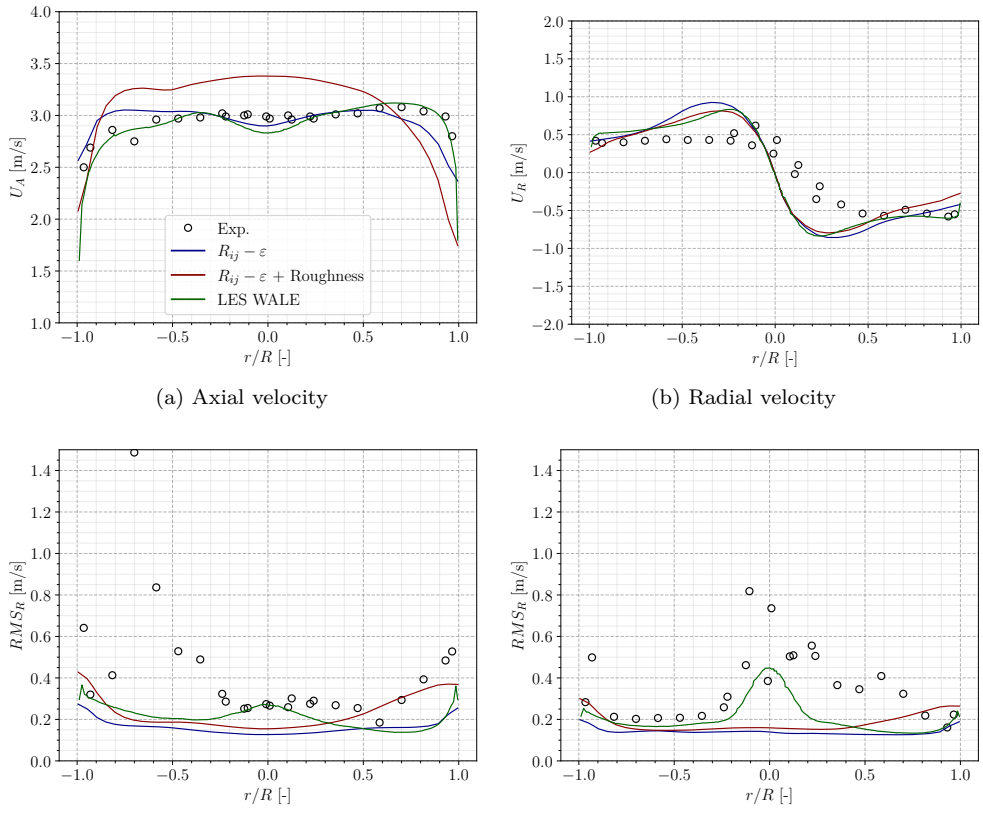

(a) Axial velocity

(b) Radial velocity

(c) Axial RMS

(d) Radial RMS

Figure 11.7: Results for $z = 10.4\ D_h$

Going further downstream, we observe that the use of the roughness law start to induce discrepancies on the axial velocity profile while the two other calculations still agree with the measurements (Figure 11.7a). Radial velocity is however equally predicted by the three simulations, with well reproduced wall

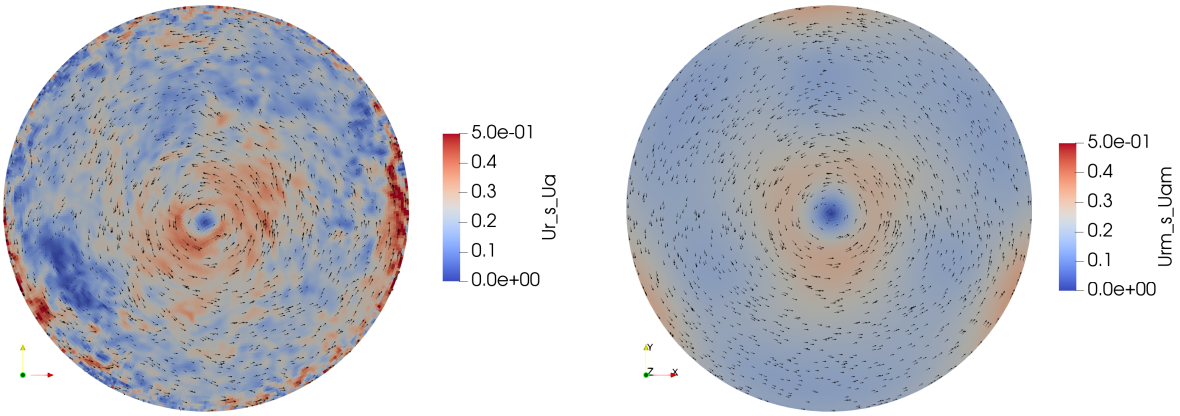

(a) Instantaneous values

(b) Time-averaged values

Figure 11.8: Visualization of the radial velocity field and ratio between radial and axial velocity obtained with the LES, $z = 10\ D_h$ downstream the MV.

values but all showing overestimation for $-0.5 \leq r/R \leq 0.5$ (Figure 11.7b), meaning that a too large bulk rotation of the fluid is predicted.

The velocity RMS are still better predicted by the LES computation (Figures 11.7c and 11.7d) but start to show underprediction compared to the 1 D_h results. Close to the wall, the three modeling all perform similarly.

Figure 11.8 shows the ratio of radial to axial velocity 10 D_h after the vanes for the LES computation.

11.2.2.3 23 D_h *After the Mixing Vanes*

Finally, Figure 11.9 present results 23.5 D_h downstream the mixing vanes, which corresponds to the distance at which two-phase flow measurements of the DEBORA-Promoteur C4800 campaign was conducted (Section 10.2.

At this distance, the axial velocity profile has been significantly degraded by using the roughness law (Figure 11.9a) where the other modelings continue to match the measurements. However, the overestimation of the rotation velocity is amplified compared to the 10 D_h results for the smooth wall simulations while adding a roughness term seem to enhance the damping of the swirl induced by the vanes, better reproducing the experimental results (Figure 11.9b).

The axial velocity RMS are now better predicted by the rough wall simulation (Figure 11.9c) while the radial RMS is more accurately reproduced by the LES computation (Figure 11.9d).

Figure 11.10 shows the ratio of radial to axial velocity 23 D_h after the vanes for the LES computation.

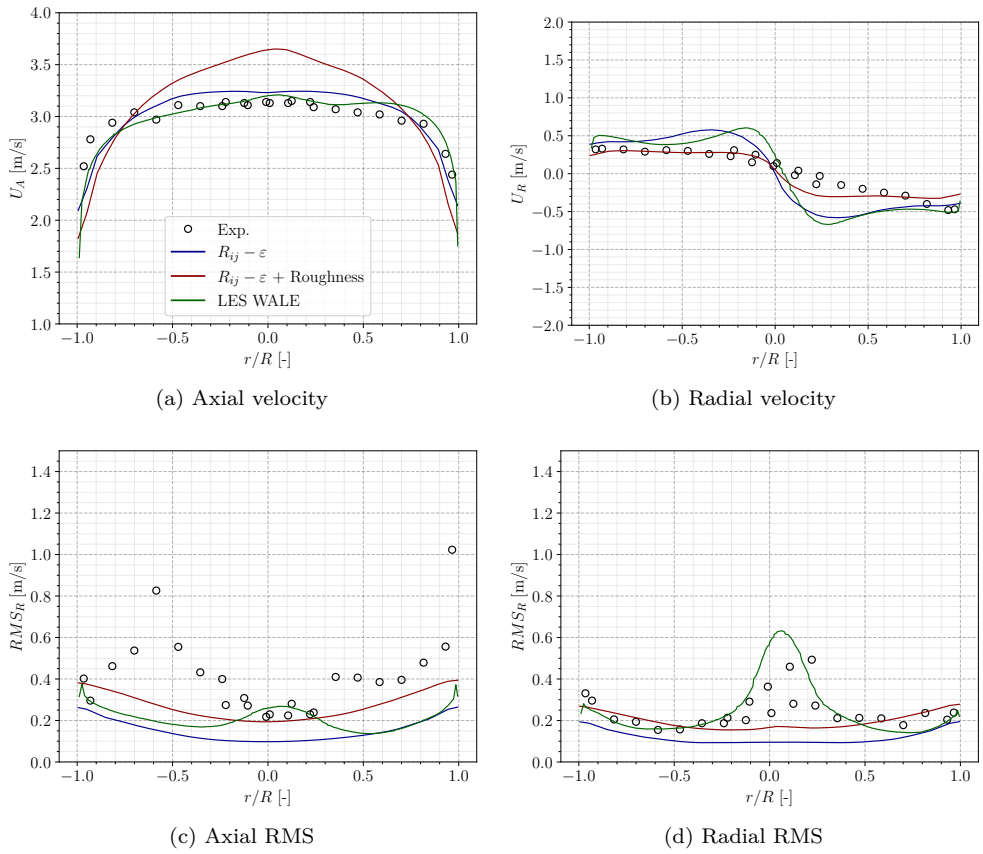

(a) Axial velocity

(b) Radial velocity

(c) Axial RMS

(d) Radial RMS

Figure 11.9: Results for $z = 22.9\ D_h$

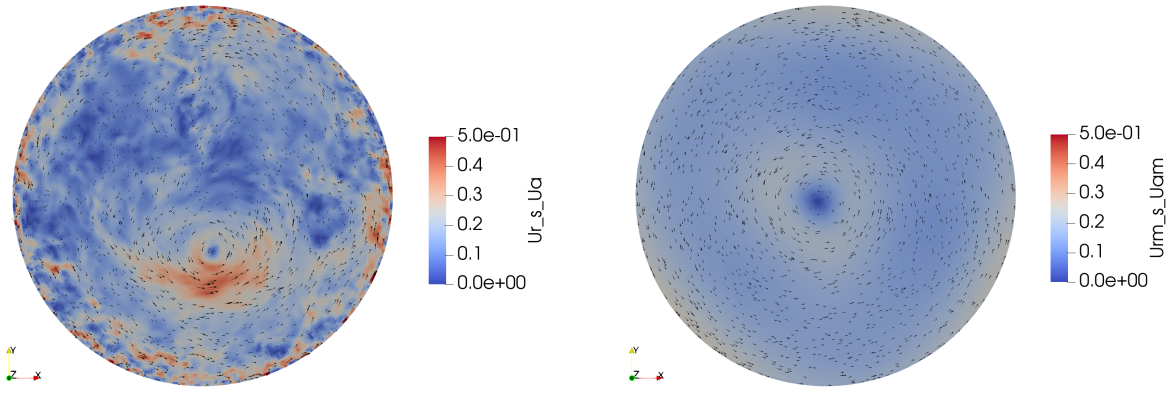

(a) Instantaneous values

(b) Time-averaged values

Figure 11.10: Visualization of the radial velocity field and ratio between radial and axial velocity obtained with the LES, $z = 23\ D_h$ downstream the MV.

11.2.2.4 *Interpretation Regarding the DEBORA-Promoteur Simulations*

Overall, the main characteristic of the single-phase simulation results on the AGATE-Promoteur case is the overestimation of the radial velocity when moving downstream the mixing vanes and reaching the axial positions corresponding to C4800 and C5200 measurements. In terms of hydrodynamics, it means the fluid's rotation is too large, which will result in a stronger pressure gradient between the wall and the center.

Transposing this result to a bubbly flow, the pressure gradient will be responsible for transverse migration of the bubbles towards the center of the pipe. If the rotation is overestimated, so will be the migration of bubbles which results in an excessive bubble accumulation in the core of the flow that should induce an overestimation of the local void fraction. This qualitative behavior is in agreement with the too large void fraction obtained in the simulations of DEBORA-Promoteur Te69 cases (Figure 11.2).

Moreover, the discrepancy on the rotation increasing with the distance to the mixing vanes implies that boiling simulations would be more accurate for the C5200 cases than the C4800 cases (measurements 10 D_h downstream the MV versus. 23.5 D_h). That is actually true when looking at the void fraction profiles for Te65 and Te69 cases (Figures 11.2a and 11.2b) where larger differences with the measurements are observed for the C4800 simulations.

Remark : The main limitation of the presented single-phase simulations is the systematic use of a wall-law, which can have a strong impact regarding this geometry where the wall presence is ubiquitous in addition to the mixing vanes presence. A LES computation using an even finer meshing allowing to reach $y^+ \sim 1$ in the computational domain could bring insightful information to investigate the rotation overestimation.

11.3 REGARDING CHF DETECTION IN MIXING VANES GEOMETRY

As a perspective test, we want to visualize the evolution of the CHF criterion of Zhang [177] (value of the CHF triplet $N_{sit,a}\pi \langle R \rangle^2 t_g f$), as in Section 9.3 on a DEBORA case, for a geometry including mixing vanes. To do so, a simulation of a boiling upward flow in a 5×5 heated rod bundle is conducted in PWR thermal-hydraulics conditions close to CHF. The geometry includes two PWR mixing grids and a non-uniform heating is applied with the 9 central rods having a larger wall heat flux. The initial NEPTUNE_CFD Heat Flux Partitioning is used (Section 2.5) to compute the CHF triplet value.

Note : As in Section 9.3, the values of the CHF triplet attained in the computation are not in the range of [0,1] as it should be prior to CHF [177] since the closure laws for boiling parameters are not precise enough.

On Figures 11.11 and 11.12 we present values obtained for the CHF triplet on the rods respectively at the first and the second grid. Wall areas where the CHF triplet is high are the zones closer to the boiling crisis.

At the inlet upwards the first mixing vane (Figure 11.11), the CHF triplet gradually increases similar to a simple tube case (Figure 9.7) with the central rods exposed to a larger heat flux reaching greater values of the CHF triplet. After the vanes, the local values of the CHF criterion are significantly diminished both for peripheral and central rods, with non-symmetric patterns related to the rotating flow induced by the mixing vanes.

When reaching the second grid (Figure 11.12), the difference in CHF triplet values between central and peripheral rods is less important which is probably an effect of the upwards mixing of the first grid. After the second grid, the CHF triplet values are also globally reduced similar to what was observed at the first grid (Figure 11.11). The CHF triplet is though larger when reaching the second grid, which is logical since the fluid is continuously heated between the two grids. Higher risk of boiling crisis would seem to be right upstream the second grid.

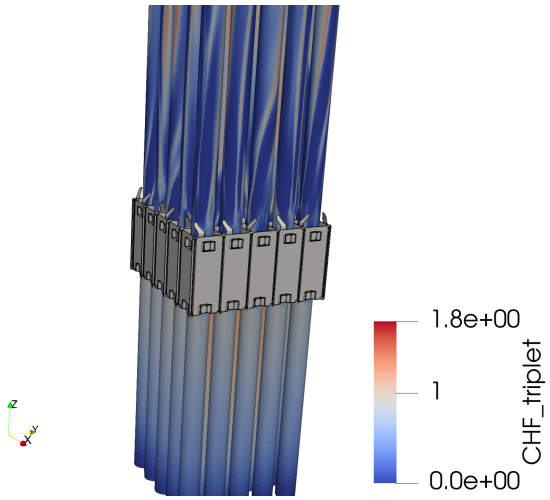

(a) Full rod bundle

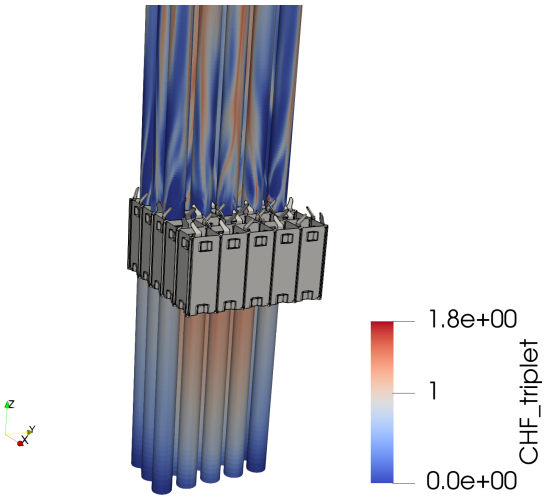

(b) Clip of the bundle, showing the central rods

Figure 11.11: Visualization of the CHF triplet value around the first grid. (Computation results courtesy of Vladimir Duffal)

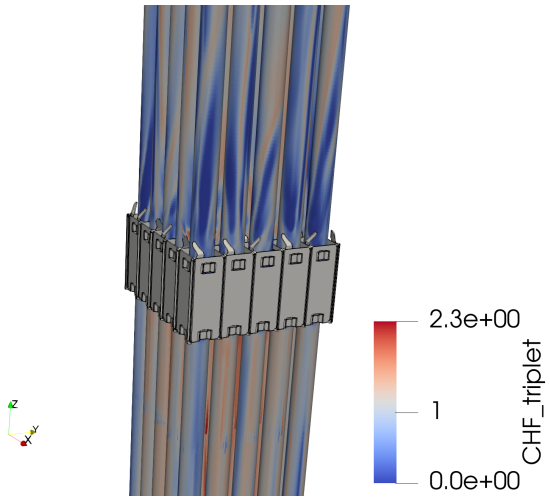

(a) Full rod bundle

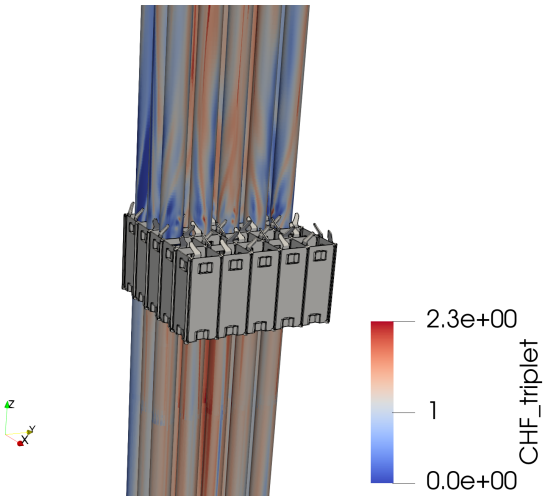

(b) Clip of the bundle, showing the central rods

Figure 11.12: Visualization of the CHF triplet value around the second grid. (Computation results courtesy of Vladimir Duffal)

Altogether, those observations, though purely qualitative, are presenting interestingly coherent features regarding boiling crisis occurrence for PWR with overheated rods have larger CHF triplet values and mixing grids actually decrease the CHF triplet thanks to their mixing effect.

11.4 CONCLUSIONS

In this Chapter, we performed CFD simulations on the tube equipped with mixing vanes geometry. Both boiling flow simulations using NEPTUNE_CFD and single-phase simulations with *code_saturne* were realized, respectively compared to DEBORA-Promoteur and AGATE-Promoteur experiments. So far, the main highlights of the results are:

- The boiling simulations of DEBORA-Promoteur cases showed reasonable qualitative behavior with bulk vapor accumulation, void fraction peak and bubble coalescence at the center, and vapor velocity increase with outlet quality.
- Yet, precise predictions of void fraction profiles could not be achieved with very large overestimation in the bulk plus the incapacity to reach void fractions higher than 70%. This could be associated to change in the multiphase flow regime that lie outside of the dispersed bubbly flow model capacity.
- Further investigations on the single phase case AGATE-Promoteur showed an excessive computed rotation of the fluid, increasingly differing from the experiments as we move downstream the mixing vanes. A too large swirl could explain the overestimation of the void fraction in the boiling case due to bubble transverse migration.
- Wall law seems to have a significant influence over the velocity profiles and may be an area of improvement, especially for confined geometries where solid walls are strongly influencing the flow.

  > **Remark :** We want to mention that achieving precise results for single-phase simulations on complex industrial geometries representative of PWR is still a very active field of research [97]. The use of RANS [8] or wall-modeled LES [54] approaches are still investigated in order to save computational time in the prospect of reaching simulations of a full fuel assembly by including, for instance, modeling of mixing vanes as source terms in the computational domain [21].

- Evaluating values of the CHF triplet as a qualitative indicator of boiling crisis risk of occurrence (Section 9.3) on a rod bundle including mixing vanes showed presented a good perspective with physically coherent evolution regarding the overheated rods and mixing grids effects. This could be compared to boiling crisis location in experiments to further validate its behavior.

12

GENERAL CONCLUSION AND PERSPECTIVES

Contents

12.1 Conclusions 191
12.2 Perspectives 193

In this ultimate Chapter, we finally draw the various conclusions emerging from the proposed work in this thesis and discuss some of the numerous perspectives that are of interest regarding the problem of boiling flows CFD simulation and Critical Heat Flux prediction in Pressurized Water Reactor conditions.

12.1 CONCLUSIONS

The main goal of this thesis was to try to bring elements of answers to the following question:

Is it nowadays possible to reach a proper modeling of the wall boiling phenomenon to predict boiling crisis occurrence in PWR using CFD simulations ?

To do so, the work presented in this document has been separated in three main parts.

First, an evaluation of the NEPTUNE_CFD code regarding the simulation of boiling flows in PWR conditions has been realized. After presenting the NEPTUNE_CFD modeling (Chapter 2), we started by analyzing the DEBORA experimental database which constitutes a rich source of physical information regarding boiling flows in thermal-hydraulic conditions close to PWR (Chapter 3). From this study we concluded that:

- The boiling flows in PWR are likely to be composed of small vapor inclusions (a few millimeters) even at high void fraction, which deviates from traditional descriptions supposing larger vapor structures.
- Bubbles clearly present coalescence and condensation effects when measuring their diameter, with coalescence being dominant close to the wall and condensation in the bulk.
- The database however shows some flaws, with a clear lack of simultaneous measurements of topology (void fraction, bubble diameter, vapor velocity) and thermal quantities (liquid and wall temperature). Those elements further complicate the precise validation of CFD models for boiling flows.

The NEPTUNE_CFD code was then confronted to the DEBORA measurements (Chapter 4) from which we can remember:

- Good predictions in the single-phase region both for the wall and liquid temperature profiles.
- Significant errors in the boiling region where the wall temperature is overestimated (up to 10%), while void fraction presents coherent results (though overestimated at the wall by approximately 10% in absolute) and vapor velocity is correctly predicted.
- Bubble diameter underestimation (10% to 20% in average) with an observed too large impact of the condensation in subcooled liquid region while coalescence alone seems fairly reproduced. Nonetheless, the order of magnitude of the computed diameter is in agreement with the experiments.
- The wall boiling closure being composed of old formulations which lead us to question its validity since resulting temperature predictions are very sensitive to modeling choices such as nucleation site density correlation.

Those results pointed towards weaknesses in the wall boiling formulation *i. e.* the Heat Flux Partitioning model, which has then become the main part of this work.

The second part of the thesis thus focused on the development of a new Heat Flux Partitioning model (HFP) to improve the modeling of wall boiling. However, such a model is a truly complicated mix of many closure laws each aiming to representing a precise physical phenomenon. Moreover, literature accounts for dozens of HFP models that propose different formulations of the heat fluxes parameters (Chapter 5). In order to achieve separate validation for the different parameters at stake, we first focused on the dynamics of boiling bubbles on a vertical wall in Chapter 6. This resulted in:

- A study of the bubble growth which resulted in a new formulation accounting for bubble subcooling that seems appropriate to pool boiling conditions. We then validated the use of a $R \propto \sqrt{t}$ law, especially at high pressure and even for sliding bubbles.
- The development of a force balance to predict the bubble dynamics parallel to the wall with both an enhanced drag coefficient accounting for wall vicinity using recent DNS results [147] and a proper evaluation of the added mass term. This force balance has then been validated against several departure diameter measurements from the literature as well as bubble sliding velocities at low and high pressures. It was also the occasion to show that the uncertainties over some parameters such as the contact angle are largely impacting the predictions, excluding the need of several extra empirical parameters.
- A discussion over the question of bubble lift-off in vertical boiling. Divergences among experimental observations lead us to consider that the lift-off of a single bubble is unlikely to happen in any conditions while it has more chances to be triggered by deformation or coalescence. A simple empirical correlation for bubble lift-off (or maximum) diameter based on measurement database from the literature covering various pressures has also been proposed.

Over the bubble dynamics, several other parameters had still to be modeled for the Heat Flux Partitioning formulation, which was the topic of Chapter 7 along with the assembling of the model:

- Validation of single-phase heat transfer coefficient, nucleation site density and bubble wait time were achieved using experimental measurements from the literature, trying to cover a large range of thermal-hydraulic conditions for water.
- The nucleation site density was a large point of improvement for the NEPTUNE_CFD modeling due to the lack of pressure dependency in the Lemmert & Chawla formulation [100]. Li *et al.* [103] recent correlation better managed to reproduce various experimental databases up to very high pressures.
- Bubble wait time has proven to be a very tricky parameter to model. The few available measurements have however been reasonably reproduced with analytic expressions, avoiding some non-physical behavior of correlations.
- Bubble interactions were modeled using an homogeneous spatial Poisson process, from which it was possible to compute different types of interactions such as nucleation site suppression and bubble static coalescence.
- The final formulation of the HFP model (Tables 7.6 and 7.5) included the previously developed force-balance dynamics for bubble departure and sliding, and supposed that bubble sliding length was the average distance between two nucleating bubbles, at which a bubble coalescence occurs and triggers lift-off.

The validation of the proposed formulation was then conducted in Chapter 8. The different tests allowed to conclude that:

- The wait and quenching time showed good agreement with the experiments as well as nucleation frequency. However, bubble growth time was too large due to a sliding length overestimation, resulting in an overestimated quenching area.
- Although the quenching flux is overestimated, fair wall temperature predictions were achieved for various experiments while choosing coherent values for the closure parameters being contact angle, bubble tilt and growth constant.

- A complicated issue regarding HFP modeling remains that different models can produce similar results regarding wall temperature while having strongly different heat flux partitioning. This further insists on the difficulty and importance of carefully choosing separately validated closure laws for each physical parameters at stake.
- A final test on a DEBORA case showed that wall temperature predictions could be largely improved compared to the initial NEPTUNE_CFD simulations.

Finally, the prediction of the Boiling Crisis is anchored as a perspective of this work and discussed in Chapter 9. Recent models based on the representation of a dry spot growing at the wall (as experimentally observed [90, 139]) have proposed good predictions of the Critical Heat Flux values [37, 177]. Testing Zhang criterion for boiling crisis detection [177] based on parameters computed in the Heat Flux Partitioning (bubble diameter, nucleation site density, bubble growth time and nucleation frequency) presented a coherent behavior for a simple tube DEBORA case in conditions close to the CHF.

Finally, **the last part** of this study is related to boiling flows in geometries including mixing devices similar to PWR grids (Figure 1.5). To that end, analysis of the DEBORA-Promoteur experiments in Chapter 10 have permitted to gather information regarding the flow structure:

- The presence of mixing vanes strongly changes the radial distribution of vapor, with a huge peak at the center in saturated conditions. The closer the vanes are, the larger the vapor accumulation will be.
- We proposed an estimation of the bubble diameter (new element to this database) which highlighted the preponderant coalescence effects in the bulk with bubble diameters greater than 2 mm at void fractions around 90%. The flow is likely to look like a foam composed of vapor bubbles and thin liquid films, deviating from the dispersed regime. In such conditions, we can expect some models validated for low to moderate void fraction flows (*e. g.* interfacial transfers) to be inappropriate to model the complex interactions between the phases (*e. g.* turbulence enhancement, change in phenomena scales).

Logically, we then finished by performing NEPTUNE_CFD simulations of boiling flows in mixing vanes geometries. Results presented in Chapter 11 showed in the end that:

- The code reproduces core vapor accumulation with bubble coalescence for DEBORA-Promoteur cases, but globally overestimates the measurements while failing to reproduce highest void fraction peak of 90%.
- Simulations of the single-phase counterpart (AGATE-Promoteur case) indicated that the rotation of the fluid is overestimated as we move downstream the mixing vanes, both with RANS and LES turbulence modeling. The result proved to be sensitive to the wall law and thus could explain the too large amount vapor in the bulk for DEBORA-Promoteur cases.
- Testing the CHF criterion of Zhang [177] on a 5×5 rod bundle with PWR mixing grids showed good qualitative features with a clearly visible effect of the mixing vanes repelling the boiling crisis risk. Although this was achieved using the old formulation of the HFP, it shows the capability of CFD codes as tools to investigate the CHF in industrial geometries and further highlights the interest of developing new HFP models to better represent the local boiling phenomena.

12.2 PERSPECTIVES

The aforementioned points offers a myriad of perspectives regarding future works. We propose to divide them in three categories : experiments, models and simulations.

Experiments :

- Since PWR-like conditions have already been achieved with simulating fluids, there is a real need for complete databases for boiling flows in such conditions. This means including simultaneous and collocated measurements of **every** physical parameters of interest, *i. e.* void fraction, phase velocity, bubble diameter, liquid and wall temperature. Otherwise, any validation based on incomplete data will still suffer from large uncertainties. This also means precisely controlling the uncertainties over the mass and energy balance.

- Performing such measurements on geometries gradually approaching the industrial configuration (*e. g.* tube → single rod → rod bundle → rods with mixing vanes, etc.) would be a very fruitful process allowing to finely quantify the difference purely arising from the specific geometry of PWR.
- Regarding wall boiling physics, recent experiments (*e. g.* Richenderfer [139] or Kossolapov [90]) proved the capacity of experimental instrumentation to capture nearly every physical parameter of interest for Heat Flux Partitioning models in conditions getting closer to PWR. We now should hope that even more data of this kind will be produced since they will provide very robust validation matter for wall boiling models in large operating conditions. **Moreover, such experiments even start to leverage fine underlying physics related to the boiling crisis (*e. g.* dry patch formation)**
- Near Boiling Crisis occurrence, bubble interactions and coalescence on the wall seem of prior interest. Experiments conducting fine analyses of the different bubble behaviors at the wall along with the statistics of interactions (coalescence, lift-off events, etc.) would be a significant step for wall boiling modeling which mostly rely on single bubbles approaches.
- The work produced in this thesis has consisted for quite some time in gathering many experimental data from separate literature sources and we are yet very far from having considered every measurements available. In that regard, it would be of common interest for researcher in the physics of boiling to build a shared open-access database that gathers up every measurements available regarding wall boiling parameters (departure and lift-off diameters, wait time, growth time, nucleation sites density, etc.). With shared efforts in that direction, this could help to establish a global validation setup for every models related to wall boiling such as Heat Flux Partitioning.

Models :

- Parallel to recent experiments, the development of Direct Numerical Simulations represents nowadays a non-negligible source of information to enrich CFD models and allow to reach data beyond the scope of measurements techniques. This has been the case in this work with the DNS results of Shi *et al.* [147] or Urbano *et al.* [163].
- Force balance approaches to model bubble dynamics at the wall shall be later achieved without the implementation of several empirical constants over which the large uncertainty can change the results by decades. This is particularly the case for bubble foot-to-diameter ratio r_w/R, contact angle θ, bubble inclination $\mathrm{d}\theta$ or bubble growth constant K which, if used in a model, must be first assessed for the aimed conditions to avoid using non-physical conclusions (*e. g.* the added mass case discussed in Subsection 6.2.6). Moreover, the expression of the forces on which those approaches rely are dedicated to isolated bubbles, which must be questioned when approaching significant void fractions (such as DEBORA cases). They could thus benefit from extensive validation in such situations (*e. g.* checking the deviation from single bubble dynamics when there is a large number of sliding bubbles at the wall).
- Bubble dynamics at the wall should systematically try to account for bubble interactions since it is predominant when approaching the CHF (*e. g.* coalescence, dry patch formation). Models based on simple homogeneous Poisson processes are easy to implement and would benefit from further efforts in that direction. For instance, inhomogeneous Poisson point processes can account for attractive or repulsive impact of events [34], which could be a way of accounting for local nucleation site thermal deactivation as suggested by Del Valle & Kenning [35].
- Regarding Heat Flux Partitioning, it is necessary to achieve separate validation of **every** closure law involved in the framework. Though this remains complicated due sometimes to a lack of experimental data, one can never ensure the validity of a HFP approach is any of the parameters remains unassessed. Otherwise, this results in diverging predictions from one model to another or in excessive sensibility to any closure law change. **This may be one of the most limiting aspects related to wall boiling modeling**. Recent approaches are though starting to better capture fine details of the physics of boiling when approaching the Critical Heat Flux [5].
- The same goes for bulk models in CFD computations who must be tested individually beforehand using dedicated experiments. For instance, a large uncertainty still lies around the closure laws for vapor condensation while it plays a primary role in controlling the subcooled boiling flows structure along with coalescence and break-up effects.

Simulations :

- Relying on Heat Flux Partitioning approaches for CFD simulations has been the common approach for decades. With the continuous improvements in computational capacities, we could consider to go down in spatial resolution by achieving a bubble-tracking at the wall. This could be a way to better rely on single bubble dynamics and actually simulate their interactions [74] and avoid looking for several closure laws to represent averaged quantities. As proposed in Zhang *et al.* [178], this could also be a way of detecting the boiling crisis by identifying bubble clusters.
- Conducting numerical optimization of models including fine bubble dynamics could be of great interest to use enriched models. We actually faced cases where very low nucleation site densities induced very large sliding length in the HFP model, which could be partially coped using an adaptive time step when computing the sliding.
- Simulation strategies for validation must first be focused on computationally cheap cases (*e. g.* simple tubes) before tackling more complicated situations in which long computational times are sometimes wasted due to insufficiently validated modeling framework.
- The capacity of simulating complex flows including multiphysics modeling on complex geometries representative of PWR is a very encouraging proof of computational capacity. **However, exigent validation of every physics at stake should be a primary focus before jumping towards very complex cases for which only limited validation is possible (often one type of measurements or very few locations)**. This even includes single phase turbulence and wall laws.
- We can yet end on a positive note with the fact that current modeling frameworks seem to present physically coherent behavior even for boiling crisis detection, indicating a good baseline to pursue efforts in that direction.

BIBLIOGRAPHY

[1] Rouhollah Ahmadi, Tatsuya Ueno, and Tomio Okawa. "Bubble dynamics at boiling incipience in subcooled upward flow boiling". In: *International Journal of Heat and Mass Transfer* 55.1 (Jan. 15, 2012), pp. 488–497. ISSN: 0017-9310. DOI: 10.1016/j.ijheatmasstransfer.2011.09.050.

[2] M. Al-Arabi. "Turbulent Heat Transferin the Entrance Region of a Tube". In: *Heat Transfer Engineering* 3 (1982), pp. 76–83. ISSN: 3-4. DOI: https://doi.org/10.1080/01457638108939586.

[3] S. Aubry, J. Olive, C. Caremoli, and P. Rascle. "The THYC three-dimensional thermal-hydraulic codes for rod bundles: Recent developments and tests". In: *Nuclear Technology* 112.3 (Dec. 1, 1995).

[4] T. R. Auton. "The lift force on a spherical body in a rotational flow". In: *Journal of Fluid Mechanics* 183 (Oct. 1987). Publisher: Cambridge University Press, pp. 199–218. ISSN: 1469-7645, 0022-1120. DOI: 10.1017/S002211208700260X.

[5] Emilio Baglietto, Etienne Demarly, and Ravikishore Kommajosyula. "Boiling crisis as the stability limit to wall heat partitioning". In: *Applied Physics Letters* 114.10 (Mar. 11, 2019). Publisher: American Institute of Physics, p. 103701. ISSN: 0003-6951. DOI: 10.1063/1.5080724.

[6] Nilanjana Basu, Gopinath R. Warrier, and Vijay K. Dhir. "Wall Heat Flux Partitioning During Subcooled Flow Boiling: Part 1—Model Development". In: *Journal of Heat Transfer* 127.2 (Mar. 15, 2005), pp. 131–140. ISSN: 0022-1481. DOI: 10.1115/1.1842784.

[7] Nilanjana Basu, Gopinath R. Warrier, and Vijay K. Dhir. "Wall Heat Flux Partitioning During Subcooled Flow Boiling: Part II—Model Validation". In: *Journal of Heat Transfer* 127.2 (Mar. 15, 2005), pp. 141–148. ISSN: 0022-1481. DOI: 10.1115/1.1842785.

[8] Sofiane Benhamadouche. "On the use of (U)RANS and LES approaches for turbulent incompressible single phase flows in nuclear engineering applications". In: *Nuclear Engineering and Design*. 16th International Topical Meeting on Nuclear Reactor Thermal Hydraulics 312 (Feb. 1, 2017), pp. 2–11. ISSN: 0029-5493. DOI: 10.1016/j.nucengdes.2016.11.002.

[9] Berne. "Analyse critique des modèles d'auto vaporisation utilisés dans le calcul des écoulements diphasiques en conduites". PhD thesis. Châtenay-Malabry, Ecole centrale de Paris, 1983.

[10] D. Bestion et al. "Review of Available Data for Validation of Nuresim Two-Phase CFD Software Applied to CHF Investigations". In: *Science and Technology of Nuclear Installations* 2009 (Oct. 14, 2008). Publisher: Hindawi, e214512. ISSN: 1687-6075. DOI: 10.1155/2009/214512.

[11] G. Bloch, W. Muselmann, M. Saier, and T. Sattelmayer. "A phenomenological study on effects leading to the departure from nucleate boiling in subcooled flow boiling". In: *International Journal of Heat and Mass Transfer* 67 (Dec. 1, 2013), pp. 61–69. ISSN: 0017-9310. DOI: 10.1016/j.ijheatmasstransfer.2013.08.014.

[12] Gregor Bloch, Moritz Bruder, and Thomas Sattelmayer. "A study on the mechanisms triggering the departure from nucleate boiling in subcooled vertical flow boiling using a complementary experimental approach". In: *International Journal of Heat and Mass Transfer* 92 (Jan. 1, 2016), pp. 403–413. ISSN: 0017-9310. DOI: 10.1016/j.ijheatmasstransfer.2015.08.063.

[13] V. M. Borishanskii, G. I. Bobrovich, and F. P. Minchenko. "Heat transfer from a tube to water and to ethanol in nucleate pool boiling". In: *Problems of Heat Transfer and Hydraulics of Two-Phase Media*. Elsevier, 1969, pp. 85–106.

[14] J Borée, G. Charnay, J. Fabre, D. Legendre, and J. Magnaudet. *Ecoulements diphasiques eau-vapeur avec changement de phase.* Technical Report. Toulouse: IMFT - Interface, 1992.

[15] R. W. Bowring. *Physical model, based on bubble detachment, and calculation of steam voidage in he sub-cooled region of a heated channel*. HPR-10. Institutt for Atomenergi (Norway). OECD Halden Reaktor Prosjekt, Dec. 1, 1962.

[16] Patrick Bricard. "Modélisation de l'ébullition sous-saturée et de la crise d'ébullition par caléfaction en convection forcée". These de doctorat. Châtenay-Malabry, Ecole centrale de Paris, Jan. 1, 1995.

[17] Moritz Bruder and Thomas Sattelmayer. “An Empirical Correlation for the Void Fraction at Critical Heat Flux Close to the Wall for Subcooled Flow Boiling of a Low Boiling Refrigerant”. In: (2018).

[18] Mattia Bucci, Jacopo Buongiorno, and Matteo Bucci. “The not-so-subtle flaws of the force balance approach to predict the departure of bubbles in boiling heat transfer”. In: *Physics of Fluids* 33.1 (Jan. 2021). Publisher: American Institute of Physics, p. 017110. ISSN: 1070-6631. DOI: 10.1063/5.0036956.

[19] Lubomír Bureš and Yohei Sato. “On the modelling of the transition between contact-line and microlayer evaporation regimes in nucleate boiling”. In: *Journal of Fluid Mechanics* 916 (June 2021). Publisher: Cambridge University Press. ISSN: 0022-1120, 1469-7645. DOI: 10.1017/jfm.2021.204.

[20] In-Cheol CHU, Hee Cheon NO, and Chul-Hwa SONG. “Bubble Lift-off Diameter and Nucleation Frequency in Vertical Subcooled Boiling Flow”. In: *Journal of Nuclear Science and Technology* 48.6 (June 1, 2011), pp. 936–949. ISSN: 0022-3131. DOI: 10.1080/18811248.2011.9711780.

[21] Luigi Capone, Sofiane Benhamadouche, and Yassin A. Hassan. “Source terms modeling for spacer grids with mixing vanes for CFD simulations in nuclear reactors”. In: *Computers & Fluids* 126 (Mar. 1, 2016), pp. 141–152. ISSN: 0045-7930. DOI: 10.1016/j.compfluid.2015.11.011.

[22] Deqi Chen, Liang-ming Pan, and Song Ren. “Prediction of bubble detachment diameter in flow boiling based on force analysis”. In: *Nuclear Engineering and Design* 243 (Feb. 1, 2012), pp. 263–271. ISSN: 0029-5493. DOI: 10.1016/j.nucengdes.2011.11.022.

[23] J. C. Chen. “Correlation for Boiling Heat Transfer to Saturated Fluids in Convective Flow”. In: *Industrial & Engineering Chemistry Process Design and Development* 5.3 (July 1, 1966). Publisher: American Chemical Society, pp. 322–329. ISSN: 0196-4305. DOI: 10.1021/i260019a023.

[24] Zhihao Chen, Atsushi Haginiwa, and Yoshio Utaka. “Detailed structure of microlayer in nucleate pool boiling for water measured by laser interferometric method”. In: *International Journal of Heat and Mass Transfer* 108 (May 1, 2017), pp. 1285–1291. ISSN: 0017-9310. DOI: 10.1016/j.ijheatmasstransfer.2017.01.003.

[25] Zhihao Chen, Xiaocheng Hu, Kang Hu, Yoshio Utaka, and Shoji Mori. “Measurement of the microlayer characteristics in the whole range of nucleate boiling for water by laser interferometry”. In: *International Journal of Heat and Mass Transfer* 146 (Jan. 1, 2020), p. 118856. ISSN: 0017-9310. DOI: 10.1016/j.ijheatmasstransfer.2019.118856.

[26] Han Chi-Yeh and Peter Griffith. “The mechanism of heat transfer in nucleate pool boiling—Part I: Bubble initiaton, growth and departure”. In: *International Journal of Heat and Mass Transfer* 8.6 (June 1, 1965), pp. 887–904. ISSN: 0017-9310. DOI: 10.1016/0017-9310(65)90073-6.

[27] SW Churchill. “Friction Factor Spans All Fluid-Flow Regimes”. In: *Chemical Engineering* 84 (1977), pp. 91–92.

[28] Robert Cole. “Bubble frequencies and departure volumes at subatmospheric pressures”. In: *AIChE Journal* 13.4 (1967), pp. 779–783. ISSN: 1547-5905. DOI: 10.1002/aic.690130434.

[29] John G. Collier and John R. Thome. *Convective Boiling and Condensation*. Clarendon Press, May 19, 1994. 646 pp. ISBN: 978-0-19-159126-6.

[30] Marco Colombo and Michael Fairweather. “Prediction of bubble departure in forced convection boiling: A mechanistic model”. In: *International Journal of Heat and Mass Transfer* 85 (June 1, 2015), pp. 135–146. ISSN: 0017-9310. DOI: 10.1016/j.ijheatmasstransfer.2015.01.103.

[31] M. G. Cooper and A. J. P. Lloyd. “The microlayer in nucleate pool boiling”. In: *International Journal of Heat and Mass Transfer* 12.8 (Aug. 1, 1969), pp. 895–913. ISSN: 0017-9310. DOI: 10.1016/0017-9310(69)90154-9.

[32] Allen G. Croff. “Introduction to Nuclear Chemistry and Fuel Cycle Separations”. Short Course. Short Course. Vanderbilt University, Dec. 16, 2008.

[33] Géraud Cubizolles. “Etude stéréologique de la topologie des écoulements diphasiques à haute pression”. These de doctorat. Ecully, Ecole centrale de Lyon, Jan. 1, 1996.

[34] D. J. Daley and D. Vere-Jones. *An Introduction to the Theory of Point Processes*. Probability and its Applications. New York: Springer-Verlag, 2003. ISBN: 978-0-387-95541-4. DOI: 10.1007/b97277.

[35] Victor H. Del Valle and D. B. R. Kenning. "Subcooled flow boiling at high heat flux". In: *International Journal of Heat and Mass Transfer* 28.10 (Oct. 1, 1985), pp. 1907–1920. ISSN: 0017-9310. DOI: 10.1016/0017-9310(85)90213-3.

[36] Jean-Marc Delhaye. *Thermohydraulique des réacteurs*. EDP Sciences, Dec. 3, 2012. 527 pp. ISBN: 978-2-7598-0308-8.

[37] Etienne Demarly. "A new approach to predicting departure from Nucleate Boiling (DNB) from direct representation of boiling heat transfer physics". Accepted: 2021-02-19T20:35:27Z ISBN: 9781237640528. Thesis. Massachusetts Institute of Technology, 2020.

[38] F. W. Dittus and L. M. K. Boelter. "Heat transfer in automobile radiators of the tubular type". In: *International Communications in Heat and Mass Transfer* 12.1 (Jan. 1, 1985), pp. 3–22. ISSN: 0735-1933. DOI: 10.1016/0735-1933(85)90003-X.

[39] Shichang Dong and Shengjie Gong. "Numerical Model for Subcooled Flow Boiling Heat Transfer and Critical Heat Flux Based on Probability of Bubble Interaction". In: 2022 29th International Conference on Nuclear Engineering. American Society of Mechanical Engineers Digital Collection, Nov. 23, 2022. DOI: 10.1115/ICONE29-93755.

[40] G. Duhar, G. Riboux, and C. Colin. "Vapour bubble growth and detachment at the wall of shear flow". In: *Heat and Mass Transfer* 45.7 (May 1, 2009), pp. 847–855. ISSN: 1432-1181. DOI: 10.1007/s00231-007-0287-y.

[41] Géraldine Duhar. "Croissance et détachement de bulles en paroi d'un écoulement cisaillé : étude expérimentale de l'injection et de l'ébullition nucléée". These de doctorat. Toulouse, INPT, Jan. 1, 2003.

[42] Géraldine Duhar and Catherine Colin. "Dynamics of bubble growth and detachment in a viscous shear flow". In: *Physics of Fluids* 18.7 (July 2006). Publisher: American Institute of Physics, p. 077101. ISSN: 1070-6631. DOI: 10.1063/1.2213638.

[43] Carlos E. Estrada-Pérez, Yassin A. Hassan, Bandar Alkhudhiri, and Junsoo Yoo. "Time-resolved measurements of liquid–vapor thermal interactions throughout the full life-cycle of sliding bubbles at subcooled flow boiling conditions". In: *International Journal of Multiphase Flow* 99 (Feb. 1, 2018), pp. 94–110. ISSN: 0301-9322. DOI: 10.1016/j.ijmultiphaseflow.2017.10.002.

[44] Gloria Faccanoni. "Etude d'un modèle fin de changement de phase liquide-vapeur : contribution à l'étude de la crise d'ébullition". These de doctorat. Palaiseau, Ecole polytechnique, Jan. 1, 2008.

[45] Amir Faghri and Yuwen Zhang. "10 - BOILING". In: *Transport Phenomena in Multiphase Systems*. Ed. by Amir Faghri and Yuwen Zhang. Boston: Academic Press, Jan. 1, 2006, pp. 765–852. ISBN: 978-0-12-370610-2. DOI: 10.1016/B978-0-12-370610-2.50015-5.

[46] F Falk. *Promoteur de Mélange - Diamètre 19.2 mm - 3 ailettes à 120 degrés*. DER/SSTH/LIEX/2006-0.13. Grenoble: CEA Grenoble, July 2007.

[47] F Falk and R Hugonnard. *Rapport d'Essais DEBORA -Promoteur de Mélange - Essais de BO et de Topologie - Campagne 4800-4900-5000*. DTP/SETEX/LTAC/02-158. Grenoble: CEA Grenoble, May 2002.

[48] F Falk and R Hugonnard. *Rapport d'Essais DEBORA - Promoteur de Mélange 10 DH - Essais de Crise d'Ebullition et de Topologie - Campagne 5200*. DTP/DETEX/LTAC/03-178. Grenoble: CEA Grenoble, Mar. 2003.

[49] Luc Favre, Stéphane Pujet, Stéphane Mimouni, and Catherine Colin. "NEPTUNE CFD Simulations of DEBORA-Promoteur Experiments: Boiling Freon in a Vertical Pipe with Mixing Vanes". In: *Proc. 19th International Topical Meeting on Nuclear Reactor Thermal Hydraulics (NURETH-19)*. 2022, pp. 1–17.

[50] H. K. Forster and N. Zuber. "Growth of a Vapor Bubble in a Superheated Liquid". In: *Journal of Applied Physics* 25.4 (Apr. 1954). Publisher: American Institute of Physics, pp. 474–478. ISSN: 0021-8979. DOI: 10.1063/1.1721664.

[51] W Frost, G. S Dzakowic, and American Society of Mechanical Engineers. *An extension of the method for predicting incipient boiling on commercially finished surfaces*. OCLC: 459788171. New York, N.Y.: ASME, 1967.

[52] R. F. Gaertner and J. W. Westwater. "Population of Active Sites in Nucleate Boiling Heat Transfer". In: *Chem. Eng. Progr.* Vol: 56: Symposium Ser. No. 30 (Jan. 1, 1960). Institution: General Electric Co., Schenectady, N.Y.

[53] J. Garnier, E. Manon, and G. Cubizolles. "LOCAL MEASUREMENTS ON FLOW BOILING OF REFRIGERANT 12 IN A VERTICAL TUBE". In: *Multiphase Science and Technology* 13.1 (2001). Publisher: Begel House Inc. ISSN: 0276-1459, 1943-6181. DOI: 10.1615/MultScienTechn.v13.i1-2.10.

[54] Marie-Charlotte Gauffre, Sofiane Benhamadouche, and Pierre-Bernard Badel. "Wall-Modeled Large Eddy Simulation of the Flow Through PWR Fuel Assemblies at ReH = 66 000—Validation on CALIFS Experimental Setup". In: *Nuclear Technology* 206.2 (Feb. 1, 2020), pp. 255–265. ISSN: 0029-5450. DOI: 10.1080/00295450.2019.1642684.

[55] C. W. M. van der Geld. "The dynamics of a boiling bubble before and after detachment". In: *Heat and Mass Transfer* 45.7 (May 1, 2009), pp. 831–846. ISSN: 1432-1181. DOI: 10.1007/s00231-007-0254-7.

[56] Craig Douglas Gerardi. "Investigation of the pool boiling heat transfer enhancement of nano-engineered fluids by means of high-speed infrared thermography". Accepted: 2010-03-24T20:38:10Z. Thesis. Massachusetts Institute of Technology, 2009.

[57] Craig Gerardi, Jacopo Buongiorno, Lin-wen Hu, and Thomas McKrell. "Study of bubble growth in water pool boiling through synchronized, infrared thermometry and high-speed video". In: *International Journal of Heat and Mass Transfer* 53.19 (Sept. 1, 2010), pp. 4185–4192. ISSN: 0017-9310. DOI: 10.1016/j.ijheatmasstransfer.2010.05.041.

[58] Lindsey Anne Gilman. "Development of a general purpose subgrid wall boiling model from improved physical understanding for use in computational fluid dynamics". Accepted: 2014-12-08T18:48:48Z. Thesis. Massachusetts Institute of Technology, 2014.

[59] Lindsey Gilman and Emilio Baglietto. "A self-consistent, physics-based boiling heat transfer modeling framework for use in computational fluid dynamics". In: *International Journal of Multiphase Flow* 95 (Oct. 1, 2017), pp. 35–53. ISSN: 0301-9322. DOI: 10.1016/j.ijmultiphaseflow.2017.04.018.

[60] V. Gnielinski. "New equations for heat and mass transfer in the turbulent flow in pipes and channels". In: *NASA STI/Recon Technical Report A* 41 (Jan. 1, 1975). ADS Bibcode: 1975STIA...7522028G, pp. 8–16.

[61] P. Griffith, J. A. Clark, and W. M. Rohsenow. *VOID VOLUMES IN SUBCOOLED BOILING SYSTEMS. Technical Report No. 12.* NP-6637. Massachusetts Inst. of Tech., Cambridge. Div. of Industrial Cooperation, Mar. 1, 1958.

[62] D. C. Groeneveld, J. Q. Shan, A. Z. Vasić, L. K. H. Leung, A. Durmayaz, J. Yang, S. C. Cheng, and A. Tanase. "The 2006 CHF look-up table". In: *Nuclear Engineering and Design.* NURETH-11 237.15 (Sept. 1, 2007), pp. 1909–1922. ISSN: 0029-5493. DOI: 10.1016/j.nucengdes.2007.02.014.

[63] Peng Guan, Li Jia, Liaofei Yin, and Zetao Tan. "Bubble departure size in flow boiling". In: *Heat and Mass Transfer* 51.7 (July 1, 2015), pp. 921–930. ISSN: 1432-1181. DOI: 10.1007/s00231-014-1461-7.

[64] Jil Gueguen. "Contribution à la modélisation multidimensionnelle des écoulements bouillants convectifs en conduite haute pression pour l'application au cas des réacteurs à eau pressurisée". These de doctorat. Grenoble, Dec. 19, 2013.

[65] Antoine Guelfi, Dominique Bestion, Marc Boucker, Pascal Boudier, Philippe Fillion, Marc Grandotto, Jean-Marc Hérard, Eric Hervieu, and Pierre Péturaud. "NEPTUNE: A New Software Platform for Advanced Nuclear Thermal Hydraulics". In: *Nuclear Science and Engineering* 156.3 (July 1, 2007), pp. 281–324. ISSN: 0029-5639. DOI: 10.13182/NSE05-98.

[66] Alexandre Guion, Shahriar Afkhami, Stéphane Zaleski, and Jacopo Buongiorno. "Simulations of microlayer formation in nucleate boiling". In: *International Journal of Heat and Mass Transfer* 127 (Dec. 1, 2018), pp. 1271–1284. ISSN: 0017-9310. DOI: 10.1016/j.ijheatmasstransfer.2018.06.041.

[67] K. E. Gungor and R. H. S. Winterton. "A general correlation for flow boiling in tubes and annuli". In: *International Journal of Heat and Mass Transfer* 29.3 (Mar. 1, 1986), pp. 351–358. ISSN: 0017-9310. DOI: 10.1016/0017-9310(86)90205-X.

[68] F. C. Gunther. "Photographic Study of Surface-Boiling Heat Transfer to Water With Forced Convection". In: *Transactions of the American Society of Mechanical Engineers* 73.2 (1951), pp. 115–123. ISSN: 0097-6822. DOI: 10.1115/1.4016160.

[69] Sang Jun Ha and Hee Cheo No. "A dry-spot model of critical heat flux in pool and forced convection boiling". In: *International Journal of Heat and Mass Transfer* 41.2 (Jan. 1, 1998), pp. 303–311. ISSN: 0017-9310. DOI: 10.1016/S0017-9310(97)00140-3.

[70] J. S. Hadamard. "Mouvement permanent lent d'une sphère liquide et visqueuse dans un liquide visqueux". In: *Comptes Rendus Hebdomadaires des Séances de l'Académie des Sciences* 155 (1911), pp. 1735–1738.

[71] Pierre-Antoine Haynes. "Contribution à la modélisation de la turbulence pour les écoulements à bulles : proposition d'un modèle (k-epsilon) multi-échelles diphasique". These de doctorat. Toulouse, INPT, 2004.

[72] G. F. Hewitt and A. H. Govan. "Phenomenological modelling of non-equilibrium flows with phase change". In: *International Journal of Heat and Mass Transfer* 33.2 (Feb. 1, 1990), pp. 229–242. ISSN: 0017-9310. DOI: 10.1016/0017-9310(90)90094-B.

[73] Takashi Hibiki and Mamoru Ishii. "Active nucleation site density in boiling systems". In: *International Journal of Heat and Mass Transfer* 46.14 (July 1, 2003), pp. 2587–2601. ISSN: 0017-9310. DOI: 10.1016/S0017-9310(03)00031-0.

[74] Heepyo Hong and Hyoung Kyu Cho. "Investigation of Bubble Merge and Nucleation Site Suppression Effect on Wall Heat Flux Partitioning Using Bubble Tracking Model". In: *Proc. International Topical Meeting on Advances in Thermal Hydraulics 2022*. Advances in Thermal Hydraulics 2022 (ATH'22). Anaheim, CA, USA, June 2022. ISBN: 978-0-89448-781-1.

[75] M. Ishii. *One-dimensional drift-flux model and constitutive equations for relative motion between phases in various two-phase flow regimes*. ANL-77-47. Argonne National Lab., Ill. (USA), Oct. 1, 1977. DOI: 10.2172/6871478.

[76] Mamoru Ishii and Takashi Hibiki. *Thermo-Fluid Dynamics of Two-Phase Flow*. New York, NY: Springer, 2011. ISBN: 978-1-4419-7984-1 978-1-4419-7985-8. DOI: 10.1007/978-1-4419-7985-8.

[77] Mamoru Ishii and Novak Zuber. "Drag coefficient and relative velocity in bubbly, droplet or particulate flows". In: *AIChE Journal* 25.5 (1979), pp. 843–855. ISSN: 1547-5905. DOI: 10.1002/aic.690250513.

[78] W. H. Jens and P. A. Lottes. *Analysis of Heat Transfer, Burnout, Pressure Drop and Density Data for High-Pressure Water*. ANL-4627. Argonne National Lab., May 1, 1951. DOI: 10.2172/4421630.

[79] R. L. Judd and K. S. Hwang. "A Comprehensive Model for Nucleate Pool Boiling Heat Transfer Including Microlayer Evaporation". In: *Journal of Heat Transfer* 98.4 (Nov. 1, 1976), pp. 623–629. ISSN: 0022-1481. DOI: 10.1115/1.3450610.

[80] B. A Kader and A. M Yaglom. "Heat and mass transfer laws for fully turbulent wall flows". In: *International Journal of Heat and Mass Transfer* 15.12 (Dec. 1, 1972), pp. 2329–2351. ISSN: 0017-9310. DOI: 10.1016/0017-9310(72)90131-7.

[81] Tristan Kamin. *Cycle #4 La fabrication du combustible*. Dose Équivalent Banana. Feb. 27, 2019. URL: https://doseequivalentbanana.home.blog/2019/02/27/cycle-4-la-fabrication-du-combustible/ (visited on 12/11/2022).

[82] Satish G. Kandlikar and Mark E. Steinke. "Contact angles and interface behavior during rapid evaporation of liquid on a heated surface". In: *International Journal of Heat and Mass Transfer* 45.18 (Aug. 1, 2002), pp. 3771–3780. ISSN: 0017-9310. DOI: 10.1016/S0017-9310(02)00090-X.

[83] William E. Kennel. "Local boiling of water and superheating of high pressure steam in annuli". Accepted: 2020-09-25T21:06:56Z ISSN: 2933-0025. Thesis. Massachusetts Institute of Technology, 1949.

[84] J. F. Klausner, R. Mei, D. M. Bernhard, and L. Z. Zeng. "Vapor bubble departure in forced convection boiling". In: *International Journal of Heat and Mass Transfer* 36.3 (Feb. 1, 1993), pp. 651–662. ISSN: 0017-9310. DOI: 10.1016/0017-9310(93)80041-R.

[85] Michel Kledy. "Développement d'une méthode de mesure des champs de vitesse et de température liquide en écoulement diphasique bouillant en conditions réacteurs ou simulantes". These de doctorat. Université Grenoble Alpes (ComUE), May 30, 2018.

[86] Michel Kledy, Fabrice François, Henda Djeridi, Stephane Barre, and Jean-Marc Delhaye. "Toward a local drift flux model for high-pressure, subcooled, convective boiling flows". In: *International Journal of Heat and Mass Transfer* 177 (Oct. 1, 2021), p. 121506. ISSN: 0017-9310. DOI: 10.1016/j.ijheatmasstransfer.2021.121506.

[87] G. Kocamustafaogullari. "Pressure dependence of bubble departure diameter for water". In: *International Communications in Heat and Mass Transfer* 10.6 (Nov. 1, 1983), pp. 501–509. ISSN: 0735-1933. DOI: 10.1016/0735-1933(83)90057-X.

[88] L. D. Koffman and M. S. Plesset. "Experimental Observations of the Microlayer in Vapor Bubble Growth on a Heated Solid". In: *Journal of Heat Transfer* 105.3 (Aug. 1, 1983), pp. 625–632. ISSN: 0022-1481. DOI: 10.1115/1.3245631.

[89] Ravikishore Kommajosyula. "Development and assessment of a physics-based model for subcooled flow boiling with application to CFD". Accepted: 2021-01-05T23:15:30Z. Thesis. Massachusetts Institute of Technology, 2020.

[90] Artyom Kossolapov. "Experimental Investigation of Subcooled Flow Boiling and CHF at Prototypical Pressures of Light Water Reactors". PhD thesis. Massachusetts Institute of Technology, 2021.

[91] Eckhard Krepper, Dirk Lucas, Thomas Frank, Horst-Michael Prasser, and Phil J. Zwart. "The inhomogeneous MUSIG model for the simulation of polydispersed flows". In: *Nuclear Engineering and Design* 238.7 (July 1, 2008), pp. 1690–1702. ISSN: 0029-5493. DOI: 10.1016/j.nucengdes.2008.01.004.

[92] N. Kurul and Michael Z. Podowski. "MULTIDIMENSIONAL EFFECTS IN FORCED CONVECTION SUBCOOLED BOILING". In: International Heat Transfer Conference 9. Begel House Inc., 1990. ISBN: 0-89116-909-1. DOI: 10.1615/IHTC9.40.

[93] S. S. Kutateladze. "On the transition to film boiling under natural convection". In: *Kotloturbostroenie* 3 (1948), pp. 10–12.

[94] Sir Horace Lamb. *Hydrodynamics*. University Press, 1895. 632 pp. ISBN: 978-1-4086-1332-0.

[95] Jérôme Laviéville, Nicolas Mérigoux, Mathieu Guingo, Cyril Baudry, and Stéphane Mimouni. "A Generalized turbulent dispersion model for bubbly flow numerical simulation in NEPTUNE_CFD". In: *Nuclear Engineering and Design*. 16th International Topical Meeting on Nuclear Reactor Thermal Hydraulics 312 (Feb. 1, 2017), pp. 284–293. ISSN: 0029-5493. DOI: 10.1016/j.nucengdes.2016.11.003.

[96] C. H. Lee and I. Mudawwar. "A mechanistic critical heat flux model for subcooled flow boiling based on local bulk flow conditions". In: *International Journal of Multiphase Flow* 14.6 (Nov. 1, 1988), pp. 711–728. ISSN: 0301-9322. DOI: 10.1016/0301-9322(88)90070-5.

[97] Jae Ryong Lee, Jungwoo Kim, and Chul-Hwa Song. "Synthesis of the turbulent mixing in a rod bundle with vaned spacer grids based on the OECD-KAERI CFD benchmark exercise". In: *Nuclear Engineering and Design*. SI : CFD4NRS-4 279 (Nov. 1, 2014), pp. 3–18. ISSN: 0029-5493. DOI: 10.1016/j.nucengdes.2014.03.008.

[98] Dominique Legendre, Jacques Borée, and Jacques Magnaudet. "Thermal and dynamic evolution of a spherical bubble moving steadily in a superheated or subcooled liquid". In: *Physics of Fluids* 10.6 (June 1998). Publisher: American Institute of Physics, pp. 1256–1272. ISSN: 1070-6631. DOI: 10.1063/1.869654.

[99] Dominique Legendre and Jacques Magnaudet. "The lift force on a spherical bubble in a viscous linear shear flow". In: *Journal of Fluid Mechanics* 368 (Aug. 1998). Publisher: Cambridge University Press, pp. 81–126. ISSN: 1469-7645, 0022-1120. DOI: 10.1017/S0022112098001621.

[100] M. Lemmert and J.M. Chawla. "Influence of flow velocity on surface boiling heat transfer coefficient". In: *Heat Transfer in Boiling*. Hemisphere. Washington D.C., 1977, pp. 236–246.

[101] Octave Levenspiel. "Collapse of Steam Bubbles in Water". In: *Industrial & Engineering Chemistry* 51.6 (June 1, 1959). Publisher: American Chemical Society, pp. 787–790. ISSN: 0019-7866. DOI: 10.1021/ie50594a045.

[102] V. G. Levich. *Physicochemical hydrodynamics*. Prentice-Hall international series in the physical and chemical engineering sciences. OCLC: 1378432. Englewood Cliffs, N.J.: Prentice-Hall, 1962. 700 pp. ISBN: 978-0-13-674440-5.

[103] Quan Li, Yongjun Jiao, Maria Avramova, Ping Chen, Junchong Yu, Jie Chen, and Jason Hou. "Development, verification and application of a new model for active nucleation site density in boiling systems". In: *Nuclear Engineering and Design* 328 (Mar. 1, 2018), pp. 1–9. ISSN: 0029-5493. DOI: 10.1016/j.nucengdes.2017.12.027.

[104] Yang Liu, Wei Liu, Jianqiang Shan, David R. Novog, Bo Zhang, Miao Gui, and Junliang Guo. "Critical heat flux measurement and visualization in R-134a on a vertical single rod with and without mixing-vanes spacer: The characteristics and phenomenon of critical heat flux". In: *Annals of Nuclear Energy* 160 (Sept. 15, 2021), p. 108399. ISSN: 0306-4549. DOI: 10.1016/j.anucene.2021.108399.

[105] Z. Liu and R. H. S. Winterton. "A general correlation for saturated and subcooled flow boiling in tubes and annuli, based on a nucleate pool boiling equation". In: *International Journal of Heat and Mass Transfer* 34.11 (Nov. 1, 1991), pp. 2759–2766. ISSN: 0017-9310. DOI: 10.1016/0017-9310(91)90234-6.

[106] R.W. Lockhart and R.C. Martinelli. "Proposed Correlation of Data for Isothermal Two-Phase, Two-Component Flow in Pipes." In: *Chemical Engineering Progress* 45 (), pp. 38–48.

[107] J. Magnaudet and I. Eames. "The Motion of High-Reynolds-Number Bubbles in Inhomogeneous Flows". In: *Annual Review of Fluid Mechanics* 32.1 (2000), pp. 659–708. DOI: 10.1146/annurev.fluid.32.1.659.

[108] Sandipan Maity. "Effect of Velocity and Gravity on Bubble Dynamics". MSc Thesis. University of California Los Angeles, 2000.

[109] Etienne Manon. "Contribution à l'analyse et à la modélisation locale des écoulements bouillants sous-saturés dans les conditions des réacteurs à eau sous pression". These de doctorat. Châtenay-Malabry, Ecole centrale de Paris, Jan. 1, 2000.

[110] Philippe (1970 March. "Caractérisation et modélisation de l'environnement thermohydraulique et chimique des gaines de combustible des réacteurs à eau sous pression en présence d'ébullition". These de doctorat. Aix-Marseille 1, Jan. 1, 1999.

[111] T. Mazzocco, W. Ambrosini, R. Kommajosyula, and E. Baglietto. "A reassessed model for mechanistic prediction of bubble departure and lift off diameters". In: *International Journal of Heat and Mass Transfer* 117 (Feb. 1, 2018), pp. 119–124. ISSN: 0017-9310. DOI: 10.1016/j.ijheatmasstransfer.2017.09.105.

[112] William H McAdams. *Heat transmission*. OCLC: 683455. New York: McGraw-Hill, 1954.

[113] Renwei Mei and J. F. Klausner. "Shear lift force on spherical bubbles". In: *International Journal of Heat and Fluid Flow* 15.1 (Feb. 1, 1994), pp. 62–65. ISSN: 0142-727X. DOI: 10.1016/0142-727X(94)90031-0.

[114] Renwei Mei and James F. Klausner. "Unsteady force on a spherical bubble at finite Reynolds number with small fluctuations in the free-stream velocity". In: *Physics of Fluids A: Fluid Dynamics* 4.1 (Jan. 1992). Publisher: American Institute of Physics, pp. 63–70. ISSN: 0899-8213. DOI: 10.1063/1.858501.

[115] B. B Mikic, W. M Rohsenow, and P Griffith. "On bubble growth rates". In: *International Journal of Heat and Mass Transfer* 13.4 (Apr. 1, 1970), pp. 657–666. ISSN: 0017-9310. DOI: 10.1016/0017-9310(70)90040-2.

[116] Louis Melville Milne-Thomson. *Theoretical Hydrodynamics*. Macmillan and Company, limited, 1938. 590 pp.

[117] S. Mimouni, C. Baudry, M. Guingo, J. Lavieville, N. Merigoux, and N. Mechitoua. "Computational multi-fluid dynamics predictions of critical heat flux in boiling flow". In: *Nuclear Engineering and Design*. CFD4NRS-5 299 (Apr. 1, 2016), pp. 28–36. ISSN: 0029-5493. DOI: 10.1016/j.nucengdes.2015.07.017.

[118] S. Mimouni, J. Laviéville, N. Seiler, and P. Ruyer. "Combined evaluation of second order turbulence model and polydispersion model for two-phase boiling flow and application to fuel assembly analysis". In: *Nuclear Engineering and Design*. 13th International Topical Meeting on Nuclear Reactor Thermal Hydraulics (NURETH-13) 241.11 (Nov. 1, 2011), pp. 4523–4536. ISSN: 0029-5493. DOI: 10.1016/j.nucengdes.2010.12.028.

[119] Michaël Montout. "Contribution au développement d'une Approche Prédictive Locale de la crise d'ébullition". These de doctorat. Toulouse, INPT, Jan. 21, 2009.

[120] P. de. Munk. *Two-phase flow experiments in a 10 m long sodium heated steam generator test section*. AED-Conf–73-445-021 INIS Reference Number: 5098086. Germany, 1973, p. 2.

[121] F. Nicoud and F. Ducros. "Subgrid-Scale Stress Modelling Based on the Square of the Velocity Gradient Tensor". In: *Flow, Turbulence and Combustion* 62.3 (Sept. 1, 1999), pp. 183–200. ISSN: 1573-1987. DOI: 10.1023/A:1009995426001.

[122] V. S. Nikolayev and D. A. Beysens. "Boiling crisis and non-equilibrium drying transition". In: *Europhysics Letters* 47.3 (Aug. 1, 1999). Publisher: IOP Publishing, p. 345. ISSN: 0295-5075. DOI: 10.1209/epl/i1999-00395-x.

[123] V. S. Nikolayev, D. Chatain, Y. Garrabos, and D. Beysens. "Experimental Evidence of the Vapor Recoil Mechanism in the Boiling Crisis". In: *Physical Review Letters* 97.18 (Nov. 2, 2006). Publisher: American Physical Society, p. 184503. DOI: 10.1103/PhysRevLett.97.184503.

[124] V. Nikolayev, Y. Garrabos, C. Lecoutre, T. Charignon, D. Hitz, D. Chatain, R. Guillaument, S. Marre, and D. Beysens. "Boiling Crisis Dynamics: Low Gravity Experiments at High Pressure". In: *Microgravity Science and Technology* 27.4 (July 1, 2015), pp. 253–260. ISSN: 1875-0494. DOI: 10.1007/s12217-015-9447-8.

[125] L'Usine Nouvelle. "La cuve de l'EPR finlandais est posée". In: (June 21, 2010). Publisher: www.usinenouvelle.com.

[126] Shiro Nukiyama. "The maximum and minimum values of the heat Q transmitted from metal to boiling water under atmospheric pressure". In: *International Journal of Heat and Mass Transfer* 9.12 (Dec. 1, 1966), pp. 1419–1433. ISSN: 0017-9310. DOI: 10.1016/0017-9310(66)90138-4.

[127] Tomio Okawa, Tatsuhiro Ishida, Isao Kataoka, and Michitsugu Mori. "Bubble rise characteristics after the departure from a nucleation site in vertical upflow boiling of subcooled water". In: *Nuclear Engineering and Design*. Festschrift Edition Celebrating the 65th Birthday of Prof. Richard T. Lahey, Jr. 235.10 (May 1, 2005), pp. 1149–1161. ISSN: 0029-5493. DOI: 10.1016/j.nucengdes.2005.02.012.

[128] Tomio Okawa, Kazuhiro Kaiho, Shintaro Sakamoto, and Koji Enoki. "Observation and modelling of bubble dynamics in isolated bubble regime in subcooled flow boiling". In: *Nuclear Engineering and Design* 335 (Aug. 15, 2018), pp. 400–408. ISSN: 0029-5493. DOI: 10.1016/j.nucengdes.2018.06.009.

[129] M. S. Plesset and S. A. Zwick. "The Growth of Vapor Bubbles in Superheated Liquids". In: *Journal of Applied Physics* 25.4 (Apr. 1954). Number: 4, pp. 493–450. ISSN: 0021-8979.

[130] Michael Z. Podowski and Raf M. Podowski. "Mechanistic Multidimensional Modeling of Forced Convection Boiling Heat Transfer". In: *Science and Technology of Nuclear Installations* 2009 (Dec. 22, 2008). Publisher: Hindawi, e387020. ISSN: 1687-6075. DOI: 10.1155/2009/387020.

[131] V Prodanovic, D Fraser, and M Salcudean. "Bubble behavior in subcooled flow boiling of water at low pressures and low flow rates". In: *International Journal of Multiphase Flow* 28.1 (Jan. 1, 2002), pp. 1–19. ISSN: 0301-9322. DOI: 10.1016/S0301-9322(01)00058-1.

[132] Stéphane Pujet. *Mémento Technique de l'Equipement: La Crise d'Ebullition dans les REP*. Internal Note D305915000442. EDF SA, 2016.

[133] W. E. Ranz. "Evaporation from drops". In: *Chemical Engineering Progress* (Jan. 1, 1952). ISSN: 0360-7275.

[134] Madhumitha Ravichandran and Matteo Bucci. "Online, quasi-real-time analysis of high-resolution, infrared, boiling heat transfer investigations using artificial neural networks". In: *Applied Thermal Engineering* 163 (Dec. 25, 2019), p. 114357. ISSN: 1359-4311. DOI: 10.1016/j.applthermaleng.2019.114357.

[135] Madhumitha Ravichandran and Matteo Bucci. "Infrared Thermometry and Artifical Intelligence Provide Real-Time Insights into Boiling Heat Transfer". In: *Proc. International Topical Meeting on Advances in Thermal Hydraulics 2022*. Advances in Thermal Hydraulics 2022 (ATH'22). Anaheim, CA, USA, June 2022. ISBN: 978-0-89448-781-1.

[136] Lord Rayleigh. "VIII. On the pressure developed in a liquid during the collapse of a spherical cavity". In: *The London, Edinburgh, and Dublin Philosophical Magazine and Journal of Science* 34.200 (Aug. 1, 1917), pp. 94–98. ISSN: 1941-5982. DOI: 10.1080/14786440808635681.

[137] H. Reichardt. "Vollständige Darstellung der turbulenten Geschwindigkeitsverteilung in glatten Leitungen". In: *Zeitschrift Angewandte Mathematik und Mechanik* 31 (Jan. 1, 1951). ADS Bibcode: 1951ZaMM...31..208R, pp. 208–219. ISSN: 0044-2267. DOI: 10.1002/zamm.19510310704.

[138] Tingting Ren, Zhiqiang Zhu, Rui Zhang, Jiangwu Shi, and Changqi Yan. "Development of force balance model for prediction of bubble departure diameter and lift-off diameter in subcooled flow boiling". In: *International Journal of Heat and Mass Transfer* 161 (Nov. 1, 2020), p. 120245. ISSN: 0017-9310. DOI: 10.1016/j.ijheatmasstransfer.2020.120245.

[139] Andrew Jonathan Richenderfer. "Experimental study of heat flux partitioning in pressurized subcooled flow boiling". Accepted: 2018-11-15T15:51:52Z. Thesis. Massachusetts Institute of Technology, 2018.

[140] Andrew Richenderfer, Artyom Kossolapov, Jee Hyun Seong, Giacomo Saccone, Etienne Demarly, Ravikishore Kommajosyula, Emilio Baglietto, Jacopo Buongiorno, and Matteo Bucci. "Investigation of subcooled flow boiling and CHF using high-resolution diagnostics". In: *Experimental Thermal and Fluid Science* 99 (Dec. 1, 2018), pp. 35–58. ISSN: 0894-1777. DOI: 10.1016/j.expthermflusci.2018.07.017.

[141] E. Ruckenstein. "On mass transfer in the continuous phase from spherical bubbles or drops". In: *Chemical Engineering Science* 19.2 (Feb. 1, 1964), pp. 131–146. ISSN: 0009-2509. DOI: 10.1016/0009-2509(64)85117-4.

[142] Pierre Ruyer and Nathalie Seiler. "Modélisation avancée de la polydispersion en taille des écoulements bouillants". In: *La Houille Blanche* 4 (Aug. 1, 2009). Number: 4 Publisher: EDP Sciences, pp. 65–71. ISSN: 0018-6368, 1958-5551. DOI: 10.1051/lhb/2009046.

[143] P. G. Saffman. "The lift on a small sphere in a slow shear flow". In: *Journal of Fluid Mechanics* 22.2 (June 1965), pp. 385–400. ISSN: 0022-1120, 1469-7645. DOI: 10.1017/S0022112065000824.

[144] V. Scheiff, F. Bergame, J. Sebilleau, P. Ruyer, and C. Colin. "Experimental study of steady and transient subcooled flow boiling". In: *International Journal of Heat and Mass Transfer* 164 (Jan. 1, 2021), p. 120548. ISSN: 0017-9310. DOI: 10.1016/j.ijheatmasstransfer.2020.120548.

[145] Valentin Scheiff. "Etude expérimentale et modélisation du transfert de chaleur de l'ébullition transitoire". These de doctorat. Toulouse, INPT, Dec. 13, 2018.

[146] L. E. Scriven. "On the dynamics of phase growth". In: *Chemical Engineering Science* 10.1 (Apr. 1, 1959), pp. 1–13. ISSN: 0009-2509. DOI: 10.1016/0009-2509(59)80019-1.

[147] Pengyu Shi, Roland Rzehak, Dirk Lucas, and Jacques Magnaudet. "Drag and lift forces on a rigid sphere immersed in a wall-bounded linear shear flow". In: *Physical Review Fluids* 6.10 (Oct. 28, 2021). Number: 10 Publisher: American Physical Society, p. 104309. ISSN: 2469-990X.

[148] Rong Situ, Takashi Hibiki, Mamoru Ishii, and Michitsugu Mori. "Bubble lift-off size in forced convective subcooled boiling flow". In: *International Journal of Heat and Mass Transfer* 48.25 (Dec. 1, 2005), pp. 5536–5548. ISSN: 0017-9310. DOI: 10.1016/j.ijheatmasstransfer.2005.06.031.

[149] Jia-Wen Song and Li-Wu Fan. "Temperature dependence of the contact angle of water: A review of research progress, theoretical understanding, and implications for boiling heat transfer". In: *Advances in Colloid and Interface Science* 288 (Feb. 1, 2021), p. 102339. ISSN: 0001-8686. DOI: 10.1016/j.cis.2020.102339.

[150] Charles G. Speziale, Sutanu Sarkar, and Thomas B. Gatski. "Modelling the pressure–strain correlation of turbulence: an invariant dynamical systems approach". In: *Journal of Fluid Mechanics* 227 (June 1991). Publisher: Cambridge University Press, pp. 245–272. ISSN: 1469-7645, 0022-1120. DOI: 10.1017/S0022112091000101.

[151] R. Sugrue and J. Buongiorno. "A modified force-balance model for prediction of bubble departure diameter in subcooled flow boiling". In: *Nuclear Engineering and Design* 305 (Aug. 15, 2016), pp. 717–722. ISSN: 0029-5493. DOI: 10.1016/j.nucengdes.2016.04.017.

[152] R. Sugrue, J. Buongiorno, and T. McKrell. "An experimental study of bubble departure diameter in subcooled flow boiling including the effects of orientation angle, subcooling, mass flux, heat flux, and pressure". In: *Nuclear Engineering and Design*. SI : CFD4NRS-4 279 (Nov. 1, 2014), pp. 182–188. ISSN: 0029-5493. DOI: 10.1016/j.nucengdes.2014.08.009.

[153] Rosemary M. Sugrue. "The Effects of Orientation Angle, Subcooling, Heat Flux, Mass Flux, and Pressure on Bubble Growth and Detachment in Subcooled Flow Boiling". PhD thesis. Massachusetts Institute of Technology, 2012.

[154] M. Sultan and R. L. Judd. "Spatial Distribution of Active Sites and Bubble Flux Density". In: *Journal of Heat Transfer* 100.1 (Feb. 1, 1978), pp. 56–62. ISSN: 0022-1481. DOI: 10.1115/1.3450504.

[155] J. R. S. Thom, W. M. Walker, T. A. Fallon, and G. F. S. Reising. "Boiling In Sub-Cooled Water During Flow Up Heated Tubes or Annuli." In: *Proc. Inst. Mech. Eng. (London), 180: Pt 3C, 226-46(1965-66).* (Oct. 31, 1967). Institution: Babcock and Wilcox Ltd., Renfrew, Eng.

[156] G. E. Thorncroft, J. F. Klausner, and R. Mei. "An experimental investigation of bubble growth and detachment in vertical upflow and downflow boiling". In: *International Journal of Heat and Mass Transfer* 41.23 (Dec. 1, 1998), pp. 3857–3871. ISSN: 0017-9310. DOI: 10.1016/S0017-9310(98)00092-1.

[157] G.E. Thorncroft, J.F. Klausner, and R. Mei. "Bubble forces and detachment models". In: *Multiphase Science and Technology* 13.3 (2001), pp. 35–76. ISSN: 0276-1459. DOI: 10.1615/multscientechn.v13.i3-4.20.

[158] V. I. Tolubinsky and D. M. Kostanchuk. "VAPOUR BUBBLES GROWTH RATE AND HEAT TRANSFER INTENSITY AT SUBCOOLED WATER BOILING". In: International Heat Transfer Conference 4. Begel House Inc., 1970. DOI: 10.1615/IHTC4.250.

[159] Akio Tomiyama, Hidesada Tamai, Iztok Zun, and Shigeo Hosokawa. "Transverse migration of single bubbles in simple shear flows". In: *Chemical Engineering Science* 57.11 (June 1, 2002), pp. 1849–1858. ISSN: 0009-2509. DOI: 10.1016/S0009-2509(02)00085-4.

[160] L. S. Tong. "Prediction of departure from nucleate boiling for an axially non-uniform heat flux distribution". In: *Journal of Nuclear Energy* 21.3 (Jan. 1, 1967), pp. 241–248. ISSN: 0022-3107. DOI: 10.1016/S0022-3107(67)90054-8.

[161] G. G. Treshchev. "The number of vapor-formation centers in surface boiling". In: *Convective Heat Transfer in Two-Phase and One-Phase Flows.* Borishanskii V.M. and Paleev I.I. Jerusalem: Israel Program for Scientific Translations, 1969, pp. 97–105.

[162] A. Urbano, S. Tanguy, and C. Colin. "Direct numerical simulation of nucleate boiling in zero gravity conditions". In: *International Journal of Heat and Mass Transfer* 143 (Nov. 1, 2019), p. 118521. ISSN: 0017-9310. DOI: 10.1016/j.ijheatmasstransfer.2019.118521.

[163] A. Urbano, S. Tanguy, G. Huber, and C. Colin. "Direct numerical simulation of nucleate boiling in micro-layer regime". In: *International Journal of Heat and Mass Transfer* 123 (Aug. 1, 2018), pp. 1128–1137. ISSN: 0017-9310. DOI: 10.1016/j.ijheatmasstransfer.2018.02.104.

[164] W. G. J. Van Helden, C. W. M. Van Der Geld, and P. G. M. Boot. "Forces on bubbles growing and detaching in flow along a vertical wall". In: *International Journal of Heat and Mass Transfer* 38.11 (July 1, 1995), pp. 2075–2088. ISSN: 0017-9310. DOI: 10.1016/0017-9310(94)00319-Q.

[165] J. Weisman and B. S. Pei. "Prediction of critical heat flux in flow boiling at low qualities". In: *International Journal of Heat and Mass Transfer* 26.10 (Oct. 1, 1983), pp. 1463–1477. ISSN: 0017-9310. DOI: 10.1016/S0017-9310(83)80047-7.

[166] L. Van Wijngaarden and D. J. Jeffrey. "Hydrodynamic interaction between gas bubbles in liquid". In: *Journal of Fluid Mechanics* 77.1 (Sept. 1976). Publisher: Cambridge University Press, pp. 27–44. ISSN: 1469-7645, 0022-1120. DOI: 10.1017/S0022112076001110.

[167] Yugong Wu, Zhigang Fan, and Yuzhu Lu. "Bulk and interior packing densities of random close packing of hard spheres". In: *Journal of Materials Science* 38.9 (May 1, 2003), pp. 2019–2025. ISSN: 1573-4803. DOI: 10.1023/A:1023597707363.

[168] G. H. Yeoh, Sherman C. P. Cheung, J. Y. Tu, and Mark K. M. Ho. "Fundamental consideration of wall heat partition of vertical subcooled boiling flows". In: *International Journal of Heat and Mass Transfer* 51.15 (July 15, 2008), pp. 3840–3853. ISSN: 0017-9310. DOI: 10.1016/j.ijheatmasstransfer.2007.11.047.

[169] Junsoo Yoo, Carlos E. Estrada-Perez, and Yassin A. Hassan. "Experimental study on bubble dynamics and wall heat transfer arising from a single nucleation site at subcooled flow boiling conditions – Part 1: Experimental methods and data quality verification". In: *International Journal of Multiphase Flow* 84 (Sept. 1, 2016), pp. 315–324. ISSN: 0301-9322. DOI: 10.1016/j.ijmultiphaseflow.2016.04.018.

[170] Junsoo Yoo, Carlos E. Estrada-Perez, and Yassin A. Hassan. "Experimental study on bubble dynamics and wall heat transfer arising from a single nucleation site at subcooled flow boiling conditions – Part 2: Data analysis on sliding bubble characteristics and associated wall heat transfer". In: *International Journal of Multiphase Flow* 84 (Sept. 1, 2016), pp. 292–314. ISSN: 0301-9322. DOI: 10.1016/j.ijmultiphaseflow.2016.04.019.

[171] Junsoo Yoo, Carlos E. Estrada-Perez, and Yassin A. Hassan. "Area of bubble influence due to sliding bubbles in subcooled boiling flow". In: *International Journal of Heat and Mass Transfer* 125 (Oct. 1, 2018), pp. 43–52. ISSN: 0017-9310. DOI: 10.1016/j.ijheatmasstransfer.2018.04.058.

[172] Junsoo Yoo, Carlos E. Estrada-Perez, and Yassin A. Hassan. "Development of a mechanistic model for sliding bubbles growth prediction in subcooled boiling flow". In: *Applied Thermal Engineering* 138 (June 25, 2018), pp. 657–667. ISSN: 1359-4311. DOI: 10.1016/j.applthermaleng.2018.04.096.

[173] Youngik Yoo, Kyounghong Kim, Kyongbo Eom, and Seongki Lee. "Finite element analysis of the mechanical behavior of a nuclear fuel assembly spacer grid". In: *Nuclear Engineering and Design* 352 (Oct. 1, 2019), p. 110179. ISSN: 0029-5493. DOI: 10.1016/j.nucengdes.2019.110179.

[174] Byong-Jo Yun, Andrew Splawski, Simon Lo, and Chul-Hwa Song. "Prediction of a subcooled boiling flow with advanced two-phase flow models". In: *Nuclear Engineering and Design*. SI : CFD4NRS-3 253 (Dec. 1, 2012), pp. 351–359. ISSN: 0029-5493. DOI: 10.1016/j.nucengdes.2011.08.067.

[175] L. Z. Zeng, J. F. Klausner, D. M. Bernhard, and R. Mei. "A unified model for the prediction of bubble detachment diameters in boiling systems—II. Flow boiling". In: *International Journal of Heat and Mass Transfer* 36.9 (Jan. 1, 1993), pp. 2271–2279. ISSN: 0017-9310. DOI: 10.1016/S0017-9310(05)80112-7.

[176] Lanying Zeng, Fady Najjar, S. Balachandar, and Paul Fischer. "Forces on a finite-sized particle located close to a wall in a linear shear flow". In: *Physics of Fluids* 21.3 (Mar. 2009). Publisher: American Institute of Physics, p. 033302. ISSN: 1070-6631. DOI: 10.1063/1.3082232.

[177] Limiao Zhang. "A new triggering mechanism of the boiling crisis based on the percolation theory and its implication". Accepted: 2022-06-15T12:59:30Z. Thesis. Massachusetts Institute of Technology, Feb. 2022.

[178] Limiao Zhang, Jee Hyun Seong, and Matteo Bucci. "Percolative Scale-Free Behavior in the Boiling Crisis". In: *Physical Review Letters* 122.13 (Apr. 5, 2019). Publisher: American Physical Society, p. 134501. DOI: 10.1103/PhysRevLett.122.134501.

[179] Pei Zhou, Shiyang Hua, Cai Gao, Dongfang Sun, and Ronghua Huang. "A mechanistic model for wall heat flux partitioning based on bubble dynamics during subcooled flow boiling". In: *International Journal of Heat and Mass Transfer* 174 (Aug. 1, 2021), p. 121295. ISSN: 0017-9310. DOI: 10.1016/j.ijheatmasstransfer.2021.121295.

[180] Pei Zhou, Ronghua Huang, Sheng Huang, Yu Zhang, and Xiaoxuan Rao. "Experimental investigation on active nucleation site density and bubble departure frequency in subcooled flow boiling by using bubble tracking algorithm". In: *International Journal of Heat and Mass Transfer* 148 (Feb. 1, 2020), p. 119081. ISSN: 0017-9310. DOI: 10.1016/j.ijheatmasstransfer.2019.119081.

[181] Pei Zhou, Ronghua Huang, Sheng Huang, Yu Zhang, and Xiaoxuan Rao. "Experimental investigation on bubble contact diameter and bubble departure diameter in horizontal subcooled flow boiling". In: *International Journal of Heat and Mass Transfer* 149 (Mar. 1, 2020), p. 119105. ISSN: 0017-9310. DOI: 10.1016/j.ijheatmasstransfer.2019.119105.

[182] N. Zuber. "On the dispersed two-phase flow in the laminar flow regime". In: *Chemical Engineering Science* 19.11 (Nov. 1, 1964), pp. 897–917. ISSN: 0009-2509. DOI: 10.1016/0009-2509(64)85067-3.

[183] Novak Zuber. "Hydrodynamic Aspects of Boiling Heat Transfer". PhD thesis. Los Angeles, California: University of California Los Angeles, June 1959.

[184] Novak Zuber. "The dynamics of vapor bubbles in nonuniform temperature fields". In: *International Journal of Heat and Mass Transfer* 2.1 (Mar. 1, 1961), pp. 83–98. ISSN: 0017-9310. DOI: 10.1016/0017-9310(61)90016-3.

[185] *code_saturne 7.1 Theory Guide*. Dec. 2021.

[186] H. C. Ünal. "Maximum bubble diameter, maximum bubble-growth time and bubble-growth rate during the subcooled nucleate flow boiling of water up to 17.7 MN/m2". In: *International Journal of Heat and Mass Transfer* 19.6 (June 1, 1976), pp. 643–649. ISSN: 0017-9310. DOI: 10.1016/0017-9310(76)90047-8.